TADF Copper(I) Complexes – from Synthesis to Application in OLEDs and 3D Laser Nanoprinting

Zur Erlangung des akademischen Grades einer

DOKTORIN DER NATURWISSENSCHAFTEN

(Dr. rer. nat.)

von der KIT-Fakultät für Chemie und Biowissenschaften

des Karlsruher Instituts für Technologie (KIT)

genehmigte

DISSERTATION

von

M.Sc. Clara Rosa Adam

aus Berlin

1. Referent: Prof. Dr. Stefan Bräse

2. Referent: Prof. Dr. Ulrich Lemmer

Tag der mündlichen Prüfung: 12.12.2024

“You cannot get through a single day without having an impact on the world around you. What you do makes a difference, and you have to decide what kind of difference you want to make.”

— Jane Goodall —

Declaration of honesty

This work was carried out from June 2021 through October 2024 at the Institute of Organic Chemistry, Faculty of Chemistry and Biosciences at the Karlsruhe Institute of Technology (KIT) under the supervision of Prof. Dr. Stefan Bräse.

Die vorliegende Arbeit wurde im Zeitraum vom Juni 2021 bis Oktober 2024 am Institut für Organische Chemie (IOC) der Fakultät für Chemie und Biowissenschaften am Karlsruher Institut für Technologie (KIT) unter der Leitung von Prof. Dr. Stefan Bräse angefertigt.

Hiermit versichere ich, CLARA ROSA ADAM*, die vorliegende Arbeit selbstständig verfasst und keine anderen als die angegebenen Hilfsmittel verwendet sowie Zitate kenntlich gemacht zu haben. Die Dissertation wurde bisher an keiner anderen Hochschule oder Universität eingereicht.*

Hereby I, CLARA ROSA ADAM, declare that I completed the work independently, without any improper help and that all material published by others is cited properly. This thesis has not been submitted to any other university before.

Karlsruhe, October 29th 2024

German Title of this Thesis

TADF Kupfer(I) Komplexe – Von der Synthese zu Anwendungen in OLEDs und 3D Laser Nanodruck

Table of contents

Kurzzusammenfassung

In unserer heutigen Gesellschaft sind Materialen, die in der Lage sind, mit Licht zu interagieren, unverzichtbar geworden. Unter anderem werden organische und metallorganische Materialen bereits erfolgreich in zahlreichen Gebieten angewendet, wie beispielsweise in organischen Leuchtdioden (OLEDs) oder im 3D-Laser Druck.[1-4] Um der stetig wachsenden Nachfrage nach schnelleren und effizienteren Lösungen unter Berücksichtigung ökologischer Fragen nachzukommen, ist die Entwicklung neuer Emitter-Materialien essenziell. In der vorliegenden Arbeit, wurden neue mono-, di-, und tetranukleare Kupfer(I)-Komplexe hergestellt und untersucht. Die ersten beiden Projekte konzentrierten sich auf die strukturellen und photophysikalischen Eigenschaften der Komplexe. Im ersten Projekt wurde die Koordinationschemie von 3-Pyridylphosphin (3-PyrPhos) mit verschiedenen Kupfer(I)-(pseudo)halogeniden (CuX = I, Br, Cl, CN, SCN) und Silber(I)-halogeniden untersucht. Dies führte zu einem neuartigen zweifach verbrückten Kupfer(I)-Komplex vom Typ $(3\text{-PyrPhos})_4Cu_2X_2$. Die Struktur zeigte einen außergewöhnlich hohen intramolekularen Cu···Cu Abstand, mit einer durchschnittlichen Länge von 6.238 Å. Die Kupfer(I)-Komplexe zeigten eine ungewöhnliche Anregungswellenlängen-abhängige Emission, mit Maxima im Bereich von 510 bis 570 nm. Zur genaueren Untersuchung wurden temperaturabhängige Messungen durchgeführt. Im zweiten Projekt wurden einkernige Kuper(I)-Komplexe mit Chinolin- und Isochinolin-Liganden untersucht, die mehrere Emissionsmaxima zwischen 485 nm und 635 nm mit Quanteneffizienzen bis zu 24% aufwiesen. Das dritte Projekt konzentrierte sich auf die Entwicklung, vernetzbarer Kupfer(I)-Komplexen, mit terminalen Alkin- oder Methacrylat-gruppen im Liganden, um in einer späteren autokatalysierten Klick-Reaktion oder Photopolymerisation reagieren zu können. Erhaltene zweikernige Komplexe wiesen eine hohe Löslichkeit von mehr als 20 mg/ml in mindestens einem Lösungsmittel (Toluol, Chlorbenzol, DCM) auf, was sie zu idealen Kandidaten für lösungsprozessierte OLEDs macht. Die Komplexe zeigten eine hervorragende Photolumineszenz im grün-blauen bis gelben Bereich mit Quantenausbeuten von bis zu 99%. Ausgewählte Komplexe wurden während eines Forschungsaufenthalts an der Universität Durham (UK) in lösungsgefertigten OLEDs verbaut, was zu externen Quanteneffizienzen bis zu 8,9% und Leuchtdichten bis zu ~5000 cd m^{-2} führte. Darüber hinaus wurden zweikernige Komplexe mit Methacrylat-Liganden im 3D Laser-Nanodruck mit 2-Photonen-Absorption eingesetzt, was zu hochauflösenden Strukturen führte.

Abstract

Materials that can interact with light are becoming indispensable in modern society. Among many, organic or organometallic materials have been successfully applied in various applications, such as organic light emitting diodes (OLEDs) or 3D printing.[1-4] The design of novel emitting materials is essential to meet the steady need for faster solutions and improved performance while addressing environmental issues, that are more important than ever. In this work, new mono-, di- and tetranuclear copper(I) complexes were synthesized and investigated with the aim to use their emitting properties in various applications.

The first two projects focused on the structural and photophysical properties of the complexes. In the first project, the coordination chemistry of 3-pyridylphosphine (3-PyrPhos) with various copper(I) (pseudo)halides (CuX, X = I, Br, Cl, CN, SCN) and silver(I) halides was investigated. This resulted in a novel dibridged dinuclear copper(I) complex structure of the type $(3\text{-PyrPhos})_4Cu_2X_2$. The examination of the structure revealed an exceptionally high intramolecular Cu···Cu distance, with an average distance of 6.238 Å. The complexes showed an uncommon excitation-dependent behavior, with emission maxima ranging from 510-570 nm. Temperature-dependent measurements were conducted to study this in more detail. In the second project, mononuclear complexes featuring quinoline and isoquinoline ligands were investigated, showing variable emission maxima between 485 nm and 635 nm, with quantum yields up to 24%.

The third project focused on the design of crosslinkable copper(I) complexes featuring either terminal alkynes or methacrylate units at the ligands to be able to react in an autocatalyzed click-reaction or photopolymerization. A series of new mononuclear, dinuclear, and tetranuclear complexes were synthesized, which all obtained at least two crosslinking sites. For all dinuclear complexes, a high solubility of larger than 20 mg/ml in at least one solvent out of toluene, chlorobenzene, or DCM was observed, making them ideal candidates for solution-processed OLEDs. The complexes showed superior photoluminescence in the greenish-blue to yellow region with quantum yields up to 99%. During an international research stay at the University of Durham (UK), selected complexes were applied in solution-processed OLEDs, resulting in devices with external quantum efficiencies (EQE) of up to 8.9% with luminances (L_{max}) up to ~5000 cd m^{-2}. Moreover, dinuclear complexes featuring methacrylate ligands were applied in 3D laser nanoprinting using 2-photon absorption, resulting in high-resolution structures.

1 Introduction

In modern society, materials which use or emit light in some form, have become indispensable. They are employed as emitting compounds in light emitting diodes (LEDs) or advanced display technologies based on organic light emitting diodes (OLED) which can be used in mobile phones or televisions. In an OLED, electrical energy is converted into light by emissive compounds, which results in several advantages compared to established technologies like LEDs and LCDs (liquid crystal diodes).[3] They don't need a background lighting as used for LCDs for instance, which makes them more energy efficient and results in higher contrasts and the possibility to fabricate semi-transparent and thin, flexible and large sized devices.[3] However, emissive materials also play an important role in less obvious areas, and are applied in a variety of applications, including bioimaging,[5-7] photovoltaics,[8-10] sensors[11-12] or as photoinitiators in 3D laser printing.[1-2] The investigation on novel materials, which exhibit specific luminescent properties gained significant importance in recent years, in particular to meet the steadily increasing need for enhanced performances, but also to address environmental issues, that are more in the focus than ever. Given that the described applications are all based on fundamental processes caused by the interactions of matter and light, the basic photophysical principles will be presented in the following sections. A particular interest will be on the emission pathway of thermally activated delayed fluorescence (TADF), which allows a theoretical quantum yield of 100% and therefore gained significant attention in recent years.[13] Among various organic materials, copper(I) complexes have emerged as promising material emitter class, as they are earth-abundant and often intrinsically exhibit TADF.[3] A particular focus will be on the presentation of the theoretical background of OLEDs and 3D laser nanoprinting *via* photopolymerization, since the emissive compounds in the present work were explored in these areas. The last subsections cover the chemistry and structural diversity of luminescent copper(I) complexes in general.

1.1 Photophysical basics

The understanding of the photophysical background is crucial for the development of novel emitters. In general, luminescence describes the emission of light upon relaxation from an energetically excited state to a ground state of a molecule.[14] Depending on the application this excited state can be initiated by photons (photoluminescence) or by applying of a voltage

(electroluminescence). For a better understanding, the fundamental processes after excitation will first be discussed for the case of photoluminescence and be later related to the excitation in OLEDs (electroluminescence).

Photoluminescence. All molecules exhibit discrete energy levels in their ground and excited states. When a molecule is excited with a photon, it can absorb the energy and depending on the photon energy an electron gets excited from the ground singlet state S_0 to a higher electronic singlet state S_n. This transition happens in the femtosecond range (10^{-15} s) and therefore follows the Franck-Condon principle, which can be applied when the electronic transition is faster than the nuclear motion.[15-17] The probability and degree of absorption is directly proportional to the extent of overlap between the vibrational wave functions of the ground and excited states. This phenomenon is quantified by the Franck-Condon factor.[18] The Perrin-Jabłoński diagram illustrates the different pathways which follow this excitation.[19-20] However, this Jabłoński diagram gives a simplified version without including energy differences through nuclear distances.

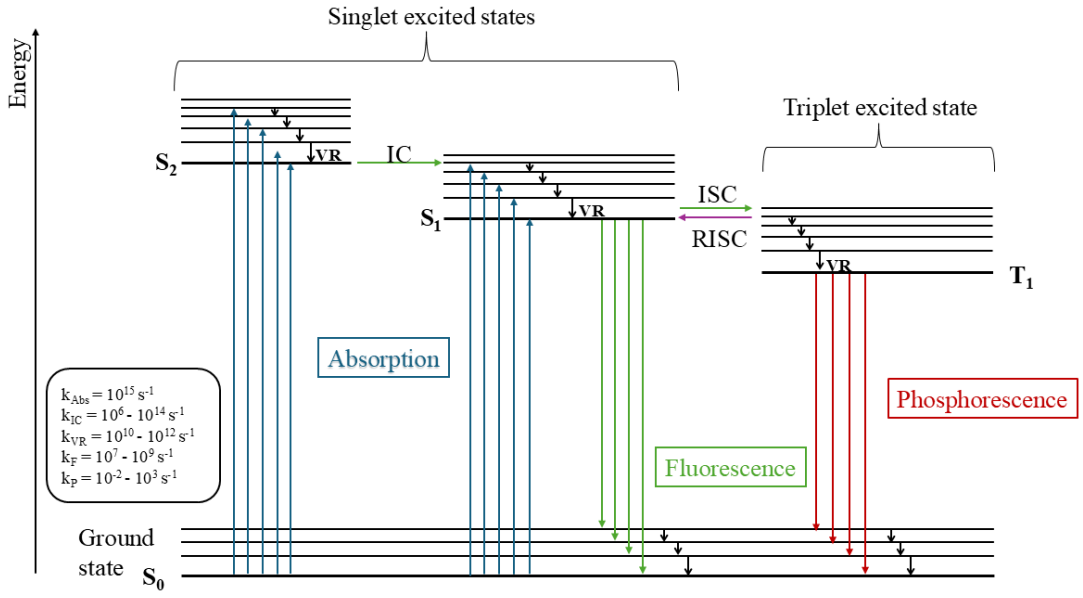

Figure 1. Simplified Jablonski diagram to illustrate the different photoluminescent transitions. Adapted from the literature.[19-22]

The absorption process is illustrated by blue arrows. Through vibrational relaxation (VR), transitions between higher excited states S_n to the respective energetically lower excited ground state occur. Through the non-radiative internal conversion (IC), a transition between isoenergetic vibrational levels of two different states of the same multiplicity is possible and

the lowest excited ($S_n \rightarrow S_1$).[22] In Figure 1 this is shown as an example for $S_2 \rightarrow S_1$. It is noteworthy, that the term 'vibrational' refers to changes of vibrational energy levels within an electronic state, whereas 'vibronic' refers to a transition where a combination of vibrational and electronic transition is observed.[19] All following processes, radiative or non-radiative are coming from the vibrational ground state of the electronic excited state , following the Kasha's rule.[23-24] The following vibronic transition to the electronic ground state, can occur *via* different processes, namely fluorescence, phosphorescence and thermally activated delayed fluorescence (TADF).[22] Typical time ranges for each transition are found in Figure 1.

If the first excited singlet state directly deactivates to the energy ground state ($S_1 \rightarrow S_0$), this can either happen non-radiatively through vibronic relaxation or radiatively through fluorescence (10^{-9}-10^{-7} s).[20] However, for metal complexes and some organic molecules, intersystem crossing (ISC) can occur, which describes the non-radiative transition between two electronic states with different multiplicity, for instance $S_1 \rightarrow T_1$.[19] This process is usually forbidden for organic molecules, which exhibit a low spin-orbit coupling (SOC), since it requires a change in the spin state of the electron.[19] However, by thoughtful design of organic molecules (donor-acceptor emitters) or metal complexes, with intrinsically high SOC, the process of ISC gets enabled.[3] A strong SOC results in an increased interaction between the total orbital angular momenta of spin and orbit.[22, 25] This is naturally given for heavy atoms (heavy-atom effect), which is why metal complexes often exhibit a high SOC and with that an efficient ISC.[22] The radiative deactivation from the excited triplet state T_1 to the electronic ground state S_0, called phosphorescence, follows the same principal, and thus is observed at a significantly longer timescale in the microsecond range.[20, 22]

Thermally activated delayed fluorescence. If the energy gap ΔE_{ST} between the excited singlet and triplet state is small enough, a reverse intersystem crossing (RISC) can occur through thermal activation, and the radiative decay occurs through depopulation of the excited singlet state S_1, *via* the triplet, to S_0 ($S_1 \rightarrow S_0$), which is known as thermally activated delayed fluorescence (TADF).[22]

At low temperatures, the emission lifetime of TADF is highly increased, caused by the decrease of thermal activation, and a bathochromic shift is observed, as the phosphorescence gets more dominant. For practical use ΔE_{ST} should not exceed 1000 cm^{-1} (0.12 eV) even though TADF is still observed for much higher values (ΔE_{ST} (eosin) ≈ 0.43 eV).[26]

Important parameters for TADF. The rate constant for RISC, k_{RISC} (s^{-1}) is directly related to ΔE_{ST} by following the ARRHENIUS equation, in which k_B is the Boltzmann constant and T is the absolute temperature (Equation 1).[27] The preexponential factor A describes the maximum theoretical rate, if no energy barriers were existent and is directly related to the SOC.

$$k_{RISC} \propto A * \exp\left(-\frac{\Delta E_{ST}}{k_B T}\right) \qquad \textbf{(1)}$$

This equation expresses, that k_{RISC} is enhanced with higher temperatures and smaller energy gaps ΔE_{ST}, as well as a high SOC.[28-29] Small values for ΔE_{ST} are observed by reducing the spatial overlap of the highest occupied molecular orbital (HOMO) and the lowest unoccupied molecular orbital (LUMO). This phenomenon is described through Equation 2 which shows the dependence of ΔE_{ST} from the exchange integral J of two unpaired electrons.[30-31]

$$\Delta E_{ST} = E_{S1} - E_{T1} = 2J \qquad \textbf{(2)}$$

The exchange integral is a quantum mechanical value that involves wavefunctions and electrons of the HOMO and LUMO and gives insight on the influence on the electronic interaction. With decreasing overlap of the frontier orbitals, the exchange energy J becomes smaller which directly reflects in a smaller value for ΔE_{ST}. However, it is also reported, that a too small overlap of the frontier orbitals leads to a reduction of the oscillator strength f, which results in a lower radiative rate. With that nonradiative decay channels can become more dominant.[30-31]

To sum up, for the design of an efficient TADF emitter, several points must be considered, most importantly:

1. Minimize ΔE_{ST} through a good spatial separation of HOMO and LUMO.
2. Suppress non-radiative decay.

Two important material classes are identified, that show an emission pathway *via* TADF. One major class being metal complexes, in particular copper(I) complexes, which usually intrinsically exhibit a good spatial separation of the HOMO and LUMO, with the HOMO being located on the copper core, and the electron accepting LUMO located on the ligands.[4] In recent years, additionally, silver(I) and gold(I/III) complexes were found to show TADF and studied for OLED application.[32-35]

However, for organic molecules, more specific design principles must be considered to ensure a small spatial overlap. For this, two design strategies are usually employed, either using twisted donor-acceptor (D-A) structures or large planar, polycyclic aromatic systems, which are called multi-resonance (MR) emitters.[36] In the following, the focus will be on metal complexes as no organic emitters were investigated in this work.

To determine the efficiency of the emissive material, all non-radiative and radiative transitions need to be considered. The photoluminescence quantum yield Φ_{PL} (PLQY), defined by Equation 3 describes these competing processes by including k_r and k_{nr} as rates for the radiative and non-radiative processes (s^{-1}).[37]

$$\Phi_{PL} = \frac{k_r}{k_{nr}+k_r} \qquad \textbf{(3)}$$

The lifetime of a specific transition is reciprocal related to all deactivation processes in this transition and can be calculated through the following equation:[20]

$$\tau = \frac{1}{k_{nr}+k_r} \qquad \textbf{(4)}$$

1.2 Applications

In the following two subsections, the theoretical background will be discussed for OLEDs and 3D laser printing applications, as selected complexes of this work were explored herein.

1.2.1 Organic Light Emitting Diodes (OLEDs)

1.2.1.1 Electroluminescence and exciton formation

A typical OLED consists of multiple layers, stacked between two electrodes on a glass or plastic substrate. An external voltage leads to the injection of charge carriers at the electrodes, in particular electrons and holes, which migrate through the device and recombine in the emissive layer (EML) by forming an exciton.[38] If it decays radiatively electroluminescence occurs. This form of luminescence follows the same concepts as described for photoluminescence, but some more aspects due to the interaction of the charge carrier wave functions and spin statistics need to be considered. Both charge carriers have the same magnitude of spin in an opposite direction (s = +1/2, -1/2). A linear combination of the wave functions results in four asymmetric wave functions, triplet states comprised of three substates and one singlet state.[39-40]

For distant electron-hole pairs they are assumed to be quasi-degenerated, which leads to a statistical population of a ratio of 25% for the singlet and 75% for the triplet states. At a smaller distance, due to a noticeable interaction between the wavefunctions, a splitting of the singlet and triplet energy states is observed.[39-40]

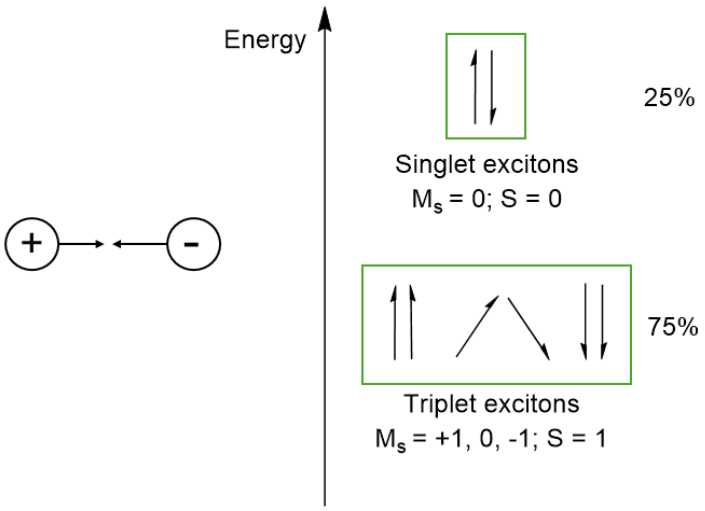

Figure 2. Hole electron recombination, resulting in exciton formation according to spin statistics. Adapted from [39, 41-42].

As described for photoluminescence, molecules, which obtain small SOC, show inefficient intersystem crossing pathways.[22] Therefore, they can only use 25% of all excitons for fluorescence, which means they show intrinsically low quantum efficiency of maximum 25%. For emitters that demonstrate a strong SOC the triplet states also get reachable and can be harvested, which leads to phosphorescence. When the singlet-triplet gap is small enough for effective RISC, TADF becomes feasable. Phosphorescent and TADF emitter can harvest all excitons, which leads to a theoretical internal quantum yield (IQE) of 100%.[3]

For some OLEDs the EML comprises of an additional host material.[4] In those cases, the exciton is often generated on the host and transferred to the emitter later on. This can either happen *via* Dexter or Förster processes. In Dexter processes the overall spin is retained and the excitons can directly be transferred to the emitter through an overlap of the wavefunctions between host and emitter.[43] Förster processes on the other hand are a transfer mechanism *via* dipole-dipole interaction.[44]

1.2.1.2 Device structure

The first efficient OLED was built in 1987 from TANG and VANSLYKE and paved the way for today's devices.[45] Their OLED was much simpler than the modern multi-layer architectures, just consisting of two organic layers between two electrodes. As emitting layer (EML) 8-hydroxyquinoline aluminum (**Alq_3**, **1**) was used, with an additional hole transporting layer consisting of an aromatic amine. This first green emitting OLED resulted in a device with an external quantum efficiency (EQE) of 1% and an operating voltage under 10 V.

Modern device architectures mostly consist of multiple layers, each having a specific role.[46] Base metals, such as aluminum, calcium or magnesium are used as cathode, followed by an electron injection layer (EIL) and electron transporting layers (ETL), the emissive layer (EML), hole injection and transporting layers (EIL/ETL), and lastly a transparent anode. A general device layout is shown in Figure 3.[4, 46].

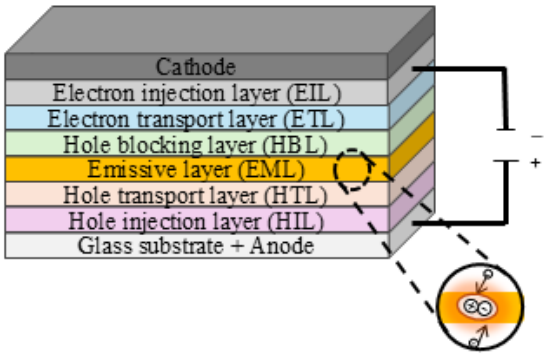

Figure 3. General device architecture of a multilayer OLED device. Adapted from the literature.[46]

The charge injections at the different layers can be treated as redox processes. By applying voltage, electrons are injected from the cathode to the ETL, whereas electrons are withdrawn by the anode from the HTL to form holes.[47] This directly corresponds to the injection of electrons into the LUMO and the removal of an electron from the HOMO and relates to the work function of the electrodes. This process of charge migration in the electric field can be imagined as electron "hopping", in which they "hop" in a row of reductions towards lower energy to the next molecule, while the holes migrate in the opposite direction upon formal oxidation (Figure 4).[48] Due to the high injection barriers, this leads to high driving voltages. Through the adjustment of the redox potential of the used layers to the work function Φ of the electrode in form of further ETLs and HTLs, the energy barrier can be reduced, which reduces the overall driving voltages.[38, 49] Moreover, blocking layers are sometimes included to confine the exciton formation on the emissive layer and suppress further charge carrier migration.[50-51]

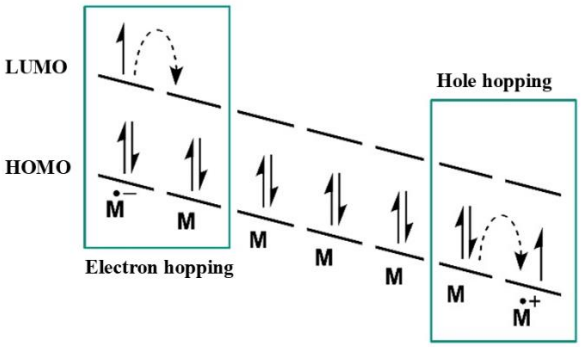

Figure 4. Illustration of the "hopping process" of charge carriers in a turned-on multi-layer OLED. Electrons move towards lower LUMO energies, whereas holes move towards higher lying HOMOs. This figure is recreated following the literature.[41, 52]

The anode is usually comprised of indium(III) tin(IV) oxide (ITO), a mixed oxide semiconductor.[51] However, also other conducting metals, such as gold, which show a high ionization energy can be used as well.[53] For the conductive layers large and rigid π-electron systems are used, that will shortly be described in the following. An overview of the mentioned materials for the conductive layers is presented Figure 5. A commonly used HIL is **PEDOT:PSS** (**2**), which displays a mixture of the two polymeric structures poly(3,4-ethylenedioxythiophene) and polystyrene sulfonate.[54] It decreases the injection barrier, smoothens the surface and transports the holes towards the EML. Typical HTL materials are 1,3-bis(N-carbazolyl)benzene (**mCP, 3**), triphenyl amine-based structures such as 4,4′,4″tris(carbazol-9-yl)triphenylamine (**TcTa, 4**) or the polymer poly(9-vinylcarbazole) (**PVK, 5**).[55-57] As they usually contain electron rich scaffolds such as carbazole, they also function as electron blocking layer of the electrons coming the cathode. The following EML consists of the emitting compound and often an additional host material. The host displays a crucial factor to obtain a favorable exciton transfer to the emitter. The HOMO and LUMO of the host must be in good alignment with the emitting material and the surrounding layers to ensure a balanced charge transport.[38] Typical host materials that were used for OLEDs with of copper(I) complexes are **mCP (3)**, 2,6-bis(9H-carbazol-9-yl)pyridine (**PYD-2Cz, 6**), 4,4′-bis(N-carbazolyl)-1,1′-biphenyl (**CBP, 7**).[58-63]

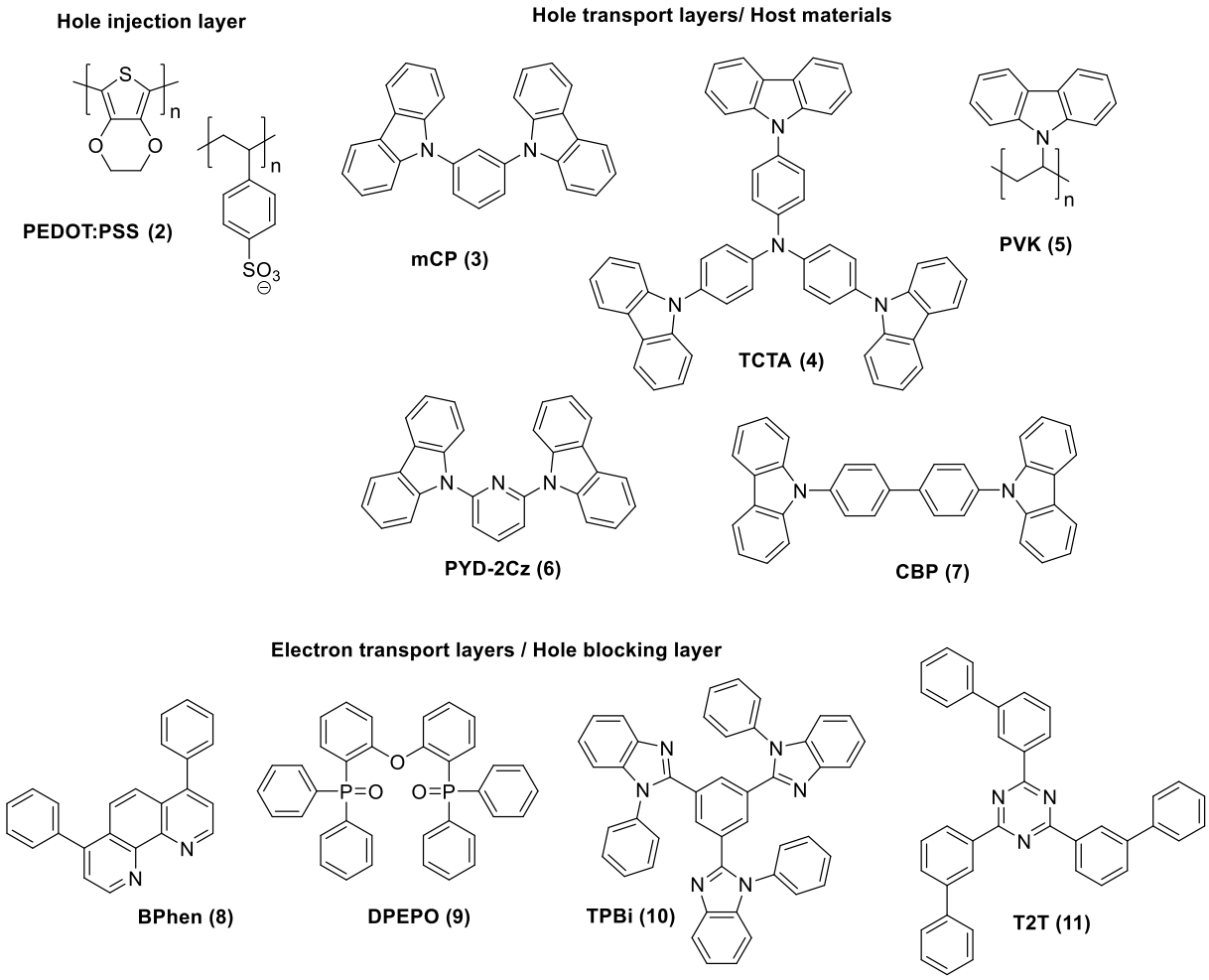

Figure 5. Overview of commonly used materials for different layers in OLED devices.[64]

Examples for hole-blocking materials are bathophenanthroline (**BPhen**, **8**) or bis(2-(diphenylphosphino)phenyl)ether oxide (**DPEPO**, **9**), which can also be used in the ETL.[65-66] Typical electron transporting materials are electron poor compounds such as 2,2′,2"-Benzol-1,3,5-triyltris(1-phenyl-1-H benzimidazole (**TPBi**, **10**) or 2,4,6-tris(biphenyl-3-yl)-1,3,5-triazine (**T2T**, **11**).[67-69] The last layer before the cathode, facilitates the electron injection and usually comprise of alkaline or earth alkaline fluorides such as lithium fluoride. Lastly, the cathode comprises of base metals, which exhibit low work function such as aluminium or magnesium.[51]

1.2.1.3 Device parameters

OLEDs are characterized through several values, such as turn-on voltage, luminance, efficiency and device lifetime.[70] The luminance L describes the brightness of the emitted light in candela per area (cd/m^2) and is highly dependent on the applied voltage.

The performance of an OLED can be described with the external quantum efficiency (EQE) which is also defined as the number of photons that are emitted compared to the injected charges.[70] The EQE can further be describes through the following formula:[38]

$$EQE = IQE \cdot \eta_{out} = \gamma \cdot \eta_r \cdot g_{eff} \cdot \eta_{out} \qquad \textbf{(5)}$$

The EQE of a device is related to the internal quantum efficiency (IQE) and the light-outcoupling factor η_{out}, which describes the ratio of photons exiting the device. Through reflections and differing refractive indexes between the different layer, a majority of the light gets lost in the outcoupling process, resulting in typically rather low values of $\eta_{out} \approx 0.20$ to 0.25.[71] The IQE is described by three factors: the charge balance factor γ, which includes the recombination rate of electrons and holes and is a measure for the charge balance; the radiative exciton fraction η_r , which includes information about the number of excitons that are available for luminescent transitions (0.25 for fluorescent, 1 for phosphorescent materials); and lastly the factor$\cdot g_{eff}$ which is determined by the photoluminescence quantum yield (Φ_{PL}).[51, 71-72]

For high brightnesses and increasing current densities, the efficiency of OLEDs tends to decrease, a phenomenon which is known as roll-off effect.[26] This effect should be minimized, to enhance the device lifetimes and decrease the power consumption.

1.2.1.4 Emitter materials

In the following, selected emitting materials will shortly be discussed. They can be divided into three main OLED generations, being fluorescent, phosphorescent and TADF materials.

First generation. The first generation of organic electroluminescent materials based on fluorescent emitters, show weak SOC and can therefore harvest the excitons through prompt fluorescence *via* the first excited singlet state, as shown in Figure 6. The IQE of these emitters is therefore intrinsically limited to 25%.[3] The already introduced emitter tri(8-hydroxyquinolinato) aluminum (**Alq$_3$**, **1**) (Chapter 1.2.1.2) of the first OLED from TANG and VANSLYKE is a prominent example of this generation, however this class is dominantly represented by organic molecules.[45]

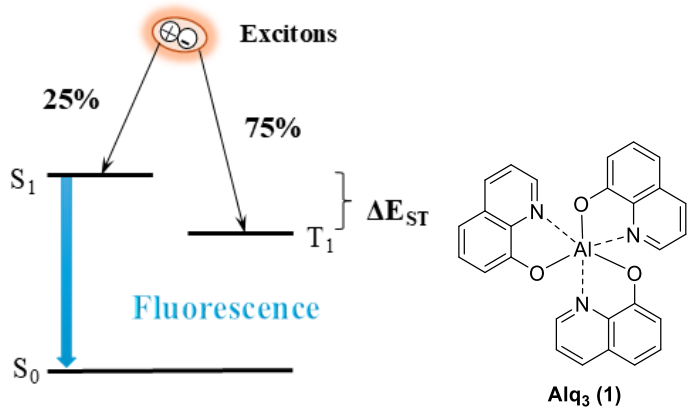

Figure 6. Fluorescence pathway after excitation of an emitter in an OLED device and Alq_3 (1) as an example fluorescent dye.[45] Adapted from literature.[73]

Second generation. The second generation are built upon phosphorescent materials, which are usually based on heavy metal atoms such as iridium(III), ruthenium(II), osmium(II), and platinum(II).[74-80] Caused by the significantly higher SOC, these emitters can additionally use the singlet excitons through ISC *via* the triplet states, leading to a theoretical IQE of 100% by an emission from the excited triplet state, as illustrated in Figure 7.[3] Most emitters of this class are based on iridium(III) metal complexes, one prominent emitter being tris(2-phenylpyridine)iridium ($Ir(ppy)_3$).[81] However, since they rely on rare and precious metals, solutions for more economically viable alternatives, that still show high efficiencies remains a significant challenge.[48]

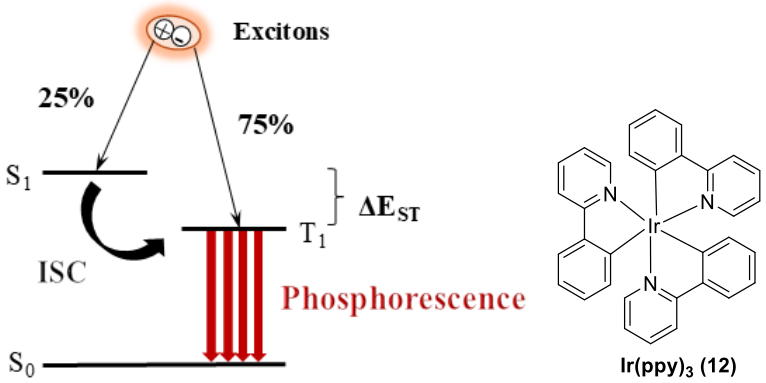

Figure 7. Phosphorescence pathway after excitation of an emitter in an OLED device and $Ir(ppy)_3$ as an example phosphorescent dye.[81] Adapted from literature.[73]

Third generation The third generation, being TADF materials, can harvest all excitons through RISC, also leading to a theoretical IQE of 100%.[4]

Compared to phosphorescent emitters, all excitons are harvested *via* the first excited singlet state, either by prompt or delayed fluorescence, as depicted in Figure 8. A major advantage of this emitter class is that they can be build out of purely organic materials or metal complexes with more earth abundant metals such as copper.[3] This offers a more cost-effective and sustainable alternative while still showing high efficiencies. In general, for organic TADF emitters three main design approaches are known: twist-induced charge transfer, through-space-induced charge transfer and multi-resonance systems.[82-84] A pioneer for the work of organic TADF materials is ADACHI, whose research group reported a series of efficient emitters based on carbazole phenyl triazine (**4CzIPN**, **13**), which were already successfully implied in an OLED with a device performance of 31%.[85-86] In the field of copper(I) complexes big efforts were made by YERSIN, who already presented the blue emitting copper(I) complex **14** with a PLQY of 90% in solid state, in 2011.[87] However, the first investigated copper(I) complexes, which emitted light from two different states was already described for some mononuclear cationic complexes in 1989 by BLASSE and MCMILLIN.[88] An example for this class is complex **15**. The chemistry of TADF copper(I) complexes will be discussed in more detail in *Chapter 1.3*.

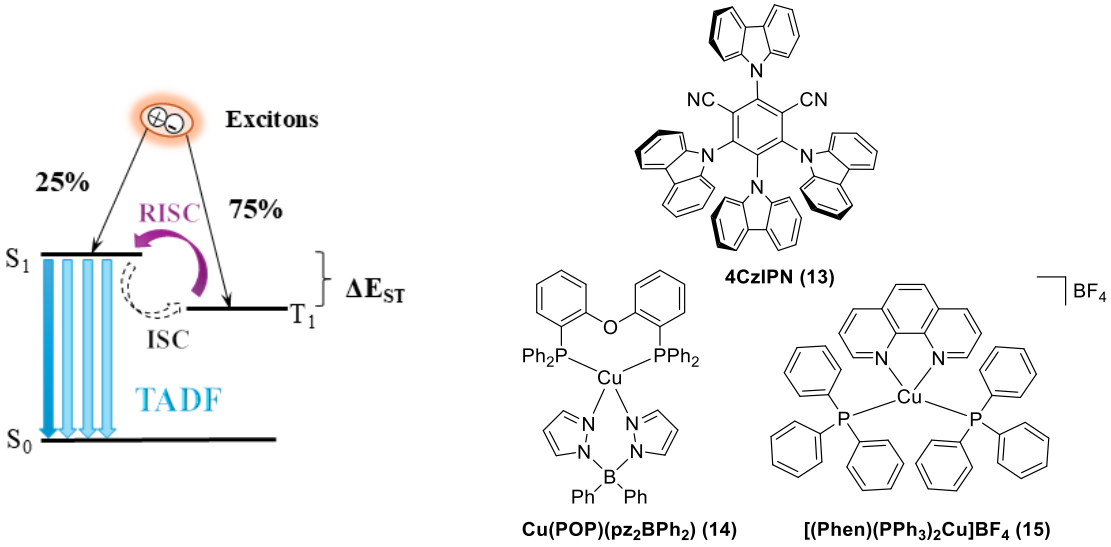

Figure 8. TADF pathway after excitation of an emitter in an OLED device and examples for a twist-induced charge transfer based organic dye and two mononuclear copper(I) phosphorescent based dyes.[85, 87-88] Adapted from literature.[73]

1.2.1.5 Challenges in the OLED processing

The different layers of an OLED device can be produced by thermal evaporation, also described as chemical vapor deposition (CVD) or solution-processed (SP) techniques.[70] The deposition *via* CVD usually leads to pure and homogenous layers, however it also leads to high material losses and high costs, as an ultra-high vacuum (10^{-6} mbar) is needed. Especially, for larger substrates, big vacuum chambers are necessary, leading to high energy consumption. Moreover, the used chemical compounds need to be sublimable and exhibit high thermal stabilities to be suitable candidates for the processing part. A favorable way for the production are solution-processed techniques, as they are highly more cost-effective and material efficient and would be suitable for the processing of large and flexible substrates.[70] Possible techniques among others are inkjet-printing[89-90] and spin-coating,[91-92] which is mostly applied in academia. However, one major drawback for solution-processed OLEDS is the dissolving of subsequent layers if more than one layer is deposited through solution, which often leads to severe roll-off effects and limited efficiencies.[70] To avoid this, orthogonal solvents need to be used, as it's done for **PEDOT:PSS** (**2**) for instance, which is water soluble and allows the next layer to be processed in organic solvents. Another approach is the crosslinking after deposit to form an insoluble layer, which will be described in more detail in *Chapter 3.3*.[93]

1.2.2 3D laser nanoprinting

Another application in which chemical compounds interact with light is 3D laser printing. The term 3D laser printing is also known as additive manufacturing, as it builds three dimensional objects with bottom-up techniques, printing layer by layer.[94] It is revolutionizing numerous industry sectors such as automotive, aerospace, medical, electronics and food, through the rapid fabrication of prototypes and customized structures. Moreover, it displays a rapidly increasing research field in academia in the last ten years (scifinder search "3D printing" gives 100 references in 2013, 4615 in 2018 and 10.239 in 2024). Several 3D laser printing techniques are known today which rely on photopolymerization, such as stereolithography (SLA), digital light processing (DLP) and direct laser writing (DLW).[94] In SLA the printing is conducted point by point using a movable light source, whereas in DLP the entire layer is exposed to the light source simultaneously. With SLA more detailed structures can be obtained compared to DLP, however it displays the slowest of the three techniques. The DLW technique allows the printing of structures in the sub-100nm scale, by using a focused pulsed femtosecond laser.[68, 95]

It should be noted, that several techniques are available that are not relying on photopolymerization, that will not be discussed here, such as selective laser sintering (SLS), fused filament fabrication (FFF) or binder jetting (BJ).[96]

In the photopolymerization techniques a liquid photo resist is irradiated with a light source, resulting in the solidifying of the exposed area, as shown for DLW in **Figure 9**.[94] The resist usually consists of one or more monomers and a photoinitiator (PI) which interacts with the light source in form of photon absorption, leading to an excitation of the electrons to an excited state, based on the same fundamental photophysics that were already discussed in *Chapter 1.1*. The excited PI can then interact with the monomer to induce the polymerization either by radical or cationic polymerization.[97] A crucial factor for the used PIs is that the applied wavelength is sufficient to excite the PI and therefore to induce the photopolymerization. Additional substances (additives), such as coinitiators or photosensitizer, can be added to the resist composition as supporting reagents, which transfer the excitation to the PI. An example of a PI is **benzil** (**16**) and related diketones, whereas common monomers are vinylic compounds, mostly as acrylates such as trimethylolpropane triacrylate (**TMPTA**, **17**) next to epoxides or cyclic ethers (**Figure 9**).[94, 97]

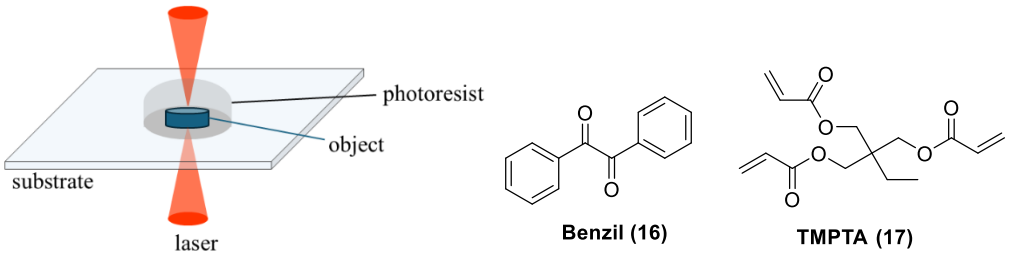

Figure 9. Schematic illustration of direct laser writing (DLW) and examples of the photoinitiator benzil and the monomer TMPTA. Adapted from the literature.[94, 97]

A big issue of most commercial printer systems is the irradiation source with wavelengths between 365 and 405 nm, although numerous PIs can only initiate polymerizations under excitation with UV-light.[97] However, visible light sources are favorable as they are significantly more eco-friendly. To bypass this problem, two-photon absorption (TPA) was recently successfully applied in 3D laser nanoprinting.[98] Usually, the PI is excited by absorption of one photon with a specific wavelength, whereas in TPA the almost simultaneous absorption of two photons with lower energy takes place. The electron is excited to a virtual intermediate state, which only exists in the light field. From this intermediate state, the electron is further excited by the help of a second photon.[98]

The simplified mechanism and an exemplary photopolymerization scheme for TMPTA for a two-photon absorption is depicted in Figure 10 and Scheme 1. TPA is already used in a variety of applications, especially bio-related areas.[99]

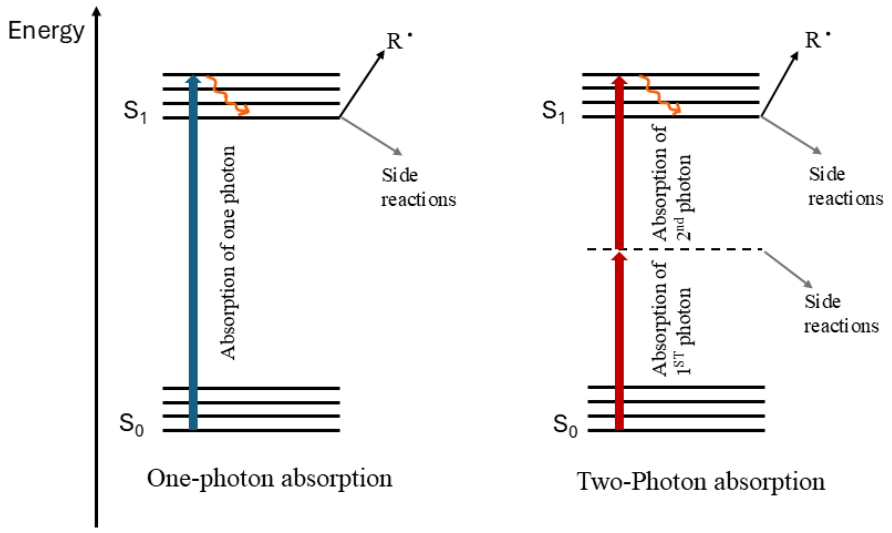

Figure 10. Simplified illustration of one-photon (left) and two-photon (right) absorption. Radiative decay pathways are omitted for clarity. Adapted from the literature.[97]

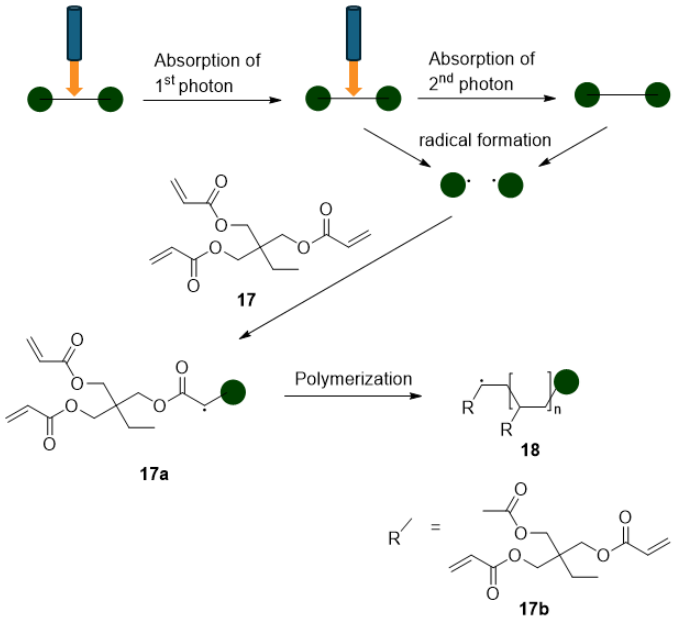

Scheme 1. Process of photopolymerization with absorption of either a single photon (side reaction, one-photon absorption) or after the absorption of a second photon (two-photon absorption) of the PI. The formed radical adds to the monomer and starts the polymerization. Adapted from the literature.[97]

Another method, the two-step absorption (TSA), was proposed by the WEGENER group.[100] They successfully used benzil derivates as PIs in combination with pentaerythritol triacrylate (PETA) for 3D laser nanoprinting.

Compared to TPA, in TSA the virtual intermediate state is replaced by a real excited state, from which the electron is further excited to higher energetic states in a second step (Figure 11).[100] This method was already conducted with single-color absorption as well as two-color absorption using laser with wavelengths of 405 and 640 nm. In cooperation with the WEGENER group, a number of benzil derivatives as possible PIs were synthesized in the BRÄSE group and investigated on their printing properties.[101] Both, TPA and TSA are used for precise printing in a nanometer to micrometer scale, however TSA is significantly more cost and size efficient due to the used light source, which makes it a highly promising method.[100]

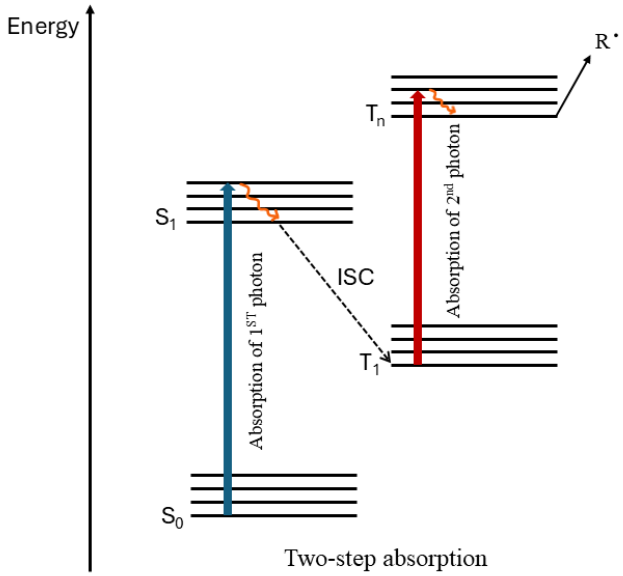

Figure 11. Simplified illustration of the mechanism for a two-step absorption induced photopolymerization. Radiative decay pathways are omitted for clarity. Adapted from literature.[94]

In addition to organic PIs, transition metal complexes are also used to initiate photopolymerization processes. They often show long-lived excited states and reversible redox properties which makes them promising candidates in the field of photopolymerization.[97] The majority of photoinitiators using metal complexes are based on precious metals iridium and ruthenium. However, copper(I) and iron(II) complexes are of growing interest due to their affordability and higher abundance making them particularly interesting candidates as PIs.[97]

1.3 Copper(I) complexes as Emitting Materials

The investigation of novel materials which show high luminescence efficiencies is still a continued research area. Metal complexes based on several metals such as iridium, platinum or even lanthanides are considered as potential candidates for optoelectronic applications and intensively studied.[39, 102-108] However, they often lack in efficiencies or show phosphorescence properties. Moreover, heavy metals such as iridium and platinum show a low earth abundancy (Ir: 0.000037 ppm, Pt: 0.0015 ppm), which comes along with high material costs.[48] In contrast, copper is more earth abundant and with that highly more affordable (Cu: ~ 9 €/kg vs. Ir: 135.000 €/kg).[109-110] Especially in material intensive production processes, as seen for thermal evaporated OLEDs, a more sustainable solution is desirable, which led to the search of novel emitting materials based on copper(I) complexes.[70]

1.3.1 Electronic-state properties

Cu(I) complexes often show efficient TADF properties as they intrinsically exhibit a desirable spatial separation of the HOMO and LUMO, which is why they are already widely explored for various applications, for instance as emitting materials in OLEDs.[111] Furthermore, for copper(I) complexes dd quenching is not observed, due to the closed shell d^{10} configuration. In the case of most transition metal complexes, dd quenching plays a crucial role.[112] This is observed for complexes based on metals with unoccupied metal-centered (MC) d states. During excitation, the unoccupied d-orbitals can be populated, which can result in non-radiative deactivation processes such as internal conversion or vibrational relaxation.[113] This is especially true for 3d transition metal complexes, such as chromium, manganese, iron and cobalt as the MC excited states exhibit rather low energies, which facilitates the path for non-radiative dd transitions.[113-115]

Compared to phosphorescent d^6 (*e.g.* Ir(III)) or d^8 (*e.g.* Pt(II)) metals, the SOC value is significantly smaller, which allows the copper(I) complexes to exhibit RISC at ambient temperatures (ξ_{Pt} = 4481 cm^{-1}, ξ_{Ir} = 3909 cm^{-1}, ξ_{Cu} = 857 cm^{-1}).[22, 116] However, compared to organic molecules, the SOC is higher, which leads to an enhanced ISC. For copper(I) complexes this often leads to the result, that no prompt emission is detected, as the ISC often occurs within picoseconds.[61] The additional large variety of copper(I) complexes with tunable emission colors due to specific ligand design makes copper(I) complexes a promising alternative to purely organic emitters.

When designing novel Cu(I) complexes a deactivation pathway needs to be considered. After excitation the complexes often tend to show a flattening distortion.[26, 113] This phenomenon was extensively studied, especially for mononuclear diimine Cu(I) complexes, but can be applied to other Cu(I) complexes as well.[117-118] Upon excitation, the complex is formally oxidized to Cu(II) with d^9 configuration. Cu(II) complexes preferably form a square-planar geometry, compared to the pseudo tetrahedral geometry of the ground state Cu(I) complex (pseudo Jahn-Teller effect). This opens the way for exciplex formation through the coordination of nucleophiles, such as solvent molecules or counter ions, which results in non-luminescent species.[118] Regarding solvent molecules, the quenching probability highly depends on the donor strength and steric properties following the row CH_2Cl_2 < THF < $CHCl_3$ ≤ EtOH < MeOH < CH_3CN < DMF.[118-119] In fact, for a variety of Cu(I) complexes, luminescence can only be observed in the solid state and is largely quenched in solution. Optimized ligand design, by introducing highly steric demanding groups can therefore be used to enhance the luminescence properties. For instance, introducing bridging ligands or dinuclear structures, can enhance the rigidity strongly.[4]

1.3.2 Structural Diversity

The structural diversity of copper(I) complexes is enormous ranging from cationic to neutral complexes and building mononuclear to polynuclear structures.[4, 26, 120-121] For neutral copper(I) halide complexes, the copper(I) centers are mostly coordinated in a tetrahedral way, however also trigonal geometries are possible.[122] In general, a variety of donating atoms can be used in organic ligands directly influencing the structural outcome, such as sulfur, phosphorus, nitrogen or carbene. Tetrahedral geometries are usually obtained when monodentate or bridging ligands based on phosphines, pyridines and halides are applied. In general, neutral complexes can be obtained, by using either the same ratio of halide to copper in addition to neutral ligands or anionic organic ligands. Especially for OLED applications, cationic complexes are less considered, caused by their counter anion, which is capable to migrate through the layers and reduce the overall efficiency of the device.[122] An overview of selected neutral copper(I) halide complexes is depicted in Figure 12, with X being a halide and L being the ligand. [4, 41, 122] It is noteworthy, that the structural variety is significantly larger when including cationic complexes, complexes that are not based on copper halides or polymeric structures, which will not be fully outlined herein.[4]

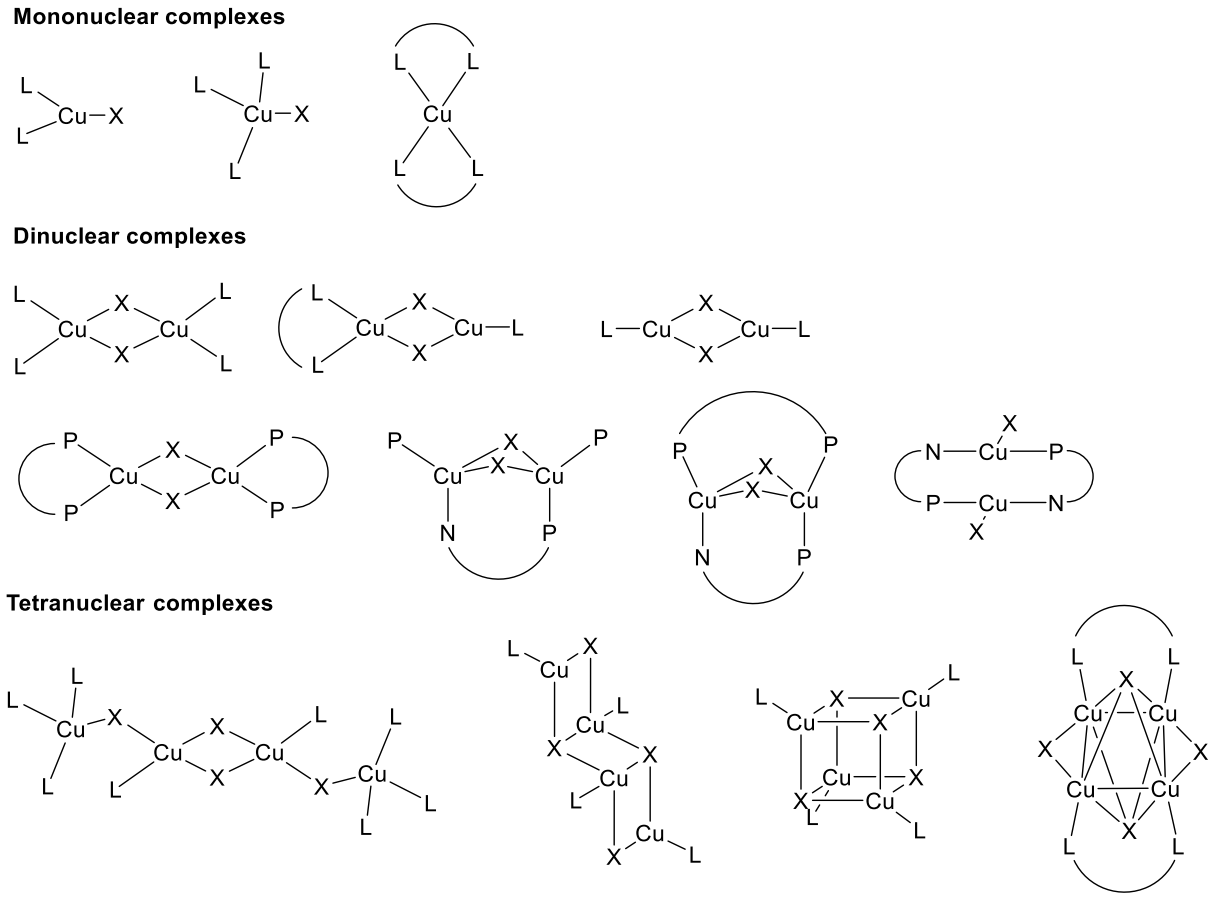

Figure 12. Overview of the structural diversity of neutral copper(I) halide-based complexes. Adapted from the literature.[4, 41, 122]

Mononuclear complexes. Mononuclear complexes display the simplest structure by only featuring one copper atom. However, they often have a higher tendency to undergo flattening distortion or ligand dissociation, which makes them less stable.[26] They are mostly designed with organic bridging ligands with additional heteroatoms such as nitrogen or phosphorus of the type N^N, N^P or P^P (N standing for nitrogen ligand, P standing for phosphine ligand, "^" standing for the intramolecular bridging).[26, 122] Examples of commonly used ligands are derivates of bipyridines (**bipy**, **18**), 1,10-phenantrolines (**phen**, **19**), bis[(2-diphenylphosphino)phenyl] ether (**DPEphos**, **20**) or 2-(diphenylphosphaneyl)pyridine (**2-PyrPhos**, **21**), which are depicted in Figure 13.[4, 123] Most of the investigated mononuclear complexes with these ligands are displaying cationic complexes of the type $[Cu(N\text{^}N)_2]^+$ and $[Cu(N\text{^}N)(P\text{^}P)]^+$ with a counter anion, such as BF_4^- or PF_6^-.[123]

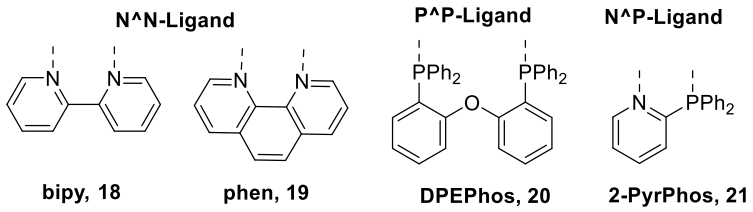

Figure 13. Commonly used bridging ligands based on two donor atoms.[4, 123]

Two examples of neutral mononuclear complexes investigated by CZERWIENIEC *et al*. are **22** and **23**, depicted in Figure 14.[124] By changing the backbone of the bridging phosphine ligand, they found a significant change in the resulting photophysical data. **22** resulted in a decay time of 3.3 µs and an PLQY of 70% at an emission wavelength of 535 nm, whereas the emission of **23** was blue shifted to 464 nm with an increased lifetime of 13 µs and a higher PLQY of 90%.

More recently, carbene based ligands such as N-heterocyclic carbene (NHC)[125-126], monoamido amino carbene[127-128] (MAC) or cyclic alkyl amino carbene (CAAC)[129] ligands gained much interest, investigated to obtain neutral mononuclear complexes with linear structures.[130] A variety of neutral carbene-Cu-amide complex of the type (MAC*)Cu(Cz) using MAC derivates and N-carbazolyl (Cz), was explored by SHI *et al.*[131] The resulting complexes showed emission maxima in the blue and green region with fast decay times of below 1 µs in neat solid. Complex **24** (**Figure 14**) of this series was already successfully applied in an OLED, resulting in a maximum EQE of 19.4%.

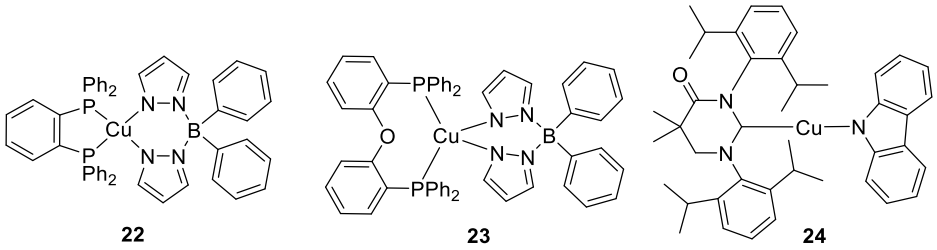

λ_{max} = 535 nm
ΦPL = 70%
τ (r.t.) = 3.3 µs
τ (77 K) = 300 µs
kr($10^5 s^{-1}$) = 2.1

λ_{max} = 464 nm
ΦPL = 90%
τ (r.t.) = 13 µs
τ (77 K) = 500 µs
kr($10^5 s^{-1}$) = 0.69

λ_{max} = 492 nm
Φ_{PL} = 53%
τ (r.t.) = 0.83 µs
τ (77 K) = 160 µs
k_r($10^5 s^{-1}$) = 6.3

Figure 14. Selected neutral mononuclear copper(I) complexes with an overview of their photophysical properties. [124, 131]

Dinuclear copper(I) halide complexes. Dinuclear copper(I) halide complexes exhibit a significantly increased rigidity compared to mononuclear structures. Moreover, the HOMO is mostly delocalized on the copper(I) halide core and not only located on one copper atom.[122] As a result, the formal oxidation upon excitation is distributed over the whole core, which leads

to a decreased structural reorganization, and thus to higher quantum yields.[26] Therefore, dinuclear structures are of particular interest as they have the potential to combine favourable emission properties, such as thermally activated delayed fluorescence (TADF), with chemical properties, such as solubility in organic solvents.[4] These complexes can be designed with a range of different organic ligand types in addition to the halides (X), for instance monodentate nitrogen (N) or phosphine (P) based and chelating ligands based on N and P donor (N^N, N^P, P^P).[4, 26, 122]

Complexes with only monodentate ligands of the type $L_4Cu_2X_2$ or with chelating ligands resulting in $L_2Cu_2X_2$ were upon the first studied dinuclear copper(I) complexes. Complexes of the type $(PR_3)_2(pyr)_2Cu_2X_2$ (**25**), featuring two ligands of pyridine (pyr) and two ligands of monodentate phosphines. By using chelating ligands, the stability can be further increased (**Figure 15**).[26, 42]

OKANO *et.al* demonstrated the tuning of the emission wavelength for dinuclear copper(I) complexes of the type $(P^P)_2Cu_2I_2$ featuring the chelating ligand 1,2-(bis(diphenylphosphino)benzene (dppb) by applying different nitrogen heterocycles in the aromatic backbone (**Figure 15**, **26a-c**).[132-133] They were able to observe of colour change in the solid state, from green (497 nm) for the phenyl to yellow (548 nm) for the pyridine and red (638 nm) for the pyrimidine **26c**. HONG *et al.* investigated the influence of different halides on a comparable complex **27** (**Figure 15**).[134] They found a bathochromic shift to 527 nm for the copper(I) chloride complex, which is in accordance with the general red shift trend observed for halides (I<Br<Cl). The emission, based on (M+X)LCT processes, resulted in PLQYs and lifetimes in a range of 28% and 2.5 µs for **27a** to 32% and 12.5 µs for **27c**.

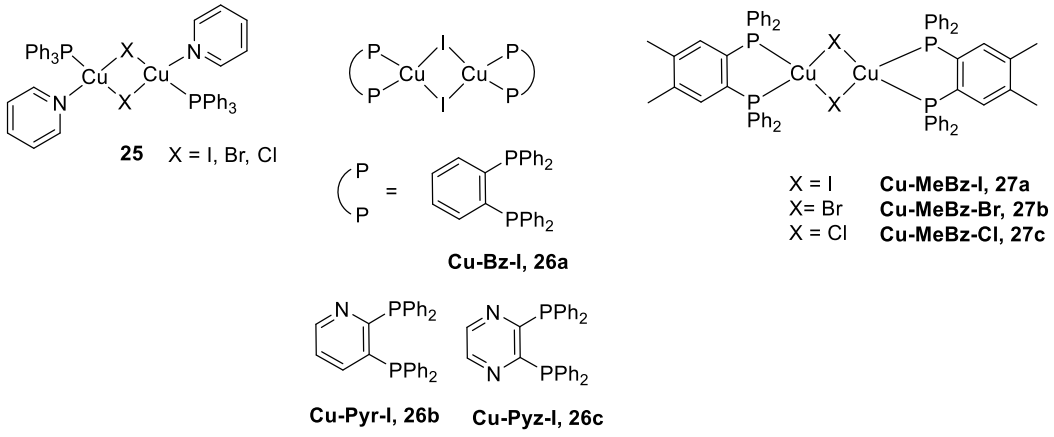

Figure 15. Selection of neutral dinuclear copper(I) complexes with an example for a WHITE complex and complexes featuring NN-bridging ligands.[42, 133-135]

By using chelating ligands based on N and P donors (N^P) instead of P^P ligands, a blue shift was obtained for complex **28**, resulting in an emission maximum of 464 nm with a PLQY of 65% and a decay time of 4.6 µs (**Figure 16**, left).[136] Another interesting class of dinuclear complexes feature a bridging N^P ligand and additional two monodentate phosphine ligands.[137] Since the ligands that were explored consisted of various *N*-heteroaromatic scaffolds combined with a phosphine, this class is also known as NHetPhos complexes. Since the structure of these complexes remind of a butterfly, they are also called butterfly-complexes (structures **29-31**, **Figure 16**).[58, 137]

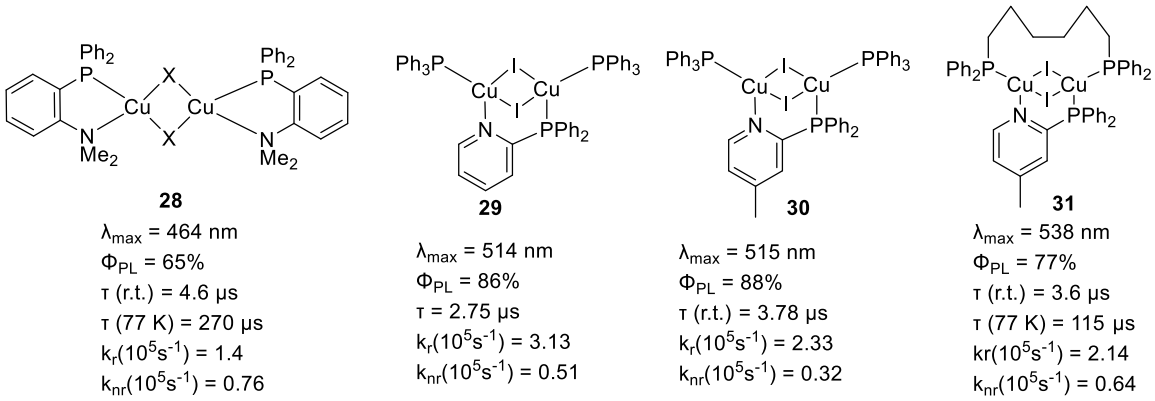

Figure 16. Selection of neutral dinuclear copper(I) complexes featuring NP-bridging ligands.[58, 136-137]

Complex **29** represents the simplest heteroleptic butterfly complex, with 2-Pyrphos serving as single bridging ligand (**Figure 16**, middle left).[137] Variations of the bridging ligand, for instance the introduction of a methyl group, can, as already described before, change the complexes properties (**30**, **Figure 16**, middle right).[137]

The stability of these complexes could even be more enhanced by VOLZ *et.al.* by employing two different bridging ligands, resulting in the rigidified double bridged structure **31** (**Figure 16**).[58] **31** has been previously explored in OLED applications, in which it exhibited an exceptional external quantum efficiency (EQE) of 23.2%.

In the BRÄSE group the primary emphasis has been on the investigation of these bridged dinuclear copper(I) complexes of the type $Cu_2X_2(P\text{^}N)(P)_2$, using phosphine ligands in combination with *N*-heteroaromatic scaffold (NHetPhos).[41, 63, 137-138] The key NP-bridging ligand that is used in these systems is 2-PyrPhos **21** and its derivatives. Due to the bite angle between the nitrogen and phosphorus of 2-PyrPhos, the formation of mononuclear complexes is typically suppressed and instead bridged dinuclear structures are formed. Another notable feature of this complexes is the Cu-halide core Cu_2X_2 with bridging halides. By altering the bridging halide, a red shift in the row of I<Br<Cl is usually observed.[41]

For this complex type, the HOMO and LUMO are typically well separated, as the HOMO is located on the Cu-Halide core whereas the LUMO is located on the bridging ligand.[63, 138] The emission properties of this complex type are typically of TADF character and can easily be tuned through specific ligand design of the bridging ligands (**Figure 17**). Additionally, the tuning of chemical properties such as solubility are accessible through the monodentate ligands.[63, 138]

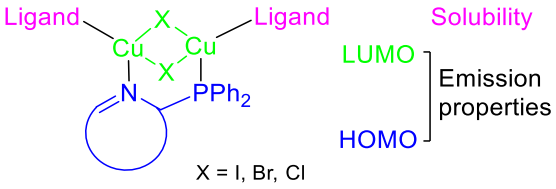

Figure 17. General structure and tuning possibilities of the dinuclear NHetPhos copper(I) complexes. Adapted from the literature.[41]

Tetranuclear complexes. Several structures, from ladder-like to cubic are known for tetranuclear copper(I) halide complexes, showing luminescent properties.[139-141] Depending on the used ligands, different structures are formed. Cubic structures often emit *via* two different triplet states, one high energy transition arising from (M+X)LCT and XLCT transitions and a second one from a triplet cluster-centered-chare (^{3}CC) excited state.[139-140] However, the emission is also highly dependent on the Cu···Cu distances, resulting in higher emission wavelengths for shorter distances. Emission through ^{3}CC is usually observed, for distances smaller than 2.8 Å. KYLE *et al.* demonstrated cubic complexes, which are formed with pyridine and its derivatives (Figure 18).[141] For **33** a dual emission with a blue emission band at 480 nm and a red emission band at 690 nm was found in toluene. Moreover, a number of complexes with monodentate phosphine ligands is described as well.[142-143]

Ladder-like structures usually demonstrate higher distances between the copper atoms, resulting in an emission only occurring from (M+X)LCT and XLCT transitions.[144] For octahedral complexes mostly dual emissions are described, although this complex class is less studied, compared to the former described. The overall rigidity of the ligands seems to have a significant impact, as CHEN *et al.* demonstrated a luminescent octahedral complex **35** using 2-PyrPhos with only one emission band at 520 nm, resulting from (M+X)LCT-transitions (Figure 18).[145-146] However, by using a more flexible ligand, LIU *et al.* found two emission bands for **36** (460 nm, 570 nm from (M+X)LCT and CC) (Figure 18).[144]

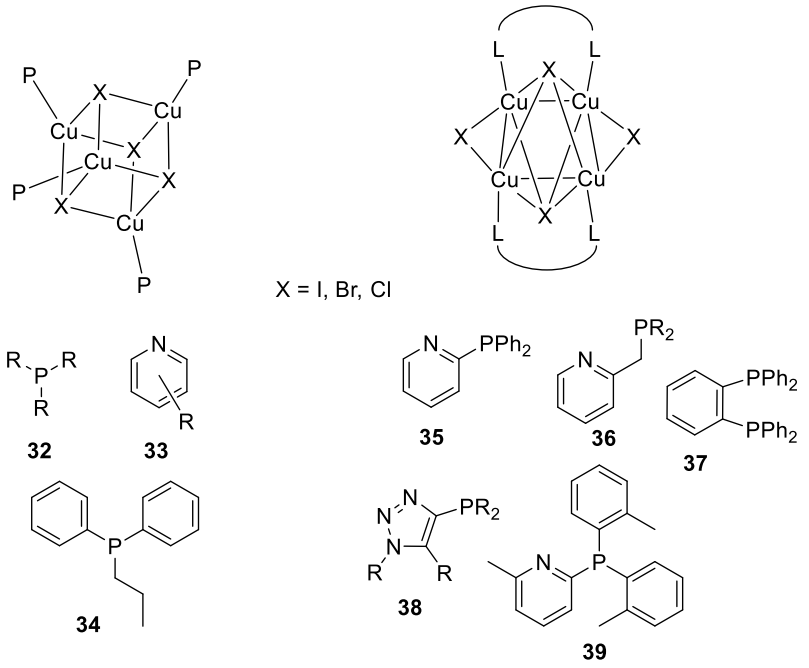

Figure 18. Overview over selected cubic (left) and octahedral copper(I) complexes. The numbering displays the corresponding complex and is attached to the used ligand. Adapted from literature.[41]

In general, tetranuclear complexes are less studied, compared to mononuclear and dinuclear structures and not many applications in OLEDs are described in literature, caused by their usually reduced solubility. ZHANG *et al.* tested the application in an OLED for the phosphorescent tetranuclear complex $Cu_4Br_4(dppb)_2$ (dppb = 1,2-bis(diphenyl-phosphino)benzene), resulting a blue device ($\lambda_{max,PL}$ = 467 nm).[147]

1.3.3 Photophysical characterization of TADF in Copper(I) complexes

To gain a deeper understanding of the emission behavior of luminescent copper(I) complexes, photophysical characterization is essential to understand the structure-property relationship. The first indicator for TADF behavior is a red-shift of the emission in cooled samples to 77 K, as only phosphorescence becomes visible.[26, 122] More advanced methods that are used to describe copper(I) complexes are based on a two-state model proposed by MCMILLIN in 1983.[122, 148] This model is relying on the assumption that the singlet and triplet excited states, here denoted as 1 and 2, are in a thermal equilibrium with the triplet state being a long-lived state, serving as exciton reservoir.[149] This is particularly relevant for copper(I) complexes, where the ISC rate (k_{ISC}) is usually faster then any direct transition from the excited singlet state to the singlet ground state.

Moreover, since the SOC constant for copper is typically too small for an efficient triplet decay, the rate of RISC is mostly higher than any transition from the excited triplet to the ground state, resulting in a rapid thermal equilibrium between the excited singlet and triplet state.

When the two states are in a fast thermal equilibrium (i.e. $k_{ISC} >> k_r^S + k_{nr}^S$ and $k_{RISC} >> k_r^T + k_{nr}^T$), they can be treated as steady-state and described using Boltzmann statistics.[122]

$$K = \frac{N_1}{N_2} = \frac{g_1}{g_2} \cdot \exp\left(-\frac{\Delta E}{k_B T}\right) \approx \frac{k_{rISC}}{k_{ISC}} \qquad \textbf{(5)}$$

K: equilibrium constant, N: population of the respective states 1 or 2, g: degree of degeneracy of the excited state 1 or 2, ΔE: energy gap between the excited singlet and triplet states 1 and 2, k_B: Boltzmann constant, T: absolute temperature.

The method used today as reported by YERSIN relies on temperature-dependent emission decay time measurements. If a quasi-degeneracy is assumed for the three triplet substates ($g_2 = 3$), the average decay time can be expressed with the following equation:[150]

$$\tau_{ave} = \frac{g_2 + g_1 \cdot \exp\left(-\frac{\Delta E}{k_B T}\right)}{K_2 + K_1 \cdot \exp\left(-\frac{\Delta E}{k_B T}\right)} \qquad \textbf{(6)}$$

With $g_1 = 1$, $g_2 = 3$, and the total decay constants $K_1 = k_r^S + k_{nr}^S$ and $K_2 = k_r^T + k_{nr}^T$.

Since $\tau_1 = (K_1)^{-1}$ and $\tau_2 = (K_2)^{-1}$ equation **6** can be simplified to:

$$\tau_{ave} = \frac{3 + \exp\left(-\frac{\Delta E}{k_B T}\right)}{\frac{3}{\tau_2} + \frac{1}{\tau_1}\exp\left(-\frac{\Delta E}{k_B T}\right)} \qquad \textbf{(7)}$$

Since the triplet state consists of three quasi-degenerate states, the factor for K_2 result in $\frac{3}{\tau_2}$. The top part of equation **7** describes the thermal population of the states, while the bottom part also considers the decay rates of the different states. For example, when the temperature is really low, the exponential terms become negligible, and the decay time reflects the phosphorescence decay time $\tau(T_1)$.

In practice, the experimental data of emission decay times are plotted versus temperature and then be fitted with equation **7**, to obtain the two fit parameters ΔE and τ_{S1}. This procedure can be used as long as the lifetimes show temperature-independent behavior.

2 Objective

Luminescence materials are already applied in a variety of fields, including bioimaging,[5-7] photovoltaics,[8-10] sensors[11-12] or as photoinitiators in 3D laser printing.[1-2] TADF materials are particularly known for their favorable properties such as high photoluminescence quantum yields and tunable emission properties. Due to their structural diversity and interesting emitting properties, copper(I) complexes are intensively studied as promising candidates for these applications.[111, 151] To meet the respective requirements, the photophysical properties of the complexes must be investigated and controlled ligand design is essential. This allows for precise tuning of the chemical properties, which is especially important for optimizing solubility and (photo-)chemical stability. This thesis focuses on the design, synthesis and photophysical characterization of novel neutral copper(I) complexes for future applications in solution-processed OLEDs and 3D laser nanoprinting. Particular emphasis is placed on dinuclear structures, with the well-studied NHetPhos complexes serving as reference points.

The first project aims to investigate the coordination chemistry of 3-pyridylphosphine (**3-PyrPhos**, **L2**) with various copper(I) (pseudo)halide salts (CuX, X = I, Br, Cl, CN, SCN) in different ratios. The wider bite angle of **3-PyrPhos**, compared to **2-PyrPhos**, enables the formation of novel complex structures, particularly a dinuclear open-core complex. The resulting dinuclear complexes will be structurally analyzed and photophysically investigated *via* temperature-dependent measurements in the solid state. For a better understanding of the emission process, the electronic states are further investigated by theoretical density functional theory (DFT) calculations. Moreover, the derivatization of the dinuclear complex is targeted, and the resulting complex is structurally explored. In addition, the coordination chemistry of the selected ligand **3-PyrPhos** is further expanded with silver(I) halides.

The second project is based on the findings of the first one and results from YERSIN *et al.*[152] and BUSCH,[41] who found similar open-core dinuclear complexes by 'blocking' the 6-position at the *N*-heteroaromatic scaffold. This part targets the investigation of the resulting complexes by using quinoline- and isoquinoline phosphine ligands in order to obtain the resulting open-core structure of the first project. The resulting mononuclear complexes of this approach are structurally and photophysically investigated, supported by theoretical calculations.

Lastly, neutral mono-, di-, and tetranuclear copper(I) (pseudo)halide complexes are examined for future crosslinking reactions, such as click reactions or photopolymerizations.

In this context, problems of solution-processed OLEDs will be addressed. Therefore, several crosslinkable ligands featuring either a terminal alkyne or a methacrylate unit should be synthesized, and their coordination with copper(I) (pseudo)halides should be approached. Again, the focus is on the exploration of dinuclear structures. The complexes are fully characterized, and their photophysical properties are explored in different host environments through steady-state and time-resolved measurements. Furthermore, initial crosslinking experiments are conducted, to investigate the general suitability of the complexes for crosslinking reactions. Lastly, selected dinuclear copper(I) complexes are tested as emissive materials for solution-processed OLEDs and as photoinitiators in 3D laser nanoprinting.

3 Results and Discussion

3.1 Neutral complexes featuring 3-pyridyl phosphine

Introduction. As previously outlined in *Chapter 1.3.2*, copper(I) complexes exhibit diverse structures based on the employed ligand structure and their relative ratios to the utilized copper precursor. For instance, the well-studied NHetPhos complexes are formed using **21** (2-PyrPhos, **L1**) in a 3:2 ratio with CuX precursor. Due to the bite angle, the formation of mononuclear complexes is usually suppressed, and instead, the bridged structures are formed. [58, 137]

KOBAYASHI *et al*. and BARANOV *et al.* indicated that the number of pyridines in the NP-bridging ligand has a directly impacts the resulting structure.[153-154] By using 2,2′-(phenylphosphino)dipyridine (Pyr_2Phos, **42**) and tris(2-pyridyl)phosphine (Pyr_3Phos, **43**), they observed the formation of **40** and **41** with the general type of $Cu_2X_2L_2$ (**Figure 19**). Compared to the dinuclear NHetPhos complexes, the halide bridges are lost due to the multidentate properties of the ligands. Both complexes show intense luminescent properties. For **40**, a PLQY of 74% was observed at an emission wavelength of 530 nm, while **41** exhibited a PLQY of 62% at 550 nm. This illustrates that a minor change in the ligand structure can significantly affect the formed complexes and, thus, their chemical and electronic properties.

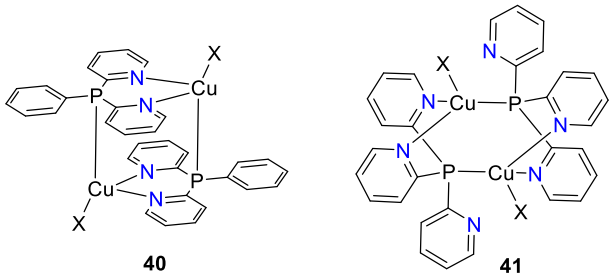

Figure 19. Dinuclear copper(I) complexes, that exhibit an open-core structure by using 2,2′- (phenylphosphino)dipyridine and tris(2-pyridyl)phosphine chelating ligands.[153-154]

BUSCH discovered that using 3-pyridyl phosphine (3-PyrPhos, **L2**) with copper(I) iodide results in a powder that exhibits a distinctive sky-blue emission.[41] While **L2** has been utilized in coordination chemistry with several metals, like iron,[155] zinc,[156-157] and rhodium,[158] no copper(I) complex has yet been identified. For a comparison, all four pyridine containing ligands relevant to this work are shown in Figure 20.

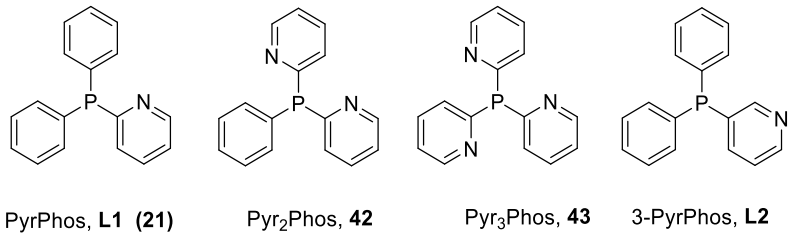

Figure 20. Comparison of bridging ligands that are based on a pyridyl phosphine scaffold. 2-PyrPhos **L1** shows the simplest of all ligands. By adding pyridines into the scaffold, Pyr_2Phos[153] and Pyr_3Phos,[154] and by altering the constitution of the nitrogen, 3-PyrPhos[41] are obtained as derivatizations of **L1**.

Accordingly, the ligand properties of 3-PyrPhos and two methylated derivatives were examined in the context of this present study. For that purpose, different ratios of **L2** were employed in combination with CuX salts (CuI, CuBr, CuCl, CuCN, CuSCN), as shown in Scheme 2. The different ratios will be separately discussed in detail in the following sections. If not otherwise noted, the ratios will represent the ligand to copper salt L:CuX in the following.

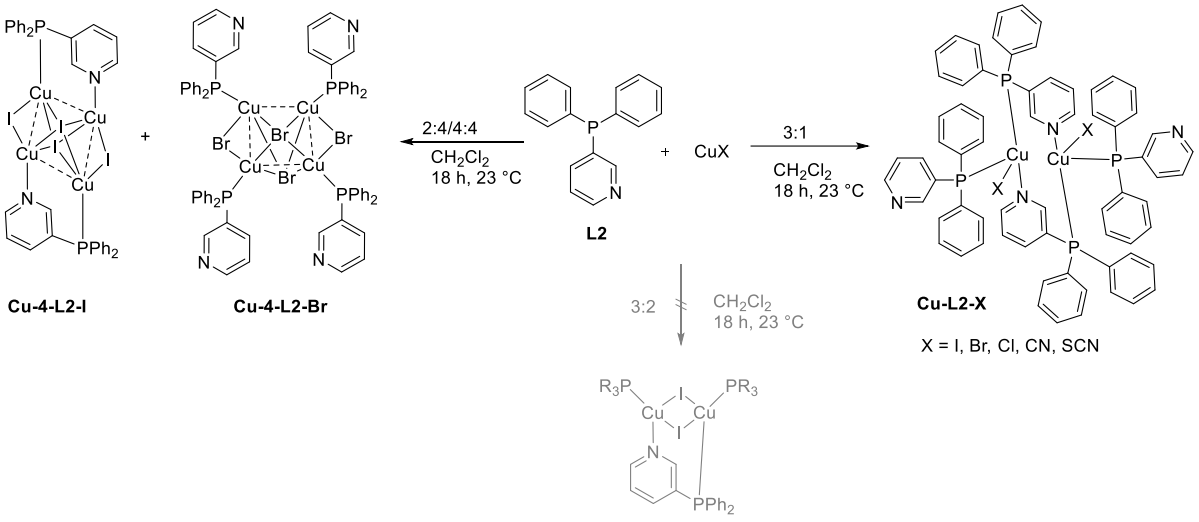

Scheme 2. Overview of the ratios, that were applied using **L2** and CuX salts to obtain tetranuclear and dinuclear structures.

After discussing general results using **L2**, the primary focus will be the detailed investigation of a novel structural class, which was obtained if a 3:1 stoichiometric ratio is used. The complexes are characterized by the presence of two bridging ligands and two ancillary ligands to form $(L_2)_4Cu_2X_2$ type structures. Thus, the derivatization of this complex class by exchanging the ancillary phosphine ligands was tested and will be described in Chapter 3.1.1.6. L2 was further subjected to complexation with silver(I) halides to form tetranuclear silver(I) complexes of the type $(L_2)_4Ag_4X_4$ (Chapter 3.1.2).

3.1.1 Copper(I) complexes featuring 3-pyridyl phosphine

3.1.1.1 Synthesis of the ligands L2 and L3

Three bridging ligands containing substituted 3-(diphenylphosphino)pyridine were synthesized to be used as NP-bridging ligands for dinuclear copper(I) complexes. **L2** was successfully synthesized according to a procedure by BUSCH *via* nucleophilic aromatic substitution of the chlorinated pyridine precursor **44** with *in situ* formed lithium phosphide (Scheme 3, route A) in 52% yield.[41] Although preparation of **L2** is already literature known *via* several routes, mostly catalyzed by palladium[159] (79% yield) or nickel catalysts[160] (68% yield), the route used here gives a more cost-efficient and less harsh alternative, although slightly lower yields. To enhance the solubility of the complexes at a later stage, the methylation of **L2** was intended. The unpublished methylated derivatives **L3a** and **L3b** were not accessible by route A. Hence, they were synthesized using diphenylphosphine and *n*-butyl lithium according to route B. Both ligands were obtained in excellent yields of 92% (para) and 97% (meta).

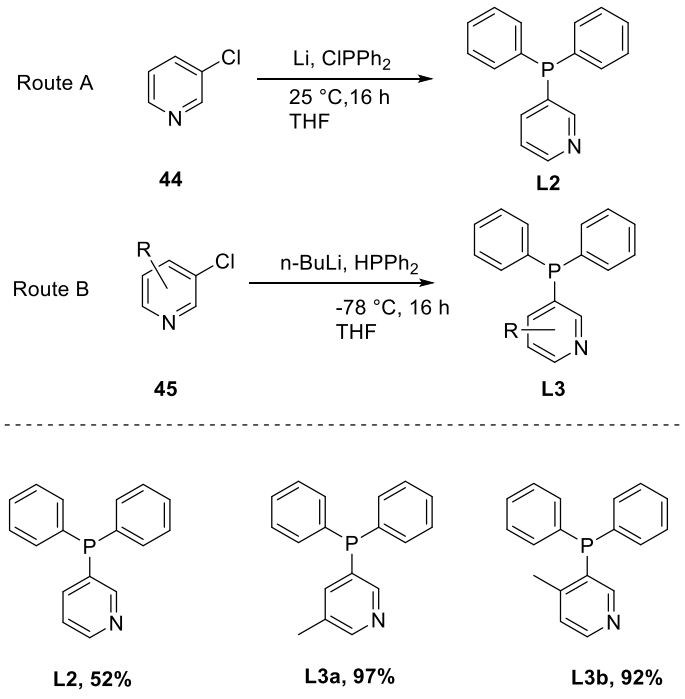

Scheme 3. Structures and synthesis of ligands **L2**, **L3a** and **L3b**. Route A shows the nucleophilic aromatic substitution using chlorodiphenylphosphine/lithium, whereas route B depicts the approach using *n*-BuLi/diphenylphosphine.

3.1.1.2 Synthesis of complexes

All complexes in this study were synthesized using an adapted synthetic procedure, established by ZINK *et al*., where the ligands and copper(I) salts are combined in precise ratios in dry, degassed dichloromethane at 23 °C for 16 hours.[41, 161] If the complex precipitated directly from the reaction, it was filtered, followed by trituration with pentane and diethyl ether (Et_2O). If no precipitate was formed, the complex was isolated by pouring the reaction solution into pentane, resulting in precipitation of the desired compound. The obtained complex was filtered off, washed with pentane and Et_2O, and dried in a vacuum.

Ratio 3:2: Butterfly-Complexes. A ratio of 3:2 was applied, aiming for a homoleptic dinuclear butterfly shaped-complex, as shown in Scheme 4 (path a).

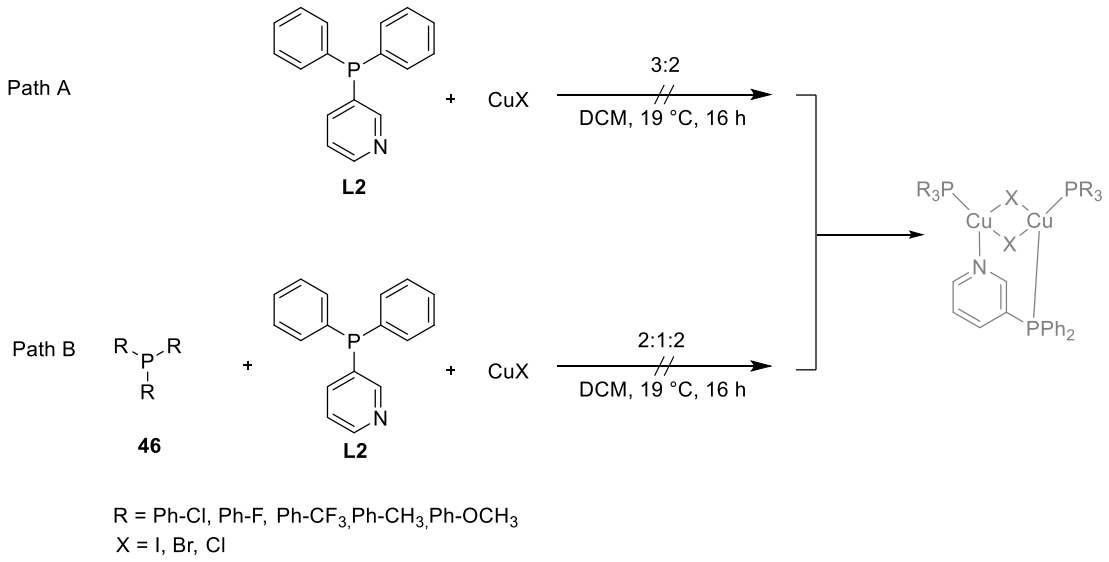

Scheme 4. Targeted reaction path with **L2** and different ancillary phosphine ligands to obtain homoleptic butterfly complexes with a precursor ratio of 3:2 and heteroleptic structures by a ratio PR_3:L2:CuX 2:1:2.

A sky-blue luminescent powdered complex was obtained for the ratio of 3:2 (Scheme 4, path a). Due to its limited solubility in all organic solvents, the structure could not be determined by any regular analytic methods. The experimental data of the corresponding elemental analysis (Table 1) suggest a ratio of 1:1 of ligand to metal halide. This leads to the hypothesis of a dibridged dinuclear or a tetranuclear complex; however, this structure could not be definitively validated.

Table 1. Comparison of calculated and experimental mass fraction of the elemental analysis of a 1:1 ratio complex **L2**:CuI versus the obtained complex for a 3:2 ratio. It is calculated for $C_{34}H_{28}Cu_2I_2N_2P_2$.

Elements	**N**	**C**	**H**
Expected for 1:1	3.09	45.00	3.11
Found for 3:2	3.13	45.20	3.11

Additionally, the substitution of CuI to CuCl or CuBr as well as several monodentate phosphines ($P(Ph\text{-}Cl)_3$, $P(Ph\text{-}F)_3$, $P(Ph\text{-}CF_3)_3$, $P(Ph\text{-}CH_3)_3$, $P(Ph\text{-}OCH_3)_3$) were as investigated to synthesize heteroleptic butterfly complexes in a ratio of 2:1:2 (PR_3:**L2**:CuI). However, no viable complexes were obtained, concluding that the 3-pyridyl ligand class is unsuitable for forming the well-known butterfly structures. This may be explained by the larger bridging angle of the ligands compared to the commonly used 2-PyrPhos, which might prevent the formation of the desired compounds.

Ratios 2:4 and 4:4: Tetranuclear complexes. By targeting tetranuclear complexes two different structures with ratios of 2:4 and 4:4 were expected to be obtained (Scheme 5).

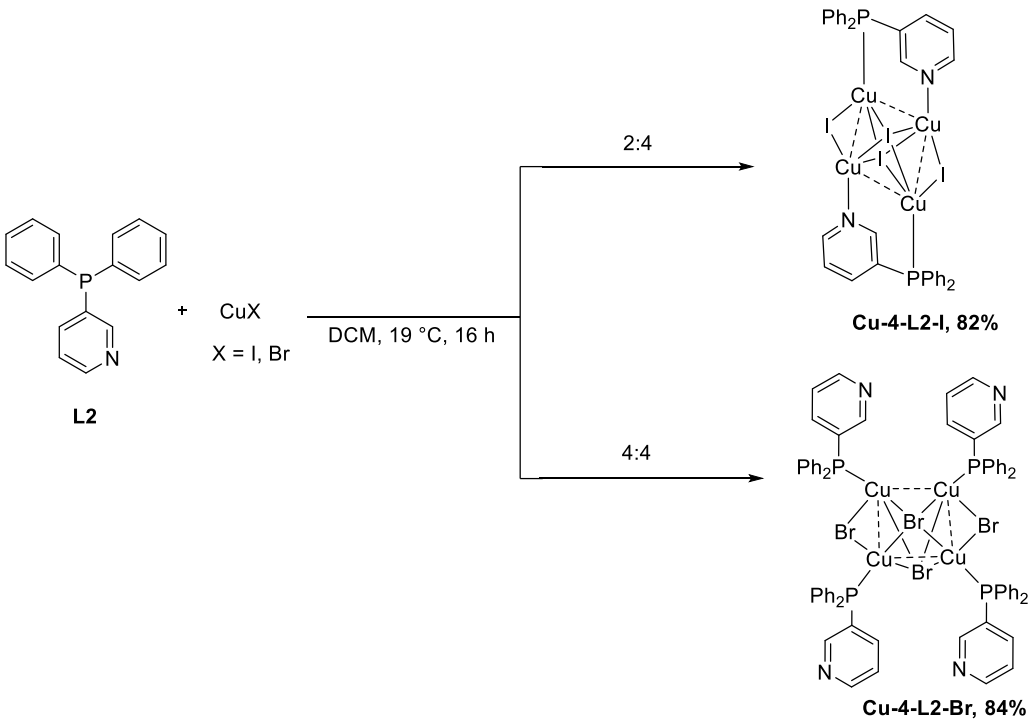

Scheme 5. Reaction path using **L2** to obtain tetranuclear complexes **Cu-4-L2-I** and **Cu-4-L2-Br** *via* a ratio of 2:4 and 4:4. The products display proposed structures.

Only two complexes, **Cu-4-L2-I** and **Cu-4-L2-Br** (Scheme 5) could be verified and confirmed *via* elemental analysis (see experimental part). Again, these complexes demonstrated

insolubility in organic solvents. Notably, a significant solubility increase was observed in pyridine. This is probably caused by a ligand exchange or the addition of pyridine. A single-crystal was obtained in pyridine. The crystal structure revealed the presence of two ligands, **L2** and two pyridine ligands, attributing the complexes to the class of WHITE complexes (Figure 21). This observation demonstrates that pyridine is not a suitable solvent, since it contributes to the dissociation of the formed complexes. Therefore, no complete characterization could be conducted on the described complexes. The detailed crystal structure data can be found in the experimental part.

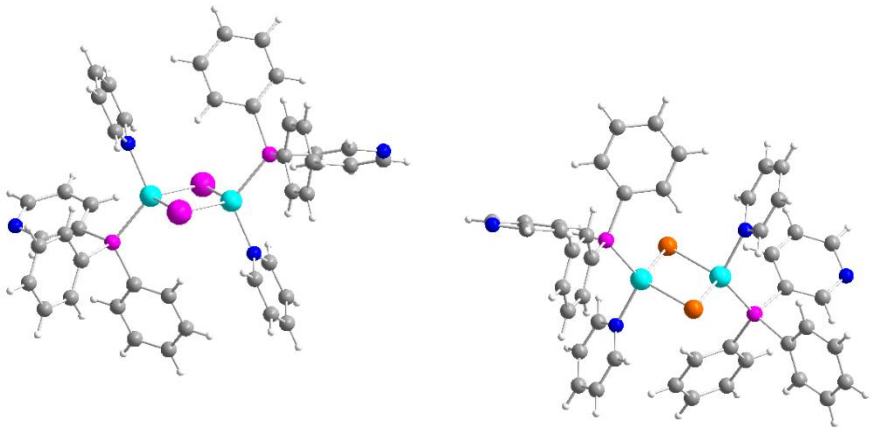

Figure 21. Crystal structures of **Cu-4-L2-I** and **Cu-4-L2-Br** in pyridine. Shown as a ball-and-stick model. Color code: turquoise (copper), violet (big: Iodine, small: phosphorus), orange (bromine), blue (nitrogen).

Ratio 3:1: Mononuclear complexes. To synthesize mononuclear complexes of the type L_3CuX, a 3:1 ligand-to-metal ratio was employed. However, a double-bridged dinuclear species of $Cu_2X_2L_4$ formed instead of the expected mononuclear complex. Five dinuclear complexes were obtained by using **L2** in a molar ratio of 3:1, equivalently expressed as a 6:2, with CuI (**Cu-L2-I**), CuBr (**Cu-L2-Br**), CuCl (**Cu-L2-Cl**), CuCN (**Cu-L2-CN**) and CuSCN (**Cu-L2-SCN**), respectively. These complexes exhibit a unique 4:2 structure of the type $Cu_2X_2L_4$, which was previously unknown. The excess of ligand is obligatory, as no complexes could be synthesized using a 4:2 ratio. All five complexes were obtained as pale-yellow powders in yields up to 97% and could be characterized *via* NMR spectroscopy, mass spectrometry and elemental analysis. The general structure with respective yields is shown in Scheme 6.

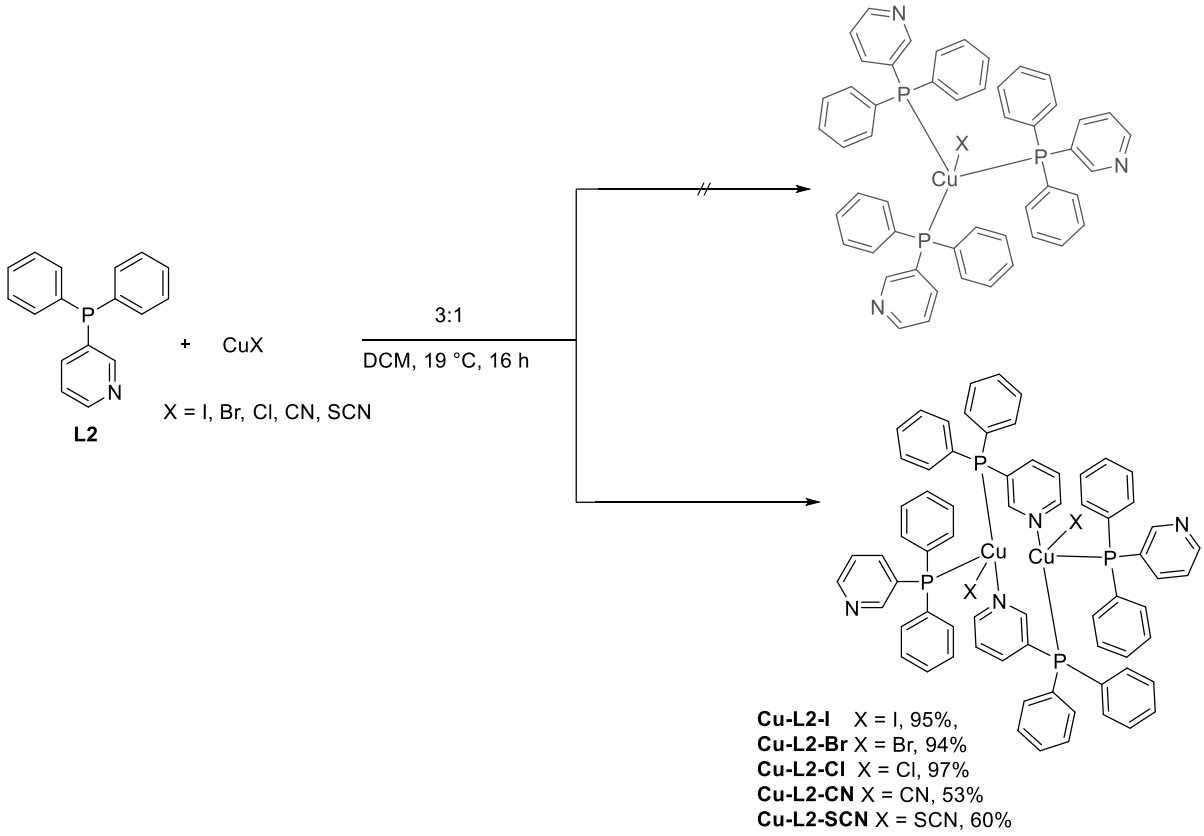

Scheme 6. Targeted reaction path using a ratio of 3:1 of **L2** and CuX (upper path) and obtained structure with yields (lower path).

Additionally, for **Cu-L2-I**, **Cu-L2-Br,** and **Cu-L2-Cl,** a single-crystal was obtained from DCM/Pentane *via* slow diffusion method. The detailed structural properties will be discussed in the following section. With **L3a** and **L3b,** the same conditions were tested, but unfortunately, no equivalent complexes were obtained.

3.1.1.3 Characterization of the Copper(I) complexes of the type $Cu_2X_2L_4$

Crystallographic analysis. For **Cu-L2-I**, **Cu-L2-Br**, and **Cu-L2-Cl**, single crystals were analyzed *via* single-crystal X-Ray diffraction, and the resulting structures will be discussed in detail in the following. The exact parameters can be found in the experimental part.

The structure is characterized by two bridging ligands and two ancillary ligands bound *via* the phosphine. Moreover, no halide bridges in the form of a Cu_2X_2-core are formed. All three structures crystallize in the triclinic P-1 space group. The structures are shown in Figure 22.

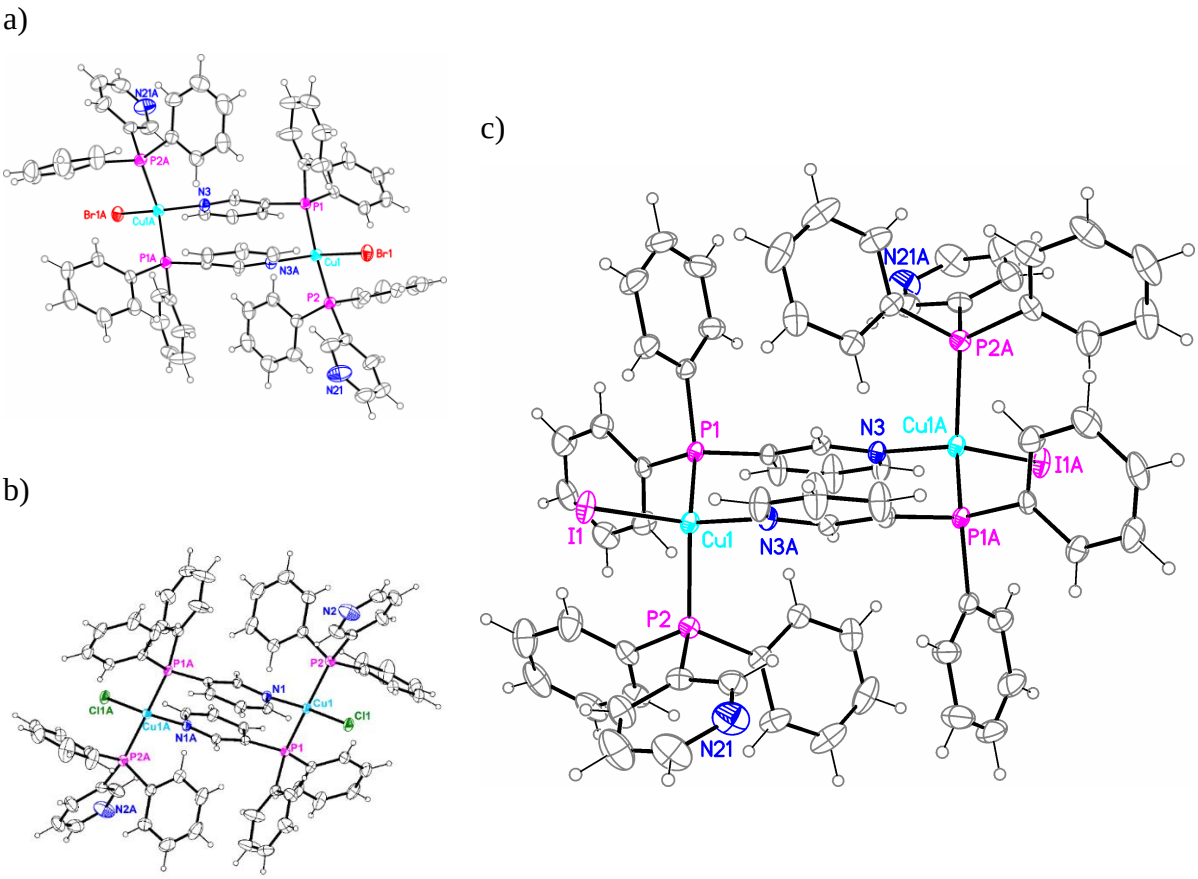

Figure 22. Molecular structure of a) **Cu-L2-Br**, b) **Cu-L2-Cl** and c) **Cu-L2-I** from single-crystal X-ray diffraction (ellipsoid at 50% probability level). Solvent molecules are omitted for clarity.

Another dibridged structure without halide bridges is the complex **47** of the type $Cu_2I_2L_2$, which was investigated by ZINK (Figure 23) and patented by MONKOWIUS and YERSIN.[162-163] In **47**, the sterically demanding methyl groups of the used ligand prevent the formation of the expected butterfly structure, which leads to the open core structure, as shown in Figure 23. In contrast to the novel structures presented in Figure 22, only two ligands are involved in total, whereas the fourth coordination site of the copper atom gets occupied through Cu-Cu interaction. This is shown through the small Cu-Cu distance of 2.67 Å.

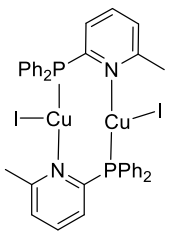

47

Figure 23. Reference dinuclear complex **47**, which has no halide bridges. Structure is patented by YERSIN and coworkers. [152, 163]

Since the phosphine is attached at the meta-position of the pyridine, the coordination of the complex core resembles that of a metacyclophane. However, the copper centers exhibit a distorted tetrahedral geometry, which is commonly observed in copper(I) complexes.[164] Table 2 provides a selected overview of bond lengths and angles, with particular attention to the intramolecular Cu···Cu distance, which is important for comparison with other dinuclear complexes. Typically, Cu···Cu distances range around 3.00 Å. For instance, the well-known butterfly-type structure generally exhibits Cu···Cu distances of approximately 2.70 Å.[41, 63, 138] For another dinuclear complex having two bridging ligands, the Cu···Cu distance was found to be 3.11 Å.[165] In the complexes presented here, the Cu···Cu distance is significantly larger, showing values of over 6.00 Å. This is caused as there is no bridged metal-halide core involved, but instead, the bridging ligands themselves are participating in the core structure, and the copper atoms do not share the same plane. The smallest intramolecular Cu···Cu distance with 5.99 Å was found for **Cu-L2-I**, whereas **Cu-L2-Br** showed the largest with 6.38 Å. The average Cu···Cu distance across all analyzed structures is 6.24 Å. The augmented distances suggest the absence of a Cu-Cu interaction, as it is longer than the sum of the van der Waals radii of Cu (2.80 Å). In the literature, only a few reports contain such high distances for dinuclear Cu(I) complexes, and those that do exist tend to involve large and flexible ligands, such as ferrocene-based ligands.[166-167]

Table 2. Selected lengths and angles of the crystallographic data of the dinuclear complex type $Cu_2X_2L_4$ for **Cu-L2-I**, **Cu-L2-Br,** and **Cu-L2-Cl**. X = corresponding halide, P1 = bridging phosphine, P2 = monodentate phosphine.

Lengths/ Å	**Cu-L2-I**	**Cu-L2-Br**	**Cu-L2-Cl**
Cu—Cu	5.9933 (6)	6.3791 (7)	6.3411(9)
X1—Cu1	2.6279 (3)	2.4612 (4)	2.3200(5)
Cu1—N1/N3	2.1266 (19)	2.1303 (19)	2.1101(15)
Cu1—P2	2.2874 (7)	2.2680 (7)	2.2587(5)
Cu1—P1	2.2683 (6)	2.2740 (6)	2.2638(5)
Angles/ °			
N1—Cu1—P2	101.57 (6)	112.60 (5)	112.32(5)
N1—Cu1—P1	114.66 (6)	102.65 (6)	102.97(4)
P2—Cu1—P1	119.46 (2)	124.74 (2)	124.03(2)
N1—Cu1—X	101.74 (5)	102.93 (5)	101.33(4)

Lengths/ Å	Cu-L2-I	Cu-L2-Br	Cu-L2-Cl
P2—Cu1—X	104.401 (19)	99.62 (2)	100.74(2)
P1—Cu1—X	112.891 (19)	112.606 (19)	113.50(2)

Depending on the nature of the ligand binding, the P—Cu—X angles change. For the bridging ligands the P—Cu—X angle is around ~113°, which is significantly larger compared to the P—Cu—X angles of the monodentate phosphine that are in the range of ~100°. A significant difference is seen in the angles of P—Cu—N. Attributed to the bigger steric demand of iodine, the trends are reversed for **Cu-L2-I** compared to **Cu-L2-Br** and **Cu-L2-Cl**. Additionally, the bond lengths of X—Cu1 correlate with the size of the halides, measuring 2.32Å for Cu—Cl, 2.46 Å for Cu—Br and 2.63 Å for Cu—I.

Solubility Study. For further applications such as OLEDs, the solubility or sublimability of the complexes plays a crucial role in the processing part. Hence, all complexes of the series **Cu-L2-X** were tested for their solubility in the common organic solvents, dichloromethane, chloroform, toluene, and *n*-hexane. The results are depicted in Table 2. For **Cu-L2-I** and **Cu-L2-CN,** no significant solubility in any of the organic solvents was observed, whereas a low solubility in chloroform was seen for **Cu-L2-Cl**. **Cu-L2-Br** demonstrated good solubility in dichloromethane and chloroform. **Cu-L2-SCN** shows the best solubility overall, exceeding 20 mg/ml in both DCM and chloroform, making it the most promising candidate for further applications such as solution-processed OLEDs.

Table 2. Overview of tested solubilities of the complex series **Cu-L2-X**. The tests were qualitatively taken of the powdered samples at 19 °C. Classification as follows: ● = > 20 mg/mL (excellent), ● = 10 – 20 mg/mL (good), ● = 1 – 10 mg/mL (low), ● = < 1 mg/m (none), n.t. not tested, due to not enough compound for testing.

Entry	Complex	Toluene	Chlorobenzene	Chloroform	Dichloromethane	*n*-Hexane
1	Cu-L2-I	●	●	●	●	●
2	Cu-L2-Br	●	●	●	●	●
3	Cu-L2-Cl	●	●	●	●	●
4	Cu-L2-CN	●	n.t	●	●	●
5	Cu-L2-SCN	●	n.t	●	●	●

Thermal stability. Since sublimability is another important factor in the OLED production, **Cu-L2-I**, **Cu-L2-Br**, and **Cu-L2-Cl** were tested for their sublimability up to 350 °C. All complexes decomposed gradually from 250 °C onwards and could not be successfully sublimed. For further exploration of the thermal stability of this complex class, a

thermogravimetric analysis (TGA) was performed exemplarily for **Cu-L2-Br**, in air at atmospheric pressure. The result of the TGA measurement is depicted in Figure 24. The data shows the weight loss in percent with increasing temperature. The complex decomposes in several steps. It is assumed that intermediate products are formed through the loss of the ligands. First, the two monodentate ligands decompose between 160 °C and 240 °C. The next 40% are lost up to 420 °C and can be attributed to the two bridging ligands. After around 550 °C, the decomposition is fully finished.

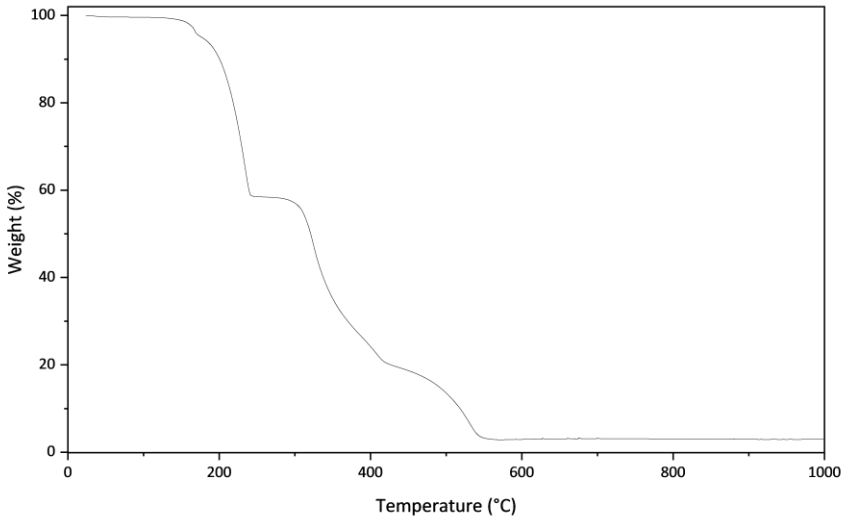

Figure 24. Thermogravimetric analysis of **Cu-L2-Br** at atmospheric pressure until 1000 °C.

3.1.1.4 Theoretical Calculation of Copper(I) complexes of the type $Cu_2X_2L_4$

To investigate the electronic properties, theoretical calculations DFT calculations of the ground states in gas-phase were performed in cooperation with Anna Mauri from the group of Wolfgang Wenzel (KIT, INT).

For all complexes, the excitation to the first singlet (S_1) and triplet (T_1) states predominantly involves transitions from the highest occupied molecular orbital (HOMO) to the lowest unoccupied molecular orbital (LUMO), with contributions of 98% and 97%, respectively. As depicted in Figure 25 the HOMO is mainly localized on the copper core, with strong contributions from the respective (pseudo-)halide. In contrast, the LUMO is primarily localized on the pyridine bridging ligand.

The HOMO composition varies significantly across the Cu-complexes, which influences the nature of the electronic transitions. In **Cu-L2-I** and **Cu-L2-SCN,** iodine and sulfur atoms dominate the HOMO contribution. This suggests a transition with a stronger halide-to-ligand

charge transfer (XLCT) character than metal-to-ligand charge transfer (MLCT). In contrast, **Cu-L2-Cl** and **Cu-L2-CN** show more contributions from the copper atoms, classifying the transitions as MLCT. **Cu-L2-Br** has similar contributions from the metal and bromine and, therefore, displays a mixed MLCT-XLCT character. Looking at the HOMO energies, these different contributions of the (pseudo-)halides have a significant influence on the HOMO energies. For **Cu-L2-CN**, the HOMO is the most stabilized, followed by **Cu-L2-Br** and **Cu-L2-Cl**. In contrast, for **Cu-L2-I** and **Cu-L2-SCN**, it gets destabilized compared to the others, which can be attributed to the higher XLCT character. Due to the fact, that the LUMOs are quite similar for all compounds, the HOMO-LUMO gap differs significantly in between the complexes. As expected, **Cu-L2-CN** shows the highest number of 3.99 eV. The energy gaps between the HOMOs and LUMOs, according to the fundamental gaps, range from 3.3 to 4.0 eV. When considering vertical excitation, which corresponds to the optical gap, the energy difference slightly narrows to 2.8–3.3 eV. The same trend of stabilization is observed in the energies of the first excited singlet and triplet states. This leads to a significantly higher energy gap between S_1 and T_1 for **Cu-L2-CN** with 0.11 eV, followed by **Cu-L2-Cl** with 0.09 eV and **Cu-L2-Br** with 0.06 eV. For **Cu-L2-I** and **Cu-L2-SCN**, the energy values are the lowest, showing values of 0.03 eV and 0.02 eV, respectively. These values lay in the range for TADF[26] and are comparable to other dinuclear complexes.[26, 63, 152]

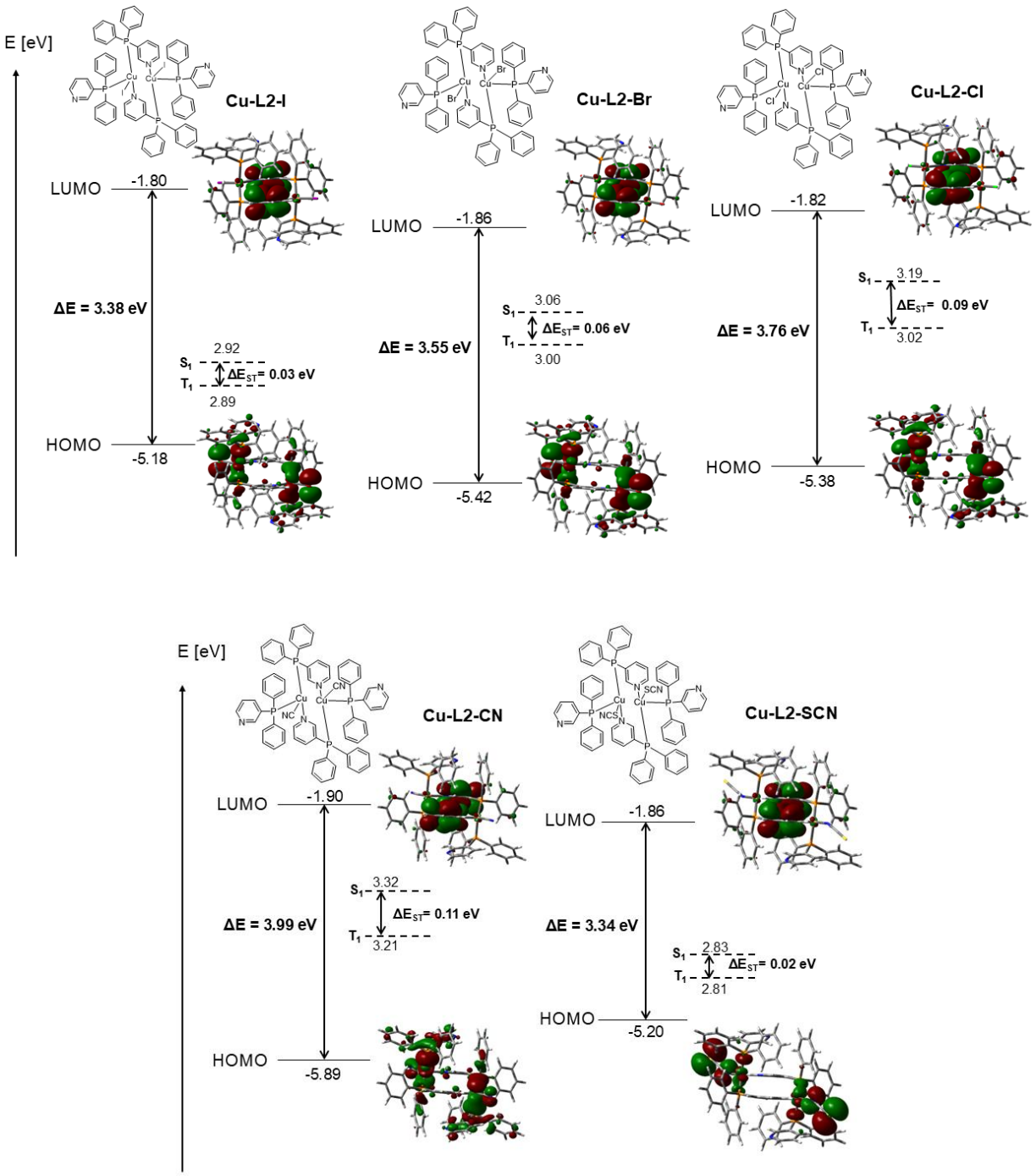

Figure 25. HOMO (up) and LUMO (down) representations of the studied complexes **Cu-L2-X** (X = I, Br, Cl, CN, SCN) The optimization was performed with the B3LYP-D3(BJ)/def2-TZVP method in gas-phase including LANL2DZ for iodine. An isovalue of 0.02 was used for visualization. Red and green indicate the positive and negative phases of the wave function, respectively. Color code: P (orange), Cu (brown), I (violet), Br (red), Cl (green), N (blue), C (grey), H (white), S (yellow). Results provided by Anna Mauri (KIT, INT).

These values provide important information on how the emission properties can be tuned in a targeted and effective way. The bridging ligand gives access to the LUMO, whereas the ancillary phosphines could be used to tune chemical properties, such as solubility.

For a more detailed investigation of the electronic transition upon excitation, the hole (electron donating) and electron/particle (electron accepting) regions for the $S_0 \rightarrow S_1$ transition as well as the $S_0 \rightarrow S_2$ transition were calculated. A representation of the hole and electron regions for these transitions is shown in Figure 26. The $S_0 \rightarrow S_2$ transition is mainly dominated by contributions of the HOMO-1 and LUMO. For **Cu-L2-SCN**, a noticeable variation in the two transitions is observed, as the HOMO (for S_1) and HOMO-1 (for S_2) orbitals are localized on the reversed thiocyanate ligands. Compared to the open core complex **47** of YERSIN *et al*. of the type $Cu_2Cl_2(N\text{^}P)_2$, the particle orbitals are located inside the core of the complex.[168] For **47**, the particle orbitals are outside directed, and a Cu-Cu-interaction is assumed, as mostly seen for dinuclear complexes, especially when they exhibit a Cu_2X_2-core. This underlines the uniqueness of this new compound class.

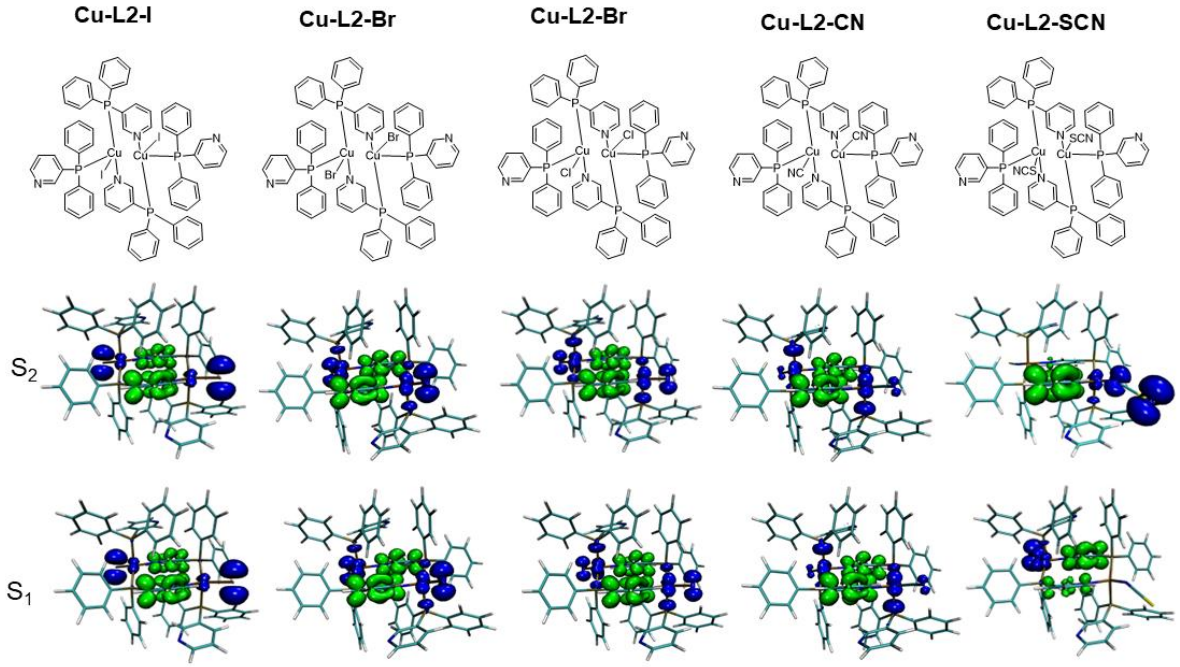

Figure 26. Representation of hole (blue) and electron (green) contribution upon excitation for **Cu-L2-X** (X = I, Br, Cl, CN, SCN) for the $S_0 \rightarrow S_1$ (bottom) and $S_0 \rightarrow S_2$ (top) transition. Data were computed in B3LYP-D3(BJ)/def2TZVP in gas-phase, including LANL2DZ for iodine. Isovalue of 0.002. Results provided by Anna Mauri (KIT, INT).

To compare the influence of the solvent, the ground state geometries of the complexes were optimized, including dichloromethane as solvent (PCM model), with two different functionals. In the ground state geometries, shown in Figure 27, only a slight rotation of the diphenyl-pyridyl-phosphine ligands in the presence of the solvent is seen.

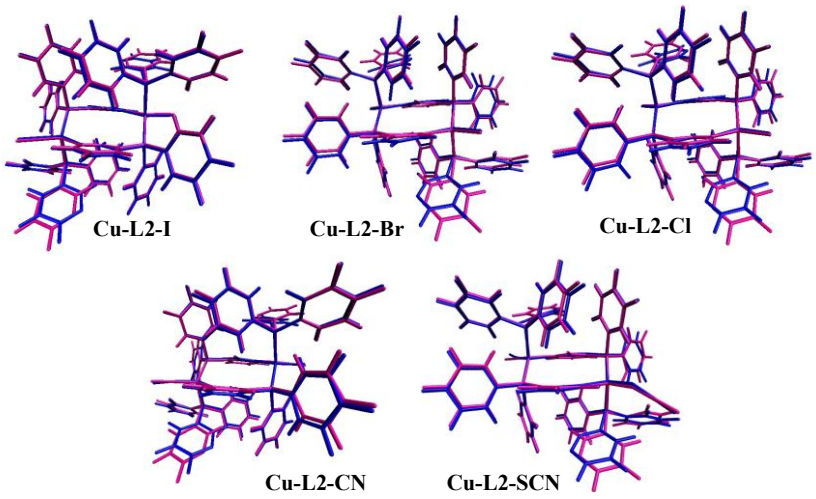

Figure 27. Visualization of the optimized ground state geometries in gas-phase (blue) and dichloromethane (magenta). Functional and basis set B3LYP-D3(BJ)/def2-TZVP (including LANL2DZ for I_2) was used for all complexes **Cu-L2-X** (X = I, Br, Cl, CN, SCN). Results provided by Anna Mauri (KIT, INT).

Additionally, the absorption properties were computed in gas-phase and dichloromethane. Depending on the functional used, significant differences can be observed. The detailed computational data and calculated absorption spectra can be found in the experimental part.

For the calculation in gas-phase, the excitation to the first singlet state, S1, is indicated to be a dark transition due to a zero oscillator strength. The excitation calculated for this transition are 424.84 nm, 405.22 nm, 400.51 nm, 373.39 nm, and 437.53 nm for **Cu-L2-I, Cu-L2-Br**, **Cu-L2-Cl**, **Cu-L2-CN**, and **Cu-L2-SCN**, respectively. The excitation to the S_2 state occurs at slightly higher energies of 421.50 nm, 401.96 nm, 397.61 nm, 371.94 nm, and 432.72 nm for **Cu-L2-I, Cu-L2-Br**, **Cu-L2-Cl**, **Cu-L2-CN**, and **Cu-L2-SCN**, with oscillator strengths of 0.0140, 0.0237, 0.0260, 0.0267, and 0.0056, respectively. Although in an expected range, these values display quite small numbers, as similar values are reported for a range of different copper(I) complexes.[169-171] The small numbers can be explained by the spatial separation of the involved molecular orbitals.[124]

3.1.1.5 Photophysical Characterization of Copper(I) complexes of the type $Cu_2X_2L_4$

In the following, the theoretical results were supported with photophysical measurements and compared to the experimental results. First, the absorption properties will be discussed, followed by a detailed investigation of the photophysical properties of the complexes at different wavelengths and temperatures.

Absorption properties. The quantitative absorption spectra of complexes **Cu-L2-I**, **Cu-L2-Br**, **Cu-L2-Cl**, **Cu-L2-CN**, and **Cu-L2-SCN** in DCM are shown in Figure 28. The general course of the absorption spectra measured in dichloromethane, plotted as molar absorbance, is comparable to the spectra of the well-studied 2-PyrPhos copper(I) complexes known from the literature.[138] Usually, three areas are determined in UV-Vis spectra in solution that can be attributed to different transitions. Between 200 and 240 nm, π-π^* transitions are observed, usually coming from the phenyl groups within the ligands. Bands between 250 and 290 nm mostly result from ligands with lone pair electrons *via* n-π^* transitions, and lastly, between 300 and 400 nm, MLCT, LLCT, and (M+X)LCT-transitions occur.[20] While the solvent masks the π-π* absorption maximum (below 240 nm), all compounds show an additional broad shoulder ranging from 250 to 300 nm. The absorption between 300 and 400 nm is absent for the free ligand, suggesting MLCT and (M+X)LCT transitions. At approximately 400 nm, all absorption spectra reach a molar extinction coefficient of zero. Overall, **L2** exhibits the lowest molar extinction coefficient, not exceeding $2\times10^4 M^{-1}cm^{-1}$. In contrast, the complexes demonstrate significantly higher ε, with the highest overall values for **Cu-L2-I**, **Cu-L2-CN**, and **Cu-L2-SCN** in the range of 5×10^4 M^{-1} cm^{-1} at ~275 nm.

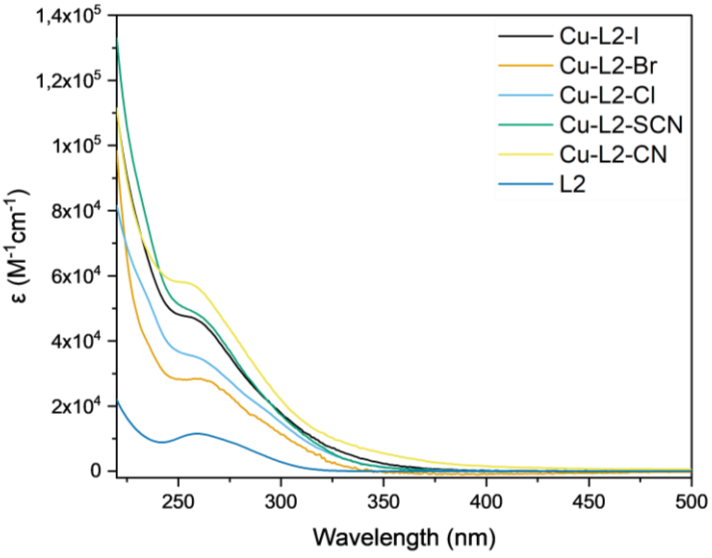

Figure 28. Quantitative UV-VIS absorption spectra in dichloromethane for complexes **Cu-L2-X** (X = Br, Cl, CN, SCN) and **L2**.

Steady-state Luminescence Spectroscopy. The following photophysical measurements were mostly taken with solid-state KBr pellets of **Cu-L2-X** (X = I, Br, Cl, CN, SCN) and **L2** as a reference. They were conducted by Daniel Marhöfer (RPTU, Prof. Niedner-Schatteburg) through collaboration. The related measurements will be called ‘pellets’ in the following. The pellets are made by mixing the powdered samples of the compounds with KBr under pressure.

For **Cu-L2-I**, **Cu-L2-Br**, and **Cu-L2-Cl,** additional steady-state luminescence spectra were measured for the powdered samples at 290 K and 77 K and photoluminescence quantum yields (PLQY) at room temperature. These were carried out by Dong-Hui Chen (KIT, IFG) and will be named 'powdered' measurements from now on. As in powdered samples, self-quenching effects can occur, the PLQY measurements for **Cu-L2-I** and **Cu-L2-Cl** were additionally conducted in films of PMMA in air and nitrogen. As the solubility of these compounds was insufficient, only low concentrations of 0.1 and 0.5% were used. For **Cu-L2-Br**, no suitable films were obtained. Therefore no PLQY measurement in PMMA was conducted for this complex. A summary of the obtained values for the emission maxima of the different measurement approaches as well as the PLQYs is given in Table 3.

In the following, a detailed analysis of the pellets including the emission and lifetime properties of the complexes at different wavelengths and temperatures will be discussed and compared to the measurements that were taken of the powdered samples.

Firstly, the luminescence properties of all five complexes were measured in pellets using various excitation wavelengths between 260 and 500 nm. Exemplarily, the obtained spectra for **Cu-L2-Cl** are shown in Figure 29 for 5 K and 290 K. Especially at the low temperature measurements, an excitation-dependent emission occurs. This effect starts between λ_{ex}=360 and 380 nm; from then on, a higher excitation wavelength leads to a bathochromic shifted emission wavelength, indicating that different states are involved in the emission process. All complexes showed this excitation-dependent emission behavior, most pronounced for **Cu-L2-Br** and **Cu-L2-Cl**.

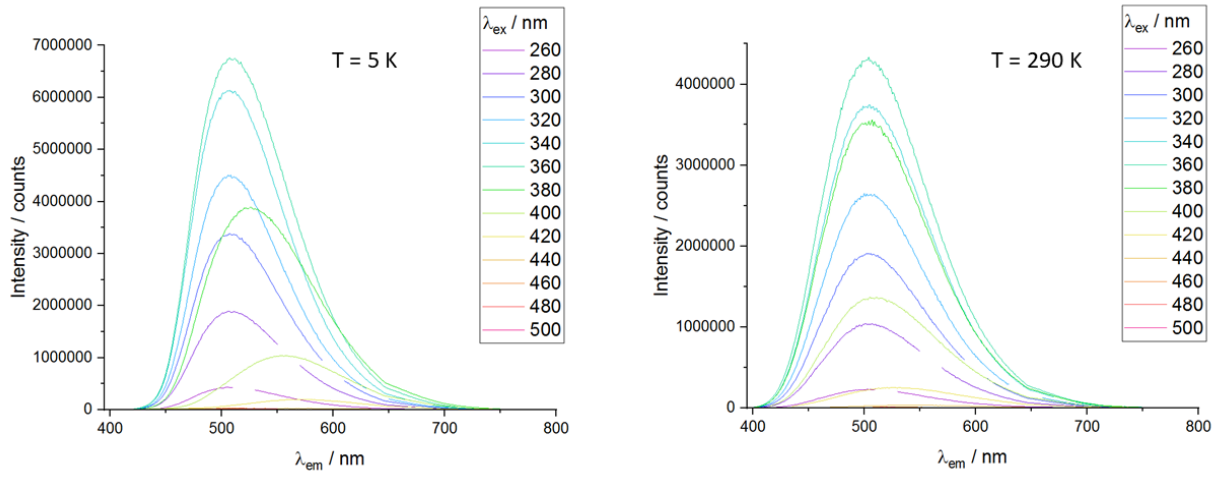

Figure 29. Luminescence spectra of **Cu-L2-Cl** at different excitation energies between 260 and 500 nm in a sintered KBr pellet at 5 K (left) and 290 K (right). Results provided by Daniel Marhöfer.

Considering this finding, temperature-dependent measurements from 5 K to 290 K were performed for all complexes in pellets at two different excitation energies. By analyzing the

emission behavior across different temperatures, insights into the participating states can be inferred. Figure 30 and Figure 31 illustrate the emission spectra of all complexes for λ_{ex}= 355 nm (left) and the respective elevated excitation wavelength between 380 and 420 nm (right) for temperatures between 5 K and 290 K.

Lower energy excitation. At lower energy excitation (380-420 nm), typical TADF behavior is observed. With decreasing temperature, a red shift with only a small intensity increase is seen for **Cu-L2-I**, **Cu-L2-Br**, and **Cu-L2-Cl**. This indicates the involvement of triplet states in the emission pathway. As explained in *Chapter 1.1*, phosphorescence becomes visible at lower energy emission, as non-radiative processes are typically suppressed at low temperatures. For **Cu-L2-CN,** a stronger decrease of the intensity is observed for higher temperatures, still showing a hypsochromic shift. For **Cu-L2-SCN**, the smallest shift is observed, resulting in a nearly constant emission maximum at all temperatures. This can indicate phosphorescence or a particular small ΔE_{ST} resulting from a degeneration of the excited singlet and triplet states involved in the emission process. This assumption is supported by the theoretical calculations, which indicate the smallest value of ΔE_{ST} for **Cu-L2-SCN** among all complexes with a value of 0.02 eV. To ascertain the specific type of emission, additional measurements, such as time-correlated single-photon counting (TCSPC) were employed and will be discussed further on. To sum up, the former described bathochromic shift was most prominent for compounds **Cu-L2-Br** and **Cu-L2-Cl**, as illustrated by Figure 30 and Figure 31 on the right sides, while the shift for the remaining compounds remained below 20 nm.

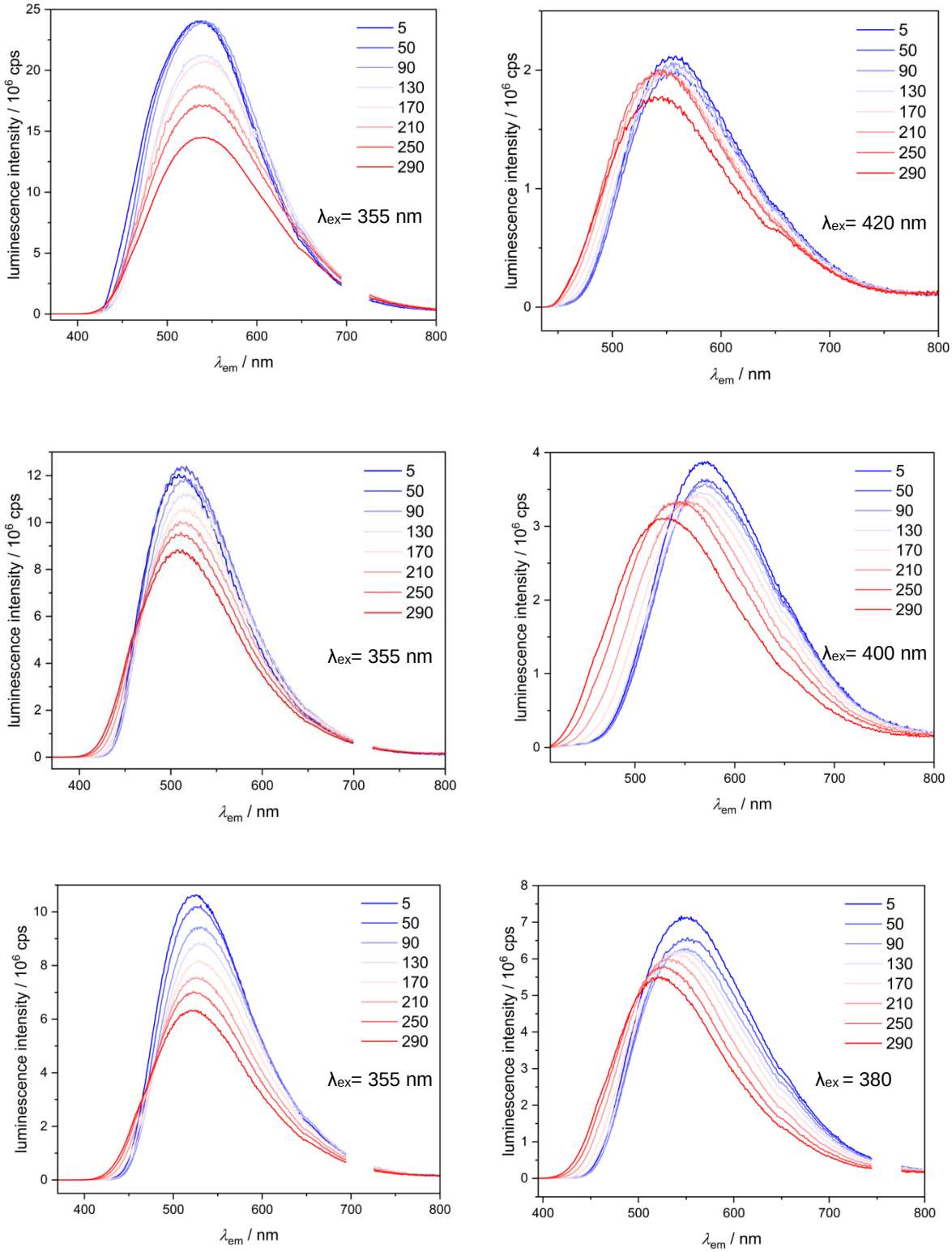

Figure 30. Luminescence spectra of **Cu-L2-I** (Top), **Cu-L2-Br** (Middle), **Cu-L2-Cl** (Bottom) at λ_{ex}= 355 nm (left, for all) and λ_{ex}= 420 nm (Top, right), 400 nm (Middle, right), 380 nm (Bottom, right) in a sintered KBr pellet between 5 and 290 K. Results provided by Daniel Marhöfer (RPTU).

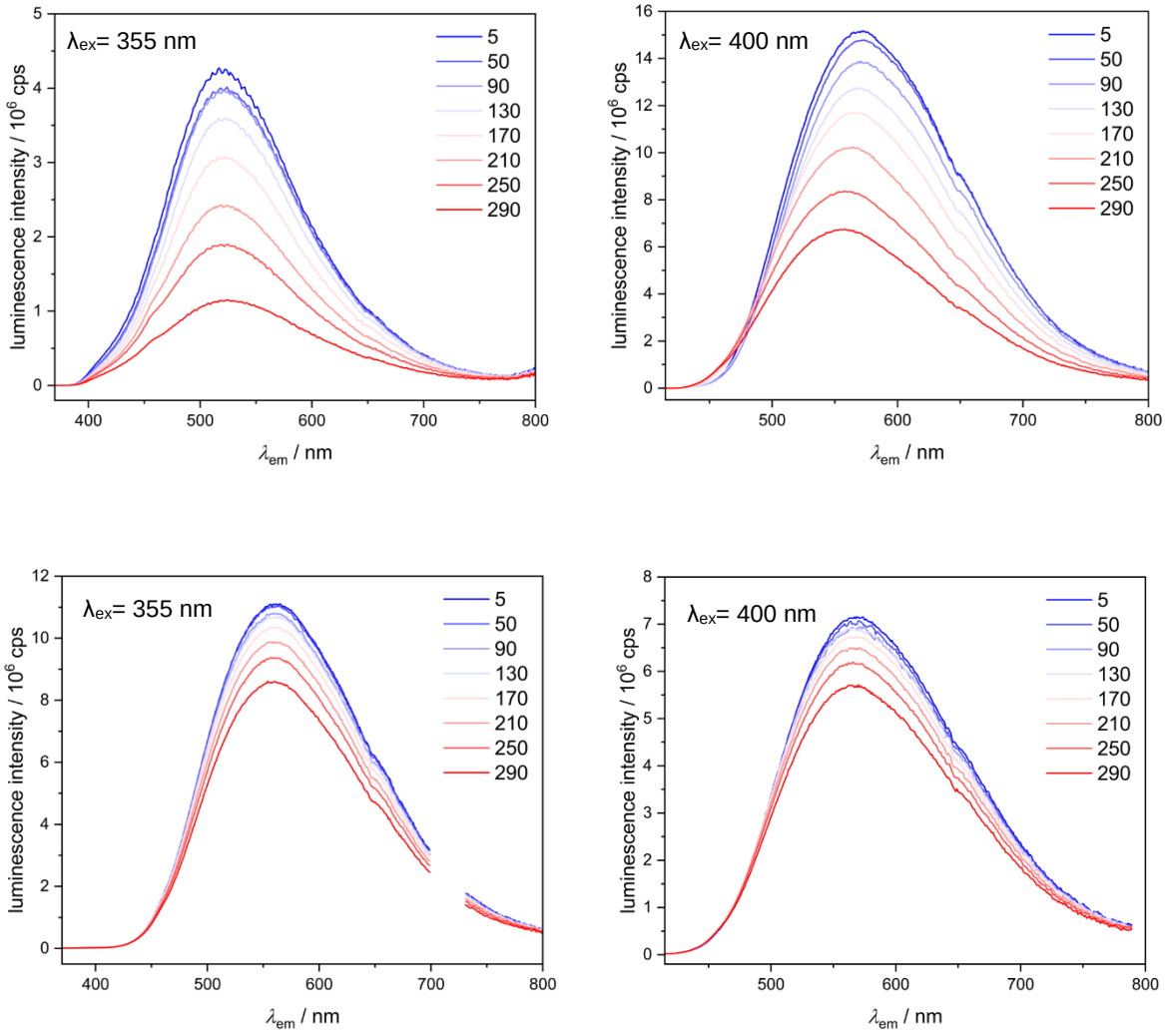

Figure 31. Luminescence spectra of **Cu-L2-CN** (Top), **Cu-L2-SCN** (Bottom) at λ_{ex}= 355 nm (left) and λ_{ex}= 400 nm (right) in a sintered KBr pellet between 5 and 290 K. Results provided by Daniel Marhöfer (RPTU).

Higher energy excitation. Using a higher energy excitation wavelength of λ_{ex} = 355 nm for the pellet samples, the emission maxima at 290 K show a blueshift for all complexes compared to lower energy excitation. As in the previous section, temperature-dependent measurements were taken for λ_{ex} = 355 nm between 5 K and 290 K. The wavelength of the emission maxima in this measurement row remained mostly identical at both 5 K and 290 K for all complexes; hence, no temperature-dependent shift was observed. Nevertheless, the intensity increases for all five complexes at lower temperatures, as can be seen in Figure 30 and Figure 31 on the left sides.

A direct comparison of the emission maxima at different excitation wavelengths indicates that a higher energy state might be involve, as the emission maximum is hypsochromic shifted for the lower excitation wavelength. This shift is even seen when compared to the emission of the free ligand, which indicates, that the origin is not a ligand-centered emission. However, the origin of this unusual emission behavior cannot be surely predicted, as further studies are necessary. For a better illustration of the emission maxima, a direct comparison of the emission for different excitation wavelengths is exemplarily shown for **Cu-L2-Br** in one spectrum in Figure 32.

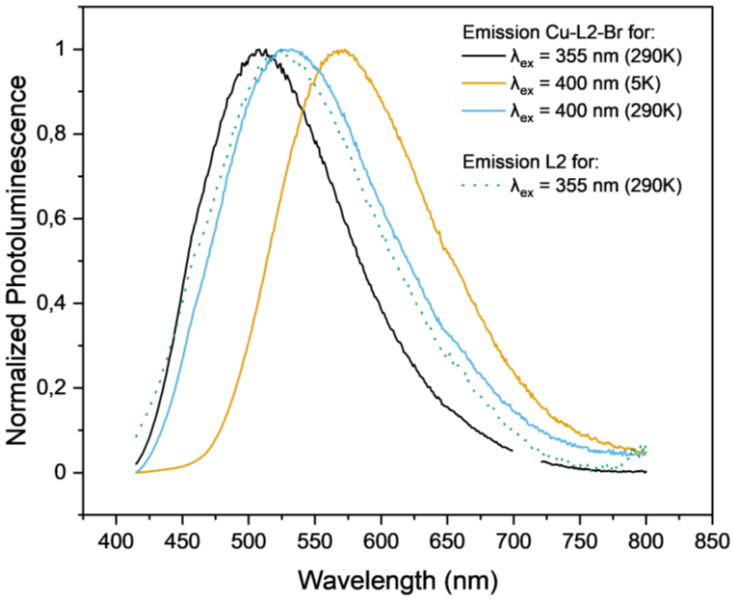

Figure 32. Comparison of the luminescence spectra of **Cu-L2-Br** and **L2** at λ_{ex} = 355 nm and 400 nm for 290 K and 5 K. Results were provided by Daniel Marhöfer (RPTU).

As a reference compound, the ligand exhibits only weak emission at both excitation wavelengths, even at 5 K, likely due to its low absorption and non-radiative relaxation processes. The luminescence spectra of **L2** for the excitation at 355 nm (left) and 300 nm (right) can be found in the experimental part.

Comparing the emission spectra of pellets and powder samples, the emission maxima of the powdered samples are significantly shifted to higher energies. Interestingly, the typical bathochromic shift with decreasing temperature, that is usually observed for TADF materials, is not found for the powdered samples. Instead, either no shift or, for example, for **Cu-L2-I**, a reversed trend of $\Delta\lambda_{em}$= -11 nm is observed. These phenomena were already intensively studied for different NHetPhos complexes by ZINK and VOLZ. [162, 172]

They were explained by rigidochromic effects, which describe the alteration of emission wavelength depending on the environment of the complex due to resulting changes in the rigidity or flexibility of the molecule. When the environment is more rigid, as is the case for powdered samples compared to solution, a blue-shift of the emission can be observed.

Interestingly, ZINK also found that a blue-shift at lower temperatures might be observed for complexes that exhibit a large Cu-Cu distance.[162] Since the here presented complexes exhibit an extraordinarily large distance between the copper atoms, this leads to the assumption that similar effects play a role here, as the rigidity of the bulk samples (powder) should be higher than for the pellet samples. The effect of rigidochromism was already described in 1974 for several rhenium complexes.[173] However, in 1995, LEES investigated the origin of this effect for several organometallic complexes and concluded, that mostly triplet-centered MLCT states are affected by this phenomenon.[174]

A significant difference can be observed in the PLQYs depending on the sample used. For instance, the powdered samples of **Cu-L2-I, Cu-L2-Br, Cu-L2-Cl** show quantum yields from 2% for **Cu-L2-I** to 67% for **Cu-L2-Cl** at room temperature. In contrast, when measuring PMMA films, the PLQY is significantly higher for **Cu-L2-I** with 16% and lower for **Cu-L2-Cl** with 23%. The PLQY also strongly depends on the sample form used and the included halide, as reported by ZINK.[161] Comparing the PLQYs in films in air and nitrogen atmosphere at an excitation wavelength of 350 nm, only a small increase of 3% is observed in nitrogen. This increase is typical if triplet states are involved in the decay process, as they are quenched through oxygen.[175]

Since the complexes **Cu-L2-X** for X = I, Br, Cl, CN, and SCN show a shift of their emission based on the used excitation wavelengths, it is assumed that different emission pathways *via* different states are occurring. For lower energy excitation, the decrease in intensity for higher temperatures and the observed blue shift indicate the involvement of triplet states, as non-radiative processes get suppressed at low temperatures and, therefore, phosphorescence becomes visible. This renders the contribution of a TADF mechanism feasible for **Cu-L2-X** (X = I, Br, Cl, CN, SCN) based on the luminescence spectra.

Overall, the sum of acquired data indicates that the complexes emit through different pathways *via* different states, one of which may be TADF, the other cannot be precisely assigned, but shows characteristics of the participation of higher lying states. The following table summarizes the key values that were obtained for the different samples (powder, pellet, doped PMMA).

Table 3: Emission wavelengths and quantum yields of **Cu-L2-X** (X = I, Br, Cl, CN, SCN) measured as powder sample at 77 K and 297 K, as sintered KBr pellet at 5 K and 290 K, or as doped PMMA film. The respective excitation wavelength is given in brackets.

	$\lambda_{max,PL}$[a] at 297 K [nm]	$\lambda_{max,PL}$[a] at 77 K [nm]	$\Delta\lambda_{max,PL}$	$\lambda_{max,PL}$[b] at 290 K [nm]	$\lambda_{max,PL}$[b] at 5 K [nm]	$\Delta\lambda_{max,PL}$	Φ[a] [%]	Φ[c] in air/N_2 [%]
Cu-L2-I	497 (385)	503 (385)	-6	539 (355)	537 (355)	-2	2	13/16 (350)[d]
				544 (420)	558 (420)	14		
Cu-L2-Br	502 (375)	502 (375)	0	510 (355)	510 (355)	0	31	-
				530 (400)	576 (400)	42		
Cu-L2-Cl	535 (369)	524 (369)	-11	523 (355)	525 (355)	2	67	20/23 (350)[e]
				523 (380)	551 (380)	28		
Cu-L2-CN	-	-		523 (355)	520 (355)	-3	-	
				557 (400)	573 (400)	16		
Cu-L2-SCN	-	-		559 (355)	561 (355)	2	-	
				566 (400)	570 (400)	4		

[a] Measured in powdered sample. [b]Measured in sintered KBr pellet. [c]Measured in a 1% film in PMMA. The film was prepared with drop-casting under air in DCM and followed curing at 30 °C. [d]Concentration of 0.1 % in PMMA. [e]Concentration of 0.5 % in PMMA

Lifetime measurements (TCSPC). To further investigate the luminescence lifetimes, TCSPC measurements were carried out for the pellet samples. The measured lifetimes are shown in the table below. For **Cu-L2-X** for X = I, Br, Cl, CN, and SCN, a strong increase in the decay lifetime is observed at lower temperatures, as commonly known for TADF emitting materials. In conjunction with the observed decrease in luminescence lifetime and the notable blue shift in emission maxima, it can be posited that the complexes are undergoing a TADF process. This is especially apparent in the case of **Cu-L2-SCN**, as this complex has the highest change in the lifetimes (7 µs for 290 K → 1600 µs for 5 K).

Table 4. Luminescence lifetimes measured at λ_{ex}= 390 nm or λ_{ex}= 341 nm and λ_{em} set to the respective emission maxima of each complex at the specific temperature measured in a sintered KBr pellet. All values are weighted averages in µs. The measurements were limited to the available excitation LEDs with excitation wavelengths of λ_{ex}= 390 nm or λ_{ex}= 341 nm.

T [K]/ τ [µs]	**Cu-L2-I**	**Cu-L2-Br**	**Cu-L2-Cl**	**Cu-L2-CN**	**Cu-L2-SCN**
5	56	1740	1810	520	1600
50	54	2070	1960	480	1610
90	46	1920	1990	250	1110
130	37	1900	1930	150	610
170	29	620	760	45	240
210	20	31	650	21	110
250	17	23	590	12	9
290	12	23	580	7	7

Additionally, by employing a sigmoidal fitting of the temperature-dependent lifetimes, the energy gaps between T_1 and S_1 were calculated for **Cu-L2-X** for X = I, Br, Cl, CN and SCN. The results are compared to the calculated values and summarized in Table 4. The fitted temperature-dependent lifetimes can be found in the experimental part.

Table 4. Comparison of experimental and calculated values for ΔE (S_1-T_1) in eV.

Compound	ΔE (S_1-T_1) exp. [eV]	ΔE (S_1-T_1) calcd. [eV]	Δ
Cu-L2-I	0.036	0.03	0.060
Cu-L2-Br	0.260	0.06	-0.200
Cu-L2-Cl	0.060	0.09	0.030
Cu-L2-CN	0.035	0.11	0.075
Cu-L2-SCN	0.046	0.02	-0.026

The gaps of S_1-T_1 of **Cu-L2-X** for X = I, Br, Cl, CN, and SCN, are in a similar range as for other dinuclear complexes in literature (0.035 eV to 0.26 eV).[26, 61] For example, the PyrPhos complex **30** (Figure 16), shows a ΔE (S_1-T_1) of 0.03 eV.[137]

The gap for **Cu-L2-Br** is significantly higher, emphasizing the observed substantial blue shift in the steady-state spectra (Figure 30). Nevertheless, the values are slightly deviating from the calculated numbers for **Cu-L2-X** for X = I, Br, Cl, CN, and SCN, with a maximum deviation for **Cu-L2-Br** of 0.20 eV. This discrepancy could be attributed to the fact, that the calculation is conducted in the gas phase, whereas the experimental procedures are performed in the solid state.

The calculation and supporting photophysical measurements indicate, that by exchanging the bridging ligands in addition to the (pseudo-)halides, the LUMO energy should be changeable, which would directly be reflected in the emission properties. By destabilizing the LUMO, complexes should be formed which show an emission at lower wavelengths. Additionally, since the ancillary ligands are not significantly involved in the frontier orbitals, there are many possibilities for fine-tuning the chemical properties, such as solubility, by including solubilizing functionalities. As this structural class exhibits highly promising features for applications in OLEDs or sensors, the next step aimed at derivatization is to get access to a variety of complexes that can be tuned according to the needs.

3.1.1.6 Derivatization of the complex type $L_4Cu_2X_2$

Various derivatization approaches were performed to investigate the described complex series' tuneable properties. An overview is given in Table 5. All syntheses described in the following chapter were carried out by the general synthetic route, only varying the ratios of the respective ligands. Firstly, the homoleptic complexes aimed to use **L3** and **L4** as bridging and monodentate ligands. Nevertheless, no similar complexes were accessible for either of the ligands for any of the CuX salts (Table 5, entry 1 and 2). This phenomenon may be attributed to the elevated steric demands of the methyl groups or the increased susceptibility of the ligands to oxidation.

The hole-electron analysis of the **Cu-L2-X** series indicated that the bridging ligands are mainly involved in the electronic transitions in form of the LUMO. Consequently, it can be postulated that a substitution of the monodentate phosphine ligands should be feasible without significantly impacting the emission properties. As a result, the tuning of chemical properties, such as solubility, should be achievable. Hence, the subsequent objective was to create heteroleptic complexes by exchanging the monodentate phosphines. A schematic representation of the exchangeable positions is provided in Figure 33, wherein violet spheres illustrate the exchangeable locations.

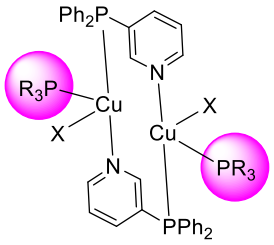

Figure 33. Illustration of exchangeable positions, highlighted *via* violet spheres.

In the first set of experiments, the commercially available ligand triphenylphosphine **48** was initially employed as an ancillary ligand. Additionally, the incorporation of fluorine-containing phosphines, such as tris(4-fluorophenyl)phosphine **49**, is expected to enhance the solubility strongly, as evidenced by the literature on the already discussed “butterfly”-complexes, and was therefore targeted as well.[138] The structures of **48** and **49** are shown in Figure 34.

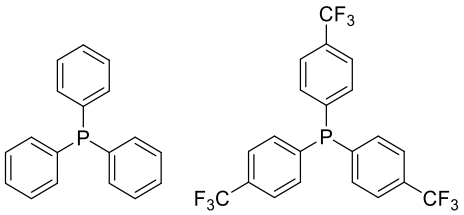

Figure 34. Structures of used monodentate phoshpine ligands triphenylphosphine **48** and tris(4-(trifluoromethyl)phenyl)phosphine **49**.

As the parent complexes were already not obtained in a straightforward manner of a 4:2 ratio, different ratio mixtures of the respective ligands and CuI were screened (Table 5, entries 3 to 9). The following table gives an overview of all screening results.

Table 5. Screening of derivatizations for the dinuclear complex class $Cu_2X_2L_4$.

Entry	Bridging Ligand	Ancillary P-Ligand	CuX	Ratio (L:P:CuX)	Yield
1 a, b, c	L3	-	CuI (a)/CuBr (b)/CuCl (c)	6:0:2	-[a]
2 a, b, c	L4	-			-[a]
3	L2	48	CuI	**3:2:2**	**81%**[c]
4				2:2:2	-[b,c]
5	L2	49	CuI	5:2:2	-[b]
6				4:2:2	-[b,c]
7				2:2:2	-[b]
8				3:3:2	-[b]
9				2:4:2	-[b]

General reaction conditions: DCM was used as solvent, 23 °C, 18 h. [a] no complex was obtained. [b] The respective P-Ligand was not found in the product. [c] a crystal structure was obtained.

Using a ratio of **3:2:2** (**L2**:**1**:CuI), a heteroleptic complex **Cu-L2-I-a,** similar to **Cu-L2-I** with **48** as the monodentate ligand was successfully obtained with an excellent yield of 81 % (Table 5, Entry 3). The targeted structure **Cu-L2-I-a**, shown in Figure 35, was determined *via* single-crystal analysis using a filtered solution to grow the crystals. However, using an unfiltered solution, a polymeric structure **Cu-L2-I-b** crystallized instead. The structures of the unit cell and the respective polymeric structure are shown in Figure 36. Nevertheless, for both structures, the two ligands are incorporated successfully in a ratio of 1:1, but **Cu-L2-I-a** crystallized in a triclinic system, while **Cu-L2-I-b** shows a tetragonal system. Table 6 summarizes a selection of the most common bond lengths and angles. For a better understanding, the values for the parent complex **Cu-L2-I** are included as a reference.

Comparing **Cu-L2-I-a** and **Cu-L2-I**, it is observed that their values are nearly identical, which can be attributed to the strong similarity in their underlying structure. A comparison between **Cu-L2-I-a** and **Cu-L2-I-b** is clearly more intriguing and reveals some differences. Most of the distances show similar lengths, with Cu—I being nearly identical. The biggest difference is displayed by the angles P1/2—Cu1—I1. While **Cu-L2-I-a** is associated with a wider angle of P1—Cu1—I1 (112.73°), **Cu-L2-I-b** shows a similar range for P2—Cu1—I1 (111.65°).

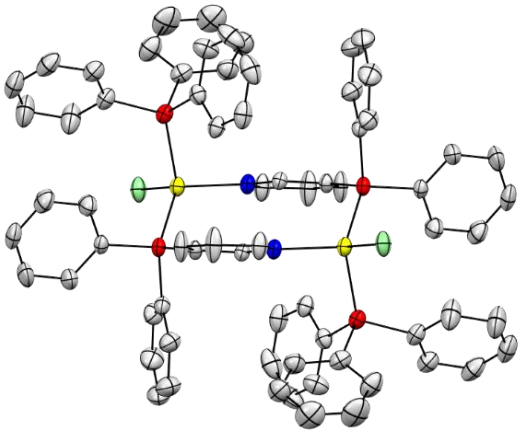

Figure 35. Structure of **Cu-L2-I-a** from single-crystal X-ray diffraction (ellipsoid at 50% probability level). Hydrogen atoms are omitted for clarity. Color code: yellow (Cu), red (P), blue (N), green(I).

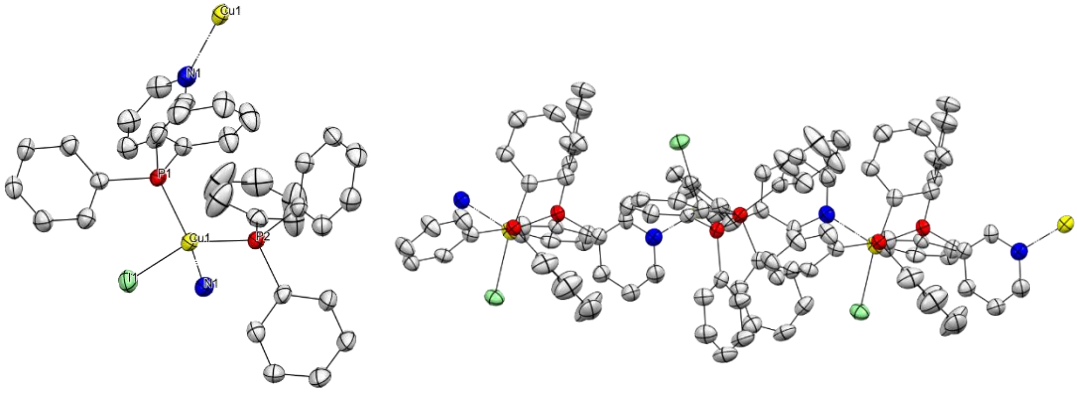

Figure 36. Structure of side product **Cu-L2-I-b**. Unit cell structure (left) and respective polymeric structure (right) from single-crystal X-ray diffraction (ellipsoid at 50% probability level). Hydrogen atoms are omitted for clarity. Color code: yellow (Cu), red (P), blue (N), green(I).

Table 6. Selected lengths and angles of the crystallographic data of **Cu-L2-I-a** and **Cu-L2-I-b**. **Cu-L2-I** is included as reference. P1 = monodentate phosphine, P2 = bridging phosphine.

Lengths/ Å	**Cu-L2-I**	**Cu-L2-I-a**	**Cu-L2-I-b**
Cu—Cu	5.9933 (6)	5.993[a]	-
X1—Cu1	2.6279 (3)	2.6243(4)	2.6195(12)
Cu1—N1/N3	2.1266 (19)	2.130(2)	2.122(6)
Cu1—P2	2.2874 (7)	2.2897(8)	2.2758(19)
Cu1—P1	2.2683 (6)	2.2723(7)	2.2639(19)
Angles/ °			
N1—Cu1—P2	101.57 (6)	101.94(6)	100.86(17)
N1—Cu1—P1	114.66 (6)	113.81(6)	113.66(18)
P2—Cu1—P1	119.46 (2)	120.26(3)	119.34(7)
N1—Cu1—I1	101.74 (5)	101.28(6)	105.65(17)
P2—Cu1—I1	104.401 (19)	104.58(2)	111.65(6)
P1—Cu1—I1	112.891 (19)	112.73(2)	105.08(6)

[a]calculated with Mercury (2024.1.0). P1: 3-PyrPhos, P2: PPh_3.

Cu-L2-I-a was further investigated with UV-Vis measurements in DCM (Figure 37). The overall structure is comparable to the reference complex **Cu-L2-I**, showing a broad absorption with a shoulder at 261 nm and an increasing absorbance below 250 nm.

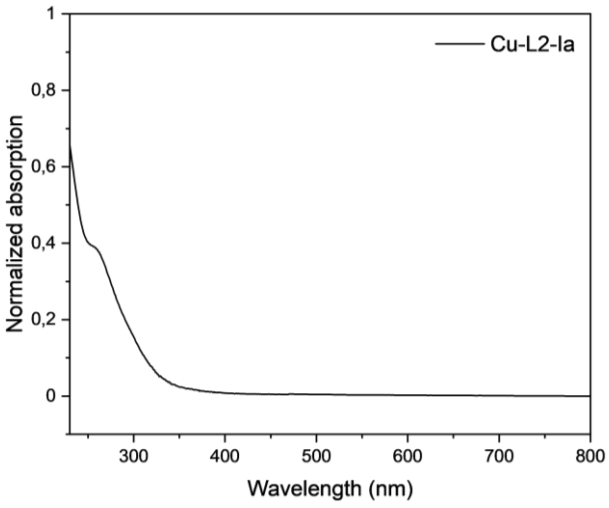

Figure 37. UV-Vis spectra of **Cu-L2-I-a**, measured in DCM.

The complex **Cu-L2-I-a** exhibits low solubility in DCM and toluene, so no quantitative UV-Vis or photoluminescence measurements could be performed in PMMA films. Nevertheless, the formation of **Cu-L2-I-a** proves that an exchange of the ancillary ligand is possible. To further enhance the solubility of this complex class, ancillary ligands with solubilizing moieties, such as tert-butyl groups or halides, should be introduced. Unfortunately, obtaining a complex with tris(4-fluorophenyl)phosphine **49** as a monodentate phosphine ligand was unsuccessful for various screened ratios (Table 5, entries 5-9). This result may be attributed to the greater steric demand imposed by the CF_3 groups.

Given the complexity of the synthesis and the difficulty in achieving the desired ratios, further investigation into the reaction conditions is recommended. For instance, the influence of solvent, temperature and concentration was not tested in the scope of this work. Furthermore, due to the steric properties, ancillary ligands featuring more flexible or smaller groups would be highly interesting for screening. There are countless possibilities to study this complex class further, as the two monodentate ligand sites show great potential for derivatization and, therefore, offer the possibility of finetuning the chemical properties according to specific requirements.

3.1.2 Silver(I) complexes of the type $L_4Ag_4I_4$

Introduction. Silver(I) complexes represent another intriguing class of luminescent materials; however, these complexes have been the subject of fewer investigations than Cu(I) complexes. This is likely due to the higher oxidation potential of Ag(I) in comparison to Cu(I), which results in the 4d orbitals being situated below ligand-centered (LC) states in terms of energy.[13, 176] This leads to a tendency to exhibit phosphorescence, determined by these low-lying ligand-centered ^{3}LC states. Nevertheless, several cases of complexes exhibit TADF properties, including a mononuclear three-coordinated complex with diphosphine ligands, as demonstrated by OSAWA and coworkers.[35] However, complexes with NP ligands are seldom reported in the literature, with only a handful of exceptions, such as complexes with tris(2-pyridyl)phosphine[177] and tris(2-pyridyl)phosphine oxide, respectively.[178]

The well-known NP-ligand **L1** 2-PyrPhos was already introduced for Ag(I) complexes in 1998 and recently subjected to further investigation, compared to copper(I) complexes.[179-180] However, no complex featuring 3-pyridylphosphine has been identified so far. The following chapter will thus examine the use of the presented ligand **L2** for the use in Ag(I) complexes.

Synthesis and Characterization. By applying the same synthesis route as shown for the complexes of the previous chapter by using AgX (X=I, Br, Cl) instead of CuX, three complexes Ag_4I_4(3-PyrPhos)$_4$ (**Ag-L2-I**, 51% yield), Ag_4Br_4(3-PyrPhos)$_4$ (**Ag-L2-Br**, 91% yield) and Ag_4Cl_4(3-PyrPhos)$_4$ (**Ag-L2-Cl**, 90% yield) were obtained and characterized *via* elemental analysis and mass spectrometry. Furthermore, crystal structures were obtained in the case of **Ag-L2-I** and **Ag-L2-Br**, which are shown in Figure 38. Despite the application of a 3:1 (= 6:2) ratio in an attempt to create an analog dibridged complex as **Cu-L2-I**, the resulting silver(I) complexes did not exhibit the anticipated structure but instead formed a tetranuclear cubane Ag_4X_4 configuration with four ligands coordinated *via* the phosphorus atom to the metal. Such structures are well-known for silver(I) complexes.[181-182] Given that the analytics for **Ag-L2-Cl** align with those for **Ag-L2-I** and **Ag-L2-Br**, they are proposed to reflect the same structure, although this cannot be definitively proven. Similar motifs were recently published by BUSCH *et al.* for 2-PyrPhos.[180] While their reaction conditions are slightly different, particularly the use of acetonitrile at 90 °C for 24 hours, the results are comparable.

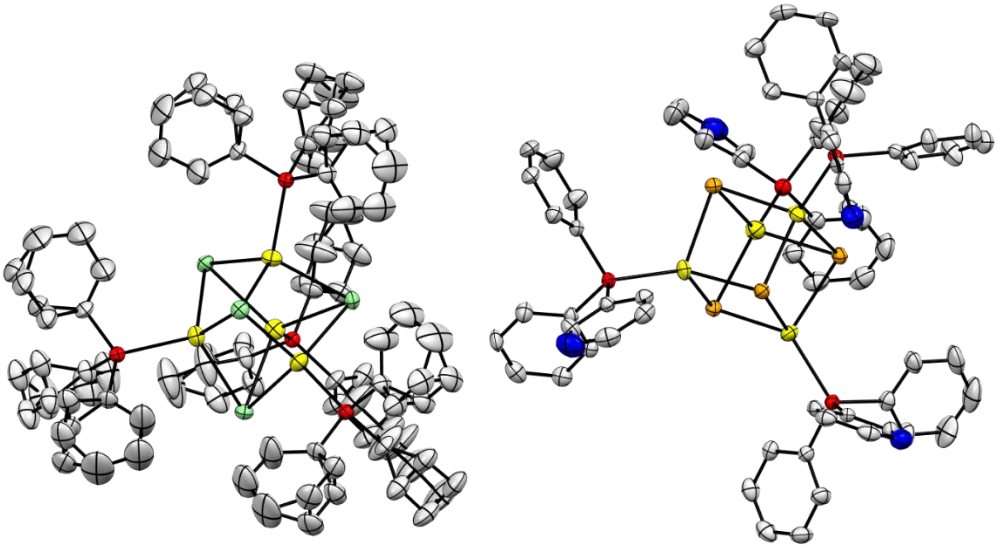

Figure 38. Structure of **Ag-L2-I** (left) and **Ag-L2-Br** (right) from single-crystal X-ray diffraction (ellipsoid at 50% probability level). Hydrogen atoms and solvent molecules were omitted for clarity. Color code: yellow (Cu), red (P), blue (N), green(I), orange (Br).

In the structure of **Ag-L2-Br**, the exact position of the nitrogen cannot be precisely determined, and it is statistically distributed across all six positions of the respective pyridine. In the case of **Ag-L2-I**, the nitrogen was not determinable and thus refined as triphenylphosphine. On closer inspection, **Ag-L2-I** crystallizes in a cubic crystal system with the highly symmetric space group *I-43m*, while **Ag-L2-Br** crystallizes in the more unsymmetric triclinic space group *P-1*. Interestingly, the previously reported complexes from BUSCH *et al*. are also not isostructural but crystallize in the monoclinic space group *C*2/*c* (Ag_4Cl_4(2-PyrPhos)$_4$) and the trigonal space groups *R*3*c:H* (Ag_4Br_4(2-PyrPhos)$_4$) and *P*31*c* (Ag_4I_4(2-PyrPhos)$_4$).[180]

In Table 7, selected lengths and angles are summarized for **Ag-L2-I** and **Ag-L2-Br**. The high symmetry of **Ag-L2-I** is directly reflected in these values. In contrast, for **Ag-L2-Br,** bond lengths and angles differ among each other, which displays the unsymmetric space group. Moreover, they are slightly smaller, except for P1— Ag1—X1/3 (139.75°/ 119.25° for **Ag-L2-Br**, 111.33°/111.33° for **Ag-L2-I**).

Table 7. Selected lengths and angles of **Ag-L2-I** and **Ag-L2-Br**.

Lengths/ Å	**Ag-L2-I**	**Ag-L2-Br**
Ag—Ag	3.284(2)	-
Ag1—X1	2.9019(9)	2.6821(5)
Ag1—X2	2.9019(9)	2.8525(5)
Ag1—X3	2.9019(9)	2.7452(5)
Ag1—P1	2.469(4)	2.4100(10)
Angles/ °		
X1—Ag1—X2	107.55(3)	95.215(15)
X1—Ag1—X3	107.55(3)	93.342(15)
X3—Ag1—X2	107.55(3)	102.236(16)
P1—Ag1—X1	111.33(3)	139.75(3)
P1—Ag1—X2	111.33(3)	99.67(3)
P1—Ag1—X3	111.33(3)	119.25(3)

For all three complexes, quantitative UV-Vis measurements in dichloromethane were performed. The complexes show a broad absorption band, stretching up to 400 nm. The solvent masks the π-π* absorption maximum (below 240 nm), however, all compounds show an additional broad shoulder ranging from 250 to 300 nm. For **Ag-L2-Cl**, the maximum of the shoulder is slightly shifted towards lower energies, resulting in a local maximum at 249 nm, compared to 258 nm and 259 nm for **Ag-L2-Br** and **Ag-L2-I**, respectively. Compared to the formerly described copper(I) complexes, no broad bands between 300 and 400 nm are observed for **Ag-L2-Br** and **Ag-L2-Cl**; however, in the case of **Ag-L2-I**, a similar trend of a broad absorption is observed, which might indicate a higher contribution of MLCT transitions for this complex. Overall, **L2** again exhibits the lowest molar extinction coefficient with 2×10^4 M^{-1} cm^{-1}, which is significantly increased in the complexes, with the highest in the range of 6×10^4 M^{-1} cm^{-1}.

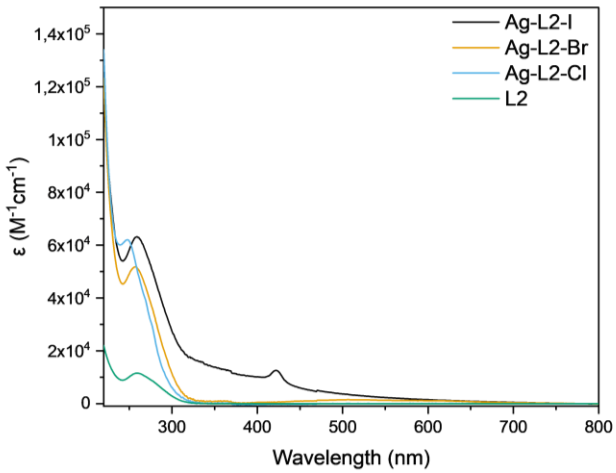

Figure 39. UV-Vis spectra of **Ag-L2-I**, **Ag-L2-Br,** and **Ag-L2-Cl** in dichloromethane.

3.1.3 Summary

The ligand **L2** was successfully applied in various structural motifs, although a butterfly-type complex was not obtained due to the higher bite angle of the ligand. The herein presented novel class of dinuclear 3-PyrPhos complexes displays a highly interesting new complex type. The two ancillary ligands give access to facile derivatization, which was successfully shown, whereas the emission properties should be tuneable *via* derivatization of the bridging ligands as they dominantly influence the LUMO energy. The presented dinuclear complexes show an uncommon excitation-dependent emission. For lower energy excitations, typical TADF behaviour is observed, whereas higher energy excitations lead to a temperature-independent emission, which could not be verified as a specific transition so far. The TADF mechanism was further proven through theoretical computations, giving HOMO-LUMO gaps in the range of 3.3 to 4.0 eV. These characteristics make this complex class a highly promising emitting material for applications such as OLEDs or sensors. The ligand **L2** was additionally applied to form silver(I) complexes, which resulted in three cubane-shaped complexes that were structurally investigated.

3.2 Mononuclear complexes featuring (iso)quinoline ligands

***Introduction*.** As outlined in the previous chapter, an open core dibridged copper(I) complex, using a methylated 2-PyrPhos ligand, was studied by HOFBECK, YERSIN and MONKOWIUS.[152] A similar structure, shown in Figure 40, was patented by CYNORA[163] and synthesized by BUSCH[41] by using a 1:1 ratio of 2-(diphenylphosphaneyl)quinoline **L4** and CuI. The ligands used to obtain these $Cu_2I_2L_2$ structures exhibit a sterically demanding group or an extended π-system adjacent to the bridging nitrogen atom, preventing the formation of a bridged Cu_2X_2-core. As the missing bridged halide-core is also found for the presented $L_4Cu_2X_2$ complexes in the previous chapter, the approach of using the same ratio of 6:2 (=3:1) with **L4** was investigated. However, the metaphane-like structure was not obtained in this case. Instead, the mononuclear complex **Cu-L4-I** with the structure $(\mathbf{L4})_3$CuI was formed, which was confirmed *via* crystal structure analysis. For comparison purposes, the structural isomer 2-(diphenylphosphaneyl)isoquinoline **L4i** was also used in the same ratio of 3:1, which resulted in the complex **Cu-L4i-I**, exhibiting only two organic ligands, $(\mathbf{L4i})_2$CuI. In the following sections the detailed structural analysis as well as the photophysical characterization and theoretical analysis of both complexes will be discussed.

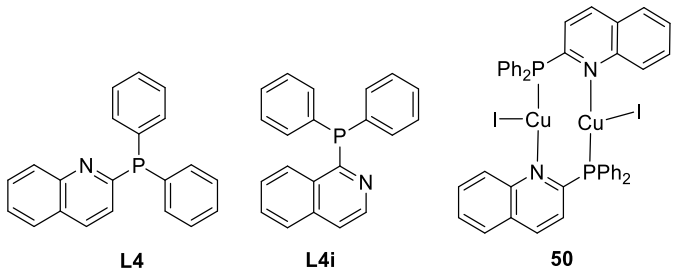

L4 **L4i** **50**

Figure 40. Structure of ligands 2-(diphenylphosphaneyl)quinoline **L4** and 2-(diphenylphosphaneyl)isoquinoline **L4i** and structure of dibridged dinuclear complex **50** using **L4** in a ratio of 1:1 with CuI, patented by Cynora.[163]

3.2.1 Synthesis and characterization

***Synthesis of Ligands and Complexes*.** Both ligands are known to literature and were successfully synthesized with yields of 47% for **L4** and 42% for **L4i** according to the general route A, introduced in *Chapter 3.1.1*.[161] The complexes **Cu-L4-I** and **Cu-L4i-I** were synthesized using the previously established complex synthesis route in DCM with a ratio of 3:1. For both complexes, an orange powder was obtained in good yields of 67% for **Cu-L4-I** and 49% for **Cu-L4i-I**. **Figure 41** illustrates both complexes.

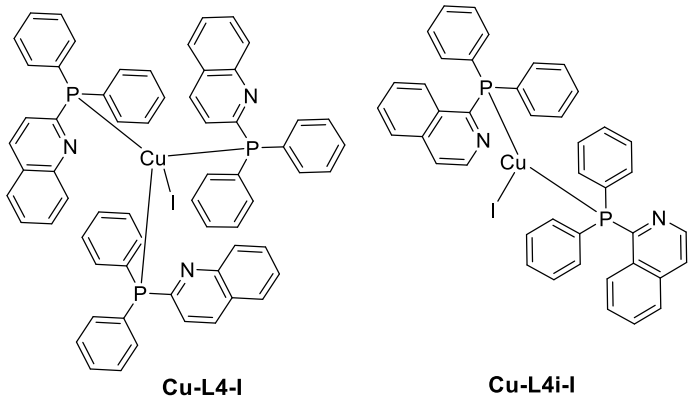

Figure 41. Illustration of obtained complexes **Cu-L4-I** and **Cu-L4i-I** by reacting 2-(diphenylphosphaneyl)quinoline **L4** and of 2-(diphenylphosphaneyl)isoquinoline **L4i** with CuI in. a 3:1 ratio.

***Crystallographic analysis*.** Crystals were obtained in DCM/pentane for both complexes. The structures are shown in Figure 42. The **Cu-L4-I** complex displays a distorted tetrahedral geometry with trigonal P-3 symmetry, while **Cu-L4i-I** has a distorted trigonal geometry with triclinic P-1 symmetry. This is directly reflected in the bond lengths and angles, which will be expressed in a rounded form in the following. For instance, the Cu—I distance for **Cu-L4-I** is 2.67 Å in contrast to 2.51 Å for **Cu-L4i-I**. This also applies to the Cu**—**P distances that are in the range of 2.30 Å for **Cu-L4-I** and 2.20 Å for **Cu-L4i-I.** The angles for both complexes differ from their respective ideal geometry (109.50° for tetrahedral and 120.00° for trigonal planar) with P—Cu—P angles of 114.05° for **Cu-L4-I** and 126.69° for **Cu-L4i-I** and P—Cu—I angles of 104.38° for **Cu-L4-I** and 115.73°(P1)/117.58°(P2) for **Cu-L4i-I**, respectively. A closer look at the crystal structures reveals why these two different structures are formed. In **Cu-L4-I**, the quinoline rings protrude from the plane, leaving more space close to the copper atom. One benzene ring is intramolecularly stacked with the benzene scaffold of the quinoline unit in a parallel displaced way, showing distances between 3.56 and 3.87 Å for the involved atoms, with an angle of 8.95° between the two planes. An illustration of the calculated planes and distances is shown in Figure 42 (middle). Since distances of 3.30 to 3.80 Å are proposed in the literature for a significant noncovalent π–π interaction, the calculated distance in this case, lies in the outer range and is therefore assumed to only show weak π–π interaction.[183] In contrast, in **Cu-L4i-I**, the isoquinoline rings and iodine face in the same direction, blocking the fourth binding site.

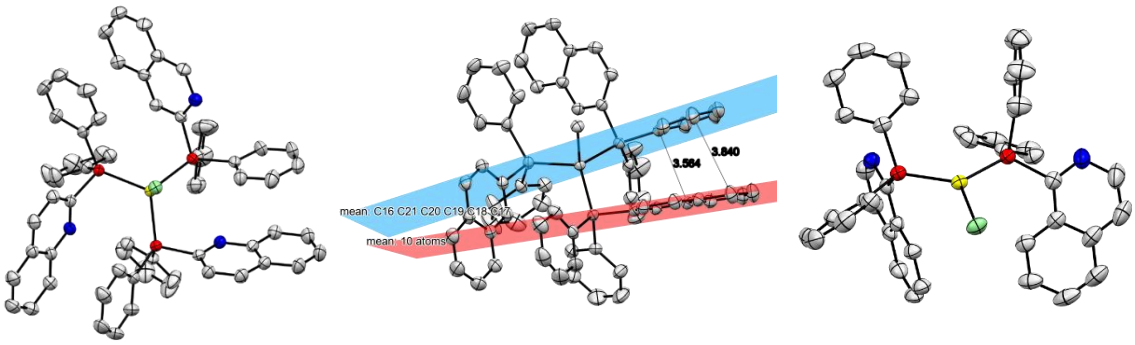

Figure 42. Structure of **Cu-L4-I** (left, middle) and **Cu-L4i-I** (right) from single-crystal X-ray diffraction (ellipsoid at 50% probability level). Hydrogen atoms and solvent molecules were omitted for clarity. Color code: yellow (Cu), red (P), blue (N), green(I).

3.2.2 Theoretical analysis

In cooperation with Dr. Christof Holzer (KIT, TFP), theoretical DFT calculations were performed on both complexes to clarify the electronic characteristics. Detailed information about the used methods can be found in the experimental part.

As illustrated exemplarily for **Cu-L4-I** in Figure 43, the frontier orbitals are well separated, with the HOMO being localized on the copper iodide, while the LUMO is primarily distributed across the (iso)quinoline ligand. Upon excitation, these complexes, therefore, exhibit an (M+X)LCT character. The HOMO-LUMO energy gap of the ground state is denoted as ΔE = - 4.4562.

Notably, in the case of **Cu-L4-I** four excited triplet states lie below the first excited singlet state and are nearly degenerate. The singlet state S_1 becoming almost degenerate with the triplet state T_4. This interaction increases the transition probability for T_4, a phenomenon known as intensity stealing.[184-185] As a result, the triplet lifetime decreases significantly, from the millisecond range to the microsecond range, approaching that of a moderately intense singlet-state emission. For **Cu-L4i-I**, the same phenomenon is found, although instead three triplets lie below S_1, and the singlet is nearly degenerated with T_3. The HOMO-LUMO energy gap of the ground state for **Cu-L4i-I** is calculated to be ΔE = -5.8677 eV.

The natural transition orbitals (NTOs) of **Cu-L4-I** for T_1 and S_1 are shown in Figure 43, with the energy gap between S_1 to T_1 (ΔE_{ST}) found to be approximately 0.46 eV. In the case of **Cu-L4i-I**, the energy gap ΔE_{ST} for S_1-T_1 is approximately 0.39 eV, which is slightly smaller compared to **Cu-L4-I**. This might be explained with a stabilization of the excited singlet state of **Cu-L4i-I** (E_{S1} = 3.0699, E_{T1} = 2.6849 eV).

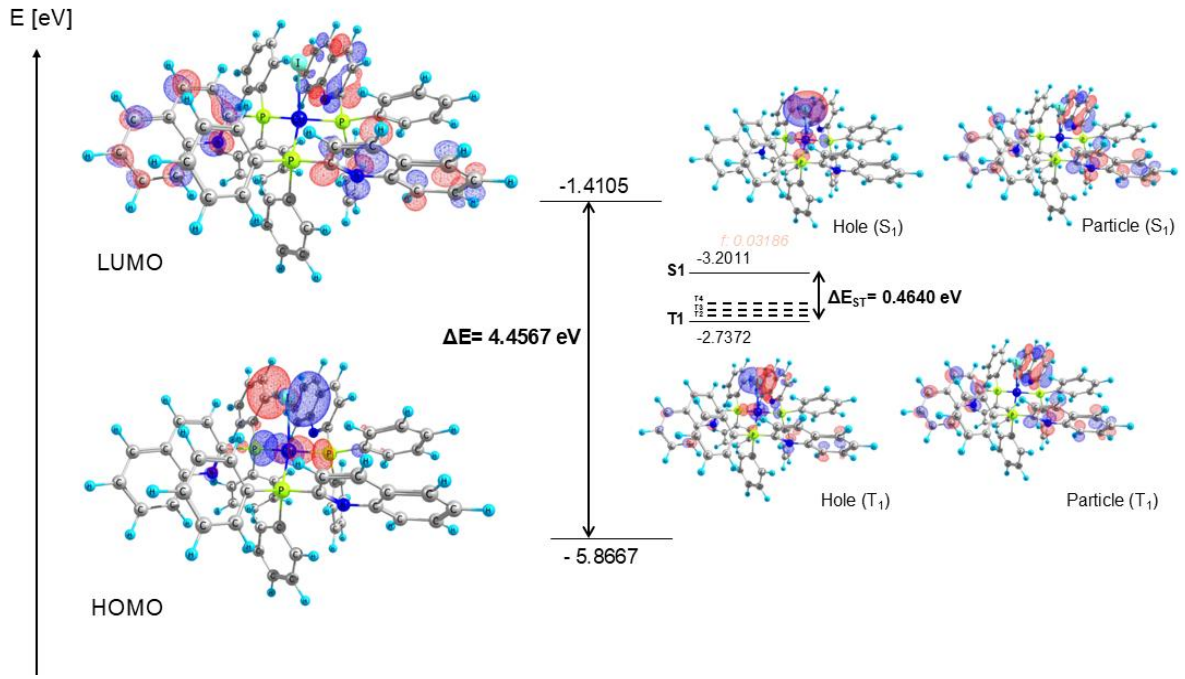

Figure 43. DFT-calculations of **Cu-L4-I**. An isovalue of 0.04 was used. Results provided by Dr. Christof Holzer (KIT).

The following table summarizes the calculated energy values for the HOMO and LUMO orbitals of the ground states, the first excited singlet states and the first four excited triplet states for **Cu-L4-I** and **Cu-L4i-I**.

Table 8. Overview of calculated energy values for the HOMO and LUMO orbitals of the ground states, as well as the first excited singlet states and the first four excited triplet states for **Cu-L4-I** and **Cu-L4i-I**. All calculations were conducted in gas phase. Values in brackets depict the oscillator strengths for the respective transition. Results provided by Dr. Christof Holzer.

	Energy (Cu-L4-I) (eV)	**Energy (Cu-L4-I)** (eV)
HOMO	-5.86669	-5.86773
LUMO	-1.41051	-1.61017
S_1	3.20111 (*f = 0.03186*)	3.06993 (*f = 0.01061*)
T_1	2.73716	2.68493
T_2	2.73957	2.69096
T_3	2.74771	3.05492
T_4	3.16634	3.13046

In the following, the computed data will be supported by experimental photophysical characterization.

3.2.3 Photophysical characterization

For both complexes, quantitative UV-Vis measurements were conducted in DCM. Both complexes show a broad absorption between 230 nm and 400 nm with several shoulders corresponding to absorption bands at around 235 nm, 270 nm and 330 nm. These are most likely related to ligand-centered (LC) transitions for the higher energies and MLCT transitions for the lower energies. **Cu-L4-I** shows a higher absorption in the whole range, which is most outstanding at higher energies, resulting in a maximum of 235 nm ($\varepsilon \approx 1.2\times10^5$ $M^{-1}cm^1$).

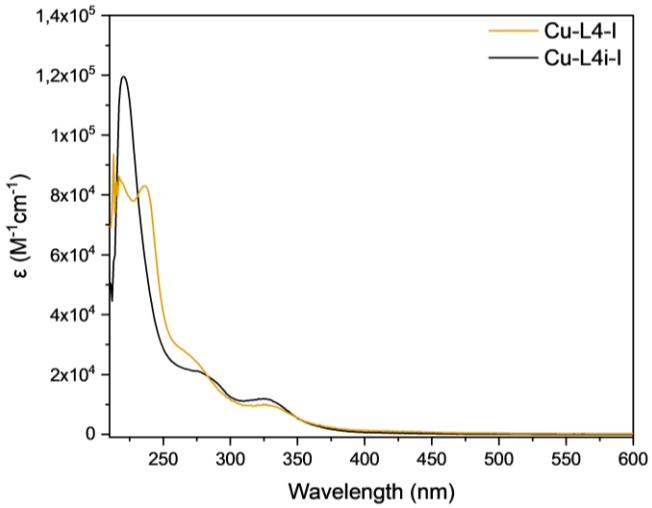

Figure 44. UV-Vis absorption for **Cu-L4-I** and **Cu-L4i-I**, measured in dichloromethane at room temperature.

Both compounds were further photophysically investigated. For that purpose, films of 1 wt% complex in PMMA were prepared, and the emission, lifetime (TCSPC), and PLQY were measured. PMMA is often used as an inert host material, which does not significantly influence the complex properties. **Cu-L4i-I** shows a broad emission in the orange-red region with a maximum at 635 nm when excited at λ_{ex} = 340 nm. However, shoulders with maxima at 511 and 551 nm emerge by exciting at a lower wavelength, as shown in Figure 45. For **Cu-L4-I**, four emission maxima (485, 516, 558 and 604 nm) can be observed when excited at 340 nm, and the emission profile does not change for a lower excitation wavelength of λ_{ex} = 290 nm. The different maxima indicate the involvement of different emission processes, such as ligand-centered emission or the emission from different energy states.

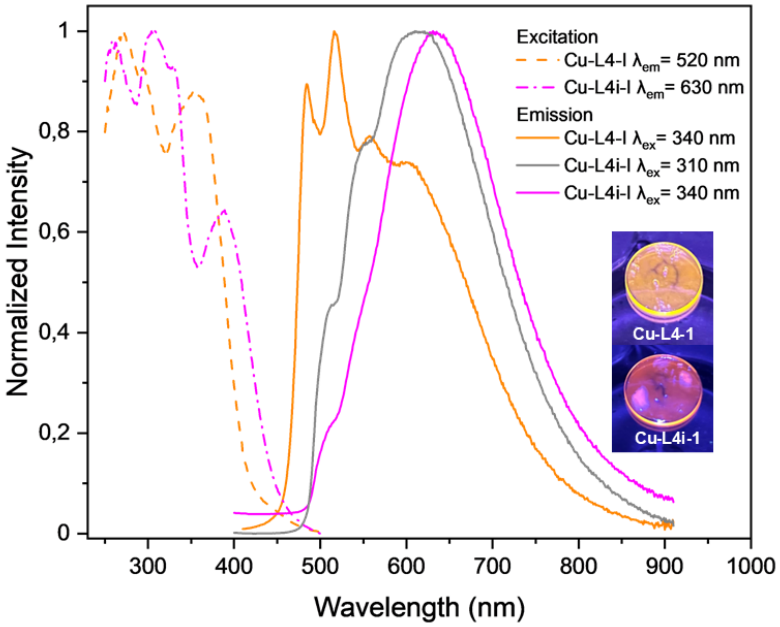

Figure 45. Steady-state photoluminescence spectra of **Cu-L4-1** and **Cu-L4i-I** in PMMA films (1 wt%) for different excitation wavelengths, left dotted spectra show the excitation spectra.

The following table summarizes the obtained photophysical results. For both complexes, the involvement of a triplet state is indicated through the decrease of the PLQY in air compared to nitrogen atmosphere, which is supported by the theoretical calculations. The PLQYs for both complexes lay in the same range, as they are measured to be 20% and 24% for **Cu-L4-I** and **Cu-L4i-I**, respectively. The lifetimes are 3.02 µs for **Cu-L4i-I** and even smaller for **Cu-L4-I** with 2.81 µs. For **Cu-L4-I**, an additional prompt fluorescence of 2.37 ns was measured, which might arise from ligand-centered fluorescence. To determine a TADF mechanism, future low-temperature measurements should be conducted.

Table 9. Summary of photophysical properties of 1 wt% doped PMMA films of **Cu-L4-1** and **Cu-L4i-1** at an excitation wavelength of 340 nm.

Compound	$\lambda_{max,PL}$ [nm]	τ_{DF}[µs]	Φ_{PL} [%] in N_2 (air)[a]
Cu-L4-I	485, 516, 558, 604	2.82	20 (13)
Cu-L4i-I	511, 551, 635	3.02	24 (17)

3.3 Crosslinkable Copper(I) complexes

Introduction. As already outlined in the introduction, solution-processing (SP) of OLEDs (SOLEDs) is an emerging research field.[70] Since it offers the potential to reduce material and power consumption, it becomes increasingly important for a more sustainable future. A crucial factor in OLED production is that separating the layers must be ensured to prevent quenching. In solution-processing, this leads to the requirement to use orthogonal solvents when applying multiple layers.[70] This drastically limits the number of suitable materials, as (metal-)organic materials are often soluble in various solvents. One potential solution is the in-situ crosslinking of the material to make it insoluble, so that the next layer can be applied without redissolving it.[93, 186] Various crosslinking approaches such as thermal[187-188], photochemical[189-190], or chemical crosslinking[132] are reported. Although this is already discussed in the literature, the main focus seems to be on organic molecules, particularly compounds for use in hole-transport layers (HTL).[187, 191] The number of reported crosslinkable emitting layers (EML) remains scarce to date. Only a few examples are reported in the literature for organic emitters, mostly relying on vinyl/styrene functionalities.[188, 192] Even less can be found for metal-organic-based EML. For instance, BUMJOON and coworkers demonstrated phosphorescent crosslinkable iridium complexes based on styrene-containing ligands.[190] VOLZ *et al.* presented two crosslinkable copper(I) complexes of the butterfly type based on styrene and alkyne-containing bridging ligands, which are illustrated in Figure 46.[132, 193]

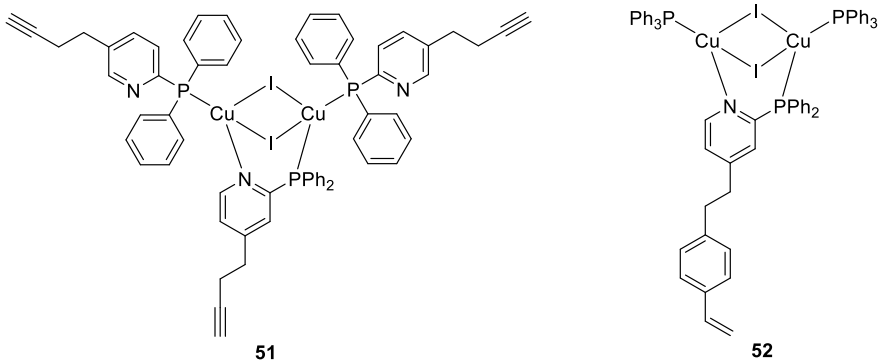

Figure 46. Literature known structures of crosslinkable dinuclear copper(I) complexes based on **51** and **52**.[132, 193]

In general, two crosslinking strategies are considered. First, self-crosslinking, based on polymerizable functionalities such as styrenes or acrylates; second, two-component crosslinking, which displays the forming of a new bond between two different functionalities such as thiol-ene reactions or copper-catalyzed alkyne-azide click reactions (CuAAC).[132, 191, 194]

In this work, the design and synthesis of several crosslinkable Cu(I) complexes was aimed at, with practical applications in mind. For the targeted crosslinking functionalities and future crosslinking reactions, the following strategic points were considered:

a. More than one crosslinking side should be available.
b. For future *in situ* applications, the crosslinking reaction should be as straightforward as possible.
c. No further additives, such as radical starter or photoinitiator, should be used. This is necessary to prevent contamination of the layers.
d. Regarding luminescence properties, the emission should not drastically change after crosslinking.
e. The complexes have to be soluble enough for solution-processing techniques.

To achieve these goals, two crosslinking functionalities were selected to be included in organic ligands, which are then used to form various crosslinkable Cu(I) complexes. To get access to a two-component crosslinking strategy, ligands exhibiting terminal alkyne scaffolds were envisioned, making access to click chemistry feasible. This allows the reaction towards azides *via* the renowned CuAAC, which was already reported independently from MELDAL[195] and SHARPLESS[196] in 2002[197-198] and even rewarded with the Nobel Prize in 2022, but also towards thiols *via* thiol-yne reactions, for instance.[199] Especially for the CuAAC, the clicking process is planned to work in an autocatalyzed manner as copper(I) is present in the complexes. This was already successfully tested and shown by VOLZ *et al*.[132] Additionally, metal-catalyzed thiol-yne reactions are reported and could therefore be prone to an autocatalyzed pathway as well.[200-202]

To access a route *via* self-polymerization, the introduction of an acrylate unit, in particular a methacrylate unit, was targeted. Methacrylates are commonly known for their polymerization potential, which was already studied for methyl methacrylate by NORRISH in 1997.[203-204] However, only few examples are reported in literature where acrylates are used in OLED devices, and are mostly exclusive to organic molecules.[189] A drawback of acrylates is that a photoinitiator and UV or heat are usually necessary to initiate the polymerization.[189, 194] As explained, contamination with any external photoinitiator should be avoided in OLED production. Some copper(I) complexes can act as photoinitiating systems themselves.[97] Therefore, complexes including methacrylate functionalities, were targeted to act as monomer and photoinitiator. Scheme 7 summarizes the targeted crosslinking strategies.

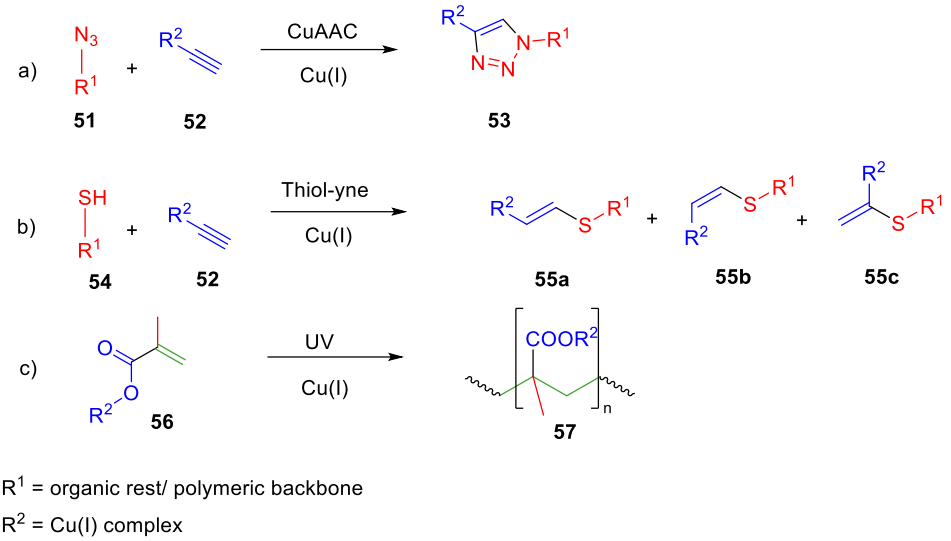

Scheme 7. Crosslinking strategies using a) terminal alkynes with azides for a CuAAC; b) terminal alkynes and thiols in a thiol-yne click reaction; c) methacrylates for self-polymerization with UV radiation. For all reactions copper(I) complexes should act as a catalyst or photoinitiator.

In this work, several neutral Cu(I) complexes were synthesized and investigated, from mononuclear and dinuclear, to tetranuclear structures, each featuring at least one crosslinkable functional group. The primary focus was on the already described butterfly-type structures, since they combine various advantages and had already been studied in autocatalyzed crosslinking experiments, and therefore seemed to be a promising material class for this purpose.[132] Furthermore, since they exhibit the advantage that the emission is mostly caused through MLCT processes between the copper core and the bridging ligands, the ancillary ligands should be available for crosslinking reactions without significantly influencing the emission behavior.[63, 137] This gives rise to at least two crosslinking sites, one at each ancillary ligand. Lastly, they often combine good chemical stabilities due to their binuclear core, but at the same time exhibit good solubilities, which might be the most important point in the context of solution-processing techniques.[41, 138]

The following sections will first discuss the synthesis of the ligands and resulting complexes, followed by the discussion of the first crosslinking experiments. For some selected complexes, additional theoretical and photophysical properties were studied in detail, and their application will be addressed in the next chapter.

3.3.1 Syntheses of crosslinkable ligands and complexes

Several ligands were synthesized for the use as either ancillary phosphine ligand (P-ligands, **P1–P3**) or NN-/NP-bridging ligand (**L5–L8**). An overview of all used ligands in this chapter is given in Figure 47.

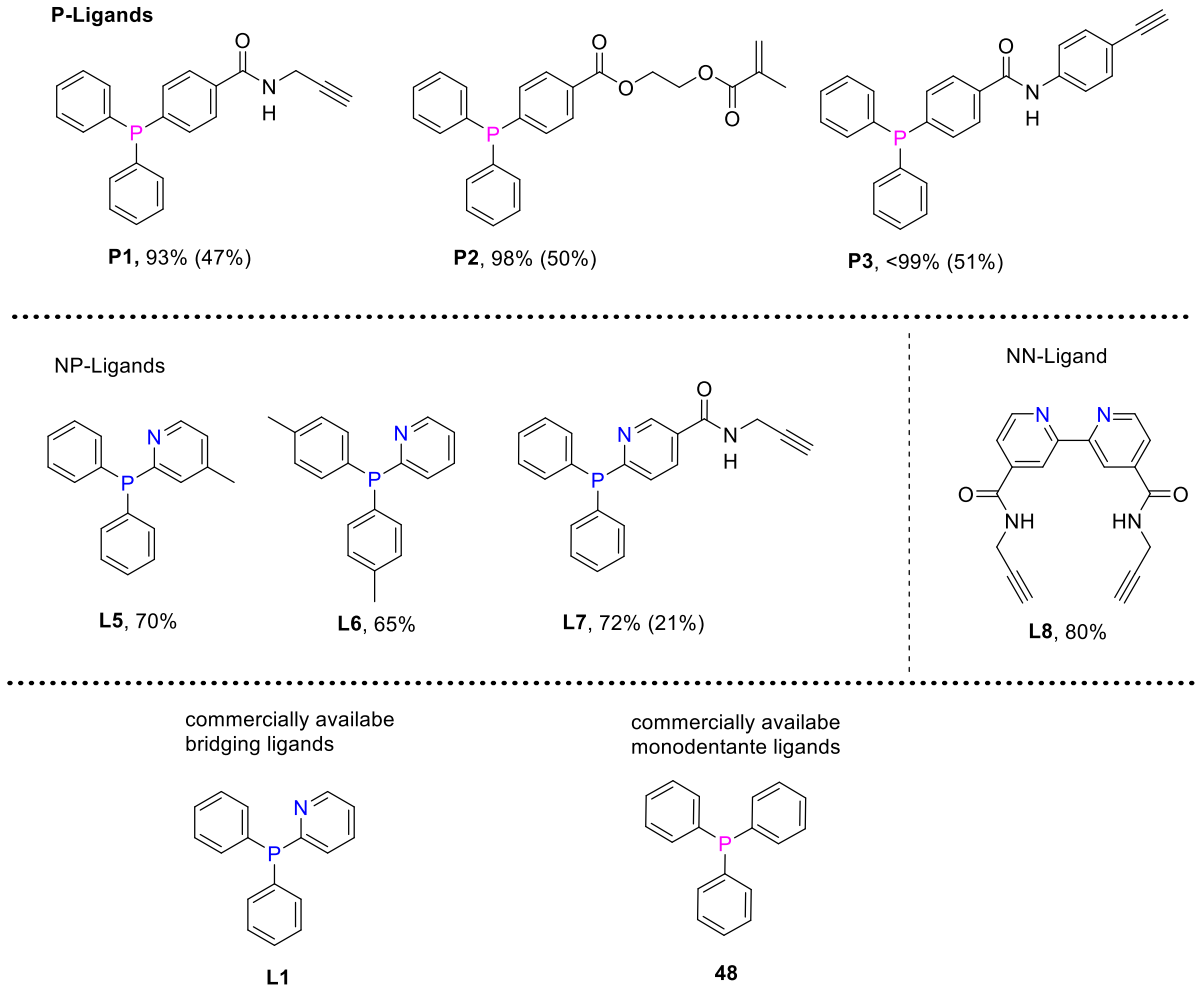

Figure 47. Overview of used ligands for the synthesis of crosslinkable complexes. In the case of several step syntheses, the overall yields are given in brackets. Color code: ancillary ligand (red), bridging ligand (blue).[205-208]

The ligands **P1**-**P3** and **L7** feature one crosslinkable functional group, either an alkyne or a methacrylate, whereas **L10** contains two terminal alkyne moieties. Although all the synthesized P-ligands have been previously reported in the literature, the reaction conditions for **P1**-**P3** were optimized and screened to improve the yields.[205-207] Additionally, attempts were made to introduce a pyridine scaffold into **P1** to obtain a similar bridging ligand. This led to the formation of **L7**, which is not described in the literature so far. Notably, **L8** has only been mentioned once in the literature as an intermediate in the synthesis of mesoporous silica particles.[208] However, it has not been employed as a ligand in coordination chemistry, and the here presented synthesis route is not reported. Thus, reaction conditions for **L8** were evaluated

and optimized. In addition, the commercially available ligands **L1** and triphenylphosphine **48** were used. The synthetic approaches will be discussed in detail in the following sections. It should be noted that a part of the ligand and complex syntheses, particularly the reaction condition screenings of the subsequent chapter, were carried out by Sebastian Roth and Paul Schündler as part of their bachelor's theses.

3.3.1.1 Ligands

Synthesis of P-Ligands. All P-Ligands were obtained by condensation (amidation/esterification) reactions of an amine or alcohol and the respective carboxylic acid. The synthesis route is visualized in Scheme 8. The phosphine carboxylic acid **59** was synthesized according to a literature-known palladium-catalyzed alkylation of diphenylphosphine.[209-210] **59** was obtained as a colorless solid with a good yield of 51%.

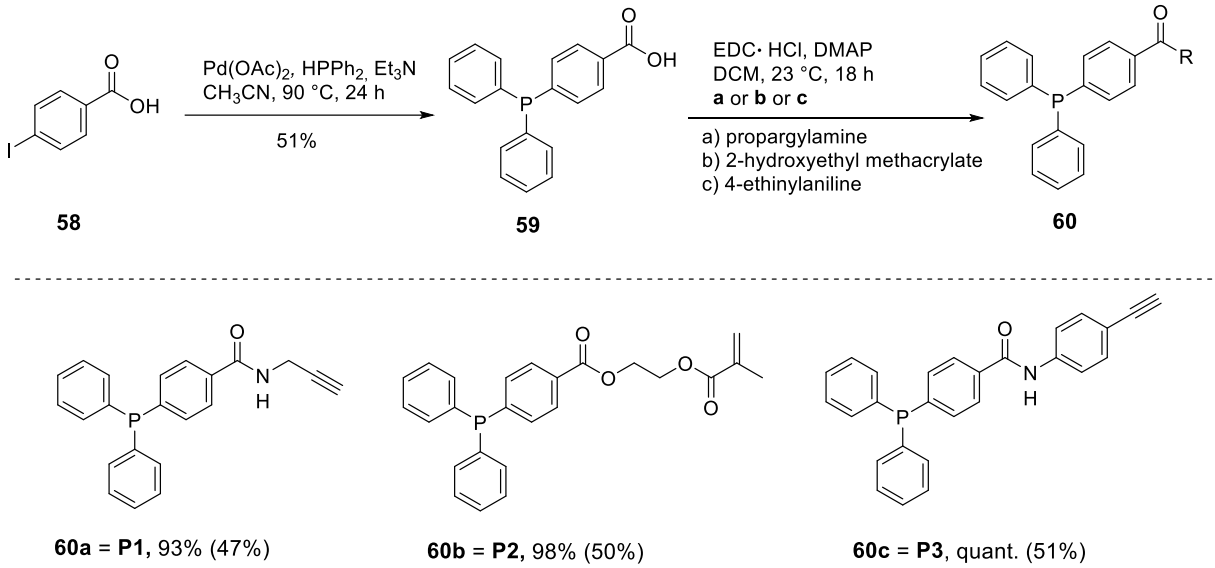

Scheme 8. Synthesis of ancillary P-Ligands **P1**[205], **P2**[206], **P3**[207] *via* two steps 1) Pd-catalyzed coupling[209], 2) esterification/amidation. Overall yields are given in brackets.

All three P-ligands in the literature were accessed *via* condensation reactions using different coupling reagents. In the case of **P1** and **P3,** 1-ethyl-3-(3-dimethylaminopropyl)carbodiimide hydrochloride (EDC) was used, and for **P2** N,N'-diisopropylcarbodiimide (DIC), respectively.[205-207] In this work, **P1** and **P2** were initially synthesized using DIC as coupling reagent (Table 10, entries 1 and 2). However, the isolation of a highly pure product was not feasible with this route since isopropyl urea, as the main impurity of the reaction, could not be fully removed from the product.

For this reason, EDC was tested with various additives and bases, including dimethylaminopyridine (DMAP) or diisopropylethylamine (DIPEA)/(1-hydroxybenzotriazole hydrate (HOBt) (Table 10, entries 3 to 7). A summary of all screened reagents is outlined in Table 10. The highest yields were obtained for P-ligands **P1** (93%), **P2** (98%) and **P3** (quant.) when using EDC and DMAP in DCM. Since the synthesis route already published by TERASHIMA and INOUE was applied for **P1** and **P3**, only the yields were improved to 93% from 75% reported in the literature for **P1** and quantitative conversion compared to the literature yield of 77% for **P3**.[205, 207] However, for **P2**, this route was not investigated before and resulted in a similar range to the yield reported from by MÜLLER *et al*.[206] With this approach, all three ligands were isolated with good purities, and the by-products of EDC were easily removed by washing the crude mixture with water.

Table 10. Screening conditions of the condensation reaction between 4-(diphenylphosphaneyl)benzoic acid and propargylamine (a) or 2-hydroxyethyl methacrylate (b) or 4-ethynylaniline (c) to yield **P1**, **P2**, or **P3**.

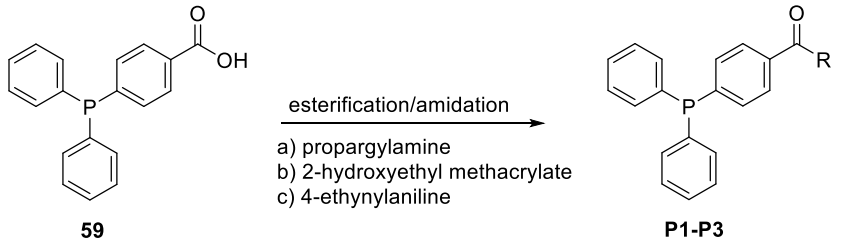

59 P1-P3

Entry	Starting material	Coupling reagents	Catalyst/Base	Solvent	Yield
1	a[a]	DIC	DMAP	DCM	86
2	b[a*]				85 (94[206])
3	a[a]	EDC HCl			93 (75[205])
4	b[a*]				98
5	c[a**]				quant. (77[207])
6	a[b]		DIPEA, HOBt	DMF	71
7	b[b]				78

General reaction conditions 18 h, 23 °C, 1.00 equiv. starting material, [a]1.20 equiv (a), 1.10 equiv (b), or 1.00 equiv (c), 1.05 equiv coupling reagent, 1.00/ *0.10/**0.20 equiv DMAP. [b] 2.50 equiv. reactant (a or b), 1.50 equiv EDC, 3.00 equiv. DIPEA, 1.50 equiv HOBt.

Synthesis of NN Ligand L8. As previously noted, only one synthetic route for *N4,N4*'-di(prop-2-yn-1-yl)-[2,2'-bipyridine]-4,4'-dicarboxamide **L8** is reported, in which the corresponding acid chloride **61** is generated as an intermediate product.[208] In contrast, the approach presented here, performs the amine coupling directly with the commercially available carboxylic acid **61** in a one-step synthesis.

To screen the best reaction conditions, different combinations of coupling reagents, solvents, and concentrations were tested and are summarized in Table 11.

Table 11. Screening conditions of the amidation of [2,2'-bipyridine]-4,4'-dicarboxylic acid **61** with propargylamine to yield N^4,$N^{4'}$-di(prop-2-yn-1-yl)-[2,2'-bipyridine]-4,4'-dicarboxamide **L8**.

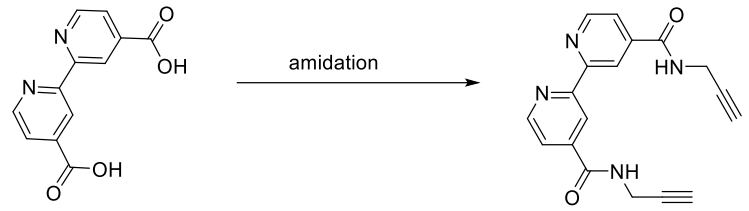

61 **L8**

Entry	Concentration[a] [mmol/l]	Coupling reagents	Base/Additive	Solvent	Yield [%]
1	193	EDC·HCl	DMAP	DCM	-
2	102		DIPEA, HOBt		-
3	333			DMF	4
4	273				14
5	20				**80**
6	330	HBTU	DIPEA	DMF	34
7	13				60

[a]Referred to [2,2'-bipyridine]-4,4'-dicarboxylic acid. Reaction conditions: 1.00 equiv. starting material, 5.00 equiv. propargylamine, 3.00 equiv. coupling reagent, 6.00 equiv. DIPEA, 0.300 equiv. HOBt, 2.00 equiv. DMAP, 18 h, 23 °C.

To optimize the direct coupling to the carboxylic acid precursor, various combinations of coupling reagents and additives were investigated. The combinations EDC/DMAP and EDC/DIPEA/HOBt were tested, as they had previously demonstrated good results with the already discussed P-ligands. In general, no product formation was observed when using DCM as a solvent. This could be explained, as the precursor exhibits poor solubility in DCM. In contrast, all reactions in DMF were successful, resulting in the desired product with yields ranging from 4% to 80%. Furthermore, the literature protocol employed a relatively high precursor concentration of approximately 200 mmol/L; therefore, different concentrations were explored. It is worth noting that EDC/DMAP was only tested in DCM, hence no comparison can be made regarding its efficiency in DMF. Moreover, HBTU/DIPEA was used to assess an alternative coupling reagent. Looking at the whole screening, the choice of solvent and concentration impacted the reaction yield the most. For instance, HBTU was the most effective coupling reagent at higher concentrations. Nevertheless, the best yield of 80% was achieved at lower concentrations with DMF and the combination EDC/DIPEA/HOBt.

Although bipyridines are primarily employed in cationic complexes, their behavior in neutral complexes was also investigated, and will be discussed in the following.

Synthesis of NP-Ligands. Efforts were made to develop a bridging ligand based on **L1** (2-PyrPhos) by incorporating a pyridine scaffold with an analogous alkyne functionality to that of **P1** to synthesize the unpublished bridging ligand 6-(diphenylphosphine)-N-(2-propyn-1-yl)-nicotinamide **L7**. The two-step reaction pathway is shown in the following scheme.

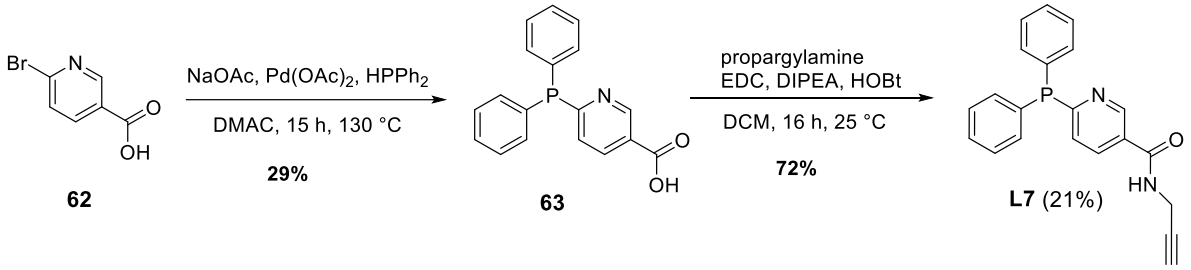

Scheme 9. Two-step synthesis of 6-(diphenylphosphine)-N-(2-propyn-1-yl)-nicotinamide **L7** through 1) Pd-catalyzed coupling[41], 2) amidation with EDC/DIPEA/HOBt.

Precursor **63** was successfully synthesized in accordance with literature *via* a palladium-catalyzed coupling of 6-bromonicotinic acid with diphenylphosphine, yielding **63** as colorless solid in 29%.[41] Product **L7** was obtained from **63** by transferring the same coupling conditions used for **L8** (EDC, DIPEA, and HOBt) with a good yield of 72% and an overall yield of 21% over two steps. Using DMF instead of DCM in the second step resulted in a lower yield of 59%. In this project, one complex was successfully synthesized, including **L7** as bridging ligand. However, due to the limited material of the ligand, the analytics for the complex are pending. With the ligand showing highly promising characteristics, the respective complexes should be explored in future projects.

The bridging ligands **L5** and **L6** were synthesized following the same procedure as described for **L2** in *Chapter 3.1.1.1.*, based on methods reported by ZINK[161] and BUSCH[63]. The reaction path is shown in Scheme 10. For **L5,** the obtained yield of 70% is slightly lower than the yield reported in literature, which is 82%, while the yield of **L6** could be improved from 44% to 65% compared to the published yields. Alternative synthetic routes are also documented in the literature for **L5**, which use diphenylphosphine as a reagent.[211] But, due to the higher stability of chlorodiphenylphosphine compared to diphenylphosphine, the first route was selected and employed here.

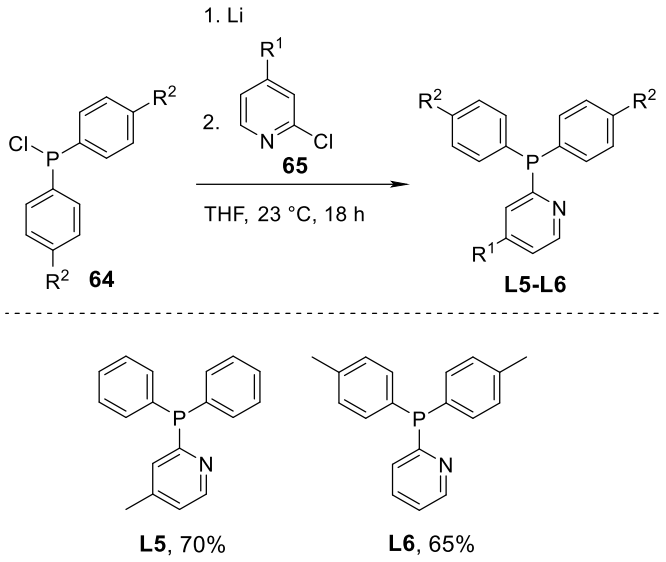

Scheme 10. Nucleophilic aromatic substitution of the chlorinated pyridine precursor with *in situ* formed lithium phosphide to obtain **L5** and **L6.**[63, 161]

3.3.1.2 Synthesis of neutral copper(I) complexes with crosslinking ligands

An overview of the general complex structures of this chapter with the respective numbering codes, which are used throughout the following sections, is given in Figure 48. For a better understanding, violet displays ancillary phosphines whereas blue depicts bridging ligands in the following sections.

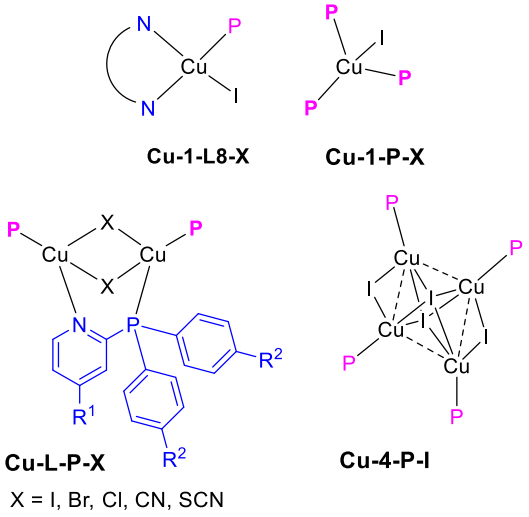

Figure 48. Targeted general structures of mononuclear (top) and dinuclear and tetranuclear (bottom) complexes. Color Code: violet (ancillary phosphine ligands), blue (bridging NN/NP-ligands).

The neutral complexes of this chapter were all synthesized by following the general procedure of mixing the respective ligands and CuX salts in specific ratios in dry, degassed dichloromethane for 18 hours at 23 °C. They were fully characterized *via* NMR analysis, mass

spectrometry and IR spectroscopy. In some cases, additional characterization by elemental analysis or single crystal x-ray diffraction was conducted (see experimental section for further details). For heteroleptic complexes containing different organic ligands, the complex ratios will be denoted as **P**:**L**:CuX, where the ratio of ancillary ligand (P) listed first, the bridging ligand (L) second, and the CuX salt last, unless otherwise stated.

Mononuclear complexes of the type P_3CuI (ratio 3:1). Mononuclear structures feature three possible crosslinking sites by only using one ligand type, which is why mononuclear complexes of the type **P_3CuI** were targeted with ligands **P1** and **P2**. The general reaction scheme is shown in Scheme 11.

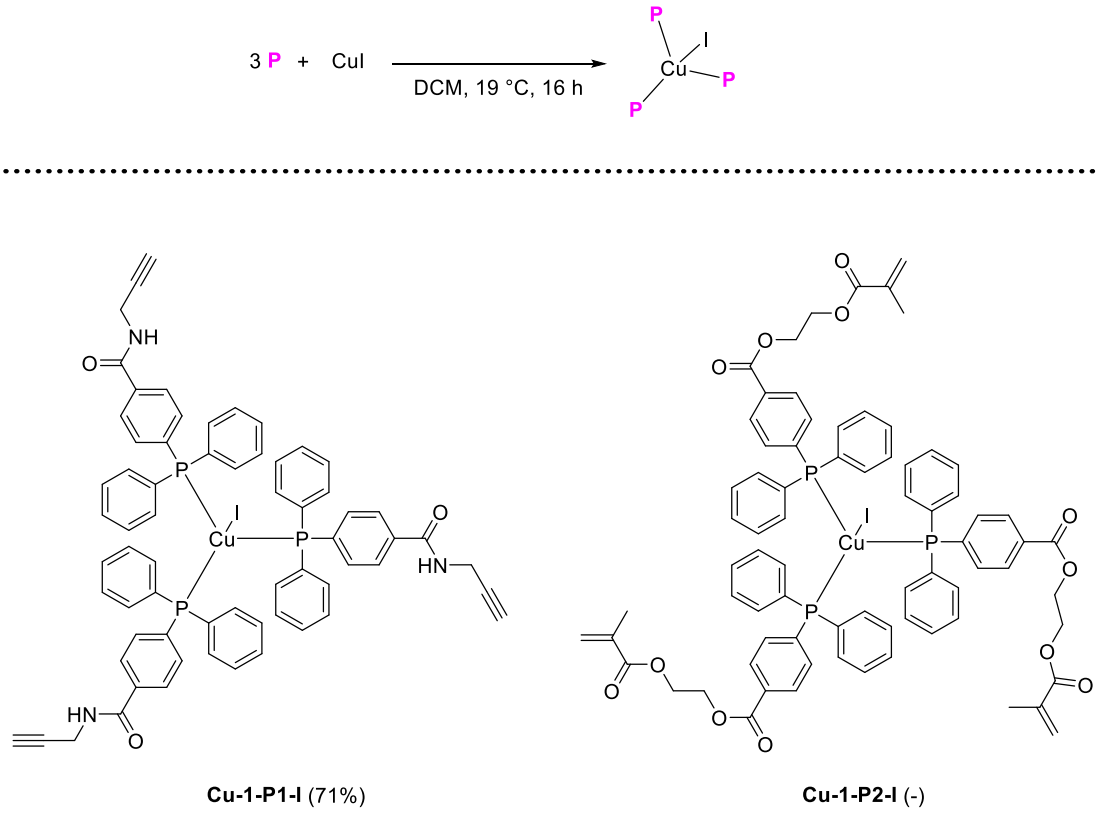

Scheme 11. Complexation reaction with a ratio of 3:1 to obtain mononuclear complexes **Cu-1-P1-I** and **Cu-1-P2-I.**

The complex **Cu-1-P1-I** using **P1** was successfully synthesized and obtained as an off-white powder with a yield of 71%. Upon UV excitation, it showed luminescent properties in the greenish to blueish region. In contrast, the attempt to synthesize the analogous complex **Cu-1-P2-I** with **P2** was unsuccessful. Although a compound was formed in the synthesis with **P2** and showed sky-blue luminescence under UV on the filter paper, it could not be isolated due to the small quantities.

This is likely due to either the increased steric hindrance by the methacrylate groups on **P2**, which may have hindered efficient coordination to the copper(I) center, or insufficient

precipitation. Both complexes are shown in Figure 49, with **Cu-1-P1-I** in the upper part at daylight (left) and UV-light (right) and the non-characterized compound resulting from the synthesis of **Cu-1-P2-I** in the lower part under UV.

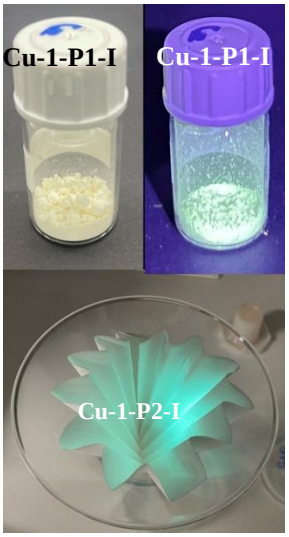

Figure 49. Picture of mononuclear complexes **Cu-1-P1-I** (top) in daylight and under UV-light, and **Cu-1-P2-I** with UV-light (bottom)

For **Cu-1-P1-I** a qualitative solubility study was conducted. The complex showed excellent solubility in dichloromethane (>20 mg/ml) and good solubility in chlorobenzene (10-20 mg/ml). Therefore, the complex is suitable for solution-processing in dichloromethane and chlorobenzene. As no solubility was observed in toluene and n-hexane, they act as antisolvent, making them good solvents for further layer production in SOLEDs.

Mononuclear complexes of the type (L8)(PPh$_3$)CuX (ratio 1:1). The neutral mononuclear complex (L8)(PPh$_3$)CuI (**Cu-1-L8-I**) was successfully synthesized by mixing the corresponding ligands with CuI in a 1:1:1 ratio in a yield of 76%. The complex was obtained as a red powder that did not exhibit visible luminescent properties under UV irradiation. Furthermore, it showed no significant solubility in toluene, chlorobenzene, DCM, or n-hexane and was therefore not further analyzed as it is no suitable candidate for an application in SOLEDs. Figure 50 illustrates the general target structure (left), the obtained complex (middle), and photographs of the sample in daylight and under UV-light (right)

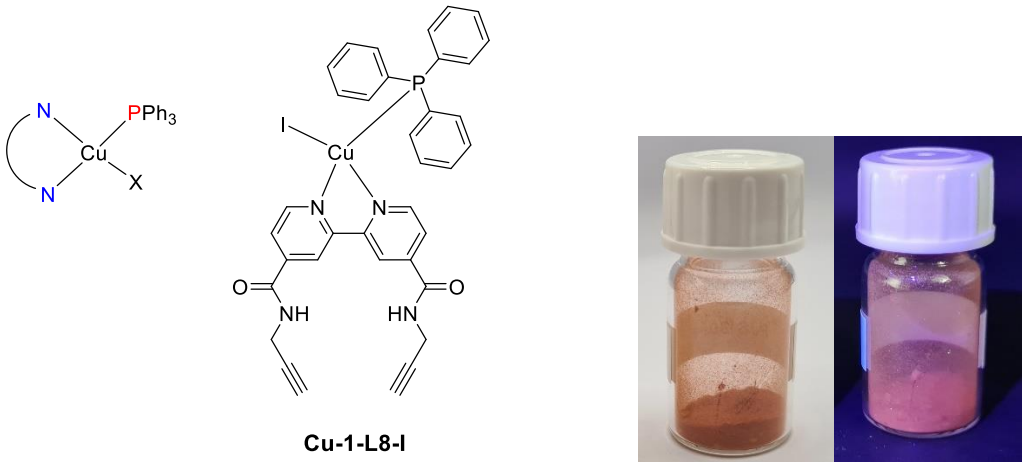

Figure 50. Aimed complex type CuI(NN)P and the resulting mononuclear complex **Cu-1-L8-I** (left) and pictures of the obtained complex in daylight and under UV (right).

The structure of the complex **Cu-1-L8-I** was confirmed *via* X-ray crystallography. It shows the typical distorted tetrahedral structure and crystallizes with two molecules of DCM. The corresponding ORTEP plot is presented in Figure 51, with solvent molecules and hydrogen atoms omitted for clarity. With this motif, a variety of complexes become accessible by exchanging the ancillary phosphine. Since no photoluminescence was observed, no further investigations on this type were conducted, even though an increased solubility could be expected by using PR_3 variations with additional functionalities.

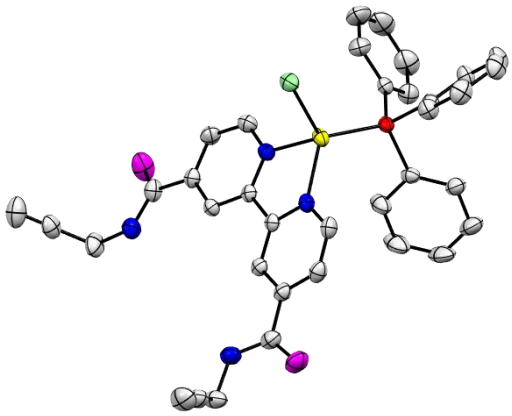

Figure 51. Crystal structure of **Cu-1-L8-I**. Hydrogen atoms and solvent molecules are omitted for clarity. Displacement parameters are drawn at a 50% probability level.

Butterfly-complexes of the type $Cu_2X_2LP_2$ (Ratio 2:1:2): The synthesis of several butterfly-type Cu(I) complexes was successfully conducted by using the P-ligands **P1**, **P2**, and **P3** in a 2:1:2 stoichiometric ratio, as shown in Scheme 12. This structure features two linkable sites through the ancillary phosphines, along with an additional site provided by the bridging ligand. Previous studies have identified the bridging ligand as the main factor, to influence the emission properties.[161] The bridging ligand **L1** was chosen as it is the easiest available ligand and commercially available. **L5** and **L6** were used because they showed the best properties in previously studied complexes such as a high PLQY and blue shift of the emission.[41, 161]. The synthesis of complexes involving **L1** and **P1**, as well as **L1** and **P2**, was first conducted during the bachelor's thesis of Sebastian Roth.

Scheme 12 shows the underlying general structures of the obtained butterfly complexes of the type $Cu_2X_2LP_2$. Three main series were prepared by using **P1**, **P2** and **P3** with the different bridging ligands **L1**, **L5** and **L6**. **L1** and **L5** were used with **P1** or **P2** and various CuX salts to obtain the **Cu-L-P1-X** and **Cu-L-P2-X** series. The monodentate phosphine **P3** was used with either **L1**, **L5**, or **L6** to form the complexes of **Cu-L-P3-X**. Together with the combination of various copper(I) salts, the complexes of **Cu-L-P1-X** and **Cu-L-P2-X** each contain five complexes (X = I, Br, Cl, CN, SCN) with **L1** and three complexes (X = I, Br, Cl) with **L5** as bridging ligand. For the complexes of **Cu-L-P3-X**, only three complexes were synthesized, all based on a Cu_2I_2-core, with **L1**, **L5**, and **L6**, respectively.

The **Cu-L-P3-I** series demonstrated the highest yields, reaching 97%. The **Cu-L-P1-X** series exhibited moderate yields, ranging from 53% to 84%, while the yields for **Cu-L-P2-X** were more variable between 15% and 77%. Generally, a trend of decreasing yields in the order I > Br > Cl can be observed. However, this is not the case for the series of **Cu-L5-P1-X** in which the yields are in the same range for all halides.

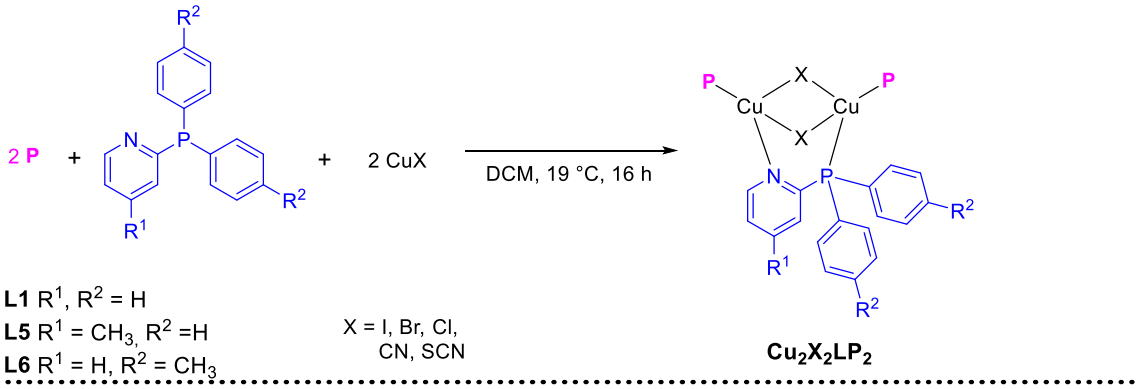

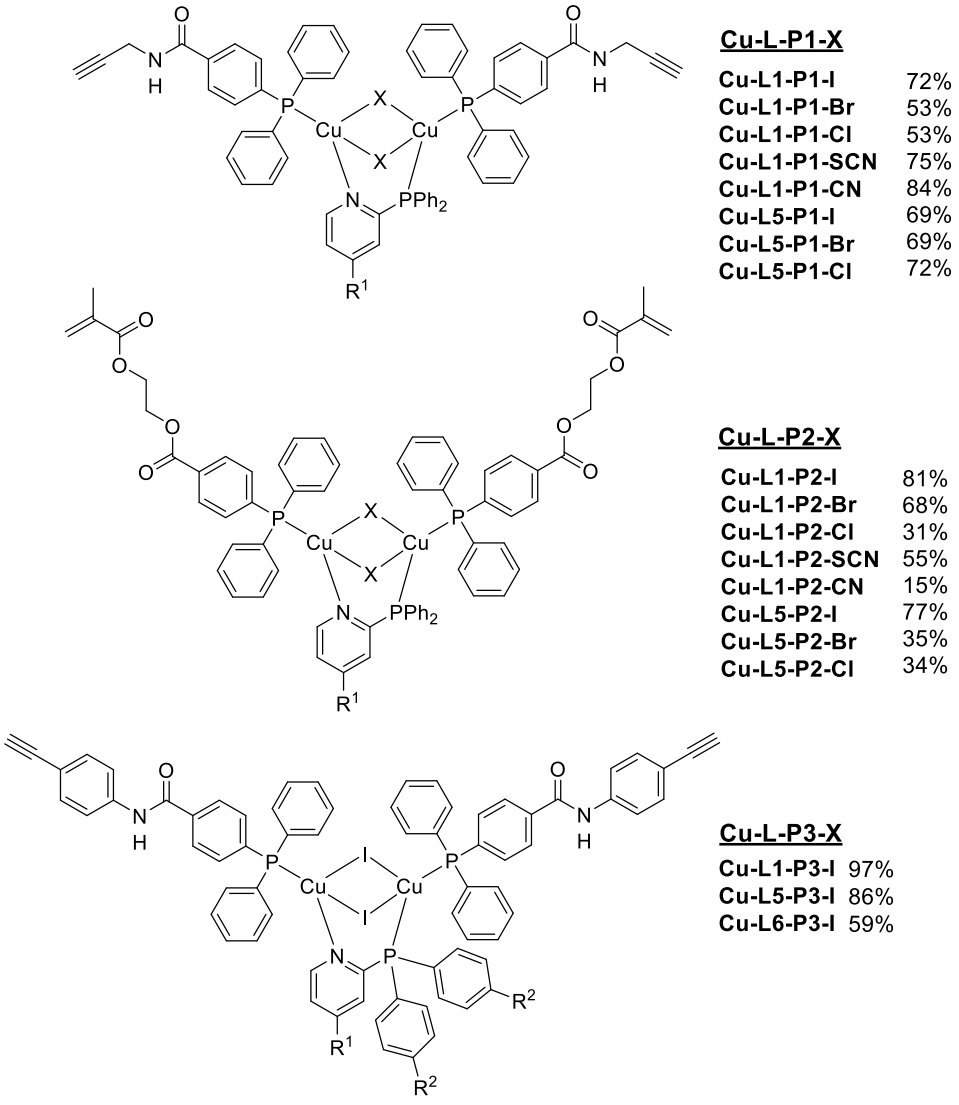

Scheme 12. Complexation reaction with a ratio of 2:1:2 to obtain the dinuclear butterfly-type complex series **Cu-L-P1-X, Cu-L-P2-X** and **Cu-L-P3-I**.

All complexes were obtained as off-white to yellow powders, that exhibit visible luminescent properties upon UV excitation. Pictures of the complexes under UV-light are shown in the following figures. Figure 52 depicts the complexes for the row of **Cu-L-P1**, Figure 53 for **Cu-**

L-P2, and Figure 54 (left) for **Cu-L-P3**. A comparison of **Cu-L1-P1-I**, **Cu-L1-P2-I**, **Cu-L1-P3-I** is shown in Figure 54 (right). The qualitative emission characteristics agree well with the influence of (pseudo-)halides, which were already discussed in *Chapter 3.1.* A clear red shift is observed for the complexes with bromine and chlorine, compared to iodine in the order of I < Br < Cl across all series. Notably, a sky-blue color was observed for **Cu-L1-P1-SCN** using thiocyanate. For the complexes of **Cu-L-P3-I**, a similar appearance in the yellow region is observed for all three. A more detailed and quantitative analysis of the spectroscopic properties is presented in *Chapter 3.3.4.2.*

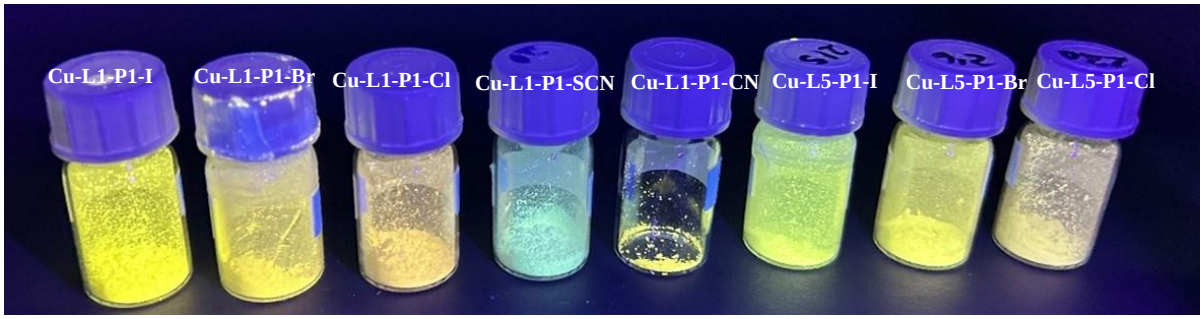

Figure 52. Picture of complex series of the type **Cu-L1-P1-X** and **Cu-L5-P1-X** under UV. From left to right: **Cu-L1-P1-I**, **Cu-L1-P1-Br**, **Cu-L1-P1-Cl, Cu-L1-P1-SCN, Cu-L1-P1-CN, Cu-L5-P1-I, Cu-L5-P1-Br, Cu-L5-P1-Cl.**

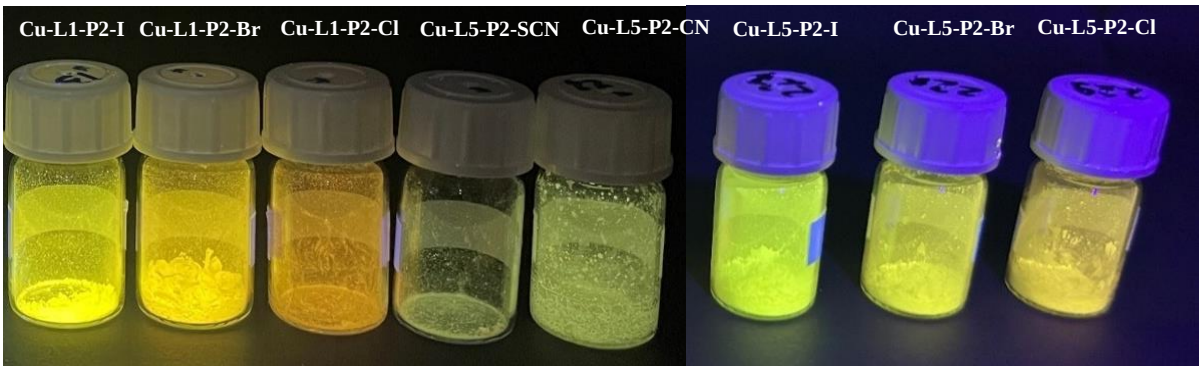

Figure 53. Picture of complex series of the type **Cu-L1-P2-X (left)** and **Cu-L5-P2-X (right)** under UV**.** From left to right: **Cu-L1-P2-I, Cu-L2-P1-Br, Cu-L1-P1-Cl, Cu-L1-P2-CN, Cu-L1-P2-SCN, Cu-L5-P2-I, Cu-L5-P2-Br, Cu-L5-P2-Cl.**

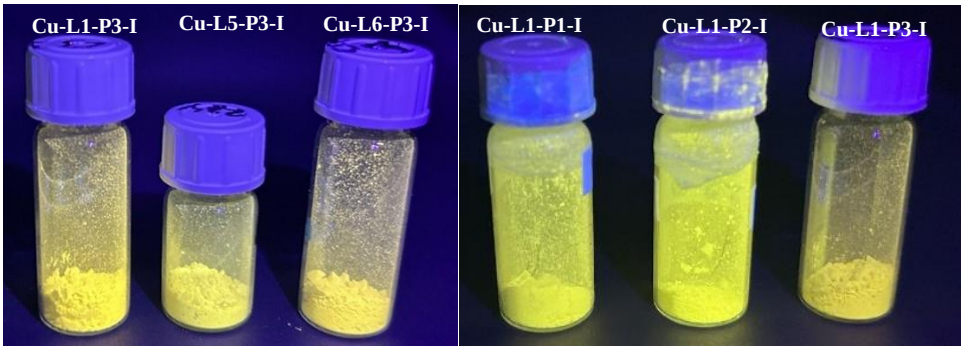

Figure 54. Left) Picture of complex series of the type **Cu-L-P3-X**. From left to right: **Cu-L1-P3-I**, **Cu-L5-P3-I**, **Cu-L6-P3-I**. Right) Comparison of **Cu-L1-P1-I**, **Cu-L1-P2-I**, **Cu-L1-P3-I**.

It should be noted, that due to the higher stability of CuI-based complexes, most of the previous research on butterfly-complexes has focused on complexes using CuI. However, the synthesis of a basic heteroleptic complex $(PPh_3)_2$(**L5**)Cu_2X_2 using CuCN and CuSCN has been previously conducted for two complexes by VOLZ, but has not been reported otherwise in the scientific literature.[42]

The series of **Cu-L1-P1-X** and **Cu-L1-P2-X** were exemplarily tested on their solubility in common solvents, which are used in the solution-processing of OLEDs such as toluene, chlorobenzene, and dichloromethane, as well as the antisolvent n-hexane. An overview of all tested solubilities is given in Table 12. The classification is as follows: low solubility for 1-10 mg/ml, good for 10-20 mg/ml, and excellent for over 20 mg/ml in the respective solvent.

Table 12. Summary of tested solubilities of the dinuclear complexes row of **Cu-L1-(P1-P3)-X** in toluene, chlorobenzene, dichloromethane and n-hexane. The tests were qualitatively taken of the powdered samples at 19 °C. Classification as follows: ● = > 20 mg/mL (excellent), ● = 10 – 20 mg/mL (good), ● = 1 – 10 mg/mL (low), ● = < 1 mg/m (none), n.t. not tested.

Entry	Complex	Toluene	Chlorobenzene	Dichloromethane	*n*-Hexane
1	Cu-L1-P1-I	●	●	●	●
2	Cu-L1-P1-Br	●	●	●	●
3	Cu-L1-P1-Cl	●	●	●	●
4	Cu-L1-P1-SCN	●	●	●	●
5	Cu-L1-P1-CN	●	●	●	●
6	Cu-L1-P2-I	●	●	●	●
7	Cu-L1-P2-Br	●	●	●	●
8	Cu-L1-P2-Cl	●	●	●	●
9	Cu-L1-P2-SCN	●	●	●	●
10	Cu-L1-P2-CN	●	●	●	●
11	Cu-L1-P3-I	●	●	●	●
12	Cu-L5-P3-I	●	●	●	●
13	Cu-L6-P3-I	●	●	●	●

All tested complexes show an excellent solubility in dichloromethane. Complexes bearing **P2** additionally demonstrate excellent solubility in chlorobenzene and toluene and are, therefore, highly suitable for various applications such as solution-processed OLEDs. The series with **P1** has variable solubilities depending on the used halide. For the complexes with iodine and bromine an additional excellent solubility is observed in chlorobenzene, compared to a good one for the chlorine and cyanide derivative and a low one for thiocyanate. Interestingly, all three complexes featuring **P3** show insufficient solubility in toluene but an excellent one in chlorobenzene and dichloromethane.

Tetranuclear complexes of the type $Cu_4I_4P_4$ (Ratio 1:1): As mentioned in the introduction, several tetranuclear structures, such as cubic or ladder-like geometries, are known. They often exhibit intense luminescence properties due to their Cu-Cu interaction.[212-213]. By applying only ancillary ligands, four linking sites become available with this structural type.

Two tetranuclear complexes, **Cu-4-P1-I** and **Cu-4-P3-I** were synthesized by following the general reaction method and mixing the ligand with **CuI** in a 1:1 ratio for the monodentate P-ligands, **P1** and **P3**. The obtained complexes were fully characterized through NMR analysis and mass spectrometry. For illustration purposes, the proposed structures are shown in Figure 55; however, as no crystal structures were obtained for these complexes, a definite statement about the detailed structure of the copper(I)-core (cubic, ladder-like) cannot be made. An analogue complex with **P2**, could not be clearly characterized, although a powder was obtained that showed blue-green emission and a good solubility in toluene.

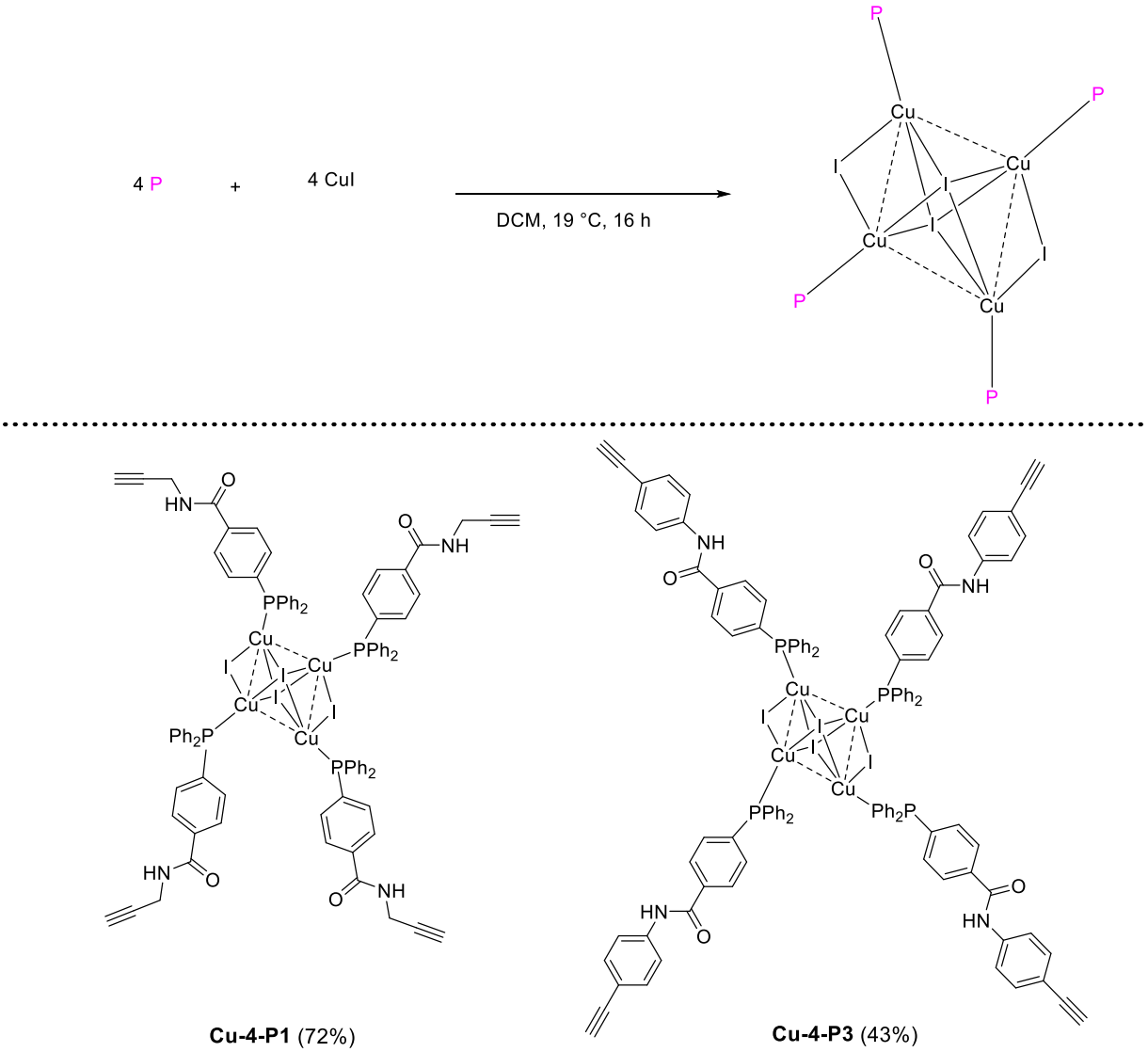

Figure 55. Complexation reaction with a ratio of 4:4 to obtain tetranuclear complexes **Cu-4-P1** and **Cu-4-P2**, and **Cu-4-P3**.

The complex **Cu-4-P1** was obtained as off-white solid with a good yield of 72%. In contrast, **Cu-4-P3** was obtained as a more yellow powder with a moderate yield of 43%. The powdered samples under normal daylight and UV-light are shown in Figure 56.

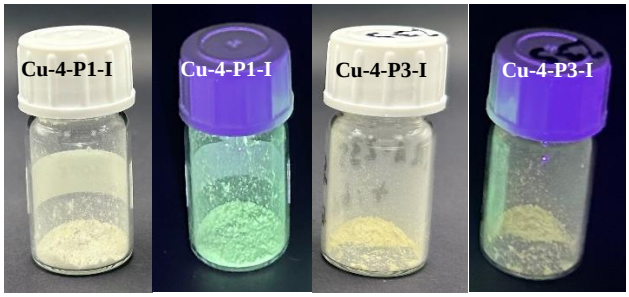

Figure 56. Pictures of tetranuclear complexes **Cu-4-P1** and **Cu-4-P3** in daylight and UV-light.

Both complexes were tested for their solubility in the common organic solvents toluene, chlorobenzene, dichloromethane, and n-hexane. The following table gives an overview over the respective solubility. The classification is as follows: low for 1-10 mg/ml, good for 10-20 mg/ml and excellent for over 20 mg/ml in the respective solvent.

Table 13. Summary of tested solubilities of the tetranuclear complexes **Cu-4-(P1-P3)** in toluene, chlorobenzene, dichloromethane and n-hexane. The tests were qualitatively taken of the powdered samples at 19 °C. Classification as follows: ● = > 20 mg/mL (excellent), ● = 10 – 20 mg/mL (good), ● = 1 – 10 mg/mL (low), ● = < 1 mg/m (none).

Entry	Complex	Toluene	Chlorobenzene	Dichloromethane	*n*-Hexane
1	**Cu-4-P1**	●	●	●	●
2	**Cu-4-P3**	●	●	●	●

Cu-4-P1 showed excellent solubility in dichloromethane but interestingly no solubility in any other solvent, whereas **Cu-4-P3** displayed no significant solubility in any of the tested solvents.

Summary. To sum up, various copper(I) complexes with different CuX cores were successfully synthesized with **P1**, **P2**, and **P3**. The majority of the complexes showed an excellence solubility of over 20 mg/ml in at least one solvent and no solubility in *n*-hexane. This makes them already ideal candidates for commonly solution-processed OLEDs without further crosslinking, as n-hexane could be perfectly used as antisolvent. In the following chapter, some exemplary crosslinking reactions were conducted to investigate the different crosslinking moieties in more detail. After that, the complexes were photophysically characterized, which was supported by calculations.

3.3.2 Crosslinking experiments

Given that the autocatalytic property of the complexes would be the crucial factor for *in situ* crosslinking in the OLED processing, some preliminary qualitative test reactions were performed to evaluate different reaction pathways and their outcomes. For this reason, the following crosslinking experiments were conducted without further additives added. The objective was to investigate whether a crosslinking reaction occurred in general, and if so, to observe the reaction conditions to study this more in-depth in future projects. Furthermore, when a bifunctional crosslinking partner was used, the aim was to obtain an insoluble product, as this would be the main goal for an application in solution-processed OLEDs.

For this purpose, a series of exemplary crosslinking reactions were carried out using the dinuclear complexes **Cu-L1-P1-I**, **Cu-L1-P1-Br** for CuAAC (Table 14, entries 1-2) and thiol-yne click reactions (Table 14, entries 3-4) and **Cu-L1-P2-I** for direct photopolymerization upon UV excitation (Table 14, entry 5). A schematic overview of the tested crosslinking reactions is given in Scheme 13.

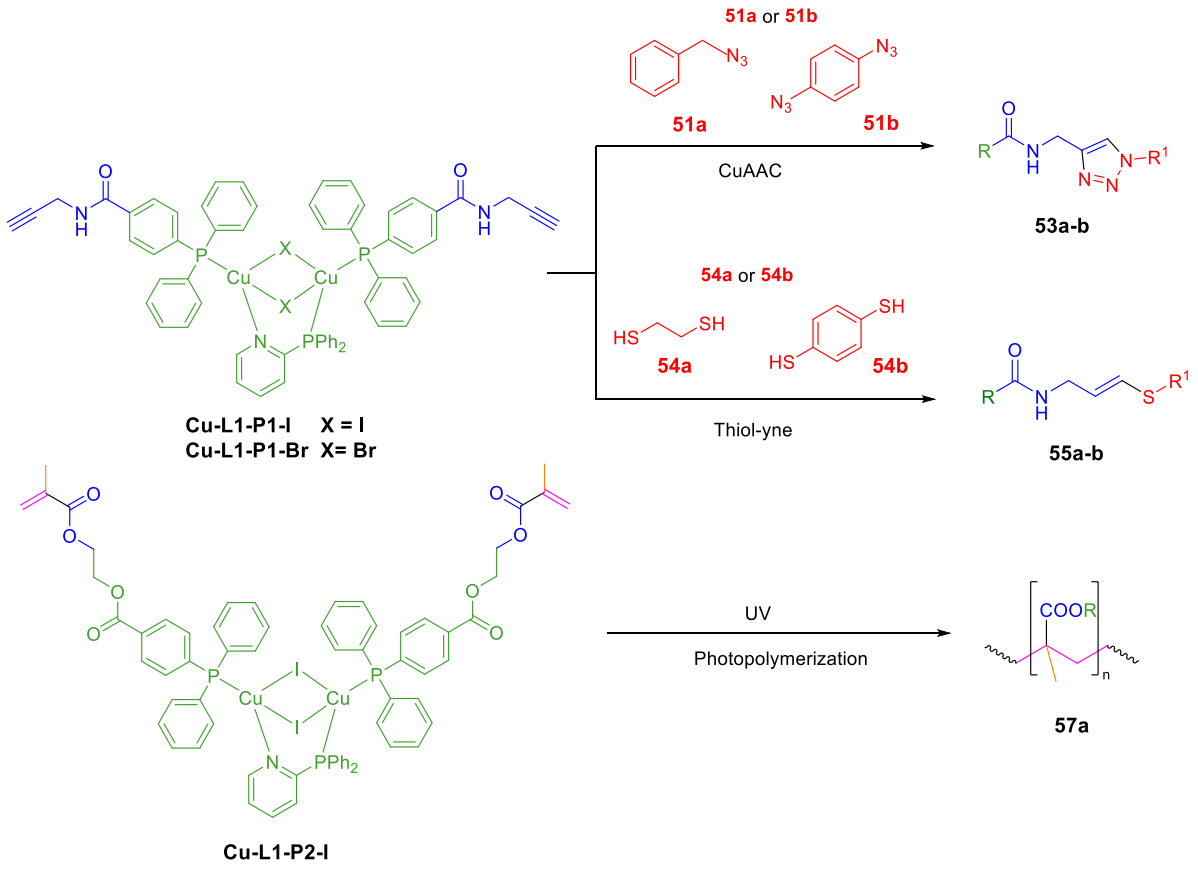

Scheme 13. Overview of crosslinking experiments and targeted products with **Cu-L1-P1-I**, **Cu-L1-P1-Br**, **Cu-L1-P2-I** by using CuAAC with azides, thiol-yne reactions with different dithiols and self-polymerization under UV.

The ligand **P2** was already successfully applied as a ligand monomer by MÜLLER *et al.* using AIBN in dioxane at 60 °C.[206] However, the objective of the present approach was to achieve a photopolymerization without any additive and by only relying on UV-light. For all crosslinking reactions DCM was chosen as solvent, as herein the complexes showed the overall best solubility. Nevertheless, as most of the complexes were also highly soluble in toluene, the crosslinking should also be tested in this solvent in future experiments, as its often used in the solution-processing of OLEDs. In all reactions, an insoluble solid precipitated from the reaction mixture, which was washed with DCM to remove possible contamination with the parent complex and dried in a vacuum afterwards. All products were analyzed *via* elemental analysis and IR spectroscopy. An overview of all tested conditions is given in Table 14.

Table 14: Overview of crosslinking experiments using CuAAC, thiol-yne and photopolymerization.

Entry	Complex	Reagent	Conditions	Product	Observation
1[a]	**Cu-L1-P1-I**[a]	51a	-	53a	Precipitate, change in color (reaction solution)
2[a*]		51b		53b	Precipitate after three hours
3[a]		54a		55a	Precipitate with orange-red color
4[a]	**Cu-L1-P1-Br**[a]	54b		55b	Precipitate with orange color
5[b]	**Cu-L1-P2-1**[b]	-	UV light	57a	Precipitate starts after 1 min

[a)] General reaction conditions: 1.00 equiv. complex, 2.00 equiv. reagents were mixed in a crimp *via*l under argon and stirred at 22 °C for 24 h/*6 h. [b]The complex was dissolved in DCM or toluene under argon and reacted for 30 min in a UV reactor with 14 W light bulbs with a maximum wavelength of 254 nm. No further additives were used

To study the proposed autocatalytic pathway of the CuAAC reaction, the simplest clicking product was aimed as a reference complex *via* the click-reaction of **Cu-L1-P1-I** with benzylazide (Table 14, entry 1). After an hour of reaction time, the reaction mixture turned cloudy, and the precipitation of a yellowish solid was observed. However, after 24 h, the reaction mixture has turned dark orange. After filtration of the reaction mixture, a colorless solid showing sky-blue emission under UV was obtained. The altered emission properties suggest the formation of a new complex in the product, likely with the triazole as a ligand. This indicates that the envisioned pathway of an autocatalyzed click reaction was successful. However, the control of the product forming needs to be further studied. Figure 57 shows the reaction mixture after 24 hours (left) and a comparison between the parent complex (right, yellow) and the obtained clicking product (right, sky-blue).

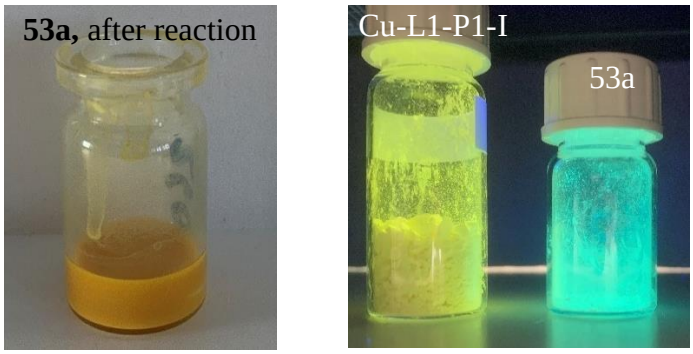

Figure 57. Left) Picture of the reaction mixture of the click-reaction between **Cu-L1-P1-I** and **51a** to form **53a** (Table 14, entry 1). Right) Comparison picture of obtained clicking product (blue,) and the parent complex **Cu-L1-P1-I** (yellow) in powdered form under UV-light.

The crosslinking of **Cu-L1-P1-I** with **53b** in DCM (Table 14, entry 2) was controlled every hour for six hours, if precipitation and a change of color occurred. Initially, the reaction mixture was a clear dark brown solution as both reagents were dissolved completely. After three hours the first precipitation was observed, and the mixture turned yellow brownish. It was then allowed to stir for three more hours, in which no noteworthy change was observed. The precipitate was filtered off and washed several times with DCM and n-pentane. The resulting precipitate showed no solubility in either solvent. Interestingly, the obtained product showed a significantly darker color; however, a yellowish luminescence was still observed under UV light. This indicates that some form of complex is still present after the reaction, as the reagents alone would not show this form of emission. Figure 58 shows the comparison of the reaction mixture before and after six hours, as well as the obtained dried product under daylight and UV.

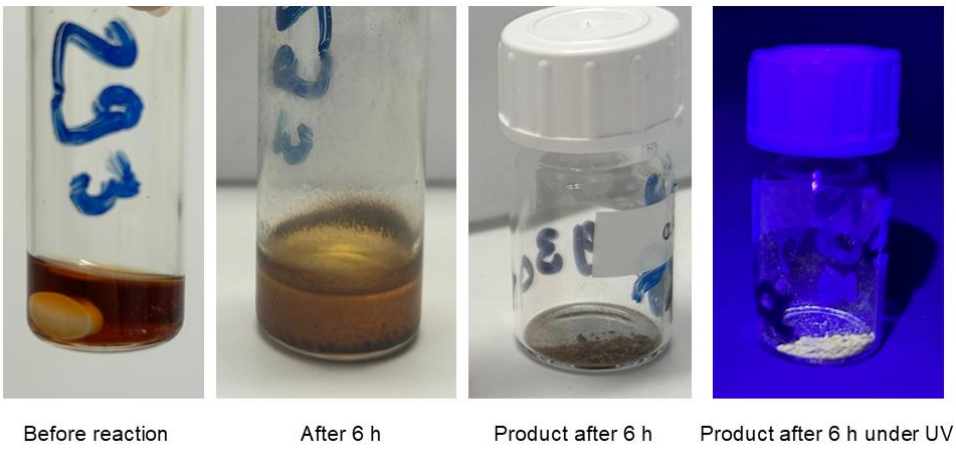

Figure 58. Crosslinking reaction of **Cu-L1-P1-I** with **51b** in an autocatalyzed CuAAc reaction (Table 14, entry 2).

For the thiol-yne reaction pathway (Table 14, entry 3-4), three reactions were carried out with various dithiols. Aliphatic and aromatic dithiols with increasing π-systems were used, to compare the influence of the enhanced π-systems on the resulting color and emission of the

formed products. For both reactions, precipitation occurred after short time. For dithioethane (**54a**), the resulting color changed the most to a more orange-red-region, whereas for the aromatic dithiol **54b** the color of the precipitate stayed yellow.

For the self-polymerization trial (Table 14, entry 7), the methacrylate functionalized complex **Cu-L1-P2-I** was dissolved in dry and degassed dichloromethane under inert atmosphere and was put in the UV-reactor for 30 minutes. Before the reaction, the solution showed a clear appearance with no traces of any precipitate; however, after completion of the reaction a precipitate was found. The colour did not change visibly, neither in daylight nor at UV-light, as shown in Figure 59.

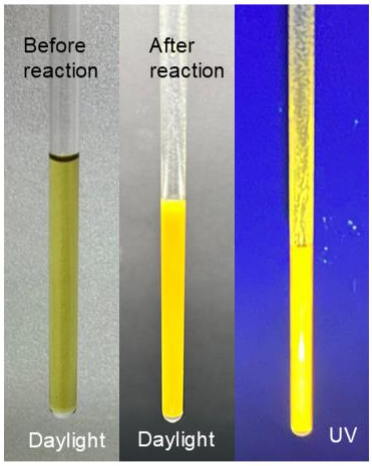

Figure 59. Self-polymerization of **Cu-L1-P2-I** in DCM under exposure of UV-light for 30 minutes (Table 14, entry 7).

A variety of crosslinking processes could be conducted with the different functionalities, resulting in non-soluble products when bifunctional crosslinking reagents were used. Moreover, no additives were required for either of crosslinking experiments, which suggests that the copper complexes may fulfil different roles, such as acting as a catalyst, or as photoinitiator and monomer.

It should be noted that these experiments represent initial tests, which aimed to determine whether non-soluble products could be obtained through crosslinking, without the intention of providing a complete analysis or full understanding of the resulting species. However, these initial experiments demonstrate the general suitability and possibilities of these complexes for a variety of crosslinking reactions.

They would be suitable candidates for a solution-processed OLED layer with subsequent *in situ* crosslinking, as the prior crosslinking experiments all resulted in non-dissolvable products. This displays a desirable property, as subsequent layers could be applied in solution without

redissolving the complex layer. However, the presented reactions and resulting products should be examined in more detail to provide a deeper understanding about the underlying structure. Moreover, the emission properties should be studied after crosslinking, for a comparison with the parent complexes.

3.3.3 Theoretical Calculations

The following theoretical calculations were conducted in a collaboration with Dr. Christof Holzer (KIT, TFP). DFT calculations of the ground and excited state were performed in gas phase. Further details can be found in the experimental section. To investigate the influence of the different functionalities, computations were made for the complex series of **Cu-L1-P1-(1-6)** and **Cu-L1-P2-(1-6)**. As not all calculations have been completed to date, herein the calculations of **Cu-L1-P1-I** and **Cu-L1-P2-I** will be presented and discussed as illustrative examples. Furthermore, for a first insight in the effect of a further click-reaction of the terminal alkyne with azides, the calculation of the crosslinked product of **Cu-L1-P1-I** with benzylazide (**51a**, Bn-N_3) was also conducted. The energy levels, frontier orbitals and NTOs of the excited S_1 and T_1 state are illustrated in Figure 60 for **Cu-L1-P1-I** and Figure 61 for **Cu-L1-P2-I**.

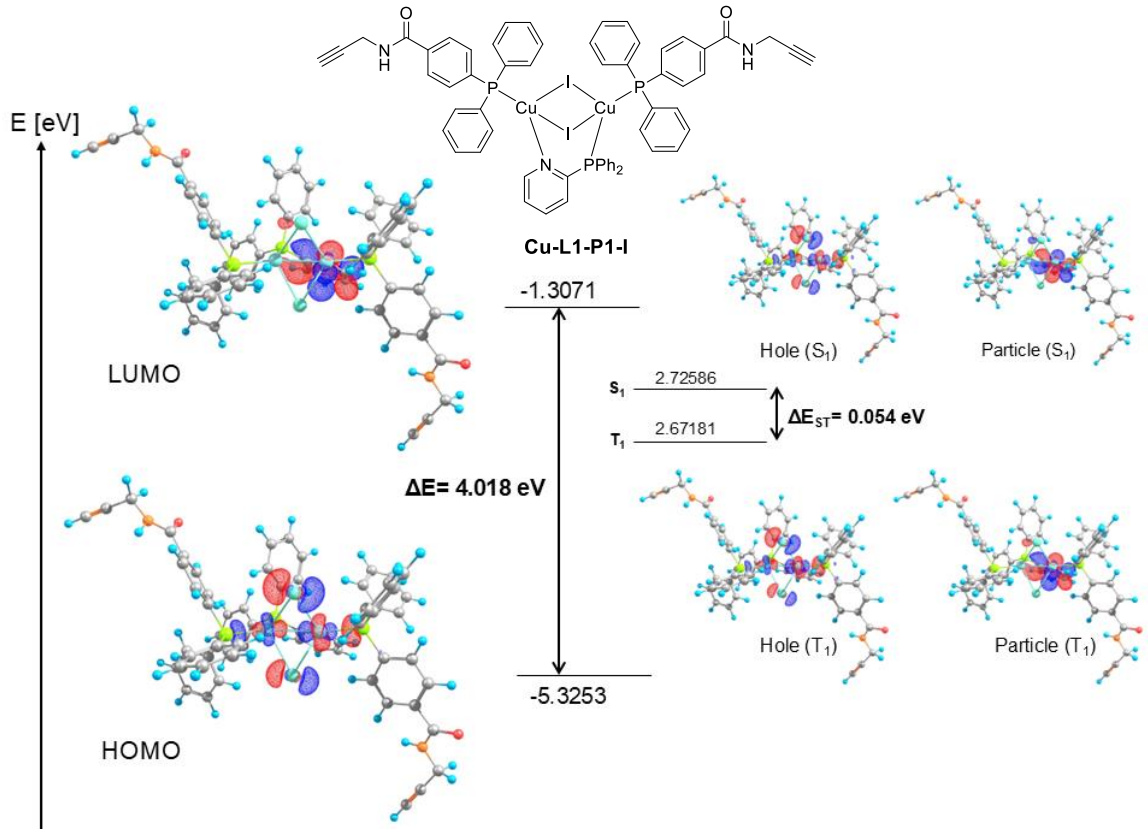

Figure 60. Visualization of the HOMO-LUMO orbitals and NTOs of the first excited singlet and triplet state of **Cu-L1-P1-I**. Note that a hole NTO denotes the initial state, while the particle NTO marks the final state of an excitation. The calculations were carried out with the TMHF functional and the def2-TZVPP basis set. Used isovalue of 0.04. Results provided by Dr. Christof Holzer (KIT, TFP).

As expected for this complex class, the HOMO is mostly located on the Cu_2I_2-core and partially on the phosphorus of the ancillary ligands. This is consistent with the observed frontier orbitals for the known butterfly complexes of the type $Cu_2X_2(PyrPhos)_3$.[138, 161, 172, 214] The calculated energy values for the HOMOs of both complexes are slightly higher, with values of around –5.3 eV, than those reported for calculations of other copper(I)complexes of this type, which are typically in the range of –4.5 eV. [63, 161] This discrepancy is most certainly attributed to the different basis sets employed. Previous studies have predominantly used the B3LYP functional with different basis sets, such as def2-SV(P), which is, for instance, markedly less accurate than the def2-TZVPP basis set that is used here.[215] A comparison is, therefore, not substantial.

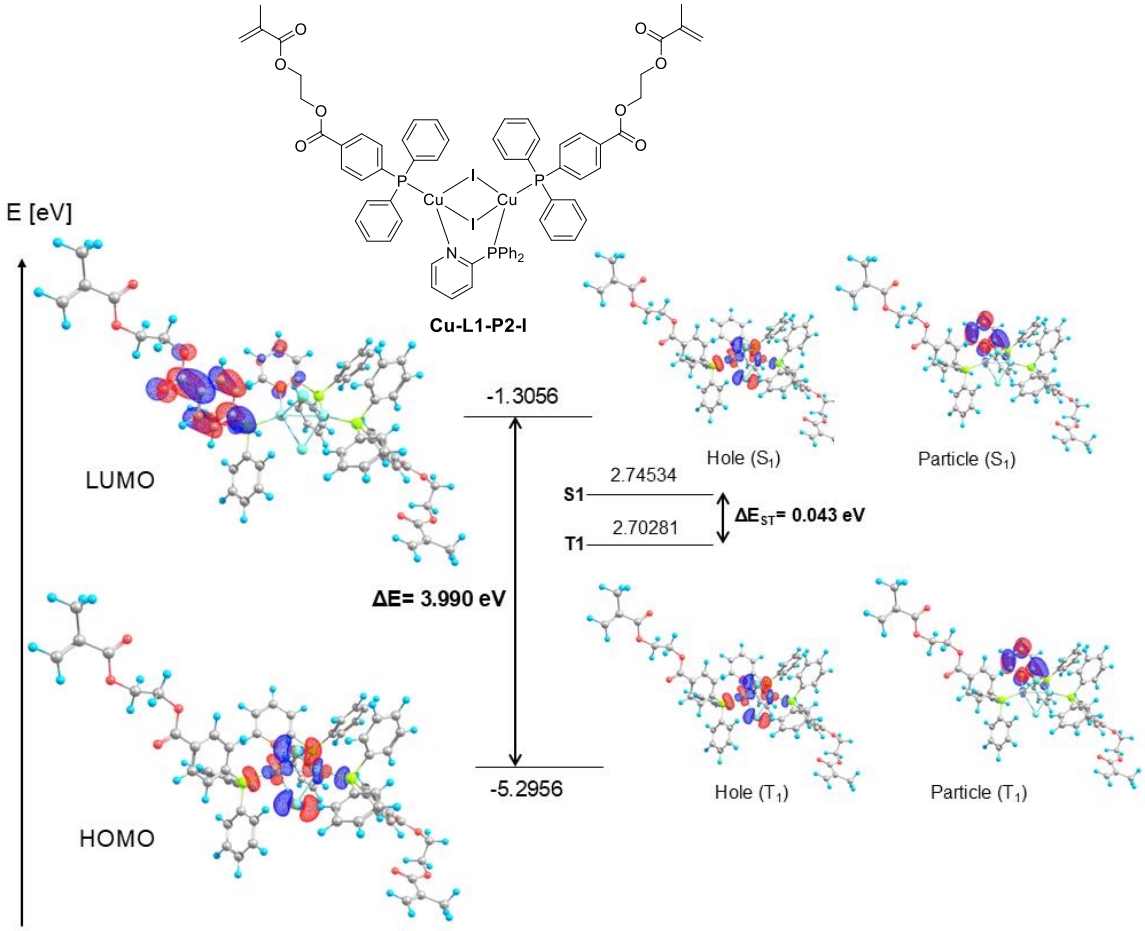

Figure 61. Visualization of the HOMO-LUMO orbitals and NTOs of the first excited singlet and triplet state of **Cu-L1-P2-I**. Note that a hole NTO denotes the initial state, while the particle NTO marks the final state of an excitation. The calculations were carried out with the TMHF functional and the def2-TZVPP basis set. Used isovalue of 0.04. Results provided by Dr. Christof Holzer (KIT,TFP).

Having a closer look at the LUMO of **Cu-L1-P2-I**, it is noticeable, that the majority of the LUMO is located on one ancillary ligand, rather than the bridging ligand. For **Cu-L1-P1-I**, the LUMO is only spread over the bridging ligand and, therefore, behaves as the reported ones. The values of the LUMOs fall within the same range as in the literature. However, due to the increased energy of the HOMOs, the energy values for the HOMO-LUMO gaps are increased

to 4.018 eV for **Cu-L1-P1-I** and 3.990 eV for **Cu-L1-P2-I** compared to the literature values in the range of 2.00 eV to 3.50 eV.

To gain further insight into the relevant transitions, the NTOs of the S_1 and T_1 states were also calculated and are included in Figure 60 and Figure 61. For **Cu-L1-P1-I**, no significant difference can be observed upon comparison between the NTOs and the frontier orbitals. For **Cu-L1-P2-I**, the particle orbitals of the excited singlet and triplet state are located on the bridging ligand and therefore differ to the corresponding LUMO of the ground state.

Due to the nature of the orbitals, for both complexes, (M+X)LCT character can be postulated and the values of ΔE_{ST} lay in the range for TADF (0.054 eV for **Cu-L1-P1-I**, 0.043 eV for **Cu-L1-P2-I**).

Given, that the HOMO is mostly located on the copper center and the LUMO on the bridging ligand, it can be assumed that further crosslinking reactions on the ancillary ligands will not have a significant effect on the respective emission. This was already shown for complex **51** after click-reaction to benzylazide.[132] For a better understanding of the electronic situation after crosslinking, particularly after click-reaction, the transition orbitals and NTOs of the first two excited states of complex **Cu-L1-P1-BnN$_3$** (**53a**) were calculated as well. In comparison with the parent complex, the energy levels of the HOMO and LUMO are stabilized to –5.366 eV and –1.351 eV, respectively, and the energy gap decreases slightly to 4.009 eV (compared to 4.018). Also, for this complex, the HOMO is located on the copper core, whereas the LUMO is partially located on the bridging ligand and one ancillary ligand.

The excited state energies stay in the same range but are slightly higher. The energy of the first excited singlet state increases to 2.759 eV compared to 2.726 eV; for T_1, it increases from 2.672 eV to 2.699 eV, respectively. This is accompanied by a total increase of ΔE_{S1T1} of 0.006 eV, to a value of 0.06 eV, which could have an impact on the emission properties, as the transition $S_0 \rightarrow S_1$ needs more energy, leading to a hypsochromic shifted emission. Additionally, as ΔE_{S1T1} increases, the probability for reverse intersystem crossing processes is lower for this complex compared to the parent complex. Nevertheless, all values for ΔE_{ST} are so small that an emission pathway through RISC as TADF is still highly probable (ΔE_{ST}: 0.043–0.06 eV << 0.1 eV).[4]

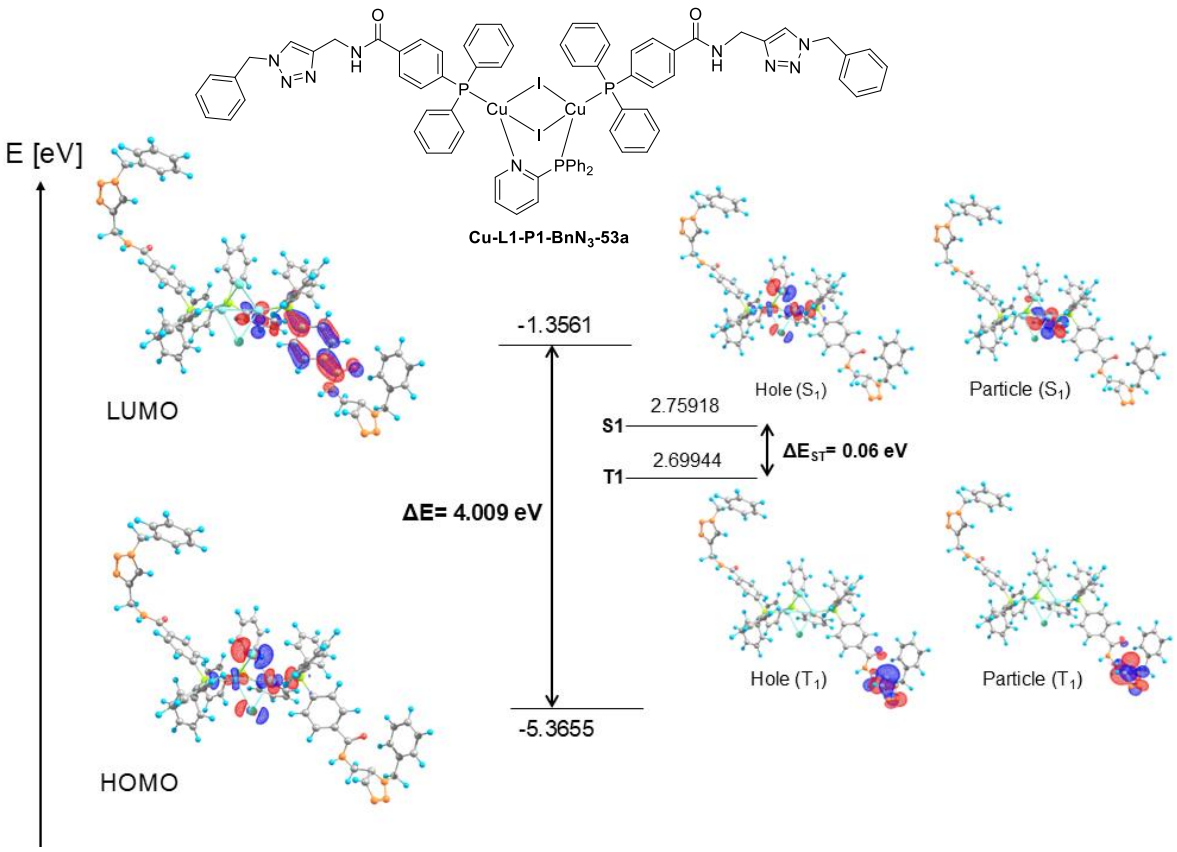

Figure 62. Visualization of the HOMO-LUMO orbitals and NTOs of the first excited singlet and triplet state of clicking product **53a** between **Cu-L1-P1-I** and benzyl azide **51a.** Note that a hole NTO denotes the initial state, while the particle NTO marks the final state of an excitation. The calculations were carried out with the TMHF functional and the def2-TZVPP basis set. Used isovalue of 0.04. Results provided by Dr. Christof Holzer (KIT, TFP).

It should be noted that the hole-particle orbitals of the first excited triplet state T_1 are located on the clicked triazole part, and therefore, they might not be part of a transition $S_1 \rightarrow T_x$. A closer examination of the NTOs of the first and second excited singlet and triplet states, as shown in Figure 63, suggests that an $S_1 \rightarrow T_2$ transition occurs more likely, given the substantial orbital overlap in this instance. Overall, it is not possible to draw a definite conclusion from the information presented here regarding the impact of the clicking process on the emission properties. However, given that the NTOs slightly change, particularly regarding T_1, which is relocated to a completely different part of the complex, it is likely that an influence may indeed be exerted.

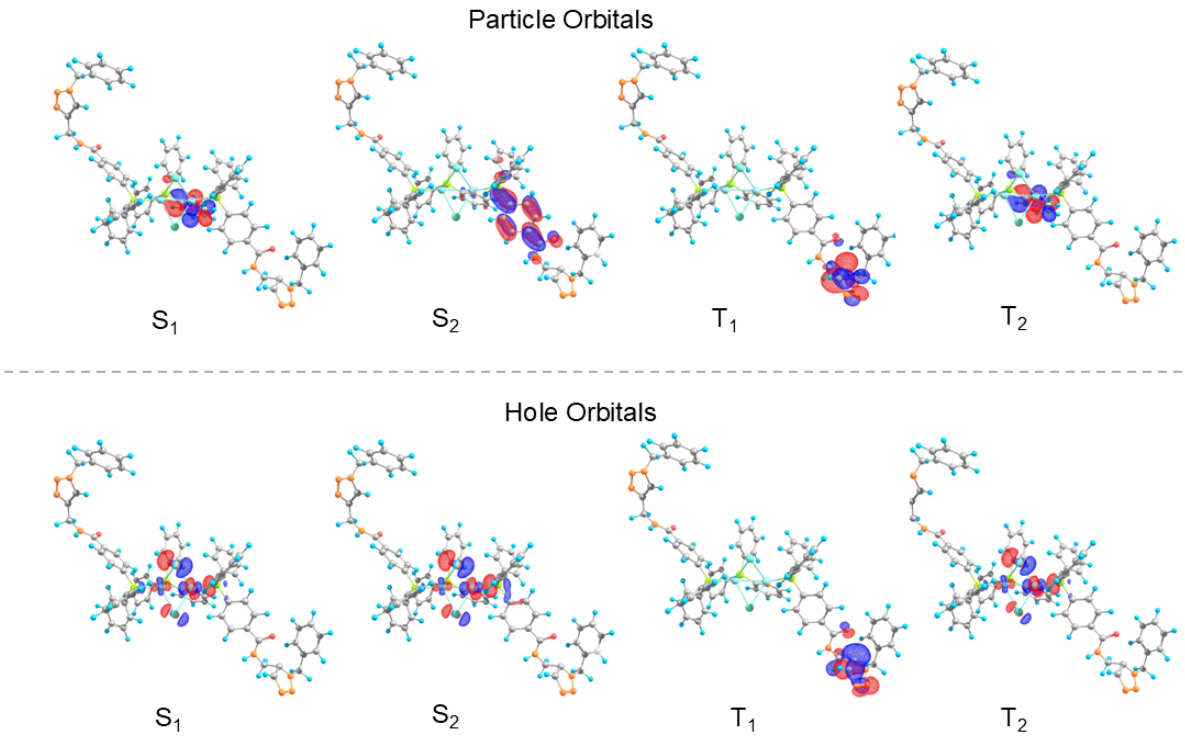

Figure 63. Visualization of the NTOs of the first and second excited singlet and triplet state of clicking product **Cu-L1-P1-I-a** between **Cu-L1-P1-I** and benzylazide**.** Note that a hole NTO denotes the initial state, while the particle NTO marks the final state of an excitation. The calculations were carried out with the TMHF functional and the def2-TZVPP basis set. Used isovalue of 0.04. Results provided by Dr. Christof Holzer (KIT, TFP).

3.3.4 Photophysical characterization

In the following, the steady-state photoluminescence, lifetimes *via* TCSPC and photoluminescence quantum yields were measured for most of the presented complexes using an FS5 spectrofluorometer from Edinburgh Instruments. For all measured complexes, the PLQY measurement was performed in an integrating sphere in air and nitrogen atmosphere, whereas the TCSPC measurements were only conducted under nitrogen. The spectroscopic measurements were conducted of selected complexes, which were fully analyzed and obtained in high purities and showed additional sufficient solubility in either DCM or Toluene. For **Cu-L1-P1-I**, **Cu-L5-P1-I**, **Cu-L1-P2-I**, and **Cu-L1-P2-Br** emitters, time-resolved gate spectroscopy with low-temperature measurements were performed as part of a stay abroad with support of Dr. Andrew Danos and Kamile Bareikaite at the University of Durham in the group of Prof. Monkman. All measurements were conducted of solid-state films of PMMA or zeonex, which were prepared by drop-casting in air in either toluene or DCM. The exact details of the used stock solutions can be found in the experimental part.

Firstly, the results for the tetranuclear and mononuclear complexes will be discussed, followed by a more detailed investigation on the dinuclear complexes of the type $P_2LCu_2X_2$.

3.3.4.1 Mononuclear and tetranuclear complexes

The UV-Vis and the photoluminescence of the tetranuclear complexes **Cu-4-P1-I, Cu-4-P3-I**, and the mononuclear complex **Cu-1-P1-I** were measured in DCM and as 1wt% doped PMMA film, respectively. Figure 64 shows the resulting UV-Vis spectra in DCM (left) and the photoluminescence spectra with the respective films (right) for an excitation wavelength at 340 nm. For comparative reasons, the photoluminescence spectrum of the dinuclear complex **Cu-L1-P1-I** is included in the graph, although the results for this complex will be discussed in the next chapter in more detail. All three complexes show a broad absorption, ranging from 250 to 350 nm, which is also observed for the free ligands. The tetranuclear complexes show additional absorption bands up to 400 nm, suggesting MLCT and (M+X)LCT transitions. At approximately 400 nm, all absorption spectra reach a molar extinction coefficient of zero. Notably, **Cu-4-P3-I** shows an additional maximum at 290 nm, which is also seen in the free ligand **P3**, and, therefore, can be attributed to a ligand centered absorption process. The photoluminescence spectra of the tetranuclear and mononuclear complexes show a notable blueshift compared to the dinuclear complex **Cu-L1-P1-I** of up to 476 nm for **Cu-1-P1-I**. The tetranuclear complexes exhibit a similar emission maxima at ~ 490 nm.

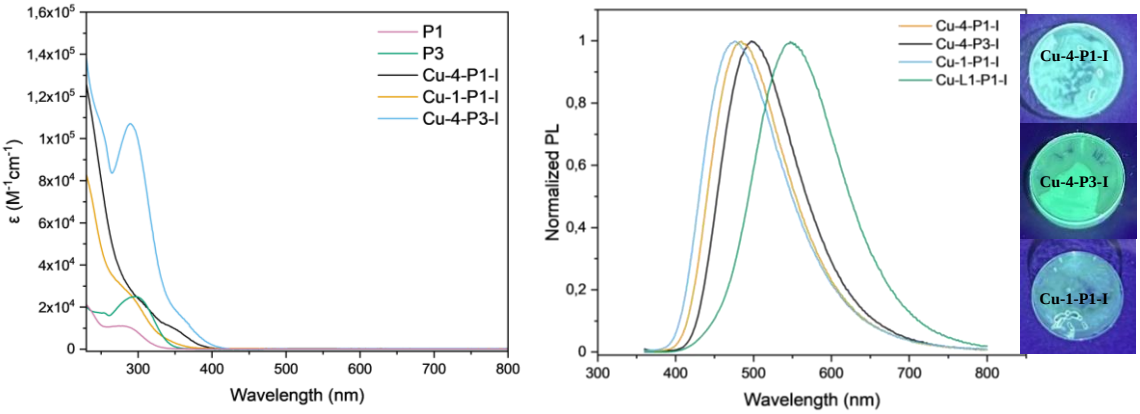

Figure 64. Left) UV-Vis spectra in DCM. Right) Steady-state photoluminescence spectra (λ_{exc} = 340 nm) of the tetranuclear complexes **Cu-4-P1**, and **Cu-4-P3**, and the mononuclear complex **Cu-1-P1**, in comparison with the dinculear complex **Cu-L1-P1-I**. All films are measured in a 1 wt% doped PMMA film in air.

Table 15 gives an overview of the photophysical properties of all four complexes. The emission decay lifetimes were measured in nitrogen atmosphere. **Cu-4-P1-I** exhibits the highest value of 11.7 µs for the tetranuclear complexes, compared to 7.11 µs for **Cu-4-P3-I**, whereas the mononuclear complex **Cu-1-P1-I** shows a lifetime of 9.55 µs.

Table 15. Summary of the photophysical properties of the mononuclear and tetranuclear complexes **Cu-1-P1-I**, **Cu-4-P1-I**, and **Cu-4-P3-I**.

Compound	$\lambda_{max,PL}$ [nm]	τ^a[µs]	Φ_{PL} [%] in N_2 (air)
Cu-1-P1-I	476	9.55	42 (35)
Cu-4-P1-I	484	11.7	94 (63)
Cu-4-P3-I	499	7.11	50 (34)

[a]biexponential decays, intensity weighted average lifetimes were calculated ($\tau = \Sigma A_i\tau_i^2 / \Sigma A_i\tau_i$).[216]

For all complexes, the PLQY increases significantly when measured in nitrogen since oxygen can strongly quench excited triplet states.[175] This underlines the involvement of excited triplet states for all investigated complexes. The mononuclear complex **Cu-1-P1-I** exhibits a significantly smaller PLQY with 42% compared to the tetranuclear complexes, which range from 50% for **Cu-4-P3-I** to 94% for **Cu-4-P1-I**, representing one of the highest values that were measured in this work. Based on the excellent solubility in dichloromethane accompanied by the exceptionally high PLQY, **Cu-4-P1-I** is a highly promising candidate for further application in solution-processed OLEDs.

3.3.4.2 Dinuclear complexes

First, the absorption was measured in DCM, followed by the investigation of the steady-state properties in neat film and doped PMMA films. As already depicted in *Chapter 3.2.*, PMMA is often used as inert host material, which usually does not significantly influence the complex properties. Photoluminescence measurements in neat film and in a 1 wt% doped film in PMMA were conducted for **Cu-L5-P1-I**, **Cu-L1-P1-I**, **Cu-L1-P1-CN**, **Cu-L1-P2-I**, and **Cu-L5-P2-I**. A summary of all photophysical properties of the dinuclear complexes in the doped PMMA films is given in Table 16.

Absorption and Steady-state Photoluminescence. The complexes all show the typical broad absorption in the range of 230 to 400 nm with extinction coefficients of up to 7×10^4 M^{-1} cm^{-1} at ~275 nm (Figure 65). Again, complexes featuring **P3** show an additional maximum at 290 nm, likely caused by ligand centered absorption. The obtained emission and excitation spectra in neat film and doped in PMMA, are exemplarily shown for **Cu-L5-P1-I** in Figure 65. For the PMMA film a slight blueshift is observed, yet the overall course of the graph remains similar.

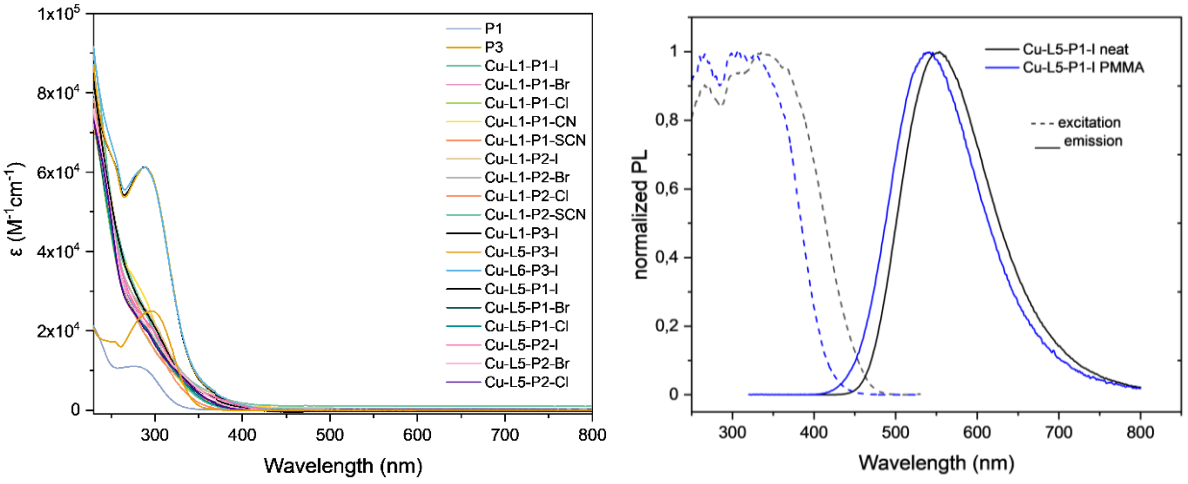

Figure 65. Left) UV-Vis absorption spectra, measured in DCM. Right) Comparison of photoluminescence spectra of a neat film and a film with 1 wt% emitter in PMMA for **Cu-L5-P1-I**. Films were prepared by drop-casting and measured in air at room temperature.

The same behavior was observed for the dinuclear complexes **Cu-L-P1-I**, **Cu-L1-P1-CN**, **Cu-L1-P2-I**, and **Cu-L5-P2-I**, and the resulting spectra can be found in the experimental part. However, as the PLQYs were found to be higher for the doped PMMA films in these cases, all remaining complexes were only measured in doped PMMA films.

The dinuclear butterfly-type complexes of the series **Cu-L-P1-X**, **Cu-L-P2-X** and **Cu-L-P3-X** show the typical broad emission, which is usually observed for these complexes due to the MLCT character upon excitation. The emission maxima for all complexes lay between 500 and 600 nm, mainly around 550 nm. Figure 66 shows the spectra for the series of **Cu-L-P1-X** and **Cu-L-P2-X**, and Figure 67 shows the ones obtained for the series of **Cu-L-P3** as well as the comparison of **Cu-L1-P1-I**, **Cu-L1-P2-I**, and **Cu-L1-P3-I**. Selected pictures of the films are included in the graphs.

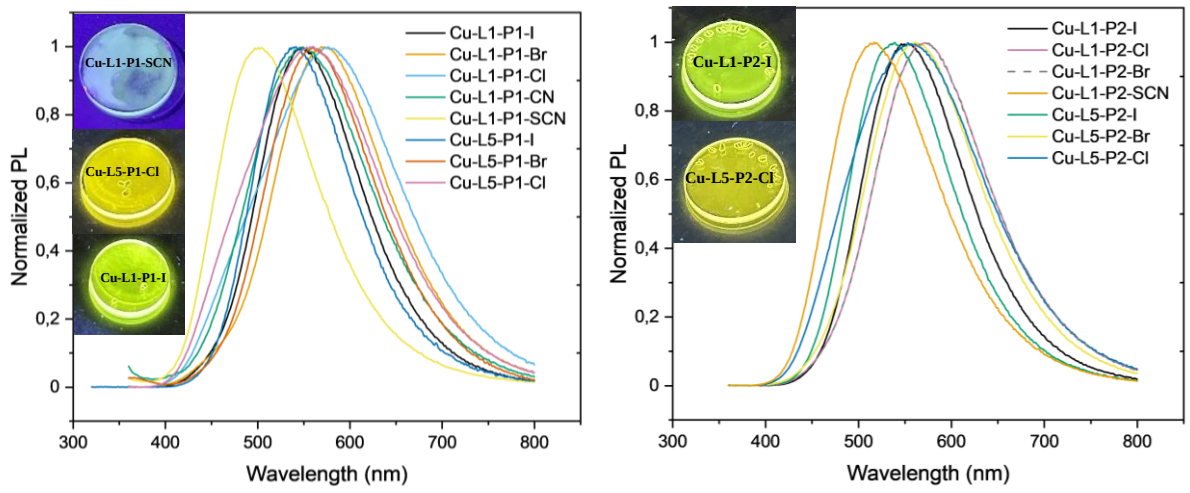

Figure 66. Steady-state photoluminescence spectra (λ_{exc} = 340 nm) of the dinuclear complex series **Cu-L-P1-X** (left) and **Cu-L-P2-X** (right) in a 1 wt% doped PMMA film.

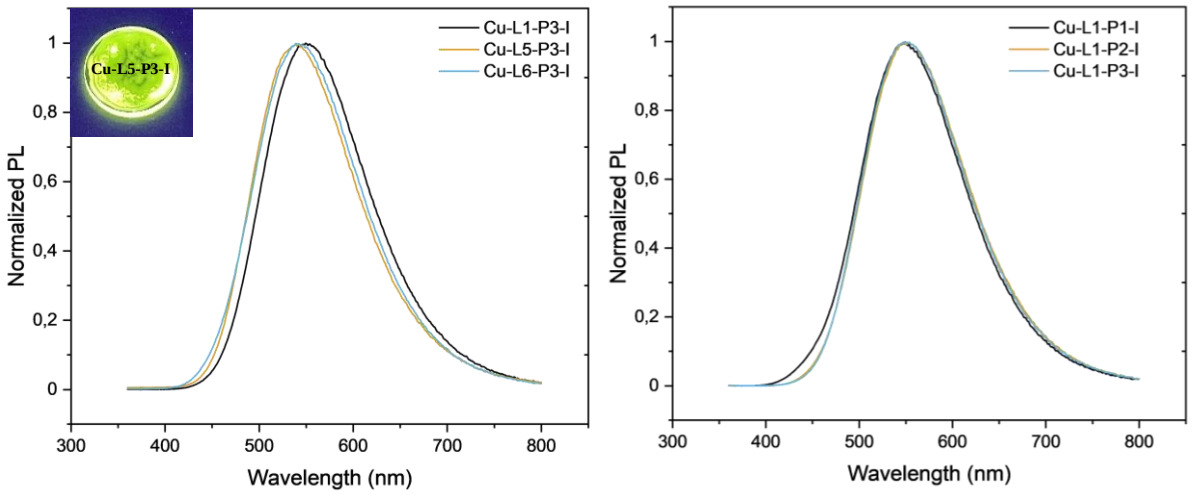

Figure 67. Steady-state photoluminescence spectra (λ_{exc} = 340 nm) of the dinuclear complex series **Cu-L-P3-X** (left) and a comparison between the three complexes featuring CuI and L1: **Cu-L1-P1-I**, **Cu-L1-P2-I** and **Cu-L1-P3-I** (right). All films are measured in a 1 wt% doped PMMA film in air.

A red shift of the bromo and chloro complexes compared to the iodo complexes is observed in all three series. This is commonly seen in this complex type and already described in the literature.[42, 161] Notably, the complexes featuring a CuSCN core show a significant blue shift compared to all other butterfly complexes, with the most significant for **Cu-L1-P1-SCN** having a maximum at 501 nm. This might be attributed to a stabilized S_1 state in these complexes. The complexes of the type of **Cu-L-P3-X** (Figure 67, left) exhibit quite similar spectra, as they all feature the same CuI-core. However, a slight blue shift is observed for bridging ligands with an increased number of methyl functionalities. This was already described in previous studies from BUSCH *et al.* and ZINK *et al.*[63, 161] The comparison between **Cu-L1-P1-I**, **Cu-L1-P2-I**, and **Cu-L1-P3-I** (Figure 67, right) underlines the negligible impact of the ancillary phosphines since all three spectra exhibit a maximum between 448 and 551 nm.

TCSPC and Photoluminescence Quantum Yield. An overview of all measured lifetimes and PLQYs is given in Table 16. All complexes show lifetimes below 10 µs, which lays in the range for delayed fluorescence. For most complexes a biexponential fit was used, and the average lifetime was calculated, although no prompt component was observed. This is quite commonly observed for copper (I) complexes due to the fast ISC in the picosecond range, which then dominates, compared to a prompt fluorescence. In Figure 68 (left) the decay curves of **Cu-L5-P1-I** and **Cu-L5-P1-Br** are exemplarily shown.

Table 16. Summary of the photophysical properties of the dinuclear complex series **Cu-L-P1-X**, **Cu-L-P2-X** and **Cu-L-P3-X**, all measured in 1 wt% films of PMMA.

Compound	$\lambda_{max,PL}$ [nm]	τ^a[µs]	Φ_{PL} [%] in N_2 (air)
Cu-L1-P1-I	548	5.94	95 (70)
Cu-L1-P1-Br	572	7.22	57 (34)
Cu-L1-P1-Cl	577	6.86	22 (18)
Cu-L1-P1-CN	548	4.40	18 (14)
Cu-L1-P1-SCN	501	4.47	32 (23)
Cu-L5-P1-I	540	5.62	73 (53)
Cu-L5-P1-Br	562	9.39	58 (35)
Cu-L5-P1-Cl	559	8.93	36 (19)
Cu-L1-P2-I	551	6.76	88 (45)
Cu-L1-P2-Br	573	6.10	36 (24)
Cu-L1-P2-Cl	573	6.69	17 (10)
Cu-L1-P2-SCN	515	3.71	25 (18)
Cu-L5-P2-I	538	5.95	94 (37)
Cu-L5-P2-Br	560	8.29	53 (22)
Cu-L5-P2-Cl	557	9.01	26 (12)
Cu-L1-P3-I	551	5.87	94 (76)
Cu-L5-P3-I	539	5.80	<99* (79)
Cu-L6-P3-I	542	3.38	50 (34)

[a]For biexponential decays, intensity weighted average lifetimes were calculated ($\tau = \Sigma A_i\tau_i^2 / \Sigma A_i\tau_i$).[216] *A PLQY over 100% was detected.

A clear trend can be observed for the complexes exhibiting a CuSCN core for the lifetimes since they are among the smallest lifetimes. **Cu-L1-P2-SCN** exhibits the second fastest decay among all, with 3.71 µs. However, the fastest decay is observed for **Cu-L6-P3-I** with 3.38 µs. The complexes featuring CuBr or CuCl cores, show a slightly increased lifetime compared to those with CuI. All values are above 3 µs, which fits the predictions by YERSIN in general for copper(I) complexes.[13, 26, 61, 168]

The PLQY values give a clear trend for the different halides. Complexes featuring CuI show remarkably high PLQYs over 90% except for **Cu-L5-P1-I**, **Cu-L1-P2-I**, and **Cu-L6-P3-I**, which still exhibit high PLQYs of 73%, 88%, and 50%, respectively. Interestingly, complexes formed with CuCN, CuSCN, and CuCl, show the lowest PLQYs, below 30%. For **Cu-L5-P3-I**, a PLQY slightly exceeding 100% was detected in nitrogen. This phenomenon can be caused by various reasons, e.g., for bright samples or the reabsorption of emitted light and its subsequent re-emission. This can falsely increase the number of detected photons, causing an overestimation of the PLQY. This is currently being investigated further and will be declared in the table with the following symbol: *****. However, the complex **Cu-L5-P3-I** exhibits a high PLQY of 79% even when measured in air. In general, among all complexes, the iodo ones showed the lowest lifetimes along with the highest PLQYs, which might be the result of a higher SOC due to the heavier iodine.

Host screening. **Cu-L1-P1-I** was further investigated with different small molecule hosts, which are often used in OLEDs, precisely **mCP (**1,3-bis(N-carbazolyl)benzene) and **PYD-2Cz** (2,6-bis(9H-carbazol-9-yl)pyridine). Since it is envisioned to crosslink the complex to the host material, a doping concentration of 50 wt% was chosen. The comparison of emission spectra of the 50 wt% doped host films and the 1 wt% doped PMMA film is shown in Figure 68. It should be noted that due to the varying doping concentrations, a direct comparison is limited, which should be considered when interpreting the results. No notable shift can be observed in any of the host materials, except a slight narrowing of the overall spectra for both host materials.

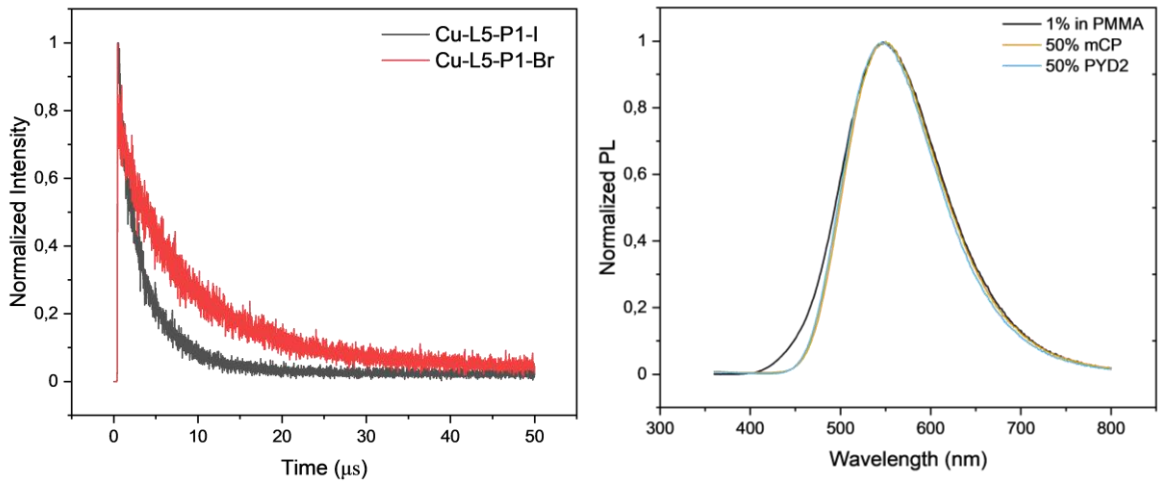

Figure 68. Left) Decay curves of **Cu-L5-P1-I** and **Cu-L5-P1-Br** (1 wt% doped PMMA film). Right)Comparison of steady-state photoluminescence spectra (λ_{exc} = 340 nm) of 50 wt% doped host (**mCP**, **PYD-2Cz**) films of the dinuclear complex **Cu-L1-P1-I**. For a comparison, the spectra of the 1 wt% doped PMMA film is included.

Table 17 summarizes the photophysical results of the host screening for **Cu-L1-P1-I**. For clarity, the results for the 1 wt% doped PMMA film are included again. Notably, the host films

show highly increased performances with differences of 20-30% in air compared to the PMMA films. Again, the differing concentrations need to be considered. However, the lifetimes stay similar, with a slight decrease for **PYD-2Cz** (5.04 µs). In between the two small molecule host materials **mCP** and **PYD-2Cz** no notable difference is observed. Interestingly, the difference between the PLQY values in air and nitrogen is no longer observed anymore for both hosts. These findings strongly support further applications in *in situ* crosslinking approaches for solution-processed OLEDs.

Table 17. Host screening for **Cu-L1-P1-I** with **mCP** and **PYD-2Cz**.

	50 wt% mCP	**50 wt% PYD-2Cz**	**1 wt% PMMA**
λ_{PL} [nm]	548	548	548
τ^a[µs]	5.59	5.04	5.94
Φ_{PL} [%] in N_2 (air)	99* (99)	93 (89)	95 (70)

[a]biexponential decays, intensity weighted average lifetimes were used ($\tau = \Sigma A_i\tau_i^2 / \Sigma A_i\tau_i$).[216] *A PLQY over 100% was detected.

Time-resolved gate spectroscopy (iCCD). In the context of a research stay in the group of Prof. Monkman at the University Durham, time-resolved spectroscopy measurements were conducted for **Cu-L1-P1-I**, **Cu-L5-P1-I**, **Cu-L1-P2-I** and **Cu-L1-P2-Br** in 1 wt% doped zeonex films with support of Dr. Andrew Danos and Kamile Bareikaite (University of Durham). In these experiments, zeonex functions as an inert polymer matrix similar to PMMA, which is useful for the preparation of smooth and homogenous films of the emitter. The time-resolved measurements were performed using a spectrograph (Horiba Triax) and a Stanford Computer Optics 4 Picos intensified charge-coupled device camera (iCCD) for gated detection, where samples were excited with an Nd:YAG laser (EKSPLA, 10 Hz, 355 nm) under a vacuum or stream of dry nitrogen in a cryostat. For these iCCD measurements, emission spectra at different time delays after pulsed excitation are collected. In the case of **Cu-L1-P1-I**, additional low-temperature measurements at 80 K were also taken to get a deeper understanding of the underlying emission pathway and access the emission from the triplet state. In the following, firstly the spectra of **Cu-L1-P1-I** are discussed in more detail, as for **Cu-L5-P1-I**, **Cu-L1-P2-I**, and **Cu-L1-P2-Br**, only room temperature measurements were performed. The spectra of **Cu-L1-P1-I** at room temperature and 80 K for the 1 wt% doped Zeonex film are shown in Figure 69. For a better illustration, they are displayed together with their corresponding contour plots, which display a graphical representation of the data through the plot of the intensity vs.

wavelength and time. With those, changes in the emission properties over time, such as intensity or wavelength, can be visualized directly.

At room temperature (Figure 69a), the luminescence is characterized by a fast component in the nanosecond regime with a maximum located at 538 nm. Going to the microsecond regime, a steady red shift up to 552 nm is observed, which can directly be seen in the contour plot. This can be caused by various reasons, one of which may be the presence of different molecular conformers. Similar effects have already been studied for organic TADF molecules in the groups of MONKMAN and ADACHI.[217-220] The key findings were that different molecular conformers could obtain different frontier orbitals and energy states, which can directly translate into various rates of reverse intersystem crossing (k_{RISC}) and ΔE_{ST}, which is then seen as time-dependent spectral shift. In a rigid environment, which is the case for polymeric hosts, this effect gets more pronounced as the motions are more suppressed and the different conformers cannot freely transform into each other. However, as copper(I) complexes usually undergo structural reorganization in the excited state, another reason could be that a structural relaxation is observed over time, which results in the stabilization of the excited state and therefore to a red shift. A possible explanation for the red shift at 'late' times could be that a small contribution of phosphorescence is already observed at room temperature. A direct comparison of the phosphorescence spectra at low temperature and spectra at late times for room temperature can be found in the experimental part.

Compared to the measurement in PMMA the spectrum is blue shifted about 10 nm, which is likely caused by the more fluid and less polar host environment in PMMA compared to zeonex.[221-222] However, it should be noted that as the measurement in PMMA was conducted as steady-state, a direct comparison should be done with caution.

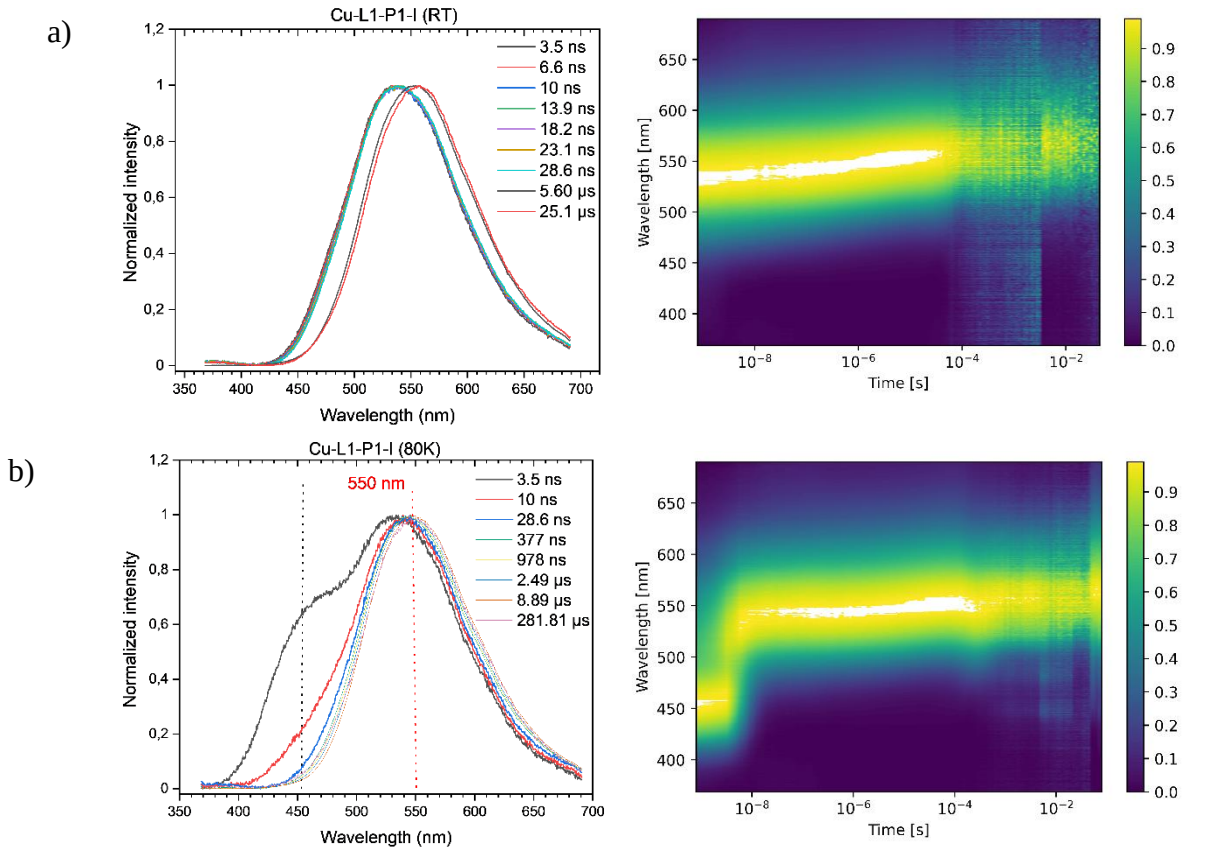

Figure 69. Normalized time-resolved photoluminescence spectra (λ_{exc} = 355 nm) of **Cu-L1-P1-I** in 1 wt% doped zeonex film at a) room temperature and b) 80 K and associated contour plot. All measurements were taken under vacuum.

For the spectra of **Cu-L1-P1-I** at 80 K (Figure 69b), two different emitting states can be directly observed. In the 'early' nanosecond spectra, a peak at 453 nm is observed. One possible explanation for this phenomenon could be the emission of ligand-centered fluorescence, which, at lower temperatures gets visible due to suppressed relaxation. At much longer times in the milliseconds regime, the luminescence at these low temperatures is presumably dominated by phosphorescence, with a maximum of around 550 nm.

Figure 70 shows the room temperature measurements and contour plots for **Cu-L5-P1-I**, **Cu-L1-P2-I**, and **Cu-L1-P2-Br**, which demonstrate the same trend of red-shift for later times, with emission maxima of 531/557 nm and 535/551 nm, respectively.

Among all complexes, **Cu-L1-P2-Br** shows the smallest shift from 554 to 563 nm, which is directly visualized in the contour plots.

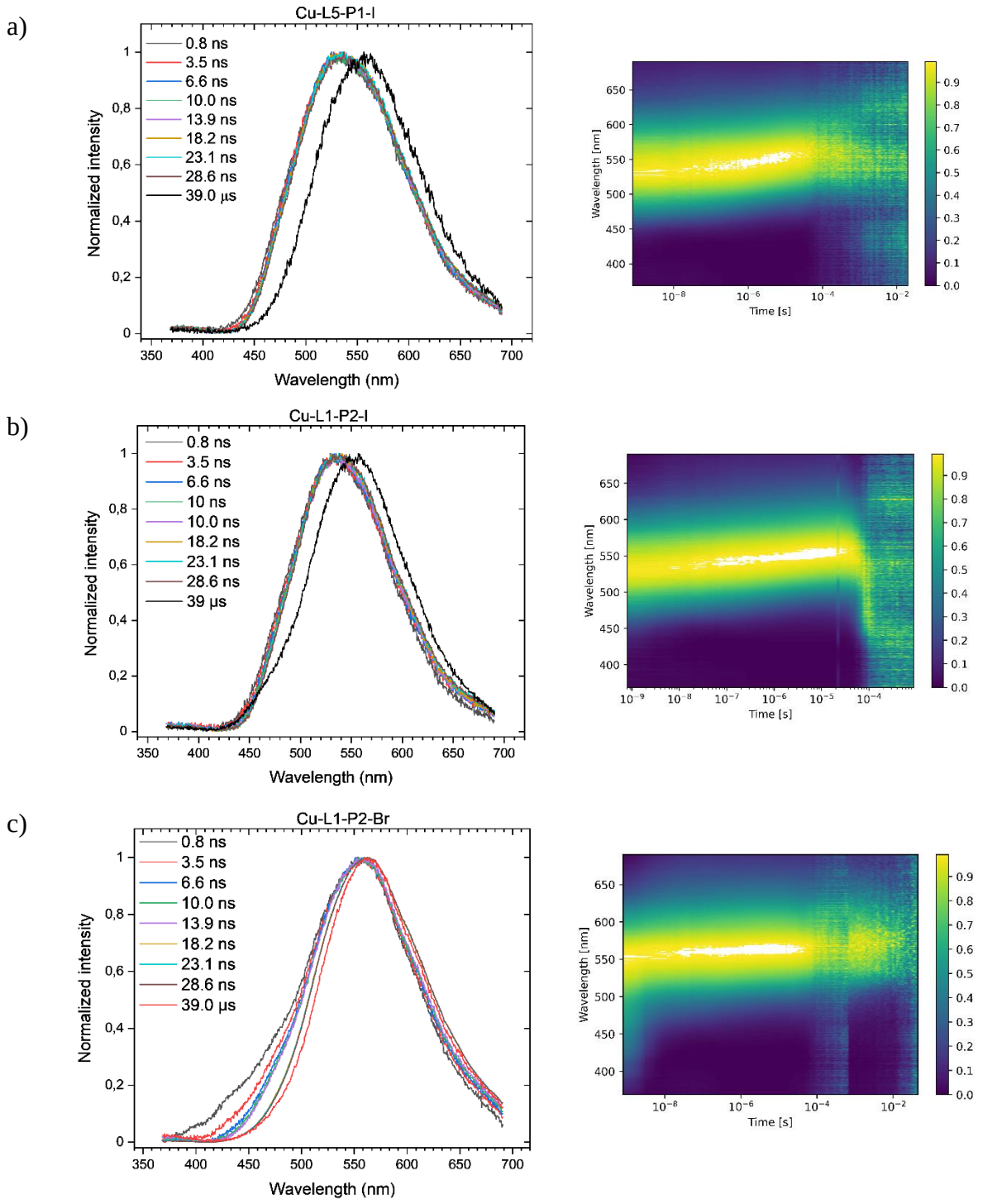

Figure 70. Normalized time-resolved photoluminescence spectra (λ_{exc} = 355 nm) and corresponding contour plot of a) **Cu-L5-P1-I**, b) **Cu-L1-P2-I** and c) **Cu-L1-P2-Br**. All were measured in a 1 wt% doped Zeonex film at room temperature. All measurements were taken under vacuum.

The emission decay curves are obtained by normalizing each time-resolved spectrum's intensity by its integration time. The decay curves at room temperature and 80 K are exemplarily shown for **Cu-L1-P1-I** in Figure 71 (right). A slower decay is observed at low temperature, indicating that the emission occurs from a longer-lived triplet state.

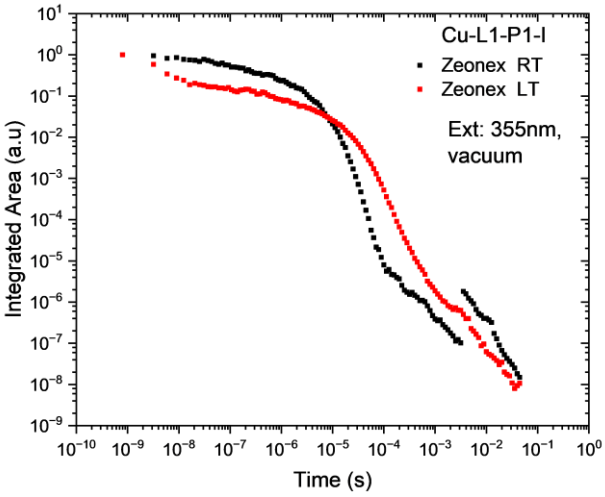

Figure 71. Decay curves of 1 wt% **Cu-L1-P1-I** in zeonex film at room temperature (black) and 80 K (red). Each datapoint represents the integrated area of each spectrum at the respective time point.

At room temperature a lifetime of 3.73 µs is obtained, compared to a lifetime of 13.1 µs at 80 K. This demonstrates that a significant proportion of triplet excitons is efficiently emitted *via* TADF at ambient temperature with this process suppressed at lower temperatures, as expected. The lifetimes for **Cu-L5-P1-I** and **Cu-L1-P2-I** were only determined at room temperature and lay in the same range, whereas for **Cu-L1-P2-Br** a slightly higher value of 5.69 µs was obtained.

Table 18. Summary of photoluminescence lifetimes, measured with iCCD.

	τ^a (RT) [µs]	τ^a (80 K) [µs]
Cu-L1-P1-I	3.73	13.1
Cu-L5-P1-I	3.25	-
Cu-L1-P2-I	3.87	-
Cu-L1-P2-Br	5.69	-

[a] All data obtained by fitting photoluminescence decay by biexponential fit. Intensity weighted average lifetimes were used ($\tau = \Sigma A_i\tau_i^2 / \Sigma A_i\tau_i$).[216] Film of 1 wt% doped Zeonex in vacuum.

Summary. Across this project, all dinuclear complexes demonstrate highly efficient luminescence with photoluminescence quantum yields of up to 99% and decay lifetimes within a low microsecond range. Additionally, all complexes exhibit emission maxima between 500 and 600 nm at room temperature. The change in emission kinetics, in combination with the variation in the PLQYs at air and nitrogen, strongly support the assignment of a TADF emission mechanism. This was further supported by low-temperature measurements for **Cu-L1-P1**,

where a red shift and increase of the decay lifetime was observed, indicating the suppression of TADF and the emergence of dominant phosphorescence emission. Therefore, these complexes represent a highly promising class of emitting materials for application in OLEDs, particularly for solution-processing as they show excellent solubility in various solvents.

For this reason, **Cu-L1-P1-I**, **Cu-L5-P1-I**, **Cu-L1-P2-I**, and **Cu-L1-P2-Br** were selected as exemplar complexes for the fabrication of solution-processed OLEDs during the international stay at the University of Durham. Furthermore, as the methacrylate containing complex **Cu-L1-P2-I** showed self-polymerization upon UV exposure in the crosslinking experiments, some selected complexes featuring **P2** were used as photoinitiators in 3D laser nanoprinting in collaboration with Aleksandra Vranic (Prof. Bräse/ Prof. Wegener). The results of the OLED fabrication and 3D laser nanoprinting will be discussed in the next chapter.

3.4 Applications of selected crosslinkable complexes

In the following chapter, the application of previously discussed emissive complexes is explored for emitting layers (EML) of solution-processed OLEDs and as photoinitiators in 3D laser nanoprinting.

The OLED fabrication was conducted in the context of a research stay at the University of Durham (UK) in the group of Prof. Monkman. For OLED fabrication, the two complexes **Cu-L1-P1-I** and **Cu-L5-P1-I**, as well as **Cu-L1-P2-I** and **Cu-L1-P2-Br**, were selected. All these complexes showed favorable properties for SOLED fabrication, such as high solubility in DCM, toluene or chlorobenzene, and high PLQYs in the solid state. Given, that the methacrylate containing complexes showed self-polymerization upon UV irradiation in the crosslinking experiments, some selected complexes of the type **Cu-L-P2-X** were used as photoinitiators in 3D laser nanoprinting in collaboration with Aleksandra Vranic (Prof. Bräse/ Prof. Wegener).

3.4.1 Solution-processed OLEDs

A variety of different OLED architectures were tested for their performance. For all solution-processed OLEDs, the hole injection layer (water-soluble PEDOT:PSS) and organic-soluble emitting layer were spin-coated on patterned indium-tin-oxide-coated glass, with the subsequent electron transport and hole blocking layer, as well as the cathode (LiF/Al) thermally evaporated afterwards. The evaporation techniques were supported by Dr. Andrew Danos and Kamile Bareikaite (University Durham, UK). After fabrication, the electrical and emission properties were tested under air at 298 K using a calibrated integrating sphere (Labsphere), fibre spectrometer (Ocean Optics), and source measure unit (Keithley). Detailed information on the procedures and devices can be found in the experimental part. An overview of the selected complexes is given in the following Figure.

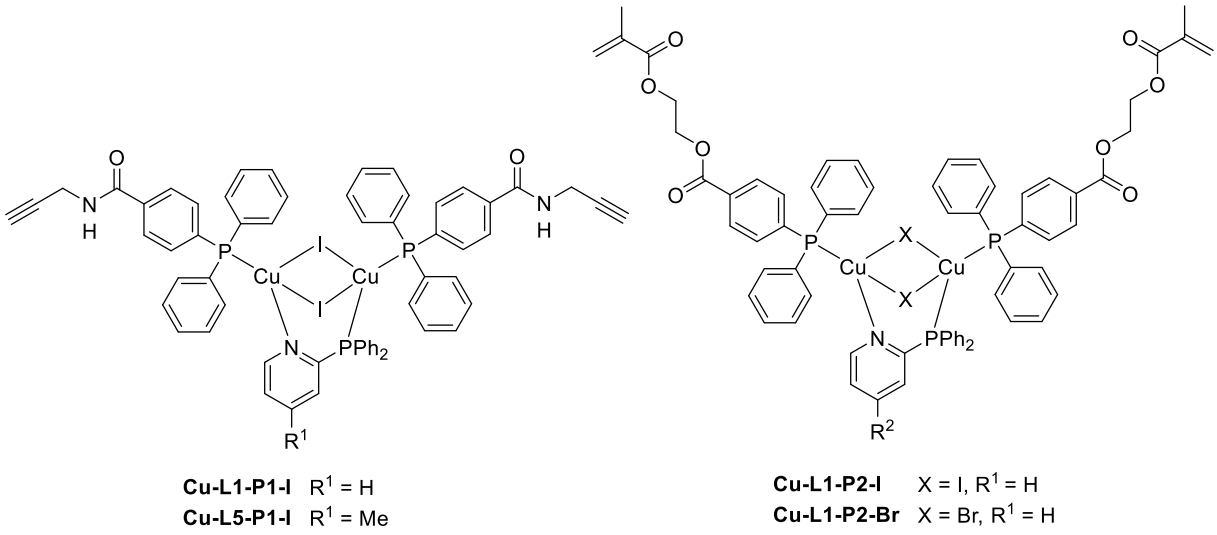

Figure 72. Overview of selected complexes for application in OLEDs.

For the initial optimization of devices, three different sets were fabricated as shown in Figure 73, each comprising an anode, a hole injection layer, the emitting layer, one or more electron transport or hole blocking layers, and a cathode. As anode, the widely used indium tin oxide (**ITO**) was used, followed by **PEDOT:PSS** as hole-injection layer. **PEDOT:PSS** consists of an aqueous mixture of the polymers poly-3,4-ethylenedioxythiophene and polystyrene sulfonate, which form a layer that is not washed away by subsequent depositions of layers from organic solvents. The following emissive layer consisted of the complex under investigation in either its neat form or dispersed at various concentrations with a host. The following evaporated layers were subsequently changed in all three sets: *Set 1* OLEDs consist of 2,4,6-tris(biphenyl-3-yl)-1,3,5-triazine (**T2T**) and 2,2',2''-(1,3,5-benzinetriyl)-tris(1-phenyl-1-H-benzimidazole) (**TBPi**) as electron transporting layers, in *Set 2* OLEDS only **TBPi** was used as single ETL, and in *Set 3* bis[2-(diphenylphosphino)phenyl]ether oxide (**DPEPO**) was included instead of **T2T**. **DPEPO** has electron-transporting and hole-blocking properties and is therefore able to better confine the triplet excitons. For all three sets, the cathode consisted of lithium fluoride and aluminum (LiF/Al), which additionally protects the device from atmospheric water and oxygen for the short time required for measurements (~5 minutes). The overlap of the **ITO** and Al electrodes defined individual pixels of 2×2 mm, two 2×4 mm, and one 4×4 mm on each individual device (photo Figure 74), of which the one with the best performance is typically reported.

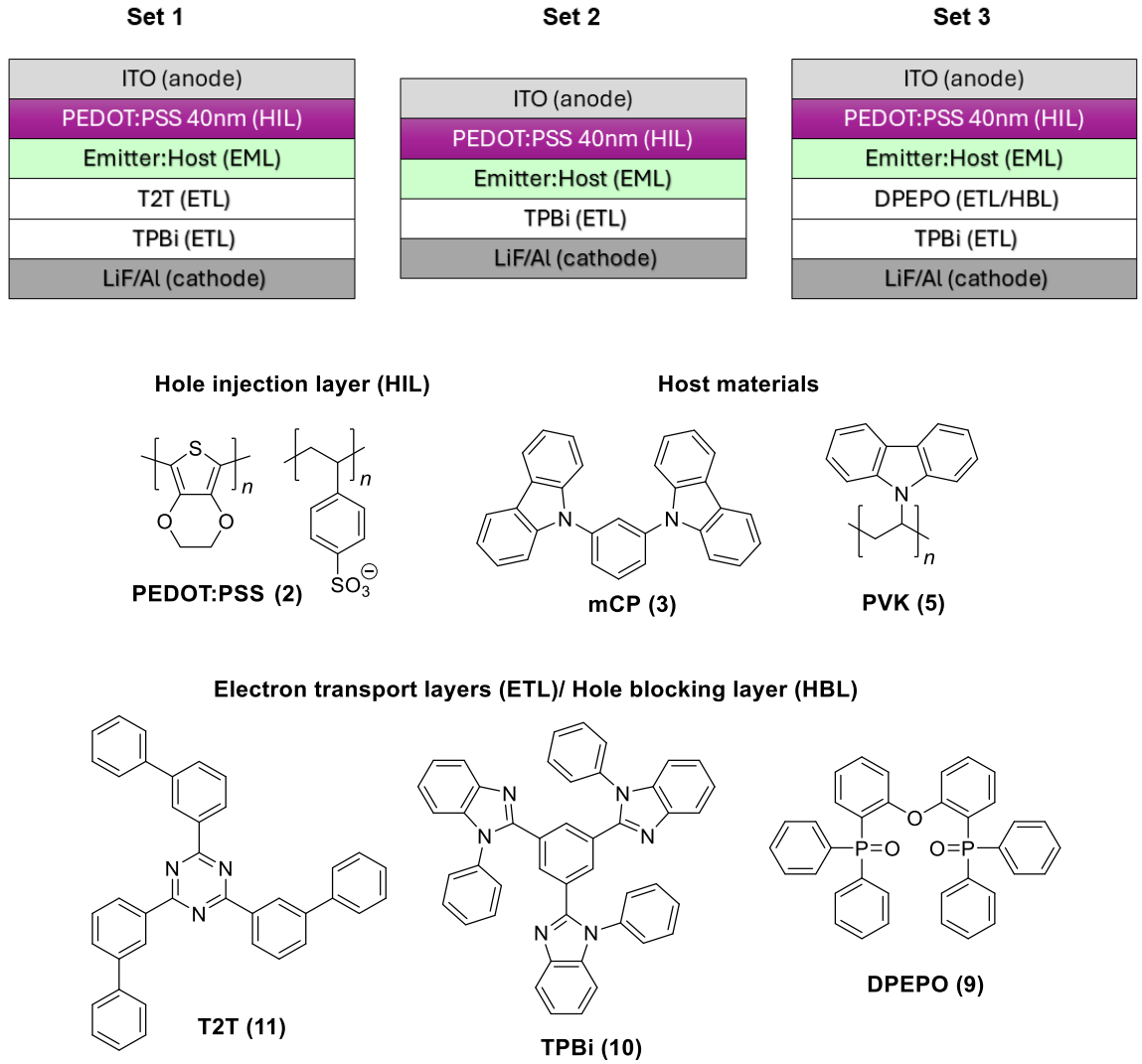

Figure 73. Overview of the general OLED structures of Set 1-3 and used materials for HIL, host and ETL.

The OLEDs were first optimized by screening various experimental parameters in the EML, such as different spin-coating speeds, solvents, annealing times, and concentrations. The main focus was on abundant reference material **Cu-L1-P1-I**, which is why the following optimization is based on this complex. For further optimization, different host materials in the emitting layer (EML), and different electron transport and hole blocking layers were also screened. At the time of writing, the envisioned crosslinking of device EML using these complexes has not yet been attempted, as this would require use of specially designed hosts with additional polymerizable functional groups. This work with standard host materials (of similar chemical structures) forms the important foundation for manufacturing more complex system, e.g. self-polymerizable hosts. In this context, attempts were made to synthesize a crosslinkable version of **mCP** and **PYD-2Cz**, which is discussed in the next subchapter.

An overview of all fabricated OLEDs, with processing details, is given in the experimental part, using the naming conventions based on the aforementioned sets, *e.g.* OLED 1.x, OLED 2.x or OLED 3.x.

Optimization of EML with Cu-L1-P1-I. To enhance the film properties of the EML, the spin-coating process was optimized throughout all sets. Both dynamic (deposit while spinning) and static spin-coating (deposit, then spin) with different settings for substrate rotation (2000-4000 rpm) were tested to obtain different layer thicknesses. The best films were achieved using dynamic spin coating at 3000 rpm (100 µl; 10 mg/ml) and then applied for different solvents (chlorobenzene, toluene, dichloromethane and chloroform). Chlorobenzene resulted in films with a uniform appearance with the best external quantum efficiency (EQE_{max}) being 3.6%. However, when using dichloromethane or chloroform the device performances could be increased significantly to EQE_{max} values between 6 and 9%. Toluene resulted in nice-looking films, with performances between 2 and 4%. Annealing the films after spin-coating only had a minor effect, with the best results obtained when annealing the DCM film for five minutes at 70 °C.

A small molecule and polymeric hosts featuring carbazole were investigated as host materials. As a small molecule host, **mCP** was selected as it exhibits a low-lying HOMO energy of -5.9 eV and is widely used as host material for phosphorescent metal-organic emitters and is moreover suitable for solution-processing in organic solvents. As a polymer host, **PVK** was selected as it has a similar carbazole-based backbone and also a low-lying HOMO energy of -5.8 eV, while its physical properties as a polymer can often lead to better film-forming processes. From a chemical perspective, the carbazole scaffold on both hosts offers opportunities for chemical modifications, which could be explored for future crosslinking approaches. However, **PVK** proved to be non-suitable concerning performance, as only one of six fabricated OLEDs turned on at all with an EQE_{max} below 1%. Therefore, the main part of the research visit refocused on using **mCP** as host material. It should be noted, that for complexes containing **P1**, a concentration of 50 wt% was mostly used in anticipation of future crosslinking approaches. In contrast, complexes with **P2** were mostly tested without any host material, as they have the potential to self-crosslink. However, to allow for comparison with commonly reported solution-processed OLEDs, lower concentrations of emitter doping (3, 10 and 20 wt%) were also explored. All obtained OLEDs had similar properties regarding the EQE_{max} (~ 6%). However, a trend could be observed for the turn-on voltage, which significantly increased for lower concentrations.

For instance, using the following architecture:

ITO | PEDOT:PSS (40) | **Cu-P1-L1-I**:**mCP** | DPEPO (10) | TPBi (40) | LiF (1) | Al (100),

the turn-on voltages differed from 7.5 V for 3 wt% and 10 wt% to 4.5-5 V for 20 wt% and 50 wt%. This indicates that the copper complex itself likely contributes to electron conductivity in the EML, with hole mobility known to be supported by carbazole-containing hosts.[223]

Optimization of ETL. The first set of devices included **T2T** as the electron transport layer. The EQE_{max} obtained in this set ranged from 2.2% to 3.6% with turn-on voltages (V_{on}) between 7.5 and 8.0 V. The highest performance was obtained for the following architecture of *OLED 1.3*:

ITO | PEDOT:PSS (40) | **Cu-L1-P1-I**:mCP (50 wt%) | **T2T** (5) | TPBi (40) | LiF (1) | Al (100)

The EQE_{max} has a peak at a luminance of 100 cd m^{-2} but shows a strong roll-off afterwards (Figure 75, blue).

By using the same stack architecture but without **T2T** and using DCM as solvent for the EML, the device performance was further increased. For this *Set 2*, the highest EQE_{max} was 6.7% (V_{on} = 5.0-7.0 V) with an emission maximum at 541 nm for *OLED 2.2* with the following architecture:

ITO | PEDOT:PSS (40) | **Cu-L1-P1-I**:mCP | **TPBi** (40) | LiF (1) | Al (100)

The OLED showed a high maximum luminance L_{max} = 2500 cd m^{-2}. Compared to *OLED 1.3* a roll-off effect was mostly seen after ~1000 cd m^{-2} during operation. The electrical device properties for this OLED are shown in Figure 74 and Figure 75 (orange).

The best performances for **Cu-L1-P1-I** were obtained in the devices of *Set 3* by including DPEPO as an alternative ETL/HBL after the emitting layer for the following architecture:

ITO | PEDOT:PSS (40) | **Cu-L1-P1-I**:mCP | **DPEPO** (10) | TPBi (40) | LiF (1) | Al (100)

In this set, for most OLEDs EQE_{max} values in the range of 6% were obtained. However, the best result for all fabricated OLEDs was found for *OLED 3.2* with **Cu-L1-P1-I** in a concentration of 50 wt% doped **mCP** emitting layer, using DCM as solvent, and **DPEPO** as an additional layer, giving an EQE_{max} of 8.9% (V_{on} = 5.0 V). *OLED 3.2* shows a high L_{max} of ~5000 cd m^{-2} with an emission maximum of 538 nm. However, an efficiency roll-off is observed from ~2000 cd m^{-2} onwards. The device performance of the three OLEDs, *OLED 1.3, OLED 2.2, and OLED 3.2* is comparably shown in Figure 74 and Figure 75.

Moreover, the electroluminescence spectrum, corresponding CIE plot, and a picture of the turned-on device of *OLED 3.2* are shown in

Figure **76**.

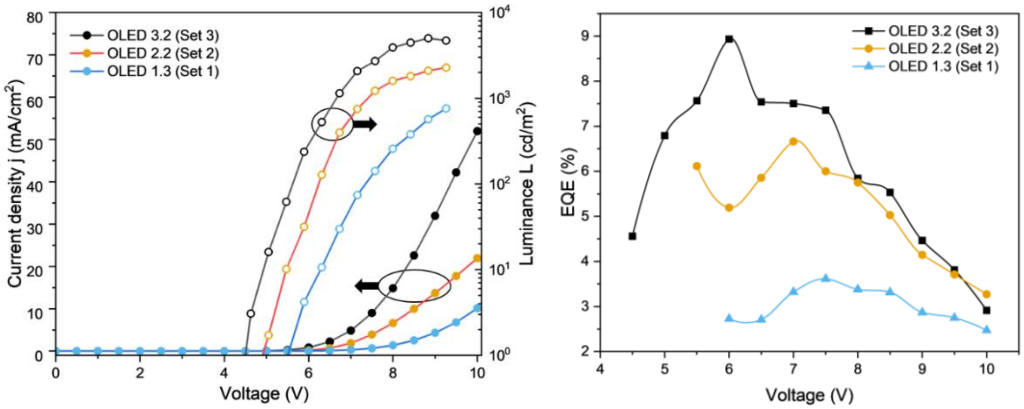

Figure 74. Device performance for *OLED 1.3*, *OLED 2.2* and *OLED 3.2* of **Cu-L1-P1-I** with 50 wt% **mCP**. Left: Current density-voltage-luminance (JVL) curves. Right: external quantum efficiency (EQE) vs voltage plot.

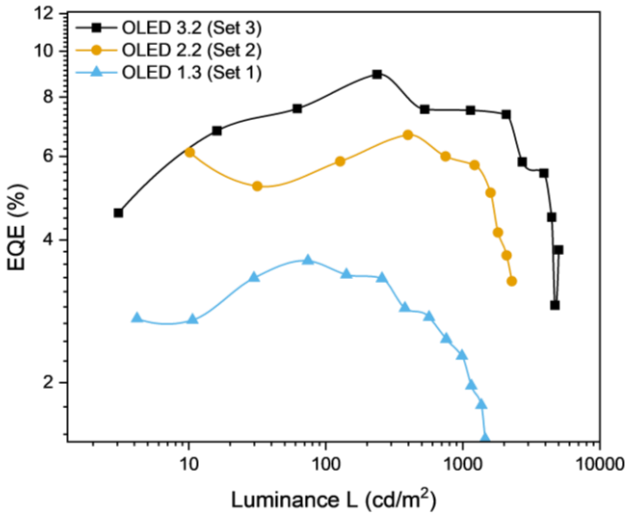

Figure 75. Device performance for *OLED 1.3*, *OLED 2.2* and *OLED 3.2* of **Cu-L1-P1-I** with 50 wt% **mCP** as external quantum efficiency (EQE) vs luminance plot.

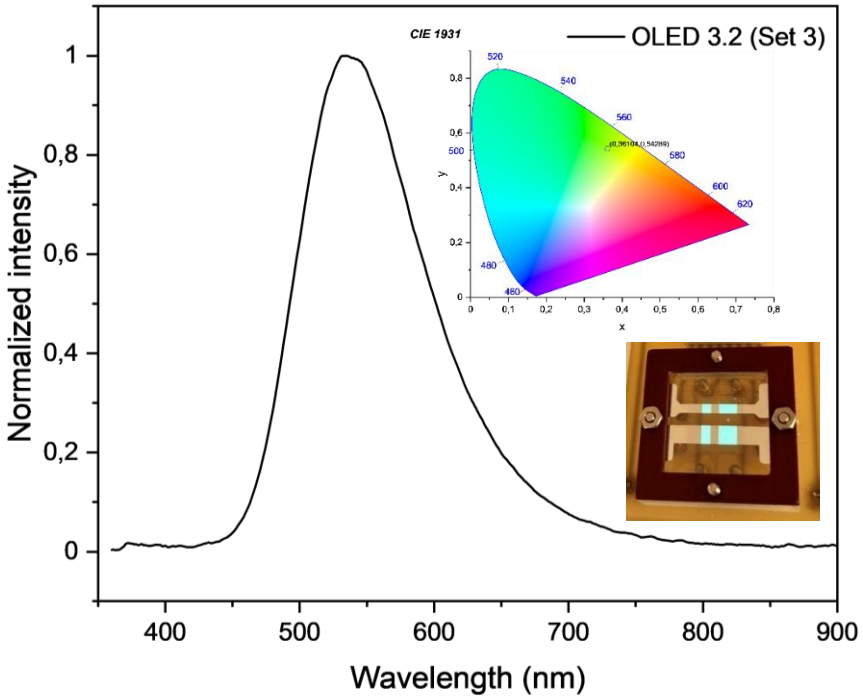

Figure 76. Normalized electroluminescence spectra, CIE plot, and picture of the turned-on device of *OLED 3.2.*

The obtained results lie in an expected range, when compared to other devices containing solution-processed Cu(I) complexes.[42, 59, 224-226] For instance, WALLESCH *et al*. introduced devices exhibiting a similar butterfly-type complex (tris-*m*-tolylphosphine)$_2$(L5)Cu$_2$I$_2$, which resulted in an EQE$_{max}$ of ~8% for a neat EML and of 11.4% for an optimized device using **PYD-2Cz** as a small molecule host.[227] Moreover, a variety of butterfly complexes was recently studied by BUSCH, which resulted in comparable data. [41, 63]

The enhanced performance of *OLED 3.2* may be attributed to the use of **DPEPO**, which additionally serves as a hole blocking layer. This seems to be a crucial factor in confining the excitons on the EML and ensuring they can contribute to the emission. Moreover, a trend of higher current density can be observed for *Set 3* devices, which suggests that **DPEPO** leads to better electron injection into the emissive layer.

Since *OLED 3.2* showed the best performance, two similar devices, *OLED 3.25* (20 wt% doped **mCP**) and *OLED 3.26* (50 wt% doped **mCP**), were produced with **Cu-L5-P1-I**. *OLED 3.25* resulted in an EQE$_{max}$ of 6.4% (V_{on} = 7 V), and *OLED 3.26* in an EQE$_{max}$ of 1.7% (V_{on} = 7.5 V). It should be noted that due to time constraints, these two devices were only produced once. Hence, intra-batch variability cannot be excluded as a contributor to these low values for *OLED 3.26.*

For **Cu-L1-P2-Br**, OLEDs with layer architecture matching *Set 1* and *Set 3* and EML with **mCP** as host (20 wt% and 50 wt% emitter) were produced.

For *Set 1*, the best EQE_{max} was 1.6%, compared to *Set 3*, which resulted in *OLED 3.23* and *OLED 3.24* with an EQE_{max} of 2.5 and 3.3% for 50 wt% and 20 wt%, respectively.

For **Cu-L1-P2-I**, the second highest performance of all OLEDs was found using the *Set 3* stack with a concentration of 20 wt%. An EQE_{max} of 8.5% (V_{on} = 8 V) was obtained with luminances of up to 5900 cd m^{-2}. Towards crosslinkable emissive layers, several OLEDs were made for all three sets with an undoped EML. However, *Set 3* resulted in the best-performing device, *OLED 3.14* with an EQE_{max} of 5%. Additionally, as the solution-phase crosslinking experiment for **Cu-L1-P2-I** resulted in an insoluble compound after UV curing, various attempts were made to self-polymerize the solid layer after spin-coating with UV-light. Unfortunately, the available UV-chamber (designed for substrate cleaning) was too strong and rapidly destroyed the complex films. Figure 77 shows the outcome of 30 seconds UV curing, where the top films are pristine spin-coated films of the complex, and the bottom are equivalent films after UV curing.

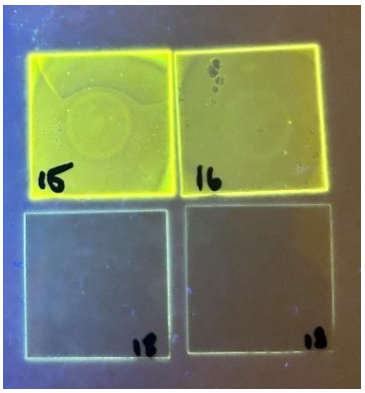

Figure 77. Self-polymerization experiment of neat films of **Cu-L1-P1-I** with UV curing of 30 seconds. Top: spin-coated films before UV from toluene (15) or DCM (16). Bottom: equivalent films after UV exposure.

Since **mCP** was successfully used as small-molecule host for these emitters, attempts have been made to include an azide functionality to enable a possible crosslinking between the host and the complex. **PYD-2Cz** was also used as an additional host, as it shows similar electrical properties as **mCP**. The synthesis approaches for these modified hosts will be discussed in the outlook.

3.4.2 3D-Laser nanoprinting *via* two-step absorption

Given the successful outcome of the self-polymerization experiment for **Cu-L1-P2-I**, the complexes of the series **Cu-L1-P2-X** and **Cu-L5-P2-X** with X = I, Br, Cl were evaluated as photoinitiators in 3D laser nanoprinting in collaboration with Aleksandra Vranic (KIT).

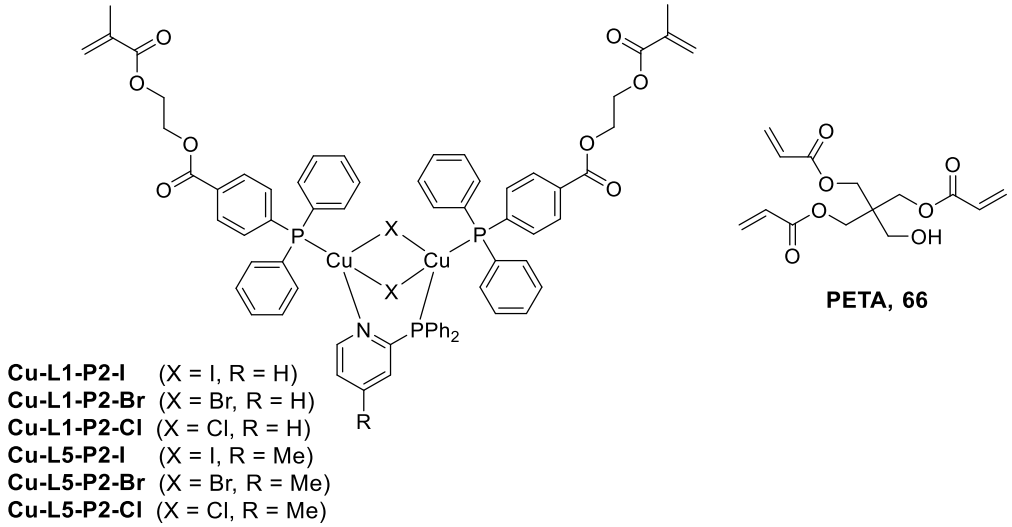

Figure 78. Overview of tested complexes in 3D laser nanoprinting and structure of used monomer PETA.

For this purpose, a photoresist is prepared by adding the respective complex to the viscous monomer PETA (**66)** with a concentration of 50 mM and without any further additives. Subsequently, the photopolymerization is conducted through precise irradiation of a 780 nm femtosecond pulsed laser into selected areas of the photoresist, which causes the photopolymerization of the photoresist and the creation of 3D structures. The complexes were investigated by using two printing methods: two-step absorption[100-101] and two-photon absorption.[228] However, only the latter process led to printable structures in these cases.

The first challenge is always the solubility in **66**; since complexes containing ligand **P1** were not soluble in **66**, no further investigations of their suitability in 3D laser nanoprinting were performed. Nevertheless, the majority of the complexes with **P2**, except complex **Cu-L5-P2-Br** and **Cu-L5-P2-Cl**, were successfully dissolved in **66**. Further experiments regarding the concentrations of **Cu-L5-P2-Br** and **Cu-L5-P2-Cl** are still being analyzed at the time of this thesis was completed. Complexes **Cu-L1-P2-I**, **Cu-L1-P2-Br**, **Cu-L1-P2-Cl**, and **Cu-L5-P2-I** were successfully used in the printing process. Additionally, a printing experiment with the plain ligand **P2** and **66** is planned to study the impact of the complexes on the polymerization process.

All complexes were printed in good resolutions in the two-photon experiment; however, the highest resolution was obtained for **Cu-L1-P2-Cl**.

Figure 79 depicts the scanning electron microscopy (SEM) pictures for the printed structures with **Cu-L1-P2-Cl**. In the pictures, it is displayed, that a stable structure (side view) was printed with visible details in the nanometer range (zoomed in picture, Figure 79). Most importantly, the lines thickness is evenly distributed in x, y and z direction.

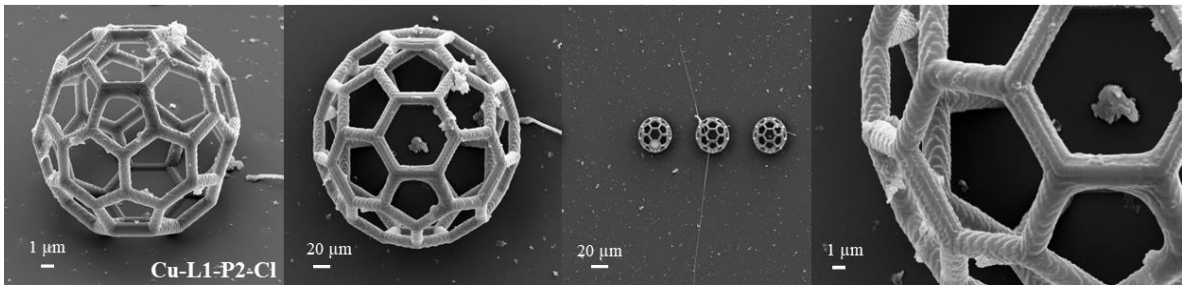

Figure 79. SEM image of the printed structures with **Cu-L1-P2-Cl**. Pictures provided by Aleksandra Vranic.

The printed structures for **Cu-L1-P2-Br** and **Cu-L5-P2-I** are depicted in Figure 80. Also, for these two complexes, the side view illustrates, that a stable structure was obtained. For **Cu-L1-P2-Br** again, details in the nanometer range can be observed.

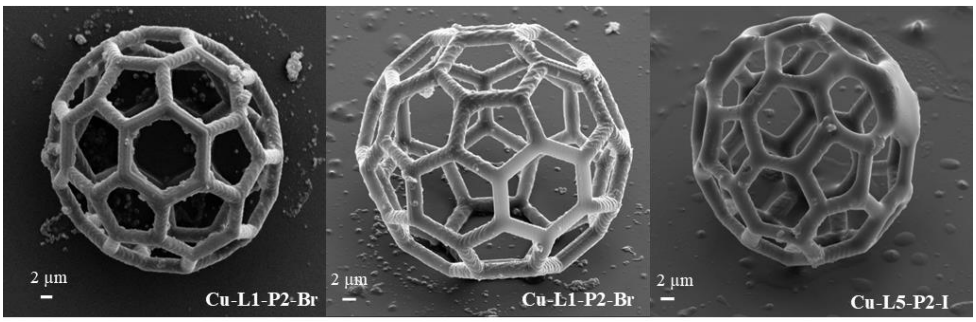

Figure 80. SEM image of the printed structure with **Cu-L1-P2-Br** and **Cu-L5-P2-I**. Pictures provided by Aleksandra Vranic.

The structures of **Cu-L1-P2-I** showed the lowest overall resolution, but still stable structures, as depicted in Figure 81.

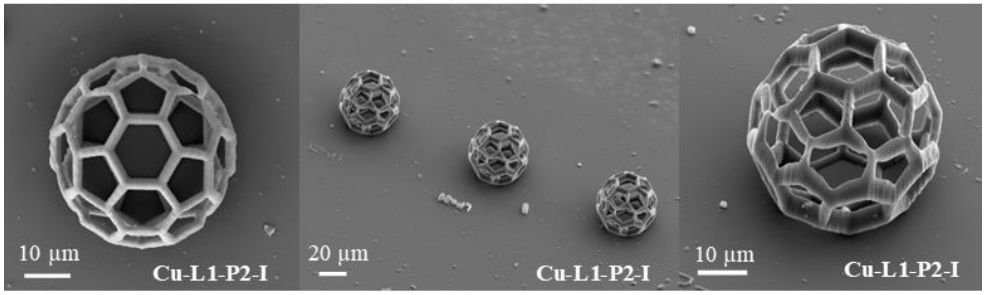

Figure 81. SEM image of the printed structure with **Cu-L1-P2-I**. Pictures provided by Aleksandra Vranic.

Since the printing was successfully conducted without further additives, the complexes are proposed to function as photoinitiators. Moreover, given that the complexes possess crosslinkable functionalities, it is highly probable that they also function as a monomer and

crosslink with **66** to form the 3D structures. However, this remains to be determined and should be investigated in future research. Although acrylates are well known in the literature for their polymerization properties,[94, 229] and even **P2** was used in polymerization already,[206] the here presented results are exceptional when compared to Cu(I) complexes that have been utilized in the context of 3D laser printing in previous literature. The described complexes in the literature predominantly rely on cationic mononuclear complexes, which function as photosensitizers or coinitiators in photoinitiating systems with several additives.[97]

To sum up, the butterfly complexes with **P2** were successfully employed as photoinitiators in a two-photon 3D laser nanoprinting process with **66** as a monomer. Further research should be performed to determine whether the complexes are solely acting as photoinitiator or to what extent they also act as monomer. Furthermore, it is essential to investigate if the complexes remain intact after polymerization and whether the printed structures exhibit luminescent properties. This would especially be promising in the context of printable OLEDs.

4 Summary and Outlook

In this thesis, three projects were completed, each targeting new neutral copper(I) halide complexes. The first two projects concentrated on exploring the coordination chemistry and photophysical properties of these new complex structures, whereas the third part aimed to further develop the well-studied dinuclear butterfly-type complex for a future use in crosslinking applications, such as solution-processed OLEDs or 3D laser nanoprinting.

4.1 Neutral complexes featuring 3-pyridyl phosphine

Summary. Targeting copper(I) complexes, the coordination properties and formed structures using 3-PyrPhos (**L2**) as bridging ligand were investigated. Various ratios of **L2** with different copper(I) halides (X = I, Br, Cl) were applied through an established synthesis route, by combining **L2** with the respective copper(I) salt. An overview of the obtained structures is given in Scheme 14. In some cases, ancillary phosphine ligands, such as triphenylphosphine, were added. The most promising structure, a dinuclear complex, $Cu_2X_2L_4$ (**Cu-L2-X**), was obtained by employing an excess of **L2** in a 3:1 (= 6:2) ratio.

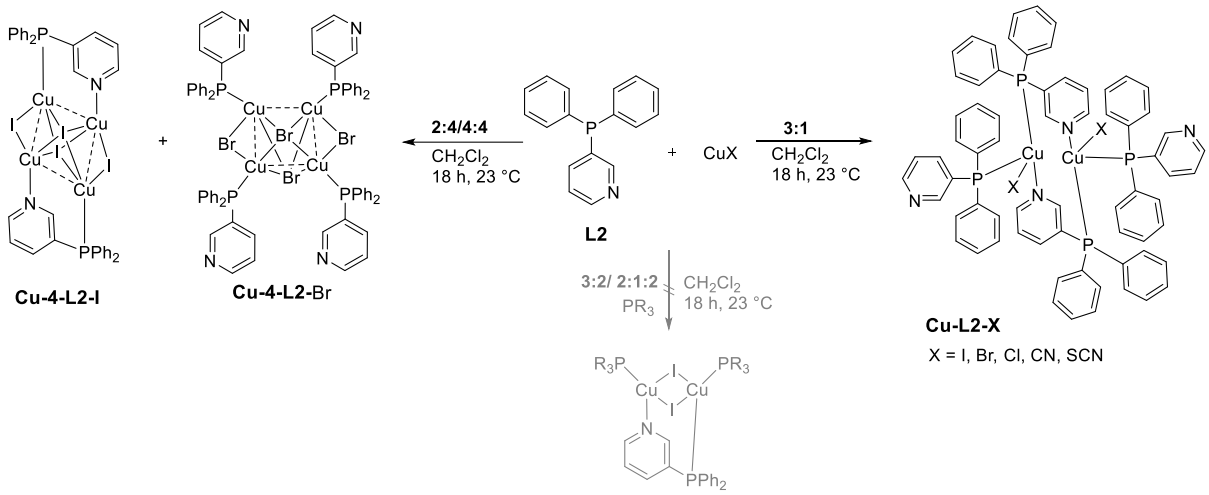

Scheme 14. Overview of the ratios, that were applied using **L2** and CuX salts to obtain tetranuclear and dinuclear structures.

Single crystal analysis confirmed the structures for **Cu-L2-I**, **Cu-L2-Br**, and **Cu-L2-Cl**, revealing an open-core structure where two ligands **L2,** act as bridging ligands, to form a structure reminiscent of a metacyclophane, as well as two monodentate ligands (Figure 82). Notably, all three structures demonstrated an extraordinarily large Cu···Cu distance, with an average distance of 6.238 Å, a separation that has not been observed in any other dinuclear structures of similar structures.

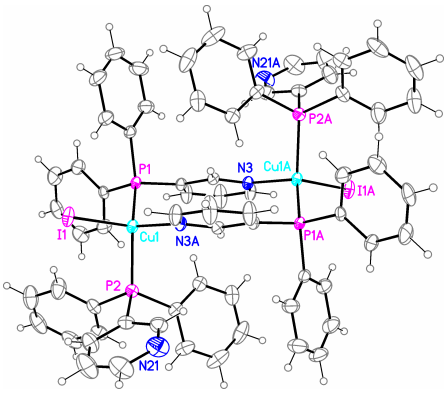

Figure 82. Molecular structure of **Cu-L2-I** from single-crystal X-ray diffraction (ellipsoid at 50% probability level). Solvent molecules are omitted for clarity.

Theoretical and detailed photophysical studies were conducted in collaboration with Anna Mauri (KIT, INT) and Daniel Marhöfer (RPTU) for all five complexes. The calculations indicated an (M+X)LCT character upon excitation, with the HOMO localized on the copper centers and the ancillary ligands, while the LUMO was found on the bridging ligands, giving HOMO-LUMO gaps between 3.3 and 4.0 eV. Photophysical measurements revealed excitation-dependent emission behavior.

Temperature-dependent studies demonstrated typical TADF behavior for longer wavelengths (λ_{ex} > 380 nm), with emission wavelengths between 523 nm and 566 nm at 298 K and an observable red shift at 5 K, resulting at emission maxima between 551 nm and 576 nm. Under shorter excitation wavelengths (λ_{ex} = 355 nm), most complexes displayed a blue shift in their emission maxima at room temperature, with increasing intensity at lower temperatures. However, no significant shift in the emission was observed at 5 K. These findings suggest the involvement of a higher-lying excited state. Figure 83 depicts the spectra exemplarily for **Cu-L2-Br**.

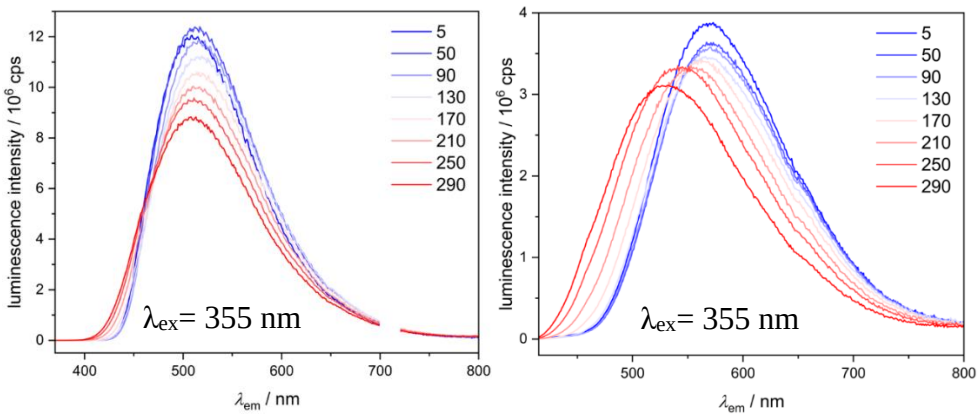

Figure 83. Luminescence spectra of **Cu-L2-Br** at λ_{ex}= 355 nm (left) and λ_{ex}= 400 nm (right) in a sintered KBr pellet between 5 and 290 K. Results provided by Daniel Marhöfer (RPTU).

To sum up, the novel class of dinuclear **3-PyrPhos** complexes represents an intriguing new complex type. The two ancillary ligands allow for facile derivatization, which was demonstrated successfully. At the same time, the emission properties can potentially be tuned by modifying the bridging ligands, as these dominantly influence the LUMO energy. These features make this complex class a highly promising material for applications in OLEDs or sensors. Additionally, the ligand **L2** was similarly reacted with different silver(I)-halides (AgI, AgBr, AgCl), yielding three novel silver(I) complexes of the general type $Ag_4X_4(L2)_4$, which crystallized in a cubane-like structure.

Outlook. The dibridged copper(I) complex structure presents an opportunity to replace the ancillary ligands with other phosphine-based ligands, as illustrated in Figure 84. Successful derivation has already been achieved with triphenylphosphine. Future projects should focus on incorporating more solubilizing phosphine ligands to further evaluate the impact of this ligand exchange, on the resulting chemical and photophysical properties. Another interesting modulating point is the incorporation of further bridging ligand derivatives to understand their influence on the emission behavior. Most importantly, the origin of the observed emission at lower excitation wavelength in this complex class should be addressed. Therefore, additional measurements, such as time-resolved photoluminescence or time-resolved FTIR spectroscopy, are necessary.

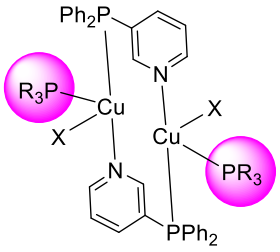

Figure 84. Illustration of exchangeable positions, highlighted *via* violet spheres.

4.2 Mononuclear complexes featuring (iso)quinoline ligands

In the second project, two neutral mononuclear complexes featuring quinoline (**L4**) and isoquinoline phosphine (**L4i**) based ligands were synthesized in a 3:1 ratio with copper(I) iodide. Both complexes were structurally characterized through single-crystal analysis, and their photophysical properties were investigated in a 1 wt% PMMA film. The experimental findings were supported by theoretical calculations of the ground and excited states in collaboration with Christof Holzer (KIT, TFP).

The structure revealed that **Cu-L4-I** consists of three ancillary ligands, resulting in a distorted tetrahedral geometry, while **Cu-L4i-I** has two ancillary ligands, leading to a distorted trigonal geometry. For **Cu-L4i-I**, broad emission in the red region was detected, with blue shifted shoulders if exciting at a lower wavelength. This behavior was even more pronounced for **Cu-L4-I**. The measured lifetimes were 2.82 µs for **Cu-L4-I** and 3.02 µs for **Cu-L4i-I**. Additionally, a short component lifetime of 2.37 ns was recorded for the emission maxima at 520 nm for **Cu-L4-I**, suggesting a contribution of ligand-centered fluorescence. In future studies, low-temperature photoluminescence measurements should be conducted to confirm the presence of a TADF mechanism for these complexes. Moreover, the influence of the used ligands on the formed structures should be studied in more detail, to identify the structure-property relationship.

4.3 Crosslinkable copper(I) complexes

Summary. This project aimed to include crosslinkable functionalities into copper(I) complexes, specifically terminal alkynes or methacrylate moieties, to eventually test them in autocatalyzed crosslinking reactions, such as CuAAC or photopolymerization. A range of crosslinkable ligands, based on pyridines and phosphines, were synthesized and subsequently reacted with copper(I) halides to obtain mono-, di- and tetranuclear neutral copper(I) complexes. An overview of the obtained complexes is given in Figure 85.

The primary objective was to develop highly soluble complexes that could transition into an insoluble product after crosslinking. This approach aims to enhance solution-processing in OLEDs by ensuring that the deposited layer becomes insoluble, thus allowing for better solvent orthogonality of the subsequent layers. Initial experiments demonstrated that for **Cu-L1-P2-I**, an insoluble product was formed after treating the compound in DCM with UV irradiation for 30 minutes, without further additives, notably without any visible color change This finding indicates that the complex participates in the photopolymerization, not only as monomer but also as photoinitiator. Moreover, some preliminary click-reactions involving either azides/diazides or thiols/dithiols with selected alkyne-containing complexes resulted in insoluble precipitates. However, most of these reactions demonstrated a noticeable color change, making further studies essential. Overall, these results strongly suggest that the envisioned strategy for the complexes generally works and that they undergo autocatalytic photopolymerization without additives.

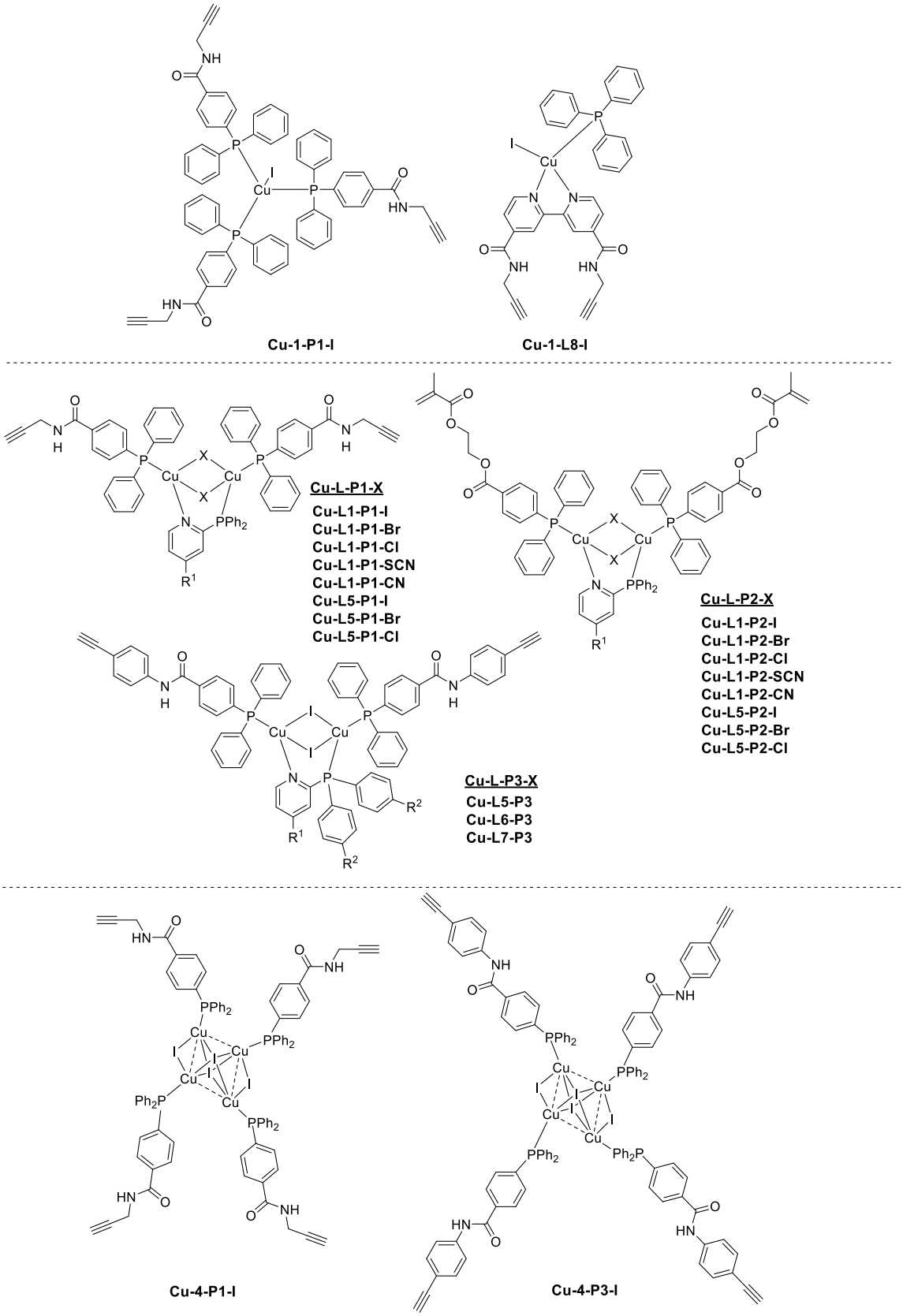

Figure 85. Overview of obtained complexes featuring either a terminal alkyne or a methacrylate unit.

All non-crosslinked complexes demonstrated excellent solubilities, with the dinuclear complexes standing out in particular, as their solubilities exceeded 20 mg/ml in chlorobenzene

and dichloromethane. All complexes, except for **Cu-1-L8-I**, were photophysically characterized in 1 wt% doped PMMA films, resulting in extraordinarily high PLQYs of over 94% for **Cu-4-P1-I**, **Cu-L1-P1-I**, **Cu-L5-P2-I** and **Cu-L5-P3-I**. The emission maxima were observed between 500 and 600 nm, primarily around 550 nm, with lifetimes ranging from 3.38 to 9.39 µs for the dinuclear complexes. In contrast, the mono- and tetranuclear complexes exhibited blue shifts in their emission, towards 476 to 499 nm, with lifetimes between 7.11 and 11.7 µs. A trend for the used halides was observed, showing an increased red shift in the following order: SCN<I<Br<Cl. For instance, **Cu-L1-P1-SCN**, demonstrated the most significant hypsochromic shift among all dinuclear complexes, with an emission maximum of 501 nm. Iodo complexes showed the lowest lifetimes along with the highest PLQYs, which might be attributed to increased spin-orbit coupling (SOC) due to the heavier iodine atoms. The changes in emission lifetimes, along with variations in the PLQYs under air and nitrogen, strongly support an underlying TADF emission mechanism. This was further supported by low-temperature measurements for **Cu-L1-P1**. In summary, these complexes represent a highly promising class of emitting materials for applications in OLEDs, particularly for solution-processing, given their excellent solubility in various solvents.

The experimental results were supported by theoretical calculations of the ground and excited states for **Cu-L1-P1-I** and **Cu-L1-P2-I**, as well as the click product from **Cu-L1-P1-I** with benzylazide **51a**. The calculations indicated HOMO-LUMO gaps around 4.00 eV and ΔE_{ST} values of 0.054 eV for **Cu-L1-P1-I**, 0.043 eV for **Cu-L1-P2** and 0.06 eV for **Cu-L1-P1-I-BnN$_3$**.

***Outlook*.** From a chemical point of view, the structural diversity of copper(I) complexes holds nearly limitless potential for creating novel complexes. Given the ligand's highly promising crosslinking features, future projects should aim to explore novel structures to exploit the potential in further applications. Figure 86 provides an overview of several target structures that were initially explored but remain challenging to isolate and were therefore omitted from this thesis.

For example, bipyridines are often used in cationic complexes, as in **67** and **68**, making **L8** a potential ligand for similar structures. Another promising complex structure reported in the literature is demonstrated by **70**, showing blue luminescence and a high PLQY of 92% for the respective CuBr complex.[230] Attempts were made to synthesize similar mononuclear complexes with the general structure of **71** using ligands **P1** and **P2**, resulting in sky-blue to green emissive powders that were not fully characterized to date. This structure could also be

approached with **P3**. Furthermore, the bridging ligand **L7 (**6-(diphenylphosphaneyl)-N-(prop-2-yn-1-yl)nicotinamide) should be investigated as a bridging ligand in butterfly complexes such as **71**, as it may significantly influence the emission properties. Given that **L7** is a bridging ligand itself, it opens up the possibility of incorporating additional PP-bridging ligands in place of two ancillary phosphine ligands, enhancing the complexes' structural rigidity.

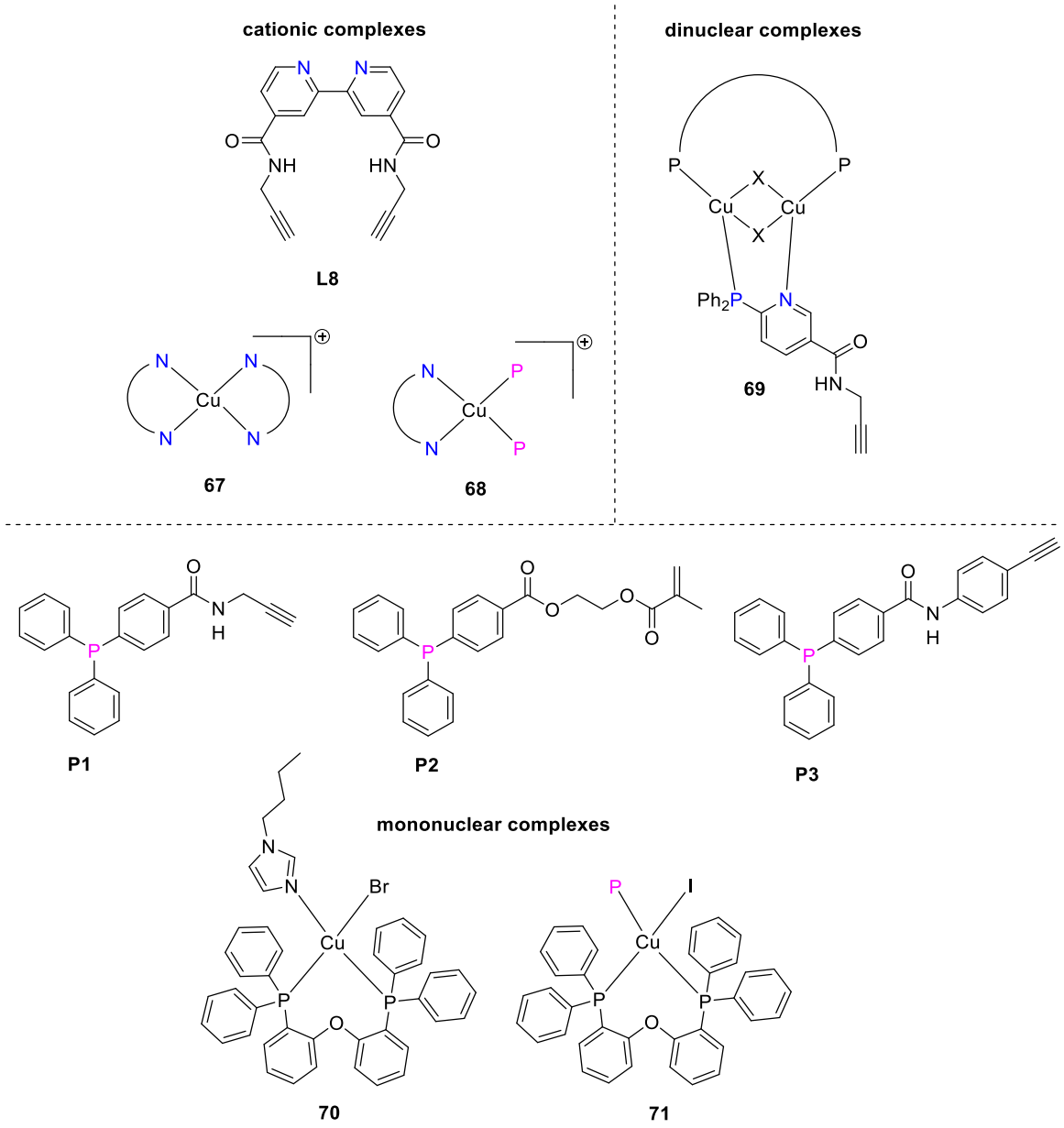

Figure 86. Overview of possible structures aimed at future projects with crosslinking ligands.

NHC ligands represent a highly promising ligand class and already resulted in efficient complexes in the literature.[125, 131] Therefore, initial efforts were made to replace the monodentate phosphines with NHC-ligands derived from benzimidazole scaffolds.

To bridge this thesis's first and third projects, established NHC-ligands based on benzimidazolium salts, featuring terminal alkynes were already used to form butterfly

complexes, resulting in red emitting powders, although full characterization is still pending. NHC ligands offer a range of possible structures by substituting the phosphine ligands. However, deprotonating the imidazolium salt is crucial and presents challenges, especially when terminal alkynes are involved. Addressing these challenges in future reaction condition optimizations will be essential for achieving a controlled complex synthesis.

Most importantly, the crosslinking experiments require further optimization. Key parameters, such as the need for an initiator, optimal temperature, concentration, and choice of solvent, must be carefully evaluated. The resulting precipitates should be fully characterized, and the effect of the crosslinking on the complexes' photophysical properties should be systematically explored.

4.4 Applications

The dinuclear complexes **Cu-L1-P1-I**, **Cu-L5-P1-I**, **Cu-L1-P2-I** and **Cu-L1-P2-Br** were selected as representative complexes for the fabrication of solution-processed OLEDs during an international research stay at the University of Durham (UK). Furthermore, given that the methacrylate containing complex **Cu-L1-P2-I** showed self-polymerization upon UV exposure in initial crosslinking experiments, the dinuclear complexes featuring **P2** were successfully utilized as photoinitiators in 3D laser nanoprinting in collaboration with Aleksandra Vranic (Prof. Bräse/ Prof. Wegener).

4.4.1 Solution-processed OLEDs

A range of OLED architectures was fabricated and evaluated on their performance. In general, three primary OLED stacks were constructed (*Set 1-3*), which differed in the used electron transporting layer (ETL). *Set 1* included **T2T** and **TPBi**, *Set 2* exclusively used **TPBi,** and *Set 3* combined **DPEPO** with **TPBi**. The optimization of the overall OLED structure was conducted using **Cu-L1-P1-I**. Since the EML was fabricated by spin-coating, initial optimization aimed for good film properties by screening different solvents, spin-coating processes, and concentrations. Additionally, different host materials, in particular **PVK** and **mCP,** were tested. The **mCP** host proved to be suitable, whereas devices using **PVK** showed only weak efficiencies and low brightness, if any. By exchanging the ETL and using **DPEPO** (*Set 3*) instead of **T2T** (*Set 1*), superior devices regarding efficiency and luminance were obtained. Figure 87 illustrates the general OLED architecture for *Set 3* and presents the external quantum efficiency (EQE) versus luminance (L) plot for the best-performing OLED.

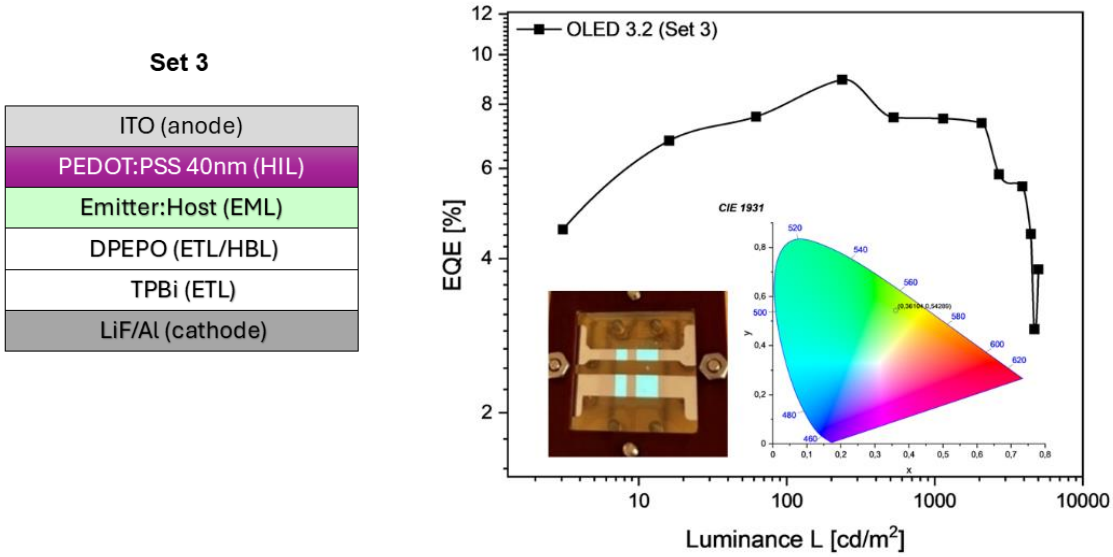

Figure 87. Left) Overview of the general OLED structures of *Set 3*. Right) Device performance for *OLED 3.2* of **Cu-L1-P1-I** with 50 wt% **mCP** as external quantum efficiency (EQE) vs luminance (L) plot. Additionally, the CIE plot and picture of the turned-on device are shown

The best performing OLED among all devices was achieved with the following architecture of *Set 3*:

ITO | PEDOT:PSS (40) | **Cu-L1-P1-I**:mCP | **DPEPO** (10) | TPBi (40) | LiF (1) | Al (100)

This device used an EML of 50 wt% **Cu-L1-P1-I** in **mCP**, resulting in an EQE_{max} of 8.9% (V_{on} = 5.0 V). It exhibited a high luminance L_{max} of approximately 5000 cd m^{-2} and an emission maximum of 538 nm. An efficiency roll-off was observed starting at around 2000 cd m^{-2}. Using **DPEPO** as a host seemed to have a significant impact, as higher current densities were observed, indicating improved electron injection into the emissive layer.

Outlook. Future work should prioritize the investigation of *in situ* crosslinking during OLED production, both for click reactions and direct polymerization, as this would allow for solution-processing of subsequent layers.

Since **mCP** was successfully used in this work as small molecule host OLED devices, attempts were made to include an azide functionality into the host scaffold to synthesize 1,3-bis(3-azido-9H-carbazol-9-yl)benzene **78a** for potential crosslinking with functionalized complexes. **PYD-2Cz** was modified in a similar way aiming for 2,6-bis(3-azido-9H-carbazol-9-yl)pyridine **78b**, as it shows similar properties, such as a good hole transporting ability and a high triplet energy level (3.03 eV) (Scheme 15). The introduction of the azide group was approached by treating the dibrominated intermediates with *n*-BuLi, followed by a reaction with tosyl azide. The dibrominated intermediates are reported in the literature and are, for instance, accessible *via* the nucleophilic aromatic substitution of the difluorinated precursor with 3-bromo-9H-carbazole

and potassium phosphate. FAB-MS analysis confirmed the mass of the target compound **78a**; however, the product isolation remains incomplete. Therefore, further optimization of the reaction conditions is essential.

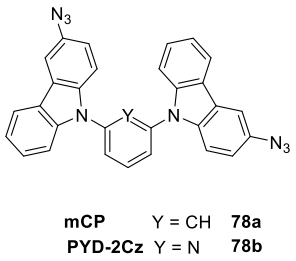

Scheme 15. Targeted structures of **78a** and **78b** based on **mCP** and **PYD-2Cz**.

4.4.2 3D-Laser Nanoprinting *via* two-step absorption

Summary. Complexes **Cu-L1-P2-I**, **Cu-L1-P2-Br**, **Cu-L1-P2-Cl**, and **Cu-L5-P2-I** were successfully used in 3D laser nanoprinting. Pentaerythritol triacrylate (PETA) was utilized as the monomer in a concentration of 50 mM without further additives. By employing a 780 nm femtosecond pulsed laser with a two-step absorption process, printed structures were created in the lower micrometer range, with thicknesses in the nanometer range. Among the complexes, **Cu-L1-P2-Cl** exhibited the highest resolution, with evenly distributed line thicknesses in the x, y and z direction. The respective scanning electron microscopy (SEM) images are shown in Figure 88.

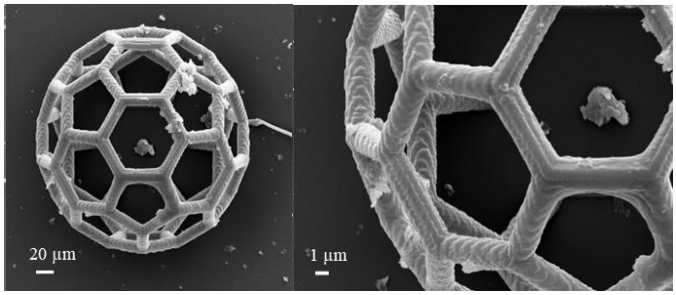

Figure 88. SEM image of the printed structures with **Cu-L1-P2-Cl**. Pictures provided by Aleksandra Vranic.

Outlook. The findings of the 3D nanoprinting still face some unresolved questions that must be addressed. For example, the mechanism of the photopolymerization remains unclear, and whether the complex functions solely as photoinitiator or also as a monomer is uncertain. Moreover, it should be investigated whether the complex structure remains intact in the printed structures, as this would, for example, open possibilities towards printable OLEDs. Future work should also involve using the plain ligand to determine the influence of the actual complex structure on the printing process.

5 Experimental section

5.1 General remarks – Materials and Methods

The starting materials, solvents, and reagents were purchased from abcr, Acros, Alfa Aesar, Apollo Scientific, Carbolution, ChemPUR, Fluka, Fluorochem, Merck, Riedel-de Haën, Sigma Aldrich, Strem, TCI, or Thermo Fisher Scientific and used without further purification unless stated otherwise.

The starting materials, (dry) solvents, and reagents were purchased from Acros Organics, Fisher Scientific, ABCR, Alfa Aesar, Merck, Sigma-Aldrich, Roth, or Riedel-deHaën and used without further purification. All solvents were purchased in HPLC grade. Solvents of technical quality were purified by distillation or with the solvent purification system MB SPS5 (acetonitrile, dichloromethane, diethyl ether, tetrahydrofuran, toluene) from MBraun.

All reactions with reagents sensitive to air or moisture were performed under argon with common Schlenk technique. Solvents were generally removed at preferably low temperatures (<50 °C) under reduced pressure with a rotary evaporator. Solvents for solvent mixtures were separately volumetrically measured. If not indicated otherwise, inorganic salts were used as aqueous, saturated solutions.

Flat-bottom crimp neck vials from ChromaGlobe with an aluminum crimp cap were used for certain reactions. Liquids were added with a stainless-steel cannula, and solids were added in powder form.

Reactions at low temperatures were cooled using shallow vacuum flasks produced by Isotherm, Karlsruhe, filled with a water/ice mixture for 0 °C, water/ice/sodium chloride for –20 °C or isopropanol/dry ice mixture for –78 °C. The reaction flask was equipped with a reflux condenser and connected to the argon line for reactions at high temperatures.

Flash column chromatography was performed using Merck silica 60 (0.040 × 0.063 mm, 230–400 mesh ASTM) and quartz sand (glowed and purified with hydrochloric acid). Reactions in liquid phase were controlled by analytical thin-layer chromatography (TLC) with aluminium silica gel plates from Merck (TLC Silica gel 60 F_{254}, d = 0.25 mm) with fluorescent quencher. Detection was performed by examination under UV light (λ = 254 nm & λ = 365 nm).

The RAYONET reactor Model RPR-100 with (16) 14W light bulbs (254 nm) was used to irradiate with UV light.

An Omnilux UV lamp (160W, 368 nm) was used for irradiation with a blacklight.

Nuclear magnetic resonance spectroscopy

NMR spectra were recorded at 21 °C using the following devices: ^{1}H NMR: BRUKER Avance 400 (400 MHz), BRUKER Avance 500 (500 MHz); ^{13}C NMR: BRUKER Avance 400 (100 MHz), BRUKER Avance 500 (126 MHz), ^{31}P NMR: BRUKER Avance 400 (162 MHz), BRUKER Avance 500 (202 MHz).

The NMR spectra were recorded in deuterated solvent from EURISOTOP, SIGMA ALDRICH, OR DEUTERO. The chemical shift δ were expressed in parts per million (ppm) and referenced to: chloroform-d_1, DMSO-d_6, and Chemical shifts δ chloroform-d_1 (^{1}H: δ = 7.26 ppm, ^{13}C: δ = 77.0 ppm), DMSO-d_6 (^{1}H: δ = 2.50 ppm, ^{13}C: δ = 39.5 ppm), CD_2Cl_2 (^{1}H: δ = 5.32 ppm, ^{13}C: δ = 53.8 ppm) and Pyridine-d_5 (^{1}H: δ = 7.58 ppm, ^{13}C: δ = 135.5 ppm). Centrosymmetrical signals were characterized through the median point; for multiplet signals the signal range was annotated. The signal structures are described with the following abbreviations: s = singlet, d = doublet, t = triplet, q = quartet, br. s = broad singlet, m = multiplet, dd = doublet of doublets, dt = doublet of triplets. All coupling constants are absolute values expressed in Hertz (Hz), with the largest values first. Spectra were measured as broadband and proton decoupled. Characterization of the ^{13}C NMR signals was done by DEPT techniques (distortionless enhancement by polarization transfer or with 2D NMR spectroscopy: ^{1}H-^{1}H COSY-Spectra (COSY = *Correlated Spectroscopy*), ^{1}H-^{13}C-HMBC-Spectra (HMBC = *Heteronuclear Multiple Bond Correlation*), ^{1}H-^{13}C-HSQC (HSQC = *heteronuclear single quantum coherence*).

The following abbreviations were used for aromatic proton/carbon signals CH_{Ar} and C_q for quaternary carbon atoms, CH_3 for methyl substituents, CH_2 for alkane units and CH_{Alkene} for alkene units.

Infrared spectroscopy (IR)

IR spectra were recorded on a Bruker Alpha T using ATR (attenuated total reflection) for solids. All samples were analyzed at 21 °C. The absorption is given in wave numbers $\bar{\upsilon}$ [cm^{-1}] and was measured from 3600 cm^{-1} to 400 cm^{-1}.

Mass spectrometry (FAB-MS, EI-MS, ESI-MS)

The mass spectra were measured on a FINNIGAN MAT 95 (70 eV) for EI-MS (Electron ionization mass spectrometry) or FAB-MS (Fast atom bombardment mass spectrometry) (with 3-nitrobenzyl alcohol (3-NBA) as matrix). ESI-MS (Electron spray ionization mass spectrometry) was conducted on a Thermo Scientific Q Exactive Plus. For the interpretation of the mass spectra, the molecular ion $[M]^+$, peaks of pseudo molecules, such as $[M + H]^+$, and characteristic fragments are indicated as mass per charge ratio (*m/z*), and their intensity given in percent, relative to the main peak (100%). The following high-resolution mass spectroscopy (HR-MS) abbreviations were used: calc. = calculated mass, found = mass found in the analysis.

Elemental analysis (EA)

Elemental analysis (EA) was performed on an Elementar vario MICRO instrument with a weight scale from Sartorius M2P. The calculated and found percentages for carbon, hydrogen, nitrogen, and sulfur are given in fractions of 100%.

Melting point

Melting points were measured on an OptiMelt MPA100 device from the STANFORD RESEARCH SYSTEM.

X-Ray structure analysis

The crystal structure determination was done in cooperation with Dr. Martin Nieger (University Helsinki) or Dr. Olaf Fuhr (KIT).

For structures from Martin Nieger: the single-crystal X-ray diffraction studies were carried out on a Bruker D8 Venture diffractometer with PhotonII detector at 173(2) or 298(2) K using Mo-Kα radiation (λ = 0.71073 Å) or Cu-Kα radiation (λ = 1.54178 Å). Dual space methods (SHELXT)[231] were used for the structure solution, and refinement was carried out using SHELXL-2014 (full-matrix least-squares on F^2)[232]. Hydrogen atoms were localized by difference electron density determination and refined using a riding model (H(water) free). Semi-empirical absorption corrections were applied. Unknown solvent was squeezed out (using the module SQUEEZE in Platon).[233-234]

For structures from Olaf Fuhr: the crystals were investigated on a Stoe StadiVari diffractometer with a Dectris Eiger4M detector using Ga-Kα (λ = 1.34143 Å) radiation generated by an Excillium MetalJet X-ray source. The crystal was kept at 150 K during data collection. Using Olex2[235], the structures were solved with the ShelXT[236] structure solution program using Intrinsic Phasing and refined with the ShelXL[232] refinement package using Least Squares

minimization. Nonhydrogen atoms were refined with anisotropic displacement parameters; hydrogen atoms were modeled on idealized positions. Unknown solvent molecules were squeezed out using the "solvent mask" algorithm implemented in Olex2.

Absorption

Absorption spectra were recorded using a SPECORD 50 plus device from Analytic Jena.

Photophysical characterization

Photoluminescence measurements were done in different media; powder samples, KBR-pellets, or in films.

KBr pellets. The KBr pellet measurements were performed by Danile Marhöfer (TUK, Prof. Niedner-Schatteburg). The pellets were fabricated by preparing 1.9 – 2.4 mg of powder and mixed with 180 mg of potassium bromide purchased from Merck. The mixture was stored in a compartment dryer at 70 °C until it was ground to a homogeneous mixture. The mixture was sintered inside an evacuable pellet (Ø = 13 mm) at a pressure of 7.5 kbar for at least 3 minutes. The pellets were measured inside a closed-cycle helium cryostat model 101J cryocooler from ColdEgde. The static luminescence spectra were measured on a Horiba Jobin Yvon Fluorolog 3-22 τ and excited with a 450 W xenon short-arc lamp. The emission light was detected by a R928 P photomultiplier detector. The measurements were performed at 5 K to 290 K in steps of 40 K (45 K for the first step).

Luminescence lifetimes were recorded on a Horiba Deltaflex spectrometer equipped with a single-photon counting detector for short lifetimes up to 100 µs and a phosphorescence detector for longer lifetimes. Excitation was done by either a pulsed NanoLED with a peak wavelength of 389 nm for the short lifetimes or a spectra LED with peak wavelengths of 341 nm or 390 nm for the longer lifetimes. The emission wavelength was set to the respective emission maxima of the sample and temperature, which were measured by the excitation wavelength closest to the LED wavelength used. All measurements were carried out in the cryostat. The obtained spectra were fitted biexponentially (short lifetimes) or triexponentially (long lifetimes) using the fitting software DAS6. The lifetimes were averaged by weighting the lifetimes with their corresponding amplitudes.

Films; steady-state measurements. Films were prepared by drop-casting solutions of the compounds onto quartz substrates and then annealed at 50°C (toluene solutions) or 30 ° (DCM solutions) for 15 minutes. The stock solutions of the complexes had a concentration of 1 mg/ml, whereas the PMMA stock solutions had a concentration of 100 mg/ml. The measurements of

film samples were conducted at an Edinburgh Instruments FS5 Spectrofluorometer with the Fluoracle software. Absolute quantum yields were measured in air and nitrogen in an integrated sphere module using the direct method with excitation from a xenon lamp (340 nm).

Time-correlated single photon counting (TCSPC) measurements were conducted in a nitrogen atmosphere with a pulsed LED (340 nm, pulse width: 1 ns). The emission wavelength was set to the respective emission maxima of the sample. The software used was Fluoracle. The obtained spectra were fitted mono- or biexponentially using exponential tail fit. The lifetimes were averaged by weighting the lifetimes with their corresponding amplitudes.

Films; time-resolved measurements. Time-resolved measurements were performed at a spectrograph (Horiba Triax) and a Stanford Computer Optics 4 Picos intensified charge-coupled device camera, where samples were excited with an Nd: YAG laser (EKSPLA, 10 Hz, 355 nm) under a vacuum.

OLEDs

Fabrication. OLEDs were fabricated on patterned indium-tin-oxide-coated glass (VisionTek Systems) with a sheet resistance of 15 $\Omega\,sq^{-1}$. After sonicating in acetone and isopropanol, substrates were oxygen-plasma-cleaned and the hole injection layer (PEDOT:PSS) (250 µL, 2500 rpm, 1 min) and emitting layer (100 µL) were spin-coated. Then, the substrates were loaded into a Kurt J. Lesker Super Spectros deposition chamber, where the electron transport/hole blocking layer, and cathode (LiF/Al) were thermally evaporated at pressures below 10^{-7} mbar. The stock-solutions of the emitting layer were adjusted to the respective wt%. The host concentration war always 10 mg/ml.

Device characterization. Freshly evaporated devices were one by one transferred into a calibrated 10-inch integrating sphere (Labsphere), and their electrical properties were measured using a source meter (Keithley 2400). Emission spectra were simultaneously measured using a calibrated fiber-coupled QePro spectrometer (Ocean Optics). Devices were evaluated at 298 K and under an air atmosphere.

Theoretical Calculations

Theoretical Calculations were performed in collaboration with Dr. Anna Mauri (KIT, INT) and Dr. Christof Holzer (KIT, TFP).

Chapter 3.1. The calculation of the ground state geometry (S0) of all complexes was optimized in the gas phase by using B3LYP[237] -D3(BJ)[238]/def2-TZVP[239], with the LANL2DZ[240-242] potential applied for iodine.[243] Optimizations were also performed in

dichloromethane (DCM) using a polarizable continuum model (PCM)[244] with both B3LYP-D3(BJ)/def2-TZVP and CAM-B3LYP[245]-D3(BJ)/def2-TZVP methods, incorporating the LANL2DZ potential for iodine. Absorption spectra and vertical excitation energies were calculated in Gaussian 16 Rev. C.01, starting from the optimized ground state geometries and computing 10 excitation energies for both singlet and triplet states. Additionally, hole and electron analyses were carried out with the Multiwfn[246] analyzer (version 3.6), based on the Gaussian16 Rev. C.01 output.

Chapter 3.2. and 3.3. The calculations were done using the following methods: All geometries have been optimized using the r^2SCAN[247] functional in conjunction with the D4 dispersion correction.[248] HOMO-LUMO gaps and excitation energies have subsequently been calculated at the optimized geometries using the TMHF functional.[249] The latter functional has been shown to describe local and charge-transfer excitation well, leading to a balanced description of all possible states of interest.[249] The def2-TZVPP basis set[250] was used throughout all calculations. SCF energies are converged up to 10^{-8} a.u., with the threshold of changes in the density being set to 10^{-7}. A convergence threshold for the residuum norms of the excited states of 10^{-5} is chosen throughout. Tight grids of size 3 (r^2SCAN) and 1 (TMHF) have been used. Plots of molecular orbitals (MOs) and natural transition orbitals (NTOs) plots were generated using an iso-value of 0.04. Note that a hole NTO denotes the initial state, while the particle NTO marks the final state of an excitation. All calculations have been carried out using the TURBOMOLE package.[251]

5.2 Reaction procedures and Analytical Data

All reaction procedures and analytical data are available online and be viewed under: https://www.chemotion-repository.net/home/welcome. The abbreviations L_{NP} stand for bridging ligands, L_P for ancillary ligands.

5.2.1 Synthesis procedures and analysis to Chapter 3.1.

5.2.1.1 Ligands

***3-(Diphenylphosphaneyl)pyridine* (L2)[41]**

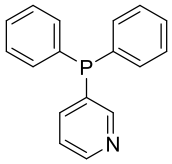

Lithium (803 mg, 116 mmol, 2.20 equiv) was suspended in dry, degassed tetrahydrofuran (100 mL). The suspension was stirred at 21 °C for 1 h. Chloro(diphenyl)phosphine (11.6 g, 9.44 mL, 52.6 mmol, 1.00 equiv) was added dropwise *via* a syringe into the reaction mixture. The mixture was stirred at 21 °C for another 2 h until the suspension turned dark orange-red. 3-Chloropyridine (5.97 g, 5.15 mL, 52.6 mmol, 1.00 equiv) was also added dropwise *via* a syringe. After stirring for 15 h, the reaction mixture was quenched by the addition of water (10 mL). The solvent was removed under reduced pressure. The crude was purified *via* column chromatography (cHex:EtOAc, 20:1 to 2:1). 3-(Diphenylphosphaneyl)pyridine (7.17 g, 27.2 mmol, 52% yield) was obtained as a colorless solid.

R_f (cHex:EtOAc, 2:1) = 0.59 – **^{1}H NMR** (500 MHz, DMSO-d_6 [2.50 ppm], ppm) δ = 8.59 (td, *J* = 1.2 Hz, *J* = 4.7 Hz, 1H, C*H*$_{Py}$), 8.41–8.40 (m, 1H, C*H*$_{Py}$), 7.62–7.58 (m, 1H, C*H*$_{Py}$), 7.45–7.43 (m, 7H, C*H*$_{Ph}$, C*H*$_{Py}$), 7.31–7.27 (m, 4H, C*H*$_{Ph}$). – **^{13}C NMR** (126 MHz, DMSO-d_6 [39.5 ppm], ppm) δ = 153.3 (d, *J* = 24.5 Hz, 1C, *C*H$_{Py}$), 150.4 (1C, *C*H$_{Py}$), 140.7 (d, *J* = 15.1 Hz, 1C, *C*H$_{Py}$), 135.4 (d, *J* = 10.5 Hz, 2C, C_q), 133.3 (d, *J* = 19.7 Hz, 4C, *C*H$_{Ph}$), 132.9 (d, *J* = 15.9 Hz, 1C, C_q), 129.4 (2C, *C*H$_{Ph}$), 129.0 (d, *J* = 6.9 Hz, 4C, *C*H$_{Ph}$), 124.5 (d, *J* = 4.5 Hz, 1C, *C*H$_{Py}$). – **^{31}P NMR** (162 MHz, DMSO, ppm) = -13.33 (s, 1P). – **MS** (FAB, 3-NBA), m/z (%): 280 (11) $[M+H+O]^+$, 264 (100) $[M+H]^+$, 185 (13) $[M-Py]^+$. – **HRMS**-FAB *(m/z)*: $[M+H]^+$ calcd for $C_{17}H_{15}NP$, 264.0937; *found*. 264.0934. – **IR** (ATR, ṽ) = 3064 (w), 3047 (w), 3024 (w), 3013 (w), 2997 (w), 2990 (w), 2962 (w), 1567 (w), 1555 (w), 1475 (m), 1466 (w), 1432 (s), 1398 (s), 1323 (m), 1307 (w), 1271 (w), 1188 (w), 1179 (w), 1156 (w), 1089 (w), 1069 (w), 1021 (m), 993 (w), 805 (w), 744 (vs), 721 (m), 710 (s), 693 (vs), 620 (s), 509 (s), 499 (vs), 489 (vs), 432 (m), 418 (m), 405 (m), 390 (m) cm^{-1}. – **EA** ($C_{17}H_{14}NP$) Calcd. C 77.56, H 5.36, N 5.32; Found. C 77.24, H 5.28, N 5.29. – **M.p**. 56 °C.

Additional information on the chemical synthesis is available *via* the Chemotion repository: https://dx.doi.org/10.14272/reaction/SA-FUHFF-UHFFFADPSC-HXRGCRJVGW-UHFFFADPSC-NUHFF-NUHFF-NUHFF-ZZZ.

Additional information on the analytical data is available via: https://dx.doi.org/10.14272/HXRGCRJVGWWNCU-UHFFFAOYSA-N.1.

3-(Diphenylphosphaneyl)-5-methylpyridine (L3)

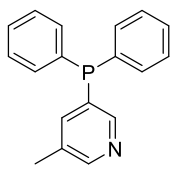

To a stirred solution of diphenylphosphine (149 mg, 0.139 mL, 0.800 mmol, 1.00 equiv) in dry, degassed tetrahydrofuran (5 mL), *n*-BuLi (2.5 M in hexane) (102 mg, 0.640 mL, 1.60 mmol, 2.50M, 2.00 equiv) was added dropwise at 24 °C. After stirring for 1 h, the reaction was cooled to 0 °C, and a solution of 3-chloro-5-methylpyridine (102 mg, 0.887 mL, 0.800 mmol, 1.00 equiv) in 1 mL of dry, degassed tetrahydrofuran was added dropwise. After 30 min, the solution was allowed to warm up to 24 °C and was stirred for 18 h. The solution was then quenched with deoxygenated methanol (1 mL). The solvents were removed under reduced pressure and the crude mixture was purified *via* column chromatography (cHex:EtOAc 20:1 to 2:1). 3-(Diphenylphosphaneyl)-5-methylpyridine (243 mg, 0.880 mmol, 97% yield) was obtained as a yellowish brown oil.

R$_f$ (cHex:EtOAc, 20:1) = 0.38. – **^{1}H** NMR (400 MHz, DMSO-d$_6$, [2.50 ppm], ppm) δ = 8.46–8.40 (m, 1H, CH$_{Py}$), 8.17 (dd, *J* = 4.1, 2.0 Hz, 1H, CH$_{Py}$), 7.46–7.41 (m, 7H, H$_{Py}$, CH$_{Ph}$), 7.32–7.24 (m, 4H, CH$_{Ph}$), 2.26 (s, 3H, C*H*$_3$). – **^{13}C NMR** (101 MHz, DMSO-d6 [35.5 ppm], ppm) δ = 150.6 (s, 1C, *C*H$_{Py}$), 150.4 (d, *J* = 3.6 Hz, 1C, *C*H$_{Py}$), 140.9 (d, *J* = 17.1 Hz, 1C, *C*H$_{Py}$), 135.5 (d, *J* = 10.7 Hz, 2C, *C*H$_q$), 133.3 (d, *J* = 19.7 Hz, 4C, C*H*$_{Ph}$), 132.2 (d, *J* = 15.9 Hz, 1C, C$_q$), 131.5 (d, *J* = 9.9 Hz, 1C, C$_q$), 129.3 (s, 2C, C*H*$_{Ph}$), 129.0 (d, *J* = 6.9 Hz, 4C, C*H*$_{Ph}$), 17.9 (s, 1C, *C*H$_3$). – **^{31}P NMR** (162 MHz, DMSO, ppm) δ = –13.43 (s, 1P). – **FAB** (m/z (%): 278 (100) [M+H]$^+$, 109 (27) [C$_6$H$_6$P]$^+$. – **HRMS**-FAB*(m/z)*: [M+H]+ calcd for C$_{18}$H$_{17}$NP, 278.1093 *found*. 278.1094. – **IR** (ATR, ṽ) = 1561 (m), 1475 (m), 1432 (s), 1419 (s), 1409 (m), 1380 (m), 1322 (m), 1086 (m), 1023 (s), 884 (m), 741 (vs), 715 (vs), 690 (vs), 674 (vs), 545 (m), 523 (m), 504 (vs), 490 (vs), 448 (m), 419 (vs), 394 (s) cm^{-1}. – **EA** (C$_{18}$H$_{16}$NP) Calcd. C 77.96, H 5.82, N 5.05; Found. C 77.58, H 5.50, N 5.21.

Additional information on the chemical synthesis is available *via* the Chemotion repository: https://dx.doi.org/10.14272/reaction/SA-FUHFF-UHFFFADPSC-HGMDWRHHFV-UHFFFADPSC-NUHFF-NUHFF-NUHFF-ZZZ.

Additional information on the analytical data is available via: https://dx.doi.org/10.14272/HGMDWRHHFVBQCO-UHFFFAOYSA-N.1.

3-(diphenylphosphaneyl)-4-methylpyridine **(L4)**

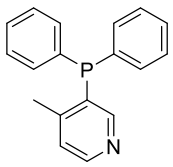

To a stirred solution of diphenylphosphine (149 mg, 0.140 mL, 0.800 mmol, 1.00 equiv) in dry, degassed tetrahydrofuran (5 mL), *n*-BuLi (2.5 M in hexane) (102 mg, 0.640 mL, 1.60 mmol, 2.00 equiv) was added dropwise at 24 °C. After stirring for 1 h, the reaction was cooled to 0 °C and a solution of 3-chloro-4-methyl-pyridine (102 mg, 0.880 mL, 0.800 mmol, 1.00 equiv) in 1 mL of dry, degassed tetrahydrofuran was added dropwise. After 30 min, the solution was allowed to warm to 24 °C and stir for 18 h. The solution was then quenched with deoxygenated methanol (1 mL). The solvents were removed under reduced pressure and the crude mixture was purified *via* column chromatography (cHex:EtOAc 20:1 to 2:1). 3-(Diphenylphosphaneyl)-4-methylpyridine (204 mg, 0.74 µmol, 92% yield) was obtained as a yellowish-brown oil.

R_f (cHex:EtOAc, 4:1) = 0.32. – **^{1}H NMR** (400 MHz, DMSO-d_6, [2.50 ppm], ppm) δ = 8.43 (d, J = 5.0 Hz, 1H, CH_{Py}), 7.71 (d, J = 2.3 Hz, 1H, CH_{Py}), 7.44 (ddt, J = 4.3, 2.9, 1.6 Hz, 6H, CH_{Ph}), 7.34–7.20 (m, 5H, CH_{Ph}, CH_{Py}), 2.28 (s, 3H, CH_3). Impurities: water from NMR solvent at 3.33 ppm. – **^{13}C NMR** (101 MHz, DMSO-d_6 [39.5 ppm], ppm) δ = 151.9 (1C, CH_{Py}), 150.6 (d, J = 24.1 Hz, 1C, C_q), 149.6 (1C, CH_{Py}), 134.2 (d, J = 9.9 Hz, 2C, C_q), 133.4 (d, J = 20.0 Hz, 4C, CH_{Ph}), 131.5 (d, J = 16.6 Hz, 1C, C_q), 129.4 (2C, CH_{Ph}), 129.1 (d, J = 7.0 Hz, 4C, CH_{Ph}), 125.1 (d, J = 3.10 Hz, 1C, CHPy), 20.2 (d, J = 18.7 Hz, 1C, CH3). **^{31}P NMR** (162 MHz, DMSO-d_6) δ [ppm] = -19.84 (s, 1P). – **IR** (ATR, ṽ) = 1572 (s), 1475 (m), 1458 (w), 1434 (s), 1397 (m), 1380 (w), 1310 (w), 1290 (w), 1220 (w), 1091 (w), 1069 (w), 1037 (w), 1026 (m), 997 (w), 829 (m), 812 (w), 747 (vs), 730 (s), 713 (w), 700 (vs), 551 (s), 535 (m), 506 (vs), 487 (vs), 456 (vs), 432 (m), 421 (m), 398 (w), 382 (w) cm^{-1}. – **EI** (m/z (%), 70 eV, 40 °C): 277 (100) $[M]^+$, 276 (74), 198 (20), 183 (17). – **HRMS**-EI(m/z): $[M]^+$ calcd for $C_{18}H_{16}NP$, 277.1015 found. 277.1013. – **EA** ($C_{18}H_{16}NP$) *calcd.* C 77.96, H 5.82, N 5.05; *found.* C 77.77, H 5.83, N 5.08.

Additional information on the chemical synthesis is available *via* the Chemotion repository: https://dx.doi.org/10.14272/reaction/SA-FUHFF-UHFFFADPSC-OSBMFEYBPF-UHFFFADPSC-NUHFF-NUHFF-NUHFF-ZZZ.

Additional information on the analytical data is available via: https://dx.doi.org/10.14272/OSBMFEYBPFTVAP-UHFFFAOYSA-N.1

5.2.1.2 Tetranuclear complexes

***(3-(Diphenylphosphaneyl)pyridine)$_2$Cu$_4$I$_4$* (Cu-4-L2-I)**

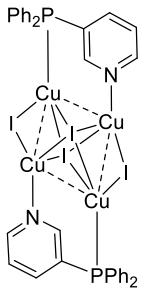

A 10 mL crimp vial was charged with 3-(diphenylphosphaneyl)pyridine (**L2**) (132 mg, 0.500 mmol, 2.00 equiv) and copper (I) iodide (190 mg, 1.00 mmol, 4.00 equiv). 3 mL of dry dichloromethane was added under argon and the suspension was degassed with argon for 5 minutes. The reaction mixture was stirred for 16 h at 25 °C. The reaction mixture was then poured into 30−40 mL of *n*-pentane. The precipitate was filtered off, washed with *n*-pentane (5−10 mL) and diethyl ether (5−10 mL) and was dried in vacuum. The complex $C_{34}H_{28}Cu_4I_4N_2P_2$ (262.9 mg, 0.20 mmol, 82% yield) was obtained as a colorless solid.

^{1}H NMR (400 MHz, Pyridine-d_5 [7.58 ppm], ppm) δ = 9.22 (dd, *J* = 5.5, 2.1 Hz, 2H), 8.19 (ddt, *J* = 9.6, 7.8, 2.0 Hz, 2H), 7.91–7.82 (m, 8H), 7.40–7.37 (m, 14H), 7.26–7.22 (m, 2H). Unknown impurities: 4.96, 3.36, and 1.13 ppm. − **^{13}C NMR** (101 MHz, Pyridine-d_5 [135.5 ppm], ppm) δ = 155.3 (d, *J* = 17.2 Hz, 4C), 151.6 (2C), 142.2 (d, *J* = 13.0 Hz, 2C), 134.8 (d, *J* = 15.6 Hz, 8C), 134.4 (2C), 132.0 (d, *J* = 22.5 Hz, 2C), 130.9 (4C), 129.9 (d, *J* = 9.1 Hz, 8C), 123.6 (2C). − **^{31}P NMR** (162 MHz, Pyridine-d_5, ppm) δ = -12.3. Impurity of 1% phosphine oxide at 23.55 ppm. − **IR** (ATR, ṽ) = 3051 (w), 1585 (vw), 1584 (w), 1477 (w), 1434 (m), 1404 (m), 1326 (w), 1191 (w), 1119 (w), 1095 (m), 1043 (w), 1027 (w), 999 (w), 799 (w), 741 (m), 734 (s), 690 (vs), 643 (w), 518 (vs), 510 (vs), 494 (vs), 431 (m) cm^{-1}. − **EA** ($C_{34}H_{28}Cu_4I_4N_2P_2$): Calcd: C: 31.70; H: 2.19; N: 2.17. Found C: 31.74; H: 2.07; N: 2.28.

Additional details on the chemical synthesis can be accessed at the research data repository Chemotion:https://dx.doi.org/10.14272/reaction/SA-FUHFF-UHFFFADPSC-ZPNCGONLMX-UHFFFADPSC-NUHFF-LUHFF-NUHFF-ZZZ.

Additional information on the analytical data is available via:

https://dx.doi.org/10.14272/ZPNCGONLMXIRAC-UHFFFAOYSA-L.1

***(3-(Diphenylphosphaneyl)pyridine)$_4$Cu$_4$Br$_4$* (Cu-4-L2-Br)**

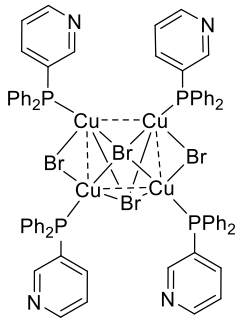

A 10 mL crimp vial was charged with 3-(diphenylphosphaneyl)pyridine (**L2**) (50.0 mg, 0.190 mmol, 4.00 equiv) and copper (I) bromide (27.2 mg, 0.190 mmol, 4.00 equiv). The substances were dissolved in 2 mL of dry dichloromethane under argon and the suspension was degassed with argon for 5 minutes. The reaction mixture was stirred for 16 h at 25 °C. The reaction mixture was then poured into 10 mL of *n*-pentane. The precipitate was filtered off, washed with *n*-pentane (5 mL) and diethyl ether (5 mL) and was dried in vacuum. The complex $C_{68}H_{56}Br_4Cu_4N_4P_4$ (65.0 mg, 0.040 mmol, 84% yield) was obtained as a colorless solid.

IR (ATR, $\tilde{\nu}$) = 1578 (w), 1482 (w), 1469 (w), 1434 (w), 1405 (w), 1196 (w), 1094 (w), 1028 (w), 810 (w), 758 (m), 745 (m), 731 (w), 697 (vs), 642 (w), 523 (s), 499 (vs), 436 (w), 426 (w) cm^{-1}. − **EA** ($C_{68}H_{56}Br_4Cu_4N_4P_4$): Calcd C: 50.08; H: 3.71; N: 3.44. Found C: 50.38; H: 3.32; N: 3.69.

Additional details on the chemical synthesis can be accessed at the research data repository Chemotion: https://dx.doi.org/10.14272/reaction/SA-FUHFF-UHFFFADPSC-JDXZPYBJJH-UHFFFADPSC-NUHFF-LUHFF-NUHFF-ZZZ.

Additional information on the analytical data is available via:

https://dx.doi.org/10.14272/JDXZPYBJJHICGX-UHFFFAOYSA-L.1.

5.2.1.3 Dinuclear complexes

***(3-(Diphenylphosphaneyl)pyridine)$_4$Cu$_2$I$_2$* (Cu-L2-I)**

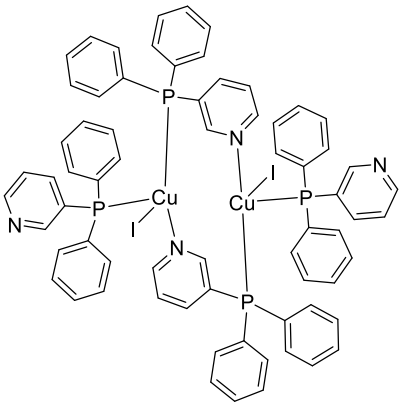

A 10 mL crimp vial was charged with the 3-(diphenylphosphaneyl)pyridine (**L2**) (415 mg, 1.58 mmol, 6.00 equiv) and copper (I) iodide (100 mg, 0.520 mmol, 2.00 equiv). The substances were dissolved in 5 mL of dry dichloromethane under argon and the suspension was degassed with argon for 5 minutes. The reaction mixture was stirred for 16 h at 25 °C in the dark. The reaction mixture was then poured into 10 mL *n*-pentane. The precipitate was filtered off, washed with *n*-pentane (5 mL) and diethyl ether (5 mL) and was dried in vacuum. The complex (358 mg, 0.250 mmol, 95% yield) was obtained as a colorless solid.

^{1}H NMR (500 MHz, DMSO-d_6 [2.50 ppm], ppm) δ = 8.63–8.58 (m, 4H, CH_{Py}), 8.49 (s, 4H, CH_{Py}), 7.71–7.62 (m, 4H, CH_{Py}), 7.50–7.43 (m, 8H, CH_{Ph}), 7.40–7.29 (m, 36H, CH_{Py}, CH_{Ph}). – **^{13}C NMR** (126 MHz, DMSO-d_6 [39.5 ppm], ppm) δ = 140.8 (4C, C*H*$_{Py}$), 133.4 (d, *J* = 16.3 Hz, 16C, *C*H$_{Ph}$), 129.9 (8C, *C*H$_{Ph}$), 128.9(d, *J* = 7.8 Hz, 16C, *C*H$_{Ph}$), 123.8 (4C, *C*H$_{Py}$). Missing signals (20C, C_{Py}, C_q) due to bad solubility. Evaluated with HSQC and COSY. – **^{31}P NMR** (202 MHz, DMSO-d_6, ppm) δ = –13.00 (s, 4P). Bad resolution due to bad solubility of the compound. – **MS** (ESI, DCM) m/z (%): 1305 (15) $[M\text{-}I]^+$, 980 (6) $[C_{51}H_{42}Cu_2IN_3P_3]^+$,852 (100) $[C_{51}H_{42}CuN_3P_3]^+$, 589 (26) $[C_{34}H_{28}CuN_2P_2]^+$. – **HRMS** ($[C_{51}H_{42}CuN_3P_3]^+$): calcd 852.1888, found 852.1779. – **IR** (ATR, $\tilde{\nu}$) = 1435 (m), 1404 (w), 1095 (w), 1027 (w), 800 (w), 747 (s), 730 (w), 704 (s), 694 (vs), 643 (w), 533 (m), 506 (vs), 492 (s), 484 (m), 428 (w) cm^{-1}. The molecular structure of the complex was determined by single-crystal X-ray diffraction.

Additional details on the chemical synthesis can be accessed at the research data repository Chemotion:https://dx.doi.org/10.14272/reaction/SA-FUHFF-UHFFFADPSC-MSWWFXVWFI-UHFFFADPSC-NUHFF-LUHFF-NUHFF-ZZZ.

Additional information on the analytical data is available via:

https://dx.doi.org/10.14272/MSWWFXVWFILBNM-UHFFFAOYSA-L.1

***(3-(Diphenylphosphaneyl)pyridine)$_4$Cu$_2$Br$_2$* (Cu-L2-Br)**

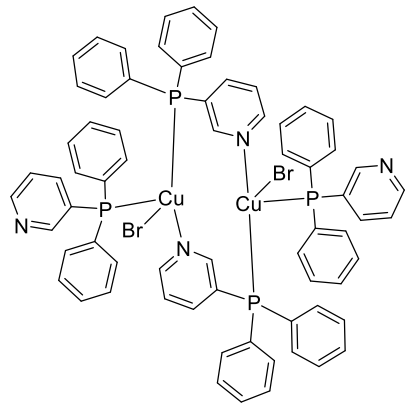

A 10 mL crimp vial was charged with 3-(diphenylphosphaneyl)pyridine (**L2**) (551 mg, 2.09 mmol, 6.00 equiv) and copper (I) bromide (100 mg, 0.700 mmol, 2.00 equiv). The substances were dissolved in 5 mL of dry dichloromethane under argon and the suspension was degassed with argon for 5 minutes. The reaction mixture was stirred for 16 h at 25 °C in the dark. The reaction mixture was then poured into 10 mL of *n*-pentane. The precipitate was filtered off, washed with *n*-pentane (5 mL) and diethyl ether (5 mL) and was dried in vacuum. The complex (440 mg, 0.328 mmol, 94% yield) was obtained as a colorless solid.

^{1}H NMR (500 MHz, DMSO-d$_6$ [2.50 ppm], ppm) δ = 8.62 (d, *J* = 5.5 Hz, 4H, C*H*$_{Py}$), 8.44 (s, 4H, C*H*$_{Py}$), 7.64 (t, *J* = 8.0 Hz, 4H, C*H*$_{Py}$), 7.46–7.39 (m, 8H, C*H*$_{Ph}$), 7.38–7.27 (m, 36H, C*H*$_{Py}$, C*H*$_{Ph}$). Impurities: 1% DCM (5.76 ppm), water from solvent (3.33 ppm). − **^{13}C NMR** (126 MHz, DMSO-d$_6$ [39.5 ppm], ppm) δ = 153.3 (d, *J* = 17.5 Hz, 4C, *C*H$_{Py}$), 150.4 (4C, *C*H$_{Py}$), 140.8 (d, *J* = 11.8 Hz, 4C, *C*H$_{Py}$), 133.4 (d, *J* = 15.4 Hz, 16C, *C*H$_{Ph}$), 132.5 (8C, C$_q$, *C*H$_{Ph}$), 132.3 (4C, C$_q$, *C*H$_{Py}$), 130.1 (8C, *C*H$_{Ph}$), 128.7 (d, *J* = 8.4 Hz, 16C, *C*H$_{Ph}$), 123.8 (4C, *C*H$_{Py}$). − **^{31}P NMR** (202 MHz, DMSO, ppm) δ = –12.59 (s, 4P). − **MS** (ESI, DCM) m/z (%): 1259 (11) [M-Br]$^+$, 996 (2) [$C_{51}H_{42}Cu_2BrN_3P_3$]$^+$, 852 (100) [$C_{51}H_{42}CuN_3P_3$]$^+$, 589 (18) [$C_{34}H_{28}CuN_2P_3$]$^+$. − **HRMS** ([$C_{51}H_{42}CuN_3P_3$]$^+$): calcd 852.1888, found 852.1782. − **IR** (ATR, ṽ) = 3047 (w), 1575 (w), 1557 (vw), 1477 (w), 1469 (w), 1434 (m), 1400 (m), 1330 (w), 1190 (w), 1159 (w), 1094 (m), 1035 (vw), 1026 (w), 994 (w), 812 (w), 795 (vw), 755 (m), 745 (s), 728 (m), 696 (vs), 640 (w), 623 (w), 518 (s), 504 (vs), 489 (vs), 425 (m), 418 (m) cm^{-1}.

The molecular structure of the complex was determined by single-crystal X-ray diffraction.

Additional details on the chemical synthesis can be accessed at the research data repository Chemotion: https://dx.doi.org/10.14272/reaction/SA-FUHFF-UHFFFADPSC-OKJYZNMQBK-UHFFFADPSC-NUHFF-LUHFF-NUHFF-ZZZ.

Additional information on the analytical data is available via:

https://dx.doi.org/10.14272/OKJYZNMQBKIKLJ-UHFFFAOYSA-L.1.

***(3-(Diphenylphosphaneyl)pyridine)$_4$Cu$_2$Cl$_2$* (Cu-L2-Cl)**

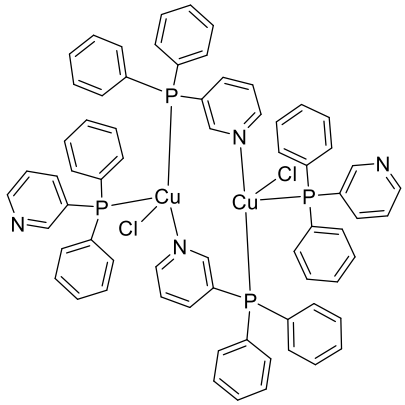

A 10 mL crimp vial was charged with 3-(diphenylphosphaneyl)pyridine (**L2**) (798 mg, 3.03 mmol, 6.00 equiv) and copper (I) chloride (100 mg, 1.01 mmol, 2.00 equiv). The substances were dissolved in 5 mL of dry dichloromethane under argon and the suspension was degassed with argon for 5 minutes. The reaction mixture was stirred for 16 h at 24 °C in the dark. The reaction mixture was then poured into 10 mL of *n*-pentane. The precipitate was filtered off, washed with *n*-pentane (5 mL) and diethyl ether (5 mL) and was dried in vacuum. The product (610 mg, 0.488 mmol, 97% yield) was obtained as a colorless solid.

^{1}H NMR (500 MHz, DMSO-d$_6$ [2.50 ppm], ppm) δ = 8.60 (d, *J* = 4.8 Hz, 4H, C*H*$_{Py}$), 8.48–8.44 (m, 4H, C*H*$_{Py}$), 7.65 (t, *J* = 8.0 Hz, 4H, C*H*$_{Py}$), 7.47–7.39 (m, 8H, C*H*$_{Ph}$), 7.39–7.27 (m, 36H, C*H*$_{Py}$, C*H*$_{Ph}$). Impurities: DCM (5.76 ppm), water (3.33 ppm). − **^{13}C NMR** (126 MHz, DMSO-d$_6$ [39.5 ppm], ppm) δ = 153.4 (d, *J* = 18.9 Hz, 4C, *C*H$_{Py}$), 150.3 (4C, *C*H$_{Py}$), 140.8 (d, *J* = 12.6 Hz, 4C, *C*H$_{Py}$), 133.4 (d, *J* = 16.3 Hz, 16C, *C*H$_{Ph}$), 130.0 (8C, C$_q$, *C*H$_{Ph}$), 128.8 (d, *J* = 8.4 Hz, 16C, *C*H$_{Ph}$), 123.9 (4C, *C*H$_{Py}$). Missing Signals (12C, C$_q$) due to bad solubility. Impurities: methylene chloride at 54.9 ppm. − **^{31}P NMR** (202 MHz, DMSO-d$_6$, ppm) δ = –12.38 (s, 4P). − **MS** (ESI, DCM) m/z (%): 950 (1) $[C_{51}H_{42}Cu_2ClN_3P_3]^+$, 689 (39) $[C_{34}H_{28}Cu_2ClN_2P_2]^+$, 589 (98) $[C_{34}H_{28}CuN_2P_3]^+$, 264 (100) $[C_{17}H_{15}NP]^+$. − **HRMS** ($[C_{34}H_{28}Cu_2ClN_2P_2]^+$): calcd 688.9985, found 688.9823. − **IR** (ATR, $\tilde{\nu}$) = 1479 (w), 1435 (m), 1401 (w), 1094 (m), 1026 (w), 812 (w), 755 (m), 745 (m), 728 (m), 696 (vs), 518 (s), 504 (vs), 490 (vs), 438 (w), 419 (m) cm^{-1}.

The molecular structure of the complex was determined by single-crystal X-ray diffraction.

Additional details on the chemical synthesis can be accessed at the research data repository Chemotion:https://dx.doi.org/10.14272/reaction/SA-FUHFF-UHFFFADPSC-NKRBFPOZJU-UHFFFADPSC-NUHFF-LUHFF-NUHFF-ZZZ.

Additional information on the analytical data is available via:

https://dx.doi.org/10.14272/NKRBFPOZJUPLQX-UHFFFAOYSA-L.1.

***(3-(Diphenylphosphaneyl)pyridine)$_4$Cu$_2$SCN$_2$* (Cu-L2-SCN)**

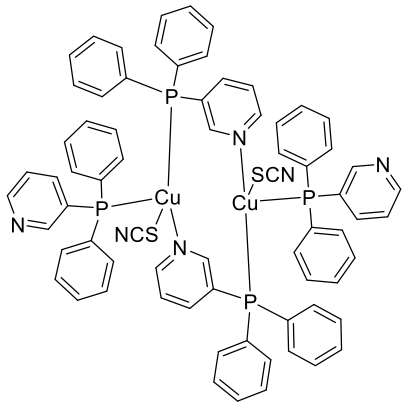

A 10 mL crimp vial was charged with 3-(diphenylphosphaneyl)pyridine (**L2**) (195 mg, 740 µmol, 6.00 equiv) and copper (I) thiocyanate (30.0 mg, 246 µmol, 2.00 equiv). The substances were dissolved in 5 mL of dry dichloromethane under argon and the suspension was degassed with argon for 5 minutes. The reaction mixture was stirred for 16 h at 25 °C in the dark. The reaction mixture was then poured into 10 mL *n*-pentane. The precipitate was filtered off, washed with *n*-pentane (5 mL) and diethyl ether (5 mL) and was dried in vacuum. The complex (96.0 mg, 74.1 µmol, 60% yield) was obtained as a colorless solid.

^{1}H NMR (500 MHz, DMSO-d_6 [2.50 ppm], ppm) δ = 8.59 (d, *J* = 4.8 Hz, 4H, C*H*$_{Py}$), 8.40–8.39 (m, 4H, C*H*$_{Py}$), 7.58 (t, *J* = 8.3 Hz, 4H, C*H*$_{Py}$), 7.45 (t, *J* = 7.4 Hz, 8H, C*H*$_{Ph}$), 7.39–7.33 (m, 20H, C*H*$_{Py}$, C*H*$_{Ph}$), 7.26 (t, *J* = 8.8 Hz, 16H, C*H*$_{Py}$, C*H*$_{Ph}$). − **^{13}C NMR** (126 MHz, DMSO-d_6 [39.5 ppm], ppm) δ = 153.1 (d, *J* = 18.0 Hz, 4C, *C*H$_{Py}$), 150.6 (s, 4C, *C*H$_{Py}$), 140.7 (d, *J* = 11.7 Hz, 4C, *C*H$_{Py}$), 133.2 (d, *J* = 15.4 Hz, 16C, *C*H$_{Ph}$), 131.8 (d, *J* = 26.0 Hz, 8C, *C*$_q$, *C*H$_{Ph}$), 130.4 (s, 8C, *C*H$_{Ph}$), 129.8 (d, *J* = 21.2 Hz, 4C, *C*$_q$, *C*H$_{Py}$), 129.0 (d, *J* = 8.6 Hz, 16C, *C*H$_{Ph}$), 124.1 (d, *J* = 5.2 Hz, 4C, *C*H$_{Py}$). Missing signals: (2C, SCN) due to peak broadening. − **^{31}P NMR** (202 MHz, DMSO-d_6, ppm) δ = -9.95. − **MS** (ESI, DCM) m/z (%): 1359 (4) $[M+Cu]^+$, 1236 $[M-SCN]^+$, 1096 (35) $[M-L+Cu]^+$, 973 (99) $[M-L-SCN]^+$, 852 (27) $[Cu+3L]^+$, 833 (40) $[M-2L+Cu]^+$, 710 (62) $[M-2L-SCN]^+$, 589 (100) $[Cu+2L]^+$. − **HRMS** (ESI, $[M+Cu]^+$, $[C_{70}H_{56}Cu_3N_6P_4S_2]^+$): calcd 1357.0841, found 1357.0822. − **IR** (ATR, ṽ) = 2091 (w), 2065 (m), 1479 (w), 1468 (w), 1434 (m), 1401 (m), 1093 (w), 1022 (w), 743 (s), 727 (m), 693 (vs), 639 (w), 621 (w), 505 (vs), 489 (vs), 457 (w), 452 (w), 443 (w), 432 (m), 425 (m), 422 (m), 415 (m), 405 (w) cm^{-1}.

Additional details on the chemical synthesis can be accessed at the research data repository Chemotion:https://dx.doi.org/10.14272/reaction/SA-FUHFF-UHFFFADPSC-PRRWRQFRAT-UHFFFADPSC-NUHFF-NUHFF-NUHFF-ZZZ.

Additional information on the analytical data is available via:

https://dx.doi.org/10.14272/PRRWRQFRATVSFB-UHFFFAOYSA-N.1.

***(3-(Diphenylphosphaneyl)pyridine)$_4$Cu$_2$CN$_2$* (Cu-L2-CN)**

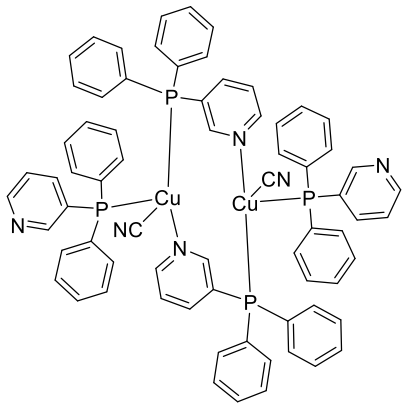

A 10 mL crimp vial was charged with 3-(diphenylphosphaneyl)pyridine (**L2**) (176 mg, 0.670 mmol, 6.00 equiv) and copper (I) cyanide (20.0 mg, 0.220 mmol, 2.00 equiv). The substances were dissolved in 5 mL dry dichloromethane under argon and the suspension was degassed with argon for 5 minutes. The reaction mixture was stirred for 16 h at 25 °C in the dark. The reaction mixture was then poured into 10 mL of *n*-pentane. The precipitate was filtered off, washed with *n*-pentane (5 mL) and diethyl ether (5 mL) and was dried in vacuum. The complex (73.0 mg, 0.59 mmol, 53% yield) was obtained as a colorless solid.

^{1}H NMR (500 MHz, DMSO-d_6 [2.50 ppm], ppm) δ = 8.58–8.28 (m, 8H, C*H*$_{Ar}$), 7.62–7.16 (m, 48H, C*H*$_{Ar}$). − **^{13}C NMR** (126 MHz, DMSO-d_6 [39.5 ppm], ppm) δ = 133.2 (16C, *C*H$_{Ar}$), 129.7 (8C, *C*H$_{Ar}$), 128.7 (16C, *C*H$_{Ar}$). Missing signals: (30C, C$_{Py}$, C$_q$) due to bad solubility. − **^{31}P NMR** (202 MHz, DMSO-d6, ppm) δ = -11.30. − **MS** (ESI, DCM) m/z (%): 1204 (10) $[M\text{-}CN]^+$, 941 (11) $[M\text{-}L\text{-}CN]^+$, 769 (31) $[M\text{-}2L+Cu]^+$, 680 (91) $[M\text{-}2L\text{-}CN+2H]^+$, 678 (100) $[M\text{-}2L\text{-}CN]^+$, 619 (37) $[M\text{-}2L\text{-}Cu\text{-}CN+4H]^+$, 589 (17) $[Cu+2L]^+$. − **HRMS** ($[M\text{-}CN]^+$, $[C_{69}H_{56}Cu_2N_5P_4]^+$): calcd 1204.2073, found 1204.2065. − **IR** (ATR, ṽ) = 2113 (vw), 1571 (w), 1560 (vw), 1480 (w), 1468 (w), 1434 (m), 1402 (w), 1328 (vw), 1193 (vw), 1093 (w), 1023 (w), 998 (vw), 801 (vw), 743 (m), 726 (w), 693 (vs), 638 (vw), 621 (w), 545 (w), 506 (vs), 489 (s), 468 (w), 443 (w), 438 (w), 431 (w), 426 (w), 421 (w), 416 (w), 405 (w) cm^{-1}.

Additional details on the chemical synthesis can be accessed at the research data repository Chemotion: https://dx.doi.org/10.14272/reaction/SA-FUHFF-UHFFFADPSC-SFEWMFDLZP-UHFFFADPSC-NUHFF-NUHFF-NUHFF-ZZZ.

Additional information on the analytical data is available via:

https://dx.doi.org/10.14272/SFEWMFDLZPYBNX-UHFFFAOYSA-N.1.

***(3-(Diphenylphosphaneyl)pyridine)$_2$(triphenylphosphine)$_2$Cu$_2$I$_2$* (Cu-L2-I-a)**

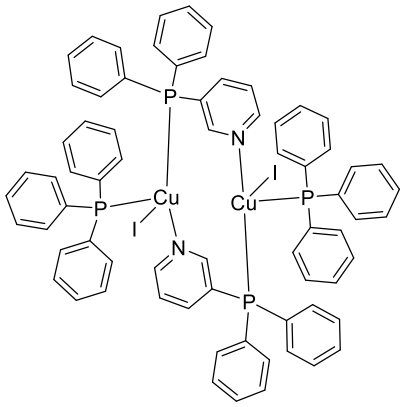

A 10 mL crimp vial was charged with 3-(diphenylphosphaneyl)pyridine (**L2**) (104 mg, 0.390 mmol, 3.00 equiv), copper (I) iodide (50.0 mg, 0.260 mmol, 2.00 equiv.) and triphenylphosphine (68.9 mg, 0.260 mmol, 2.00 equiv.). The substances were suspended in 3 mL of dry dichloromethane under argon and the suspension was degassed with argon for 5 minutes. The reaction mixture was stirred for 16 h at 25 °C in the dark. The reaction mixture was then poured into 10 mL of *n*-pentane. The precipitate was filtered off, washed with *n*-pentane (5 mL) and diethyl ether (5 mL) and was dried in vacuum. The complex $C_{70}H_{58}Cu_2I_2N_2P_4$ (154 mg, 98% purity, 0.110 mmol, 81% yield) was obtained as a colorless solid.

^{1}H NMR (ppm, CD_2Cl_2 [5.32 ppm], ppm) δ = 8.59 (dt, *J* = 4.9, 1.6 Hz, 2H, *CH*$_{Ar}$), 8.44 (dd, *J* = 4.9, 2.1 Hz, 2H, *CH*$_{Ar}$), 7.69–7.58 (m, 2H, *CH*$_{Ar}$), 7.43–7.24 (m, 50H, *CH*$_{Ar}$), 7.21 (ddt, *J* = 7.6, 4.9, 1.2 Hz, 2H, *CH*$_{Ar}$). Impurities: 8.76–8.73, 8.02–7.97, 7.60–7.41 ppm (phosphine oxide), 1.55 ppm (water from solvent). − **^{13}C NMR** (126 MHz, CD_2Cl_2 [53.8 ppm], ppm) δ = 154.4 (d, *J* = 19.6 Hz, 2C, *C*H), 150.6 (2C, *C*H), 141.6 (d, *J* = 14.9 Hz, 2C, *C*H), 134.7–143.4 (m, 10C, C_q), 134.3 (d, *J* = 5.2 Hz, 10C, *C*H), 134.1 (d, *J* = 6.7 Hz, 10C, *C*H), 132.4–132.2 (m, 2C, C_q), 130.0 (4C, *C*H), 129.9 (6C, *C*H), 129.0 (d, *J* = 8.3 Hz, 10C, *C*H), 129.2 (d, *J* = 7.9 Hz, 10C, *C*H), 123.9 (d, *J* = 5.3 Hz, 2C, *C*H).– **^{31}P NMR** (202 MHz, CD_2Cl_2) δ = -5.18 (br.s, 2P), -11.67 (bs, 2P). Impurities: 2% phosphine oxides (27.42, 25.09 ppm).− **MS** (FAB, 3-NBA) *m/z* [%] = 1233 (2) $[Cu_3I_2L^{NP}{}_2L^{P}]^+$, 1042 (1) $[M\text{-}I\text{-}L_P]^+$, 779 (20) $[Cu_2I(L_{NP})_2]^+$, 708 (16) $[Cu_3I_2L_{NP}]^+$, 588 (100) $[CuL_{NP}L_P]^+$, 516 (20) $[Cu_2IL_{NP}]^+$, 325 (53) $[CuL_P]^+$, 264 (85) $[L_{NP}+H]^+$. Mass of complex,1432, not observed.− **IR** (ATR, $\tilde{\nu}$) = 3043 (w), 1579 (w), 1479 (w), 1434 (m), 1400 (w), 1326 (w), 1310 (vw), 1188 (w), 1159 (w), 1092 (m), 1027 (w), 997 (w), 931 (vw), 846 (vw), 803 (vw), 744 (s), 727 (w), 693 (vs), 639 (w), 620 (w), 517 (vs), 503 (vs), 487 (vs), 443 (w), 428 (w), 419 (m), 395 (w) cm^{-1}. – **M.p.** decomp < 173 °C. The molecular structure of the complex was determined by single-crystal X-ray diffraction.

Additional details on the chemical synthesis can be accessed at the research data repository Chemotion: https://dx.doi.org/10.14272/reaction/SA-FUHFF-UHFFFADPSC-FXCRBPIYZX-UHFFFADPSC-NUHFF-LUHFF-NUHFF-ZZZ.

Additional information on the analytical data is available via:
https://dx.doi.org/10.14272/FXCRBPIYZXKSJI-UHFFFAOYSA-L.1.

5.2.1.4 Silver (I) complexes

***(3-(Diphenylphosphaneyl)pyridine)$_4$Ag$_4$I$_4$* (Ag-4-L2-I)**

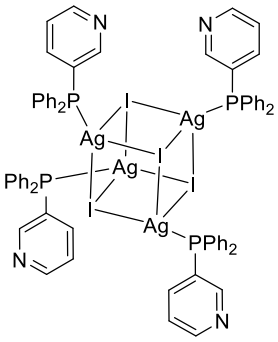

A 10 mL crimp vial was charged with 3-(diphenylphosphaneyl)pyridine (**L2**) (135 mg, 0.510 mmol, 6.00 equiv) and silver (I) iodide (40.0 mg, 0.170 mmol, 2.00 equiv). The substances were dissolved in 5 mL of dry dichloromethane under argon and the suspension was degassed with argon for 5 minutes. The reaction mixture was stirred for 16 h at 23 °C in the dark. The reaction mixture was then poured into 10 mL of *n*-pentane. The precipitate was filtered off, washed with *n*-pentane (5 mL) and diethyl ether (5 mL) and was dried in vacuum to obtain the complex $C_{68}H_{56}Ag_4I_4N_4P_4$ (43.7 mg, 0.0220 mmol, 51% yield) as colorless solid.

MS (ESI), m/z (%): 1132 (1) $[Ag_2L_3I]^+$, 869 (4) $[Ag_2L_2I]^+$, 633 (67) $[AgL_2]^+$. (Exact Mass of Complex, 1988, not found). − **HRMS** ($[Ag_2L_3I]^+$, $[C_{51}H_{42}Ag_2IN_3P_3]^+$): calcd 1131.9730, found. 1131.9701. − **EA** ($C_{68}H_{56}Ag_4I_4N_4P_4$): Calcd C: 41.00; H: 2.83; N: 2.81. Found C: 41.73; H: 2.66; N: 2.91. − **IR** (ATR, $\tilde{\nu}$) = 3055 (w), 3027 (w), 1570 (m), 1558 (m), 1480 (m), 1469 (w), 1434 (vs), 1401 (vs), 1328 (m), 1195 (m), 1095 (s), 1020 (m), 997 (w), 799 (w), 742 (s), 726 (m), 706 (s), 692 (vs), 621 (m), 504 (vs), 425 (w), 420 (w) cm. − **M.p.** decomp > 175 °C.

The molecular structure of the complex was determined by single-crystal X-ray diffraction

Additional details on the chemical synthesis can be accessed at the research data repository Chemotion: https://dx.doi.org/10.14272/reaction/SA-FUHFF-UHFFFADPSC-XVYSPWGYKA-UHFFFADPSC-NUHFF-NUHFF-NUHFF-ZZZ.

Additional information on the analytical data is available via:

https://dx.doi.org/10.14272/XVYSPWGYKABPFR-UHFFFAOYSA-N.1.

***(3-(Diphenylphosphaneyl)pyridine)$_4$Ag$_4$Br$_4$* (Ag-4-L2-Br)**

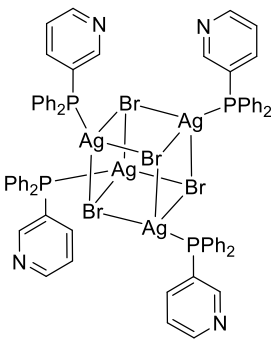

A 10 mL crimp vial was charged with 3-(diphenylphosphaneyl)pyridine (**L2**) (168 mg, 0.640 mmol, 6.00 equiv) and silver (I) bromide (40.0 mg, 0.210 mmol, 2.00 equiv). The substances were dissolved in 3 mL of dry dichloromethane under argon and the suspension was degassed with argon for 5 minutes. The reaction mixture was stirred for 16 h at 25 °C in the dark. The reaction mixture was then poured into 10 mL of *n*-pentane. The precipitate was

filtered off, washed with *n*-pentane (5 mL) and diethyl ether (5 mL) and was dried in vacuum to obtain the complex $C_{68}H_{56}Ag_4Br_4N_4P_4$ (87.9 mg, 0.490 mmol, 91% yield) as colorless solid.

^{1}H NMR (400 MHz, DMSO-d_6 [2.50 ppm], ppm) δ = 8.66 (dt, *J* = 4.3, 1.9 Hz, 4H, *CH*$_{Ar}$), 8.60 (dd, *J* = 6.2, 2.2 Hz, 4H, *CH*$_{Ar}$), 7.77 (ddt, *J* = 9.7, 7.9, 1.9 Hz, 4H, *CH*$_{Ar}$), 7.54–7.39 (m, 44H, *CH*$_{Ar}$). Impurities: 3.33 ppm (water from solvent). – **^{13}C NMR** (126 MHz, CD_2Cl_2 [53.5 ppm], ppm) δ = 153.9 (d, *J* = 15.9 Hz, 4C, *C*H$_{Ar}$), 150.8 (4C, *C*H$_{Ar}$), 141.6 (d, *J* = 16.9 Hz, 4C, *C*H$_{Ar}$), 134.0 (d, *J* = 17.2 Hz, 16C, *C*H$_{Ar}$), 131.6 (d, *J* = 23.2 Hz, 8C, C_q), 130.4 (d, *J* = 1.6 Hz, 8C, *C*H$_{Ar}$), 129.4 (d, *J* = 18.4 Hz, 4C, C_q), 129.0 (d, *J* = 9.6 Hz, 16C, *C*H$_{Ar}$), 123.5 (d, *J* = 7.3 Hz, 4C, *C*H$_{Ar}$). – **^{31}P NMR** (162 MHz, DMSO-d_6, ppm) δ = -0.18. Impurity: 23.43 ppm (phosphine oxide). – **MS** (ESI, DCM), m/z (%): 1722 (2) $[M\text{-}Br]^+$, 1272 $[M\text{-}Ag\text{-}2Br\text{-}1L]^+$, 1084 (10) $[Ag_2L_3Br]^+$, 821 (35) $[Ag_2L_2Br]^+$, 633 (100) $[AgL_2]^+$, 525 (19) $[2L+H]^+$. (Exact Mass of Complex, 1796, not found). – **HRMS** ($[M\text{-}Br]^+$, $C_{68}H_{56}Ag_4Br_3N_4P_4^+$): calcd 1722.7177, found. 1722.7170. – **IR** (ATR, ṽ) = 3071 (w), 3049 (w), 3028 (w), 3003 (w), 2987 (w), 2982 (w), 1570 (m), 1559 (m), 1479 (m), 1468 (w), 1434 (vs), 1401 (vs), 1350 (w), 1328 (m), 1312 (w), 1194 (w), 1158 (w), 1118 (w), 1112 (w), 1095 (s), 1071 (w), 1021 (m), 997 (w), 800 (w), 743 (s), 726 (m), 706 (s), 692 (vs), 621 (w), 545 (w), 504 (s), 425 (w) cm^{-1}. – **M.p.** decomp > 170 °C.

The molecular structure of the complex was determined by single-crystal X-ray diffraction.

Additional details on the chemical synthesis can be accessed at the research data repository Chemotion: https://dx.doi.org/10.14272/reaction/SA-FUHFF-UHFFFADPSC-JPVQGSZLAJ-UHFFFADPSC-NUHFF-NUHFF-NUHFF-ZZZ.

Additional information on the analytical data is available via:

https://dx.doi.org/10.14272/JPVQGSZLAJJZOP-UHFFFAOYSA-N.1.

(3-(Diphenylphosphaneyl)pyridine)$_4$Ag$_4$Cl$_4$ **(Ag-4-L2-Cl)**

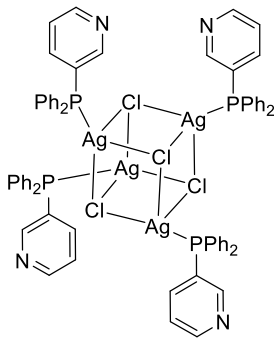

A 10 mL crimp vial was charged with 3-(diphenylphosphaneyl)pyridine (L2) (220 mg, 0.840 mmol, 6.00 equiv) and silver (I) chloride (40.0 mg, 0.280 mmol, 2.00 equiv). The substances were dissolved in 5 mL of dry dichloromethane under argon and the suspension was degassed with argon for 5 minutes. The reaction mixture was stirred for 16 h at 25 °C in the dark. The reaction mixture was then poured into 10 mL of *n*-pentane. The precipitate was filtered off, washed with *n*-pentane (5 mL) and diethyl ether (5 mL) and was dried in vacuum. The complex $C_{68}H_{56}Ag_4Cl_4N_4P_4$ (102 mg, 0.063 mmol, 90% yield) was obtained as colorless solid.

^{1}H NMR (500 MHz, CD_2Cl_2 [5.32 ppm], ppm) δ = 8.59–8.57 (m, 4H, *CH*$_{Ar}$), 8.55–8.54 (m, 4H, *CH*$_{Ar}$), 7.85 (ddt, *J* = 9.9, 7.8, 2.0 Hz, 4H, *CH*$_{Ar}$), 7.49–7.40 (m, 24H, *CH*$_{Ar}$), 7.36–7.32 (m, 16H, *CH*$_{Ar}$), 7.24–7.21 (m, 4H, *CH*$_{Ar}$). − **^{13}C NMR** (126 MHz, CD_2Cl_2 [53.5 ppm], ppm) δ = 154.3 (d, *J* = 15.9 Hz, 4C, *C*H$_{Ar}$), 151.3 (4C, *C*H$_{Ar}$), 142.0 (d, *J* = 17.2 Hz, 4C, *C*H$_{Ar}$), 134.3 (d, *J* = 17.3 Hz, 16C, *C*H$_{Ar}$), 131.9 (d, *J* = 24.2 Hz, 8C, *C*H$_{Ar}$), 130.9 (d, 8C, *C*H$_{Ar}$), 129.7 (d, *J* = 19.6 Hz, 4C, C_q), 129.4 (d, *J* = 9.6 Hz, 16C, *C*H$_{Ar}$), 124.0 (d, *J* = 7.4 Hz, 4C, *C*H$_{Ar}$). − **^{31}P NMR** (202 MHz, CD_2Cl_2, ppm) δ = 0.69. Impurity: Phosphine oxide at 25.07 ppm. − **MS** (ESI), m/z (%): 1733 $[M+Ag]^+$, 1589 (2) $[M-Cl]^+$, 1182 (9) $[M-Ag-2Cl-1L]^+$, 1040 (23) $[Ag_2L_3Cl]^+$, 777 (74) $[Ag_2L_2Cl]^+$, 633 (100) $[AgL_2]^+$. (Mass of complex, 1619, not observed). − **HRMS** ($[M+Ag]^+$): calcd 1732.7428, found 1732.7433. − IR (ATR, ṽ) = 3050 (w), 3028 (w), 1570 (m), 1559 (m), 1479 (m), 1468 (w), 1434 (vs), 1401 (vs), 1328 (w), 1194 (w), 1112 (w), 1094 (s), 1021 (m), 997 (w), 800 (w), 744 (s), 726 (m), 706 (s), 693 (vs), 621 (w), 545 (w), 504 (s), 426 (w) cm^{-1}. – **M.p.** decomp < 180 °C.

Additional details on the chemical synthesis can be accessed at the research data repository Chemotion: https://dx.doi.org/10.14272/reaction/SA-FUHFF-UHFFFADPSC-DIOALZCXAF-UHFFFADPSC-NUHFF-NUHFF-NUHFF-ZZZ.

Additional information on the analytical data is available via:

https://dx.doi.org/10.14272/DIOALZCXAFMFQD-UHFFFAOYSA-N.1.

5.2.2 Synthesis procedures and analysis to Chapter 3.2.

5.2.2.1 Ligands

***2-(Diphenylphosphaneyl)quinoline*[41] (L4)**

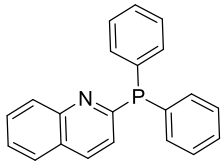

Lithium (61.1 mg, 8.80 mmol, 2.20 equiv) was suspended in 20 mL of dry, degassed tetrahydrofuran. The Suspension was stirred at 25 °C for 10 min. Chloro(diphenyl)phosphane (883 mg, 0.710 mL, 4.00 mmol, 1.00 equiv.) was added dropwise *via* a syringe into the reaction mixture. The mixture was stirred at 25 °C for 2 h until the suspension turned dark orange-red. 2-Chloroquinoline (654 mg, 0.570 mL, 4.00 mmol, 1.00 equiv) was added dropwise. After stirring for 15 h, the reaction mixture was quenched by the addition of 4 mL of water. The reaction mixture was extracted with ethyl acetate (2 x 10 mL). The organic layers were combined, and the solvent was removed under reduced pressure. The crude mixture was purified *via* flash column chromatography (cHex:EtOAc, 10:1) to afford the final product 2-

(Diphenylphosphaneyl)quinoline (626 mg, 95% purity, 1.89 mmol, 47% yield) as a light-yellow solid.

R_f (Cy/EtOAc, 5:1) = 0.6 – **^{1}H NMR** (400 MHz, $CDCl_3$ [7.26 ppm], ppm) δ = 8.22–8.12 (m, 1H, C*H*$_{Ar}$), 8.05–7.96 (m, 1H, C*H*$_{Ar}$), 7.80–7.75 (m, 1H, C*H*$_{Ar}$), 7.64–7.60 (m, 1H, C*H*$_{Ar}$), 7.54 (t, *J* = 7.5 Hz, 1H, C*H*$_{Ar}$), 7.47–7.42 (m, 4H, C*H*$_{Ar}$), 7.41–7.34 (m, 6H, C*H*$_{Ar}$), 7.19 (d, *J* = 8.4 Hz, 1H, C*H*$_{Ar}$). Impurities: 3% phosphine oxide (8.62, 8.47, 8.21–8.05, 7.90–7.83, 7.54–7.51 ppm) and 2% EtOAc (4.13, 2.05, 1.26 ppm). – **^{13}C NMR** (101 MHz, DMSO-d_6 [39.5 ppm], ppm) δ = 164.3 (d, *J* = 3.3 Hz, C_q), 147.9 (d, *J* = 13.8 Hz, C_q), 135.9–135.8 (m, 2C, *C*H$_{Ar}$), 133.9 (d, *J* = 20.0 Hz, 4C, *C*H$_{Ar}$), 131.6 (d, *J* = 9.2 Hz, C_q), 130.1 (*C*H, *C*H$_{Ar}$), 129.3 (2C, *C*H, *C*H$_{Ar}$), 128.9 (d, *J* = 7.2 Hz, 4C, *C*H, *C*H$_{Ar}$), 128.8 (*C*H, *C*H$_{Ar}$), 128.1 (*C*H, *C*H$_{Ar}$), 127.1 (*C*H, *C*H$_{Ar}$), 126.4 (C_q), 123.90 (d, *J* = 16.6 Hz, *C*H, *C*H$_{Ar}$). Impurity: phosphine oxide (132.0, 128.6 ppm). – **^{31}P NMR** (162 MHz, $CDCl_3$) δ = -2.29. Impurity: 3% phosphine oxide at 20.46 ppm. – **MS** (EI, 70 eV, 70°C), m/z (%): 313 (100) $[M]^+$, 235 (33), 205 (74), 183 (21), 163 (14), 128 (18). – **HRMS**-EI ($C_{21}H_{16}NP$) *calcd*. 313.1015; *found*. 313.1014. – **IR** (ATR, ṽ) = 3053 (w), 3040 (w), 1579 (s), 1548 (m), 1492 (s), 1476 (m), 1432 (s), 1421 (m), 1373 (w), 1292 (w), 1181 (w), 1142 (m), 1102 (w), 1091 (m), 1068 (w), 1026 (w), 994 (w), 942 (w), 829 (vs), 788 (w), 755 (vs), 744 (vs), 694 (vs), 666 (s), 633 (w), 622 (m), 603 (w), 592 (m), 526 (m), 494 (vs), 477 (vs), 439 (s), 424 (m), 408 (s), 395 (m), 375 (s) cm^{-1}. – **M.p.** 72 °C.

Additional details on the chemical synthesis can be accessed at the research data repository Chemotion: https://dx.doi.org/10.14272/reaction/SA-FUHFF-UHFFFADPSC-XZWFALQAPD-UHFFFADPSC-NUHFF-NUHFF-NUHFF-ZZZ.

Additional information on the analytical data is available via: https://dx.doi.org/10.14272/XZWFALQAPDAOON-UHFFFAOYSA-N.1.

1-(Diphenylphosphaneyl)isoquinoline[252] (L4i)

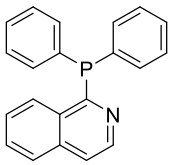

Lithium (61.1 mg, 8.80 mmol, 2.20 equiv) was suspended in 20 mL of dry, degassed tetrahydrofuran. The Suspension was stirred at 25 °C for 10 min. Chloro(diphenyl)phosphine (883 mg, 0.710 mL, 4.00 mmol, 1.00 equiv.) was added dropwise *via* a syringe into the reaction mixture. The mixture was stirred at 25 °C for 2 h until the suspension turned dark orange-red. 2-Chloroquinoline (654 mg, 0.570 mL, 4.00 mmol, 1.00 equiv) was added dropwise. After stirring for 15 h, the reaction mixture was quenched by the addition of 4 mL water. The reaction mixture was extracted with ethyl acetate (2 x 10 mL). The organic layers were combined, and the solvent was removed under reduced pressure. The crude mixture was purified twice *via* flash column chromatography

(cHex:EtOAc, 30:1) to afford 1-(diphenylphosphaneyl)isoquinoline (527 mg, 1.68 mmol, 42% yield) as an off-white solid.

R_f (cHex/EtOAc, 5:1) = 0.6 – **^{1}H NMR** (400 MHz, DMSO-d_6 [2.50 ppm], ppm) δ = 8.54 (d, *J* = 5.6 Hz, 1H), 8.46 (dd, *J* = 8.5, 4.2 Hz, 1H), 8.01 (d, *J* = 8.2 Hz, 1H), 7.82 (d, *J* = 5.6 Hz, 1H), 7.77 (ddd, *J* = 8.2, 6.8, 1.2 Hz, 1H), 7.64 (ddd, *J* = 8.3, 6.8, 1.3 Hz, 1H), 7.38-7.30 (m, 10H). – **^{13}C NMR** (126 MHz, CD_2Cl_2, ppm) δ = 164.2 (C_q), 164.1 (Cq), 143.3 (d, *J* = 3.8 Hz, *C*H), 136.5 (d, *J* = 7.2 Hz, C_q), 135.8 (d, *J* = 4.0 Hz, C_q), 135.0 (d, *J* = 20.0 Hz, 4C), 132.3 (d, *J* = 29.1 Hz, C_q), 130.5 (C*H*), 129.3 (2C, *C*H), 128.7 (d, *J* = 7.3 Hz, 4C, *C*H), 127.8 (d, *J* = 2.1 Hz, *C*H), 127.6 (d, *J* = 1.8 Hz, *C*H), 127.0 (d, *J* = 23.1 Hz, *C*H), 120.9 (*C*H). – **^{31}P NMR** (162 MHz, DMSO-d_6, ppm) δ = -9.04. – **IR** (ATR, ṽ) = 3850 (w), 3068 (w), 3045 (m), 3030 (w), 3015 (w), 3003 (w), 2986 (w), 2977 (w), 2926 (w), 1576 (m), 1542 (m), 1492 (m), 1485 (m), 1476 (m), 1434 (vs), 1417 (w), 1372 (w), 1318 (w), 1303 (s), 1292 (w), 1259 (w), 1223 (w), 1143 (w), 1090 (w), 1072 (w), 1023 (w), 978 (m), 965 (w), 957 (w), 919 (w), 871 (w), 828 (vs), 796 (w), 791 (m), 744 (vs), 741 (vs), 694 (vs), 671 (s), 656 (m), 546 (w), 539 (w), 520 (s), 495 (s), 483 (s), 464 (m), 442 (s), 429 (w), 413 (w), 402 (w) cm^{-1}. – **M.p.** 147°C.

Additional details on the chemical synthesis can be accessed at the research data repository Chemotion: https://dx.doi.org/10.14272/reaction/SA-FUHFF-UHFFFADPSC-SZVHUFSISQ-UHFFFADPSC-NUHFF-NUHFF-NUHFF-ZZZ.

Additional information on the analytical data is available via: https://dx.doi.org/10.14272/SZVHUFSISQFEMO-UHFFFAOYSA-N.1.

5.2.2.2 Mononuclear complexes

(1-(Diphenylphosphaneyl)quinoline)$_3$CuI **(Cu-L4-I)**

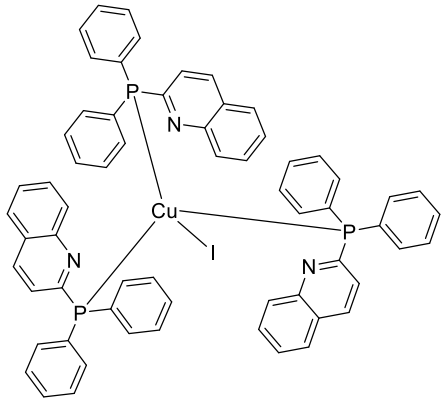

A 10 mL crimp vial was charged with 1-(diphenylphosphaneyl)quinoline (123 mg, 394 µmol, 3.00 equiv) and copper (I) iodide (25.0 mg, 131 µmol, 1.00 equiv). The substances were suspended in 3 mL of dry dichloromethane under argon and the suspension was degassed with argon for 5 minutes. The reaction mixture was stirred for 16 h at 25 °C in the dark. The reaction mixture was then poured into 10 mL of *n*-pentane. The precipitate was filtered off, washed with *n*-pentane (5 mL) and diethyl ether (5 mL) and was dried in vacuum. The complex $C_{63}H_{48}CuIN_3P_3$ (100 mg, 88.5 µmol, 67% yield)was obtained as an orange solid.

^{1}H NMR (400 MHz, CD_2Cl_2 [5.32 ppm], ppm) δ = 7.78 (m, 6H, C*H*$_{Ar}$), 7.68 (m, 3H, C*H*$_{Ar}$), 7.63–7.48 (m, 18H, C*H*$_{Ar}$), 7.38–7.33 (m, 6H, C*H*$_{Ar}$), 7.30–7.18 (m, 15H, C*H*$_{Ar}$). Impurities: *n*-pentane (1.27, 0.88 ppm), water (1.54 ppm). − **^{13}C NMR** (101 MHz, CD_2Cl_2 [53.5 ppm], ppm) δ = 135.0 (d, *J* = 16.3 Hz, *C*H$_{Ar}$), 130.0 (*C*H$_{Ar}$), 129.7 (*C*H$_{Ar}$), 128.8 (d, *J* = 8.5 Hz, *C*H$_{Ar}$), 128.1 (*C*H$_{Ar}$), 127.4 (*C*H$_{Ar}$). Missing Signals due to low solubility. − **^{31}P NMR** (162 MHz, CD_2Cl_2, ppm) δ = -3.09 (br s., 3P).− **MS** (ESI, DCM), m/z [%]: 1002 (100) $[M\text{-}I]^+$, 879 (16), 689 (92) $[M\text{-}I\text{-}L]^+$, 344 (23). − **HRMS** ($[M\text{-}I]^+$, $[C_{63}H_{48}CuN_3P_3]^+$): calcd 1002.2352 , found .1002.2351. − **IR** (ATR, ṽ) = 3050 (w), 1584 (w), 1553 (w), 1494 (m), 1480 (w), 1434 (m), 1422 (w), 1374 (vw), 1292 (w), 1186 (w), 1139 (w), 1095 (w), 1069 (vw), 1027 (w), 999 (w), 943 (vw), 824 (m), 786 (w), 741 (vs), 691 (vs), 666 (w), 626 (w), 595 (w), 530 (m), 507 (s), 489 (s), 476 (s), 455 (m), 438 (w), 428 (w), 409 (w), 388 (w) cm^{-1}. − **EA** ($C_{63}H_{48}CuIN_3P_3$ + CH_2Cl_2): Calcd C 63.25; H 4.15; N 3.46. Found C 63.05; H 4.0; N 3.5. − **M.p.** degradation 160-180 °C.

The molecular structure of the complex was determined by single-crystal X-ray diffraction

Additional details on the chemical synthesis can be accessed at the research data repository Chemotion: https://dx.doi.org/10.14272/reaction/SA-FUHFF-UHFFFADPSC-FMFPWRGMHC-UHFFFADPSC-NUHFF-MUHFF-NUHFF-ZZZ.

Additional information on the analytical data is available via: https://dx.doi.org/10.14272/FMFPWRGMHCDBED-UHFFFAOYSA-M.1.

(1-(Diphenylphosphaneyl)isoquinoline)$_2$CuI **(Cu-L4i-I)**

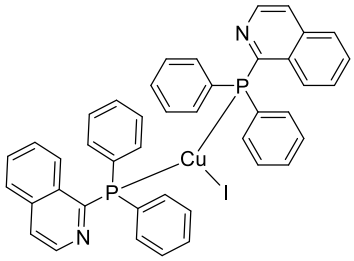

A 10 mL crimp vial was charged with 1-(diphenylphosphaneyl)isoquinoline (123 mg, 0.390 mmol, 3.00 equiv) and copper (I) iodide (25.0 mg, 0.131 mmol, 1.00 equiv). The substances were dissolved in 3 mL dry dichloromethane under argon and the suspension was degassed with argon for 5 minutes. The reaction mixture was stirred for 16 h at 25 °C in the dark and then poured into 10 mL of *n*-pentane. The precipitate was filtered off, washed with *n*-pentane (5 mL) and diethyl ether (5 mL) and was dried in vacuum to obtain the complex (52.1 mg, 0.64 mmol, 49% yield) as an orange solid.

^{1}H NMR (400 MHz, DMSO-d_6 [2.50 ppm], ppm) δ = 8.45 (d, *J* = 5.6 Hz, 2H, C*H*$_{Ar}$), 8.37 (d, *J* = 8.6 Hz, 2H, C*H*$_{Ar}$), 7.96 (d, *J* = 8.2 Hz, 2H, C*H*$_{Ar}$), 7.83 (d, *J* = 5.6 Hz, 2H, C*H*$_{Ar}$), 7.67 (ddd, *J* = 8.1, 6.9, 1.1 Hz, 2H, C*H*$_{Ar}$), 7.44–7.25 (m, 22H, C*H*$_{Ar}$). Impurity: water from solvent (3.33 ppm). − **^{13}C NMR** (101 MHz, DMSO-d_6 [39.5 ppm], ppm) δ = 142.2 (d, *J* = 10.2 Hz, 2C,

CH$_{Ar}$), 135.2 (2C, *CH*$_{Ar}$), 134.3 (d, 8C, *J* = 14.5 Hz, *CH*$_{Ar}$), 131.9 (2C, C_q), 131.7 (2C, C_q), 131.4 (2C, C_q), 130.4 (2C, *CH*$_{Ar}$), 129.9 (4C, *CH*$_{Ar}$), 129.7 (2C, C_q), 129.4 (2C, C_q), 128.4 (d, *J* = 9.1 Hz, 8C, *CH*$_{Ar}$), 127.7 (2C, *CH*$_{Ar}$), 127.4 (2C, *CH*$_{Ar}$), 121.7 (2C, *CH*$_{Ar}$). − **^{31}P NMR** (162 MHz, DMSO-d_6, ppm) δ = -5.08. − **MS** (ESI, DCM), m/z (%): 879 (1) $[M+Cu]^+$, 689 (15) [M– -I]$^+$, 440 (5) $[L+I]^+$, 344 (100) $[M–I]^{2+}$. **HRMS** ($[M+Cu]^+$, $[C_{42}H_{32}Cu_2IN_2P_2]^+$): calcd 878.9677, found. 878.9670. − **IR** (ATR, ṽ) = 1543 (w), 1435 (m), 1405 (w), 1095 (w), 827 (w), 742 (vs), 693 (vs), 540 (w), 521 (s), 503 (s), 487 (s), 462 (s) cm^{-1}. − **M.p.** degradation > 110 °C.

The molecular structure of the complex was determined by single-crystal X-ray diffraction

Additional details on the chemical synthesis can be accessed at the research data repository Chemotion: https://dx.doi.org/10.14272/reaction/SA-FUHFF-UHFFFADPSC-ISANXPFGJW-UHFFFADPSC-NUHFF-MUHFF-NUHFF-ZZZ.

Additional information on the analytical data is available via: https://dx.doi.org/10.14272/ISANXPFGJWWING-UHFFFAOYSA-M.1.

5.2.3 Synthesis procedures and analysis to Chapter 3.3.

5.2.3.1 Ligands

***2-(Diphenylphosphaneyl)-4-methylpyridine*[161] (L5)**

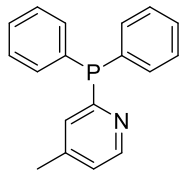

Lithium (59.8 mg, 8.62 mmol, 2.20 equiv) was suspended in 8 mL of dry, degassed tetrahydrofuran. Chloro(diphenyl)phosphine (865 mg, 0.72 mL, 3.92 mmol, 1.00 equiv) was added dropwise at 25 °C and the reaction mixture was allowed to stir for 2 h giving a red solution of lithium diphenylphosphine. At 0 °C, a solution of 2-chloro-4-methylpyridine (500 mg, 0.440 mL, 3.92 mmol, 1.00 equiv) in 1 mL of dry, degassed tetrahydrofuran was added and the mixture was allowed to warm up to 25°C. The resulting brownish solution was stirred for 16 h. After completion of the reaction, the excess of lithium diphenylphosphine was quenched with 1 mL of MeOH. The solvents were removed under reduced pressure and the crude mixture was purified twice by column chromatography (cHex:EtOAc, 4:1) to afford 2-(diphenylphosphaneyl)-4-methylpyridine (774 mg, 98% purity, 2.73 mmol, 70% yield) as a colorless oil.

R_f (Cy/EtOAc, 10:1) = 0.3 – **^{1}H NMR** (400 MHz, DMSO-d_6 [2.50 ppm], ppm) δ = 8.52 (d, J = 4.9 Hz, 1H, C*H*$_{Ar}$), 7.41-7.38 (m, 6H, C*H*$_{Ar}$), 7.33–7.29 (m, 4H, C*H*$_{Ar}$), 7.16 (d, J = 5.0 Hz, 1H, C*H*$_{Ar}$), 6.93 (s, 1H, C*H*$_{Ar}$), 2.22 (s, 3H, C*H*$_3$). Impurities: 1% phosphine oxide (8.65, 7.99, 7.80–7.74, 7.61–7.49 ppm) – **^{13}C NMR** (101 MHz, DMSO-d_6 [35.5 ppm], ppm) δ = 162.2 (d, *J* = 4.4 Hz, C_q), 149.9 (d, *J* = 12.3 Hz, *C*H$_{Ar}$), 146.8 (d, *J* = 3.6 Hz, C_q), 136.1 (d, J = 10.8 Hz, 2C, C_q), 133.8 (d, *J* = 19.9 Hz, 4C, *C*H$_{Ar}$), 129.1 (2C, *C*H$_{Ar}$), 128.7 (d, *J* = 7.11 Hz, 4C, *C*H$_{Ar}$), 128.42 (d, *J* = 19.9 Hz, *C*H$_{Ar}$), 123.6 (*C*H$_{Ar}$), 20.6 (*C*H$_3$). Impurities: phosphine oxide (132.0, 131.9 ppm). – **^{31}P NMR** (161 MHz, DMSO-d_6, ppm) δ = -5.38. Impurity: 1% phosphine oxide (18.46 ppm). – **M.p.** 73 °C.

Additional details on the chemical synthesis can be accessed at the research data repository Chemotion: https://dx.doi.org/10.14272/reaction/SA-FUHFF-UHFFFADPSC-PKLZMHUUPA-UHFFFADPSC-NUHFF-NUHFF-NUHFF-ZZZ.1.

Additional information on the analytical data is available via: https://dx.doi.org/10.14272/PKLZMHUUPARTDZ-UHFFFAOYSA-N.2.

2-(Di-p-tolylphosphaneyl)pyridine [63] **(L6)**

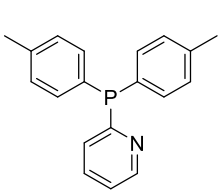

Lithium (60.9 mg, 8.81 mmol, 2.00 equiv) was suspended in 12 mL of degassed tetrahydrofuran under nitrogen. Chloro-bis(4-methylphenyl)phosphine (1.10 g, 1.00 mL, 4.40 mmol, 1.00 equiv) was added dropwise at 22 °C and the reaction mixture was allowed to stir for 2 h, giving a red solution of lithium diphenylphosphine. After that, 2-chloropyridine (500 mg, 417 µL, 4.40 mmol, 1.00 equiv) was added dropwise. The resulting brownish solution was stirred at 22 °C for 18 h. The reaction mixture was quenched with 5 mL of water. The solvents were removed under reduced pressure and the crude mixture was purified twice *via* column chromatography (cHex:EtOAc, 10:1) to afford 2-(di-p-tolylphosphaneyl)pyridine (832 mg, 2.86 mmol, 65% yield) as a colorless oil.

R_f (cHex/EtOAc, 10:1) = 0.24 – **^{1}H NMR** (400 MHz, DMSO-d_6, [2.50 ppm], ppm) δ = 8.64 (ddd, *J* = 4.8, 1.8, 0.9 Hz, 1H, C*H*$_{Ar}$), 7.70 (tt, *J* = 7.7, 1.9 Hz, 1H, C*H*$_{Ar}$), 7.29 (ddt, *J* = 7.7, 4.8, 1.0 Hz, 1H, C*H*$_{Ar}$), 7.23–7.17 (m, 8H, C*H*$_{Ar}$), 7.02 (dq, *J* = 7.8, 1.2 Hz, 1H, C*H*$_{Ar}$), 2.31 (s, 6H, C*H*$_3$). Impurities: water from solvent (3.33 ppm). – **^{13}C NMR** (126 MHz, DMSO-d_6 [39.5 ppm], ppm) δ = 163.9 (d, *J* = 4.5 Hz, 1C, C_q), 149.8 (d, *J* = 12.1 Hz, 1C, *C*H$_{Ar}$), 135.8 (d, *J* = 2.7 Hz, 1C, *C*H$_{Ar}$), 133.5 (d, *J* = 20.0 Hz, 4C, *C*H$_{Ar}$), 131.3 (d, *J* = 9.6 Hz, 2C, C_q), 129.2 (d, *J* = 7.5 Hz, 4C, *C*H$_{Ar}$), 128.8 (d, *J* = 12.1 Hz, 2C, C_q), 127.01 (d, *J* = 17.2 Hz, 1C, *C*H$_{Ar}$), 122.19 (1C, *C*H$_{Ar}$), 20.60 (2C, *C*H$_3$). Impurities: Due to long measuring time, oxidation of phosphine ligand in solution, not seen in ^{31}P and ^{1}H.: 150.7, 138.5, 136.6, 127.3, 125.4, 21.6 ppm. ^{13}C only measured until 150 ppm, evaluation of higher signals with DEPT and HSQC. – **^{31}P NMR** (162 MHz, DMSO-d_6, ppm) δ = -7.01 (s, 1P).

Additional details on the chemical synthesis can be accessed at the research data repository Chemotion: https://dx.doi.org/10.14272/reaction/SA-FUHFF-UHFFFADPSC-GCOUUCTXNL-UHFFFADPSC-NUHFF-NUHFF-NUHFF-ZZZ.1.

Additional information on the analytical data is available via: https://dx.doi.org/10.14272/GCOUUCTXNLMQAN-UHFFFAOYSA-N.2.

4-Diphenylphosphanylbenzoic acid **[210] (59)**

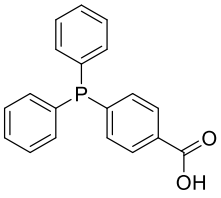

4-Iodobenzoic acid (3.00 g, 12.1 mmol, 1.00 equiv) and palladium diacetate (27.2 mg, 121 µmol, 0.010 equiv) were dissolved under argon in 18 mL of dry acetonitrile. Triethylamine (2.45 g, 3.36 mL, 24.2 mmol, 2.00 equiv) and diphenylphosphine (3.38 g, 3.16 mL, 18.1 mmol, 1.50 equiv) were added successively. The reaction mixture was stirred at 90 °C for 24 h. Then,

the solvent was removed under reduced pressure and the crude residue was dissolved in an aqueous KOH solution (1 M, 18 mL) and extracted with diethyl ether (3 x 120 mL). The aqueous phase was acidified with 6 M hydrochloric acid until the pH was 2-3. The aqueous solution was extracted with dichloromethane (3x180 mL) and the combined organic phases were dried over Na_2SO_4. The solvents were removed under reduced pressure. After purification by column chromatography (cHex:EtOAc, 8:1 to 6:1). 4-Diphenylphosphanylbenzoic acid (1.90 g, 6.20 mmol, 51% yield) was obtained as a colorless solid.

R_f (cHex:EtOAc, 3:1) = 0.35. – **^{1}H NMR** (400 MHz, DMSO-d_6 [2.50 ppm], ppm]) δ = 13.04 (s, 1H, COO*H*), 7.95–7.92 (m, 2H), 7.47–7.38 (m, 6H, C*H*), 7.36–7.23 (m, 6H, C*H*). Impurities: water from the NMR solvent at 3.32 ppm.– **^{13}C NMR** (101 MHz, CD_2Cl_2 [53.5 ppm], ppm) δ = 171.5 (*C*O, C_q), 145.9 (d, *J* = 15.2 Hz, 1C, C_q), 136.6 (d, *J* = 10.9 Hz, 2C, C_q), 134.4 (d, *J* = 20.2 Hz, 4C, *C*H_{Ar}), 133.6 (d, *J* = 18.6 Hz, 2C, *C*H_{Ar}), 130.1 (d, *J* = 6.3 Hz, 2C, *C*H_{Ar}), 129.6 (2C, *C*H_{Ar}), 129.5 (1C, C_q), 129.1 (d, *J* = 7.3 Hz, 4C, *C*H_{Ar}). – **^{31}P NMR** (161 MHz, ppm) δ = -6.40. – **IR** (ATR, ṽ) = 3062 (w), 2848 (w), 2743 (w), 2587 (w), 2468 (m), 2465 (m), 1698 (vs), 1436 (s), 1392 (w), 1249 (m), 1162 (m), 1152 (vs), 1129 (s), 1121 (vs), 1105 (vs), 1087 (vs), 1070 (m), 1015 (w), 997 (w), 932 (w), 861 (w), 759 (w), 725 (w), 709 (vs), 692 (vs), 685 (s), 568 (s), 542 (vs), 523 (w), 522 (w), 500 (w) cm^{-1}. – **M.p.** 150 °C.

Additional details on the chemical synthesis can be accessed at the research data repository Chemotion: https://dx.doi.org/10.14272/reaction/SA-FUHFF-UHFFFADPSC-GXMHDTPYKR-UHFFFADPSC-NUHFF-NUHFF-NUHFF-ZZZ.

Additional information on the analytical data is available via: https://dx.doi.org/10.14272/GXMHDTPYKRTARV-UHFFFAOYSA-N.1.

***4-(Diphenylphosphino)-N-(2-propyn-1-yl)benzamide*[205] (P1)**

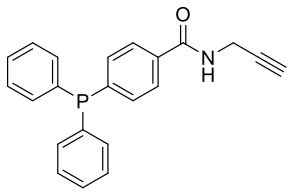

4-Diphenylphosphanylbenzoic acid (849 mg, 2.77 mmol, 1.00 equiv), N,N-dimethylpyridin-4-amine (339 mg, 2.77 mmol, 1.00 equiv) and N-(3-dimethylaminopropyl)-N′-ethylcarbodiimide-hydrochloride (558 mg, 2.91 mmol, 1.05 equiv) were dissolved in 15 mL of dry dichloromethane under an argon atmosphere. Then, propargylamine (183 mg, 211 µL, 3.33 mmol, 1.20 equiv) was added slowly to the mixture. The reaction mixture was stirred for 22 h at 25 °C. The organic phase was washed with water (70 mL), brine (3 × 15 mL), again with water (30 mL) and was dried over Na_2SO_4. The solvent was removed under reduced pressure. After purification by column chromatography (cHex:EtOAc, 8:1 to 6:1) 4-

diphenylphosphanyl-N-prop-2-ynylbenzamide (909 mg, 97% purity, 2.57 mmol, 93% yield) was obtained as a white solid.

R_f (cHex:EtOAc, 3:1) = 0.35. − **^{1}H NMR** (400 MHz, DMSO-d_6 [2.50 ppm], ppm) δ = 8.95 (t, *J* = 5.6 Hz, 1H, N*H*), 7.85 – 7.82 (m, 2H, CH_{Ar}), 7.42 (dh, *J* = 5.4, 1.9 Hz, 6H, CH_{Ar}), 7.31–7.24 (m, 6H, CH_{Ar}), 4.05 (dd, *J* = 5.6, 2.5 Hz, 2H, CH_2), 3.12 (t, *J* = 2.5 Hz, 1H, CH_{Alkyne}). Impurities: cyclohexane at 1.39 ppm. − **^{13}C NMR** (101 MHz, DMSO-d_6 [39.5 ppm], ppm) δ = 165.6 (1C, Cq, *C*O), 141.1 (d, J = 13.5 Hz, 1C, C_q), 136.2 (d, J = 11.0 Hz, 2C, C_q), 134.1 (4C, *C*H_{Ar}), 133.5 (1C, C_q), 132.8 (d, J = 19.0 Hz, 2C, *C*H_{Ar}), 129.3 (2C, *C*H_{Ar}), 128.9 (d, J = 7.0 Hz, 4C, *C*H_{Ar}), 127.5 (d, J = 6.5 Hz, 2C, *C*H_{Ar}), 81.7 (1C, C_q, C_{Alkyne}), 73.4 (1C, *C*H_{Alkyne}), 29.0 (1C, CH_2). Impurities: 26.8 ppm (cyclohexane). − **^{31}P NMR** (162 MHz, DMSO-d_6, ppm) δ = -6.88 (s, 1P). − **MS** (FAB, 3-NBA) *m/z* (%): 344 (100) $[M]^+$, 289(19) [$C_{19}H_{15}OP$], 183(28). − **HRMS** (FAB, 3-NBA, $C_{22}H_{19}NOP$): calcd. 344.1199, found 344.1198. − **IR** (ATR, ṽ) = 3288 (m), 3051 (w), 1639 (vs), 1596 (s), 1526 (vs), 1479 (vs), 1432 (vs), 1391 (m), 1351 (m), 1296 (vs), 1269 (s), 1183 (w), 1154 (m), 1115 (w), 1089 (m), 1069 (w), 1047 (w), 1026 (w), 1017 (m), 997 (w), 986 (w), 919 (w), 846 (m), 742 (vs), 717 (w), 693 (vs), 663 (vs), 640 (vs), 629 (vs), 581 (s), 500 (vs), 483 (s), 450 (w), 442 (w), 429 (w), 425 (w) cm^{-1}. – **M.p.** 107 °C.

Additional details on the chemical synthesis can be accessed at the research data repository Chemotion: https://dx.doi.org/10.14272/reaction/SA-FUHFF-UHFFFADPSC-LWSKJTFNQK-UHFFFADPSC-NUHFF-NUHFF-NUHFF-ZZZ.

Additional information on the analytical data is available via: https://dx.doi.org/10.14272/LWSKJTFNQKEMDC-UHFFFAOYSA-N.1.

2-(Methacryloyloxy)ethyl-4-(diphenylphosphino)benzoate[206] (P2)

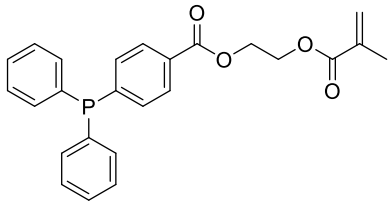

4-(Diphenylphosphin)-benzoic acid (2.50 g, 8.16 mmol, 1.00 equiv), 4-(dimethylamino)-pyridine (99.7 mg, 0.816 mmol, 0.1 equiv) and N-(3-dimethylaminopropyl)-N′-ethylcarbodiimide-hydrochloride (1.64 g, 8.57 mmol, 1.05 equiv) were dissolved in 75 mL of dry dichloromethane under an argon atmosphere. After cooling to −10 °C, 2-hydroxyethylmethacrylate (1.168 g, 1.09 mL, 8.98 mmol, 1.10 equiv) was added slowly to the mixture. The reaction mixture was brought to 25 °C and was stirred for 22 h. The organic phase was then washed with water (200 mL), brine (3 × 50 mL), again with water (100 mL) and was dried over Na_2SO_4. The solvent was removed under reduced pressure. After purification by flash column chromatography with cooled solvents (cHex:EtOAc, 10:1) 2-(methacryloyloxy)ethyl-4-

(diphenylphosphino)benzoate (2.63 g, 99% purity, 6.29 mmol, 76% yield) was obtained as a colorless oil, that was stored in the cold to prevent polymerization.

R_f (cHex:EtOAc, 10:1) = 0.5. − **^{1}H NMR** (500 MHz, DMSO-d_6 [2.50 ppm], ppm) δ = 7.93 (dq, *J* = 8.3, 1.8 Hz, 2H, C*H*$_{Ar}$), 7.46–7.38 (m, 6H, C*H*$_{Ar}$), 7.37–7.20 (m, 6H, C*H*$_{Ar}$), 6.02 (t, *J* = 1.4 Hz, 1H, C*H*$_{Alkene}$), 5.66 (p, *J* = 1.6 Hz, 1H, C*H*$_{Alkene}$), 4.56–4.50 (m, 2H, C*H*$_2$), 4.45–4.40 (m, 2H, C*H*$_2$), 1.85 (t, *J* = 1.3 Hz, 3H, C*H*$_3$). Impurity: 5.75 ppm (<1% dichloromethane). − **^{13}C NMR** (125 MHz, DMSO-d_6 [39.5 ppm], ppm) δ = 166.9 (1C, C_q, CO), 165.8 (1C, C_q, CO), 143.9 (d, *J* = 14.7 Hz, 1C, C_q), 136.4–135.4 (m, 3C, C_q), 133.5 (d, *J* = 20.1 Hz, 4C, *CH*$_{Ar}$), 133.0 (d, *J* = 18.7 Hz, 2C, *CH*$_{Ar}$), 129.5 (1C, C_q), 129.4 (2C, *CH*$_{Ar}$), 129.2 (d, *J* = 6.4 Hz, 2C, *CH*$_{Ar}$), 129.0 (d, *J* = 7.2 Hz, 4C, *CH*$_{Ar}$ 126.6 (1C, *C*H$_2$, C$_{Alkene}$), 63.06 (d, *J* = 42.8 Hz, 2C, *C*H$_2$), 18.40 (1C, *C*H$_3$). Impurity: 54.9 ppm (dichloromethane). − **^{31}P NMR** (202 MHz, DMSO-d_6, ppm) δ = -6.22 (s, 1P). − **MS** (FAB, 3-NBA) *m/z* (%): 418 (100) $[M]^+$, 289(28) $[C_{19}H_{15}OP]^+$, 183 (23), 113 (27). − **HRMS** (FAB, 3-NBA, $C_{25}H_{23}O_4P$): calcd. 418.1328, found 418.1327. − **IR** (ATR, ṽ) = 3053 (vw), 2955 (vw), 2925 (vw), 1716 (vs), 1636 (vw), 1595 (w), 1585 (vw), 1479 (vw), 1451 (vw), 1434 (w), 1394 (w), 1368 (vw), 1321 (w), 1308 (vw), 1298 (w), 1265 (s), 1161 (m), 1122 (w), 1105 (w), 1085 (w), 1049 (w), 1026 (vw), 1016 (w), 999 (vw), 942 (vw), 850 (vw), 813 (vw), 761 (w), 742 (w), 719 (vw), 694 (w), 500 (vw), 478 (vw) cm^{-1}.

Additional information on the chemical synthesis is available *via* the Chemotion repository: https://dx.doi.org/10.14272/reaction/SA-FUHFF-UHFFFADPSC-PRQNKQRDKC-UHFFFADPSC-NUHFF-NUHFF-NUHFF-ZZZ.

Additional information on the analytical data is available via: https://dx.doi.org/10.14272/PRQNKQRDKCFKFS-UHFFFAOYSA-N.1.

6-(Diphenylphosphino)-nicotinic acid[41] (63)

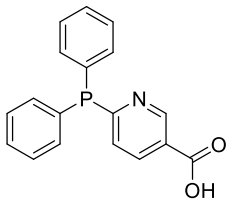

6-Bromopyridine-3-carboxylic acid (1.00 g, 4.95 mmol, 1.00 equiv), palladium diacetate (2.20 mg, 9.80 µmol, 0.00198 equiv) and sodium acetate (812 mg, 9.90 mmol, 2.00 equiv) were dissolved in 10 mL dry dimethylacetamide under argon atmosphere. Diphenylphosphine (0.920 g, 0.800 mL, 4.95 mmol, 1.00 equiv) was added. The reaction mixture was degassed for 5 minutes with argon and stirred for 15 h at 130 °C. Water (150 mL) was added to the solution and the mixture was extracted with dichloromethane (30 mL). The organic phase was washed with brine (3 × 50 mL) and water (100 mL) and was dried over Na_2SO_4. The solvent was removed under reduced pressure. After purification by column chromatography (cHex:EtOAc + 0.5 %

formic acid) 6-(diphenylphosphino)-nicotinic acid (446 mg, 98% purity, 1.45 mmol, 29% yield) was obtained as a colorless crystalline solid.

R_f (EtOAc) = 0.37. – **^{1}H NMR** (500 MHz, DMSO-d_6 [2.50 ppm], ppm) δ = 13.43 (s, 1H, COO*H*), 9.11 (d, *J* = 1.6 Hz, 1H, C*H*$_{Ar}$), 8.19 (dt, *J* = 8.1, 2.1 Hz, 1H, C*H*$_{Ar}$), 7.39–7.34 (m, 6H, C*H*$_{Ar}$), 7.38–7.34 (m, 4H, C*H*$_{Ar}$), 7.15 (d, *J* = 8.1, 1H, C*H*$_{Ar}$). Impurities: 2% phosphine oxide (9.25–9.23, 8.27–8.23, 7.82–7.75, 7.65–7.53 ppm), water from solvent (3.33 ppm). – **^{13}C NMR** (100 MHz, DMSO-d_6 [39.5 ppm], ppm) δ = 168.8 (d, *J* = 1.5 Hz, C_q), 166.6 (C_q), 150.8 (d, *J* = 11.6 Hz, *C*H$_{Ar}$), 137.3 (d, *J* = 2.9 Hz, *C*H$_{Ar}$), 135.7 (d, *J* = 9.4 Hz, 2C, *C*$_q$), 134.5 (d, *J* = 20.3 Hz, 4C, *C*H$_{Ar}$), 130.0 (2C, *C*H$_{Ar}$), 129.4 (d, *J* = 8.0 Hz, 4C, *C*H$_{Ar}$), 127.4 (d, *J* = 16.7 Hz, *C*H$_{Ar}$), 125.4 (d, *J* = 1.5 Hz, *C*$_q$). – **^{31}P NMR** (161 MHz, DMSO-d_6, ppm) δ= -3.74 (s, 1P). **M.p.** 172 °C.

Additional information on the chemical synthesis is available *via* the Chemotion repository: https://dx.doi.org/10.14272/reaction/SA-FUHFF-UHFFFADPSC-QBSSTXYHFD-UHFFFADPSC-NUHFF-NUHFF-NUHFF-ZZZ.

Additional information on the analytical data is available via: https://dx.doi.org/10.14272/QBSSTXYHFDDTSM-UHFFFAOYSA-N.1.

6-(Diphenylphosphino)-N-(2-propyn-1-yl)-nicotinamide **(L7)**

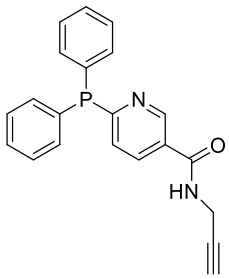

6-(Diphenylphosphino)-nicotinic acid (100 mg, 0.33 mmol, 1.00 equiv), 1-hydroxybenzotriazole hydrate (74.8 mg, 0.488 mmol, 1.50 equiv) and *N*-(3-dimethylaminopropyl)-*N′*-ethylcarbodiimide-hydrochloride (93.8 mg, 0.488 mmol, 1.50 equiv) were dissolved at 25 °C in 25 mL dry dichloromethane under argon atmosphere. Then, *N*,*N*-diisopropylethylamine (126 mg, 0.17 mL, 0.98 mmol, 3.00 equiv) was added. After stirring for 10 minutes propargylamine (44.8 mg, 0.0500 mL, 0.810 mmol, 2.50 equiv) was added slowly to the mixture and stirred for 16 h at 25 °C. Water (150 mL) was added to the solution and then the organic phase was washed with brine (3 × 20 mL) and water (50 mL) and was dried over Na_2SO_4. The solvent was removed under reduced pressure. After purification by column chromatography (cHex/EtOAc, 2:1 to 1:1) 6-(Diphenylphosphino)-*N*-(2-propyn-1-yl)-nicotinamide (80.5 mg, 0.230 mmol, 72% yield) was obtained as a light-yellow solid.

R_f (cHex/EtOAc, 2/1) = 0.47. – **^{1}H NMR** (500 MHz, DMSO-d_6 [2.50 ppm],ppm) δ = 9.14 (t, *J* = 5.5 Hz, 1H, N*H*), 9.05 (dd, *J* = 2.3, 0.9 Hz, 1H, C*H*$_{Ar}$), 8.11 (dt, *J* = 8.2, 2.1 Hz, 1H, C*H*$_{Ar}$), 7.48–7.39 (m, 6H, C*H*$_{Ar}$), 7.39–7.30 (m, 4H, C*H*$_{Ar}$), 7.13 (dt, *J* = 8.1 Hz, *J* = 0.8 Hz, 1H, C*H*$_{Ar}$), 4.07 (dd, *J* = 5.5, 2.5 Hz, 2H, C*H*$_2$), 3.16 (t, *J* = 2.5 Hz, 1H, C*H*$_{Alkyne}$). Impurities: cyclohexane

at 1.39 ppm, unknown impurity at 3.58 ppm. – **^{13}C NMR** (126 MHz, DMSO-d_6 [39.5 ppm], ppm) δ = 166.6 (d, *J* = 2.4 Hz, 1C, C_q), 164.3 (1C, C_q), 148.6 (d, *J* = 12.2 Hz, 1C, *C*H$_{Ar}$), 135.4 (d, *J* = 10.1 Hz, 1C, *C*H$_{Ar}$), 135.0 (d, *J* = 2.8 Hz, 2C, C_q), 134.0 (d, *J* = 20.0 Hz, 4C, *C*H$_{Ar}$), 129.5 (2C, *C*H$_{Ar}$), 128.9 (d, *J* = 7.5 Hz, 4C, *C*H$_{Ar}$), 127.8 (1C, C_q), 126.8 (d, *J* = 17.1 Hz, 1C, *C*H$_{Ar}$), 80.9 (1C, C_q, C_{Alkyne}), 73.2 (1C, *C*H$_{Alkyne}$), 28.5 (1C, *C*H$_2$). Impurities: cyclohexane at 26.3 ppm. – **^{31}P NMR** (202 MHz, DMSO-d_6, ppm) δ = -4.42 (1s, 1P). – **MS** (FAB, 3-NBA, $C_{21}H_{17}ON_2P$) m/z (%): 345 (68) $[M+H]^+$, 267 (19), 185 (26), 133 (100). – **HRMS** (FAB, 3-NBA, $[C_{21}H_{18}ON_2P]^+$, $[M+H]^+$): calcd. 345.1151, found 345.1150. – **IR** (ATR, ṽ) = 3278 (m), 3274 (m), 3216 (w), 3200 (w), 3067 (w), 3051 (w), 2922 (w), 2850 (w), 1642 (vs), 1581 (vs), 1528 (vs), 1479 (m), 1448 (s), 1434 (vs), 1418 (m), 1357 (m), 1305 (vs), 1266 (s), 1231 (m), 1183 (m), 1164 (s), 1111 (w), 1094 (m), 1068 (w), 1047 (w), 1026 (m), 999 (w), 983 (m), 918 (w), 847 (m), 824 (w), 768 (m), 741 (vs), 691 (vs), 666 (vs), 629 (vs), 579 (vs), 538 (s), 520 (s), 500 (vs), 480 (vs), 441 (s), 433 (s), 397 (s) cm^{-1}. – **M.p.** 160 °C.

Additional information on the chemical synthesis is available *via* the Chemotion repository: https://dx.doi.org/10.14272/reaction/SA-FUHFF-UHFFFADPSC-LVHPWOUALX-UHFFFADPSC-NUHFF-NUHFF-NUHFF-ZZZ.

Additional information on the analytical data is available via: https://dx.doi.org/10.14272/LVHPWOUALXRSLV-UHFFFAOYSA-N.1.

N^4,N$^{4'}$-di(propyn-1-yl)-[2,2'-bipyridine]-4,4'-dicarboxamide[208] (L8)

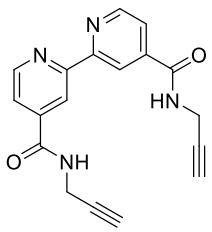

4,4´-Dicarboxy-2,2´-bipyridine (2.00 g, 8.19 mmol, 1.00 equiv.), 1-hydroxybenzotriazole hydrate (375 mg, 2.46 mmol, 0.300 equiv) and *N*-(3-dimethylaminopropyl)-*N′*-ethylcarbodiimide -hydrochloride (4.71 g, 24.6 mmol, 3.00 equiv) were dissolved at 25 °C in 400 mL of dimethylformamide. Then, *N*,*N*-diisopropylethylamine (6.35 g, 8.56 mL, 49.1 mmol, 6.00 equiv) was added. After stirring for 10 minutes propargylamine (2.26 g, 2.62 mL, 40.9 mmol, 5.00 equiv) was slowly added into the reaction mixture and stirred for 24 h at 25 °C. Water (100 mL) was added and the precipitates were collected. The crude product was dissolved in 20 mL of toluene. The solvent was removed under reduced pressure and *N*^{4},*N*$^{4'}$-di(propyn-1-yl)-[2,2'-bipyridine]-4,4'-dicarboxamide (2.08 g, 6.53 mmol, 80% yield) was obtained as a light-yellow solid.

^{1}H NMR (400 MHz, DMSO-d_6 [2.50 ppm], ppm) δ = 9.45 (t, *J* = 3.8 Hz, 2H, N*H*), 8.89 (d, *J* = 5.0 Hz, 2H, C*H$_{Ar}$*), 8.82 (s, 2H, C*H$_{Ar}$*), 7.88 (dd, *J* = 4.9 Hz, *J* = 1.4 Hz, 2H, C*H$_{Ar}$*), 4.12 (dd, *J* = 5.4 Hz, *J* = 2.4 Hz, 4H, C*H*$_2$), 3.19 (t, *J* = 2.5 Hz, 2H, C*H*$_{Alkyne}$). Impurity: water from

solvent (3.33 ppm). − **^{13}C NMR** (126 MHz, DMSO-d_6 [39.5 ppm], ppm) δ = 164.4 (2C, C_q, *C*O), 155.5 (2C, C_q), 150.2 (2C, *CH*$_{Ar}$), 142.2 (2C, C_q), 121.9 (2C, *CH*$_{Ar}$), 118.3 (2C, *CH*$_{Ar}$), 80.8 (2C, C_q, C_{Alkyne}), 75.3 (2C, *C*H$_{Alkyne}$), 28.7 (2C, *C*H$_2$). − **MS** (FAB, 3-NBA) m/z (%): 319 (5) $[M+H]^+$, 307 (31), 289 (16). − **HRMS** (FAB, 3-NBA, $C_{18}H_{15}O_2N_4$): calcd. 319.1190, found 319.1191. − **IR** (ATR, ṽ) = 3269 (s), 3241 (s), 1647 (s), 1630 (s), 1591 (m), 1530 (vs), 1463 (m), 1445 (m), 1421 (m), 1392 (w), 1358 (m), 1320 (s), 1296 (vs), 1271 (s), 1265 (s), 1247 (m), 1237 (m), 1170 (w), 1101 (m), 1068 (w), 1060 (m), 1050 (m), 993 (w), 895 (m), 864 (s), 765 (w), 734 (w), 701 (vs), 686 (vs), 662 (vs), 647 (vs), 595 (s), 571 (m), 521 (m), 504 (m), 418 (m), 397 (s), 384 (w) cm^{-1}. − **EA** ($C_{18}H_{14}N_4O_2$): Calcd C 67.91; H 4.43; N 17.60. Found C 67.69; H 4.54; N 17.55. – **M.p.** decomp. < 262 °C

Additional information on the chemical synthesis is available *via* the Chemotion repository: https://dx.doi.org/10.14272/reaction/SA-FUHFF-UHFFFADPSC-AKMKDYKCLF-UHFFFADPSC-NUHFF-NUHFF-NUHFF-ZZZ.

Additional information on the analytical data is available via: https://dx.doi.org/10.14272/AKMKDYKCLFRAJM-UHFFFAOYSA-N.1.

***4-(Diphenylphosphaneyl)-N-(4-ethynylphenyl)benzamide*[207] (P3)**

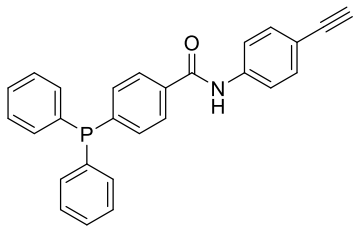

4-Diphenylphosphanylbenzoic acid (800 mg, 2.61 mmol, 1.00 equiv), 4-ethynylaniline (306 mg, 2.61 mmol, 1.00 equiv), *N*-(3-dimethylaminopropyl)-*N*′-ethylcarbodiimide-hydrochloride (549 mg, 2.87 mmol, 1.10 equiv), and 4-(dimethylamino)-pyridine (99. (70.4 mg, 576 µmol, 0.221 equiv) were dissolved in 70 mL of dry dichloromethane under an argon atmosphere. The reaction mixture was stirred for 17 h at 25 °C. The organic phase was washed with 1 M HCl, saturated $NaHCO_3$ (2 × 15 mL) and brine (20 mL), and was dried over Na_2SO_4. The solvent was removed under reduced pressure. After purification by flash column chromatography (cHex:EtOAc, 8:1 to 6:1) 4-(diphenylphosphaneyl)-N-(4-ethynylphenyl)benzamide (1.06 g, 2.61 mmol, 99% yield) was obtained as a colorless solid.

R_f (cHex/EtOAc, 5/1) = 0.18. – **^{1}H NMR (**400 MHz, DMSO-d_6 [2.50 ppm], ppm) δ = 10.43 (s, 1H, N*H*), 7.92 (dd, *J* = 8.3, 1.5 Hz, 2H, C*H*$_{Ar}$), 7.83–7.75 (m, 2H, C*H*$_{Ar}$), 7.49–7.47 (m, 1H, C*H*$_{Ar}$), 7.46–7.42 (m, 8H, C*H*$_{Ar}$), 7.39–7.27 (m, 5H, C*H*$_{Ar}$), 4.11 (s, 1H, C*H*, C_{Alkyne}). Impurities: water from solvent at 3.33 ppm – **^{13}C NMR** (126 MHz, DMSO-d_6 [39.5 ppm], ppm) δ = 165.4 (1C, C_q, CO), 141.4 (d, *J* = 13.7 Hz, 1C, C_q), 139.7 (1C, C_q), 135.9 (d, *J* = 11.0 Hz, 2C, C_q), 135.1 (1C, C_q), 133.5 (d, *J* = 19.9 Hz, 4C, CH_{Ar}), 132.9 (d, *J* = 19.0 Hz, 2C, CH_{Ar}),

132.3 (2C, CH_{Ar}), 129.3 (2C, CH_{Ar}), 128.9 (d, *J* = 7.1 Hz, 4C, CH_{Ar}), 127.90 (d, *J* = 6.4 Hz, 2C, CH_{Ar}), 120.0 (2C, CH_{Ar}), 116.6 (1C, C_q), 83.6 (1C, C_q, C_{Alkyne}), 80.0 (1C, CH_{Alkyne}). – **^{31}P NMR** (162 MHz, DMSO-d_6, ppm) δ = -6.74 (s, 1P). – **MS** (FAB, 3-NBA), m/z (%): 422 (31) $[M+O]^+$, 406 (100) $[M^+]$, 289 (61), 183 (42), 154 (47). – **HRMS** (FAB, 3-NBA): m/z = calcd for $C_{27}H_{21}PON$ $[M+H]^+$: 406.1356; found 406.1378. – **IR** (ATR, ṽ) = 3285 (w), 2921 (w), 1650 (m), 1587 (s), 1507 (vs), 1486 (s), 1479 (s), 1434 (m), 1402 (s), 1316 (vs), 1293 (s), 1239 (s), 1176 (m), 1105 (w), 1088 (m), 1069 (w), 1016 (m), 832 (vs), 741 (vs), 693 (vs), 660 (s), 654 (s), 642 (s), 616 (s), 567 (w), 537 (vs), 504 (vs), 484 (s), 475 (s), 452 (m), 433 (m), 414 (w), 405 (w), 399 (w) cm^{-1}. – **M.p.** 125 C.

Additional information on the chemical synthesis is available *via* the Chemotion repository: https://dx.doi.org/10.14272/reaction/SA-FUHFF-UHFFFADPSC-LVHPWOUALX-UHFFFADPSC-NUHFF-NUHFF-NUHFF-ZZZ.

Additional information on the analytical data is available via: https://dx.doi.org/10.14272/LVHPWOUALXRSLV-UHFFFAOYSA-N.1.

5.2.3.2 Mononuclear complexes

(4-(Diphenylphosphino)-N-(2-propyn-1-yl)benzamide)$_3$CuI **(Cu-1-P1-I)**

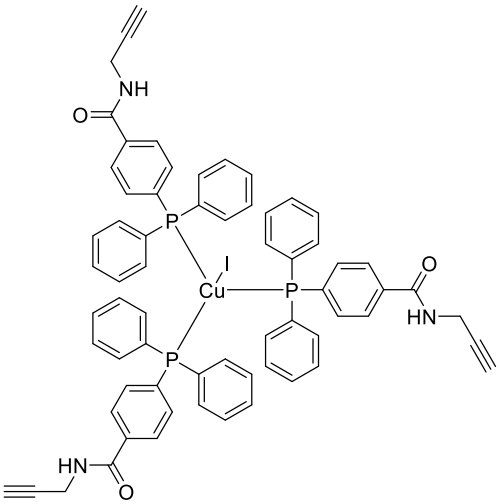

Copper (I) iodide (0.037 g, 0.194 mmol, 1.00 equiv) and 4-(diphenylphosphino)-N-(2-propyn-1-yl)benzamide (0.200 g, 0.582 mmol, 3.00 equiv) were dissolved in 5 mL of dry dichloromethane in a 10 mL crimp vial under a nitrogen atmosphere. The reaction mixture was degassed for 5 minutes with Argon and stirred for about 16 h at 22 °C. Afterward, the volume of the suspension was reduced under removed pressure to 1.5 mL. The complex was precipitated in 150 mL *n*-pentane, filtrated and washed with *n*-pentane (2 × 50 mL) and diethyl ether (15 mL). After removing the solvent residues under removed pressure, $C_{66}H_{54}CuIN_3O_3P_3$ (169 mg, 37% purity, 137 µmol, 69% yield) was obtained as a colorless powder.

^{1}H NMR (500 MHz, DMSO-d_6 [2.50 ppm], ppm) δ = 8.96 (t, *J* = 5.6 Hz, 3H, N*H)*, 7.76 (d, *J* = 7.9 Hz, 6*H*, CH_{Ar}), 7.44–7.29 (m, 36H, C*H*$_{Ar}$), 4.05 (dd, *J* = 5.6, 2.5 Hz, 6H, C*H*$_2$), 3.13 (t, *J* = 2.5 Hz, 3H, C*H*$_{Alkyne}$). Impurities: phosphine oxide (9.14, 7.99–7.87.66–7.62, 2.63 ppm), unknown impurities (1.10 ppm, 0.86 ppm). – **^{13}C NMR** (125 MHz, DMSO-d_6 [39.5 ppm], ppm)

δ = 165.9 (3C, C_q, CO), 135.0 (3C, C_q), 134.1 (d, *J* = 16.3 Hz, *C*H$_{Ar}$), 133.6 (d, *J* = 15.4 Hz, *C*H$_{Ar}$), 130.3 (*C*H$_{Ar}$), 129.1 (d, *J* = 8.2 Hz, *C*H$_{Ar}$), 127.6 (d, *J* = 8.2 Hz, *C*H$_{Ar}$), 81.7 (3C, C_q, C_{Alkyne}), 73.4 (3C, *C*H$_{Alkyne}$), 29.0 (3C, CH_2). Impurities: phosphine oxide (131.9 ppm, 129.3 ppm, 127.9 ppm), n-pentane (21.7 ppm, 13.9 ppm), diethyl ether (15.2 ppm), unknown impurity (64.9 ppm – **^{31}P NMR** (202 MHz, DMSO-d_6, ppm) δ = -7.55 (s, 3P, L_1). Impurities: unknown impurities at 25.11 ppm and 22.13 ppm. – **MS** (ESI) m/z (%): 1282 (1) $[M+Cu]^+$, 1220 (2) $[M+H]^+$, 1092 (9) $[M-I]^+$, 877 (15) $[L_2CuIH]^+$, 765 (15), 749 (17) $[L_2Cu]^+$, 704 (13), 687 (100) $[L_2H]^+$.– **HRMS** (ESI, $[M+H]^+$): calcd. 1220.1791, found 1220.1789. – **IR** (ATR, ṽ) = 3289 (w), 3050 (w), 1647 (m), 1523 (s), 1480 (s), 1434 (s), 1295 (m), 1094 (s), 744 (vs), 693 (vs), 509 (vs), 487 (s) cm^{-1}. – **M.p.** 117 °C.

Additional information on the chemical synthesis is available *via* the Chemotion repository: https://dx.doi.org/10.14272/reaction/SA-FUHFF-UHFFFADPSC-HNBUCRNOLH-UHFFFADPSC-NUHFF-MUHFF-NUHFF-ZZZ.

Additional information on the analytical data is available via: https://dx.doi.org/10.14272/HNBUCRNOLHWPMD-UHFFFAOYSA-M.1.

(N^4,N$^{4'}$-Di(propyn-1-yl)-(2,2'-bipyridine)-4,4'-dicarboxamide)(PPh$_3$)CuI **(Cu-1-L8-I)**

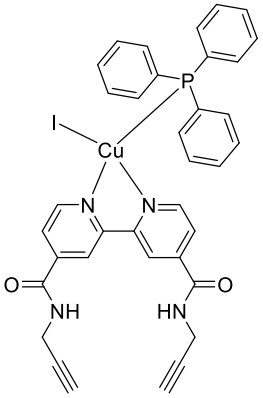

N^4,*N*$^{4'}$-di(propyn-1-yl)-[2,2'-bipyridine]-4,4'-dicarboxamide (130.0 mg, 0.410 mmol, 1.00 equiv), copper (I) iodide (77.8 mg, 0.410 mmol, 1.00 equiv) and triphenylphosphine (107 mg, 0.410 mmol, 1.00 equiv) were dissolved in dry dichloromethane (7 mL) in a 10 mL crimp vial under argon atmosphere. The reaction mixture was degassed with argon for 5 minutes and stirred for 20 h at 25 °C. The reaction mixture was filtrated, and the obtained solid was washed with *n*-pentane (20 mL) and diethyl ether (5 mL). The complex in the filtrate was precipitated in *n*-pentane (150 mL), filtered, and washed with *n*-pentane (20 mL) and diethyl ether (5 mL). After removing the solvent residues under reduced pressure, $C_{36}H_{29}CuIN_4O_2P$ (238 mg, 309 µmol, 76% yield) was obtained as a red powder.

^{1}H NMR (500 MHz, DMSO-d_6 [2.50 ppm], ppm) δ = 9.53 (t, *J* = 5.5 Hz, 2H, N*H*), 8.91 (s, 2H, C*H*$_{Ar}$), 8.79 (d, *J* = 5.2 Hz, 2H, C*H*$_{Ar}$), 7.95 (d, *J* = 5.3 Hz, 2H, C*H*$_{Ar}$), 7.66–7.59 (m, 1H, C*H*$_{Ar}$), 7.57–7.52 (m, 1H, C*H*$_{Ar}$), 7.39 (tdd, *J* = 17.8, 14.1, 7.4 Hz, 13H, C*H*$_{Ar}$), 4.17 (dd, *J* = 5.4, 2.6 Hz, 4H, C*H*$_2$), 3.24 (t, *J* = 2.6 Hz, 2H, *C*H$_{Alkyne}$).– **^{13}C NMR** (126 MHz, DMSO-d_6 [39.5 ppm], ppm) δ = 163.6 (2C, C_q, CO), 151.7 (2C, C_q, C_{Ar}), 150.0 (2C, *C*H$_{Ar}$), 142.5 (2C, C_q, *C*$_{Ar}$), 133.1 (d, *J* = 15.0 Hz, 6C, *C*H$_{Ar}$), 131.5 (d, *J* = 9.6 Hz, 3C, *C*$_q$), 129.9 (2C, *C*H$_{Ar}$), 128.7 (d, *J* = 9.1

Hz, 9C, *C*H$_{Ar}$), 123.8 (1C, *C*H$_{Ar}$), 119.9 (1C, *C*H$_{Ar}$), 80.5 (2C, C$_q$, C$_{Alkyne}$), 73.6 (2C, C*H*$_{Alkyne}$), 28.8 (2C, C*H*$_2$). Impurities: unknown (132.9, 132.3, 132.02 ppm). – **^{31}P NMR** (202 MHz, DMSO-d$_6$, ppm) δ = -3.27 (1P). Impurity: phosphine oxide (25.50 ppm). – **MS** (ESI, DCM), m/z (%): 1415 (1) $[2M-I]^+$, 1151 (4) $[2M-I-PPh_2]^+$, 833 (4) $[M+Cu]^+$, 643 (100) $[M-I]^+$, 369 (40), 297 (73). – **HRMS** ($[M-I]^+$): calcd 643.1319, found 643.1312. – I**R** (ATR, ṽ) = 3271 (s), 1684 (m), 1670 (s), 1649 (m), 1630 (m), 1550 (m), 1523 (vs), 1479 (m), 1434 (s), 1418 (w), 1390 (w), 1299 (s), 1271 (m), 1264 (m), 1237 (m), 1096 (m), 866 (w), 756 (s), 745 (s), 693 (vs), 671 (vs), 664 (s), 649 (s), 628 (m), 619 (m), 596 (m), 581 (m), 557 (m), 524 (vs), 503 (vs), 492 (s), 416 (w), 397 (w) cm^{-1}. EA ($C_{36}H_{29}CuIN_4O_2P$): Calcd C 56.08; H 3.79; N 7.27. Found C 55.88; H 3.51; N 7.51. – **M.p.** decomposition > 196 °C.

The molecular structure of the complex was determined by single-crystal X-ray diffraction.

Additional information on the chemical synthesis is available *via* the Chemotion repository: https://dx.doi.org/10.14272/reaction/SA-FUHFF-UHFFFADPSC-GFHGBFOZUD-UHFFFADPSC-NUHFF-MUHFF-NUHFF-ZZZ.

Additional information on the analytical data is available via: https://dx.doi.org/10.14272/GFHGBFOZUDEQCM-UHFFFAOYSA-M.1.

5.2.3.3 Dinuclear complexes

(2-(Diphenylphosphaneyl)pyridine)(4-(diphenylphosphino)-N-(2-propyn-1-yl)benzamide)$_2$Cu$_2$I$_2$ **(Cu-L1-P1-I)**

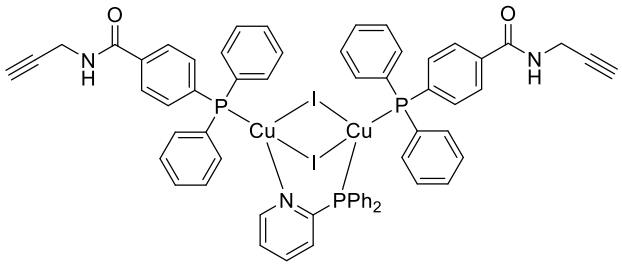

2-(Diphenylphosphaneyl)pyridine (0.058 g, 0.218 mmol, 1.00 equiv), copper (I) iodide (0.083 g, 0.437 mmol, 2.00 equiv) and 4-(diphenylphosphino)-N-(2-propyn-1-yl)benzamide (0.150 g, 0.437 mmol, 2.00 equiv) were dissolved in 5 mL of dry dichloromethane in a 10 mL crimp vial under an argon atmosphere. The reaction mixture was degassed for 5 minutes with argon and stirred for 16 h at 19 °C. The resulting complex was precipitated in 150 mL of *n*-pentane, filtrated, and washed with *n*-pentane (2 × 50 mL) and diethyl ether (10 mL). After removing the solvent residues under reduced pressure, the complex $C_{61}H_{50}Cu_2I_2N_3O_2P_3$ (209 mg, 0.16 mmol, 72% yield) was obtained as a light-yellow solid.

^{1}H NMR (500 MHz, CD_2Cl_2 [5.32 ppm], ppm) δ = 8.56 (br. s, 2H, N*H*), 7.80–7.08 (m, 42H, C*H*$_{Ar}$), 4.26 (s, 4H, C*H*$_2$), 2.30 (t, *J* = 2.6 Hz, 2H, C*H*$_{Alkyne}$). Impurities: water from solvent (1.55 ppm). – **^{13}C NMR** (126 MHz, CD_2Cl_2 [53.8 ppm], ppm) δ = 166.9 (2C, C$_q$, *C*O), 152.5 (*C*H$_{Ar}$),

137.7 (br.s, C_q), 134.8–134.0 (m, *C*H$_{Ar}$), 133.3–132.7 (m, C_q), 130.3–130.2 (m, *C*H$_{Ar}$), 129–128.9 (m, *C*H$_{Ar}$), 127.1 (d, *J* = 8.63 Hz, C_q), 125.0 (br.s, *C*H$_{Ar}$), 80.3 (2C, C_q, *C*H$_{Alkyne}$), 71.3 (2C, *C*H$_{Alkyne}$), 30.0 (2C, *C*H$_2$). – **^{31}P NMR** (202 MHz, CD_2Cl_2, ppm) δ = -4.72 (br.s, 1P, P_{NP}), -12.77 (br.s, 2P, P_{P1}). Signal with shoulder due to rotamers. − **MS** (FAB, 3-NBA) m/z (%): 1394 (1) $[M+Cu]^+$, 1204 (1) $[M-I]^+$, 859 (15) $[M-P-I]^+$, 779 (6) $[L_2Cu_2I]^+$, 708 (27) $[LCu_3I_2]^+$, 516 (76) $[LCu_2I]^+$, 344 (34) $[P]^+$, 326 (100) $[LCu]^+$, 264 (42) $[L]^+$. Mass of complex, 1329, not observed. **HRMS** (FAB, 3-NBA, $C_{17}H_{14}CuNP$): calcd. 326.0160, found 325.9893.− **IR** (ATR, ṽ) = 3289 (w), 3046 (vw), 1649 (m), 1598 (w), 1520 (m), 1482 (m), 1455 (w), 1434 (s), 1422 (w), 1391 (w), 1350 (w), 1295 (w), 1186 (w), 1156 (w), 1094 (m), 1027 (w), 999 (w), 987 (w), 847 (w), 742 (s), 720 (w), 693 (vs), 632 (w), 619 (w), 582 (w), 509 (vs), 492 (s), 455 (w), 449 (w), 429 (w) cm^{-1}. – **M.p.** 140 °C.

Additional information on the chemical synthesis is available *via* the Chemotion repository: https://dx.doi.org/10.14272/reaction/SA-FUHFF-UHFFFADPSC-BLWZYKXZKY-UHFFFADPSC-NUHFF-LUHFF-NUHFF-ZZZ.

Additional information on the analytical data is available via: https://dx.doi.org/10.14272/BLWZYKXZKYRBEN-UHFFFAOYSA-L.1.

***(2-(Diphenylphosphaneyl)pyridine)(4-(diphenylphosphino)-N-(2-propyn-1-yl)benzamide)$_2$Cu$_2$Br$_2$* (Cu-L1-P1-Br)**

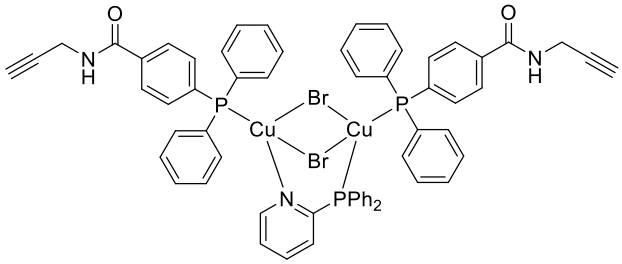

A 10 mL crimp vial was charged with 4-diphenylphosphanyl-N-prop-2-ynylbenzamide (150 mg, 437 µmol, 2.00 equiv), copper (I) bromide (62.7 mg, 0.437 mmol, 2.00 equiv) and 2-(diphenylphosphaneyl)pyridine (57.5 mg, 218 µmol, 1.00 equiv). The substances were dissolved in 5 mL of dry dichloromethane under argon and the suspension was degassed with argon for 5 minutes. The reaction mixture was stirred for 18 h at 22 °C in the dark. The reaction mixture was then poured into 10 mL of *n*-pentane. The precipitate was filtered off, washed with *n*-pentane (5 mL) and diethyl ether (5 mL) and was dried in vacuum to obtain the complex $C_{61}H_{50}Br_2Cu_2N_3O_2P_3$ (181 mg, 146 µmol, 67% yield) as an off-white solid.

^{1}H NMR (500 MHz, DMSO-d_6, ppm) δ = 8.97 (t, *J* = 5.6 Hz, 2H, N*H*), 7.87–7.75 (m 5H, C*H*$_{Ar}$), 7.39–7.25 (m, 37H, C*H*$_{Ar}$), 4.06 (dd, *J* = 5.6, 2.5 Hz, 4H, C*H*$_2$), 3.14 (t, *J* = 2.5 Hz, 2H, C*H*$_{Alkyne}$). Broad signal at 8.71 ppm corresponding to complex, evaluated with DOSY and HSQC. Impurities: 3.33 ppm (water from solvent). – **^{13}C NMR** (126 MHz, CD_2Cl_2 [53.84 ppm], ppm) δ = 166.6 (2C, *C*O), 151.9 (2C, C_q), 138.2 (2C, C_q), 136.9 (1C, *C*H$_{Ar}$), 134.7 (1C, C_q),

134.2–133.9 (m, 17C, *C*CH_{Ar}), 132 (6C, C_q), 130.0 (4C, *C*CH_{Ar}), 129.9 (2C, *C*CH_{Ar}), 128.7–128.5 (m, 13C, *C*CH_{Ar}), 126.9 (d, *J* = 8.0 Hz, 4C, *C*CH_{Ar}), 124.3 (1C, *C*CH_{Ar}), 79.9 (2C, C_q, C_{Alkyne}), 71.0 (2C, *C*H_2), 29.6 (2C, CH_{Alkyne}). – ^{31}P NMR (162 MHz, DMSO-d6, ppm) δ = -4.90 (s, 1P, L), -7.39 (s, 2P, P). – **MS** (FAB, 3-NBA) *m/z* (%): 1299 (1) $[M+Cu]^+$, 1154 (1) $[M-Br]^+$, 669 (38) $[LPCu]^+$, 548 (8) $[LCu_2Br]^+$, 468 (33) $[LCu_2Br]^+$, 406 (8) $[PCu]^+$, 344 (44) $[P]^+$, 326 (100) $[LCu]^+$, 264 (18) $[L]^+$. Exact mass of complex, 1235, not observed. – **HRMS** (FAB, 3-NBA, $C_{17}H_{14}CuNP$): calcd. 326.0160, found 325.9930. – **IR** (ATR, ṽ) = 3289 (w), 3050 (w), 1647 (m), 1598 (w), 1523 (s), 1453 (w), 1434 (s), 1391 (w), 1295 (m), 1187 (w), 1156 (w), 1095 (s), 1026 (w), 1018 (w), 999 (w), 987 (w), 919 (w), 849 (w), 744 (vs), 720 (w), 693 (vs), 582 (m), 509 (vs), 487 (s), 426 (m) cm^{-1}. – **EA** ($C_{61}H_{50}Br_2Cu_2N_3O_2P_3$): Calcd C 59.23; H 4.07; N 3.40. Found C 58.70; H 4.4; N 3.45. – **M.p.** 130 °C.

Additional information on the chemical synthesis is available *via* the Chemotion repository: https://dx.doi.org/10.14272/reaction/SA-FUHFF-UHFFFADPSC-MTTRUNXCXD-UHFFFADPSC-NUHFF-LUHFF-NUHFF-ZZZ.

Additional information on the analytical data is available via: https://dx.doi.org/10.14272/MTTRUNXCXDHDAY-UHFFFAOYSA-L.1.

(2-(Diphenylphosphaneyl)pyridine)(4-(diphenylphosphino)-N-(2-propyn-1-yl)benzamide)$_2$Cu$_2$Cl$_2$ **(Cu-L1-P1-Cl)**

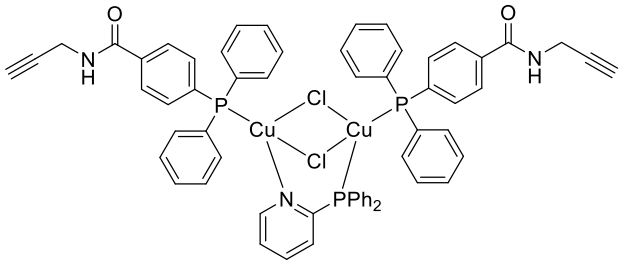

2-(Diphenylphosphaneyl)pyridine (48.8 mg, 186 µmol, 1.00 equiv), copper (I) chloride (36.7 mg, 371 µmol, 2.00 equiv) and 4-(diphenylphosphino)-N-(2-propyn-1-yl)benzamide 4-diphenylphosphanyl-N-prop-2-ynylbenzamide (127 mg, 371 µmol, 2.00 equiv) were dissolved in 5 mL of dry dichloromethane in a 10 mL crimp vial under an argon atmosphere. The reaction mixture was degassed for 5 minutes with argon and stirred for 16 h at 22 °C. The resulting complex was precipitated in 150 mL of *n*-pentane, filtered, and washed with *n*-pentane (2 × 50 mL) and diethyl ether (10 mL). After removing the solvent residues under reduced pressure, the complex $C_{61}H_{50}Cu_2Cl_2N_3O_2P_3$ (141 mg, 123 µmol, 66% yield) was obtained as a light-yellow solid.

^{1}H NMR (500 MHz, DMSO-d_6 [2.50 ppm], ppm) δ = 8.97 (t, *J* = 5.6 Hz, 2H, N*H*), 7.77 (d, *J* = 8.0 Hz, 5H, C*H*$_{Ar}$), 7.48–7.27 (m, 37H, C*H*$_{Ar}$), 4.06 (dd, *J* = 5.5, 2.5 Hz, 4H, C*H*$_2$), 3.14 (t, *J* = 2.4 Hz, 2H, C*H*$_{Alkyne}$). – **^{13}C NMR** (126 MHz, CD_2Cl_2 [53.8 ppm], ppm) δ = 167.0 (2C, C_q, *C*O), 151.9 (d, *J* = 11.4 Hz, 2C, C_q), 138.1 (d, *J* = 27.2 Hz, 2C, C_q), 137.0 (br.s, *C*CH_{Ar}), 135.3 (2C, C_q)**,** 134.7– 34.3 (m, *C*CH_{Ar}), 134.2 (d, *J* = 14.1 Hz, *C*CH_{Ar}), 132.6 (d, *J* = 30.3 Hz, 5C, C_q),

131.2 (*C*H$_{Ar}$), 130.5 (*C*H$_{Ar}$), 130.4 (*C*H$_{Ar}$), 129.2–128.8 (m, *C*H$_{Ar}$), 127.4 (d, *J* = 8.6 Hz, *C*H$_{Ar}$), 124.5 (br.s, *C*H), 80.3 (2C, C$_q$, *C*H$_{Alkyne}$), 71.5 (2C, *C*H$_{Alkyne}$), 29.9 (2C, *C*H$_2$). – **^{31}P NMR** (202 MHz, DMSO-d$_6$, ppm) δ = -4.40 (1P), -6.31 (2P). Impurity: phosphine oxide (22.13 ppm). – **MS** (FAB, 3-NBA) m/z (%): 1110 (1) [M - Cl]$^+$, 767 (4) [M - Cl -L$_{NP}$]$^+$, 749 (13), 687 (7), 669 (8), 589 (10), 344 (17) [P+H]$^+$, 326 (36) [L$_{NP}$Cu]$^+$, 154 (100). Mass of complex, 1145, not observed. – **IR** (ATR, ṽ) = 3284 (w), 3053 (w), 1647 (m), 1598 (w), 1524 (m), 1482 (m), 1455 (w), 1434 (s), 1391 (w), 1350 (w), 1296 (m), 1184 (w), 1156 (w), 1095 (m), 1018 (w), 999 (w), 986 (w), 849 (w), 744 (vs), 720 (w), 693 (vs), 629 (m), 619 (w), 582 (w), 509 (vs), 459 (w), 452 (w), 432 (w), 421 (w) cm^{-1}. – **M.p.** decomp > 120 – 200 °C.

Additional information on the chemical synthesis is available *via* the Chemotion repository: https://dx.doi.org/10.14272/reaction/SA-FUHFF-UHFFFADPSC-YXKPSJHSUS-UHFFFADPSC-NUHFF-LUHFF-NUHFF-ZZZ.

Additional information on the analytical data is available via: https://dx.doi.org/10.14272/YXKPSJHSUSFKAS-UHFFFAOYSA-L.1.

***(2-(Diphenylphosphaneyl)pyridine)(4-(diphenylphosphino)-N-(2-propyn-1-yl)benzamide)$_2$Cu$_2$CN$_2$* (Cu-L1-P1-CN)**

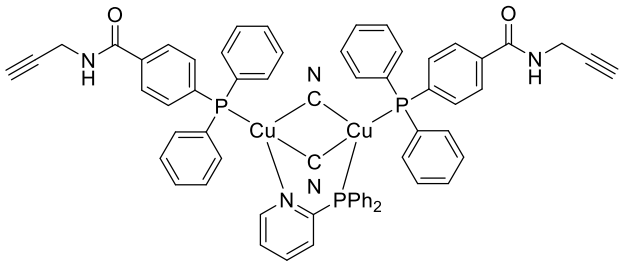

2-(Diphenylphosphaneyl)pyridine (57.5 mg, 218 µmol, 1.00 equiv), copper (I) cyanide (39.5 mg, 437 µmol, 2.00 equiv) and 4-(diphenylphosphino)-N-(2-propyn-1-yl)benzamide (150 mg, 437 µmol, 2.00 equiv) were dissolved in 5 mL of dry dichloromethane in a 10 mL crimp vial under an argon atmosphere. The reaction mixture was degassed for 5 minutes with argon and stirred for 16 h at 22 °C. The resulting complex was precipitated in 150 mL of *n*-pentane, filtered, and washed with *n*-pentane (2 × 50 mL) and diethyl ether (10 mL). After removing the solvent residues under reduced pressure, the complex $C_{63}H_{50}Cu_2(CN)_2N_5O_2P_3$ (141 mg, 123 µmol, 66% yield) was obtained as a yellow solid.

^{1}H NMR (500 MHz, CD_2Cl_2 [5.32 ppm], ppm) δ = 8.40 (br.s, 2H, N*H*), 7.48–7.17 (m, 28H, C*H*$_{Ar}$), 7.10–6.96 (m, 14H, C*H*$_{Ar}$), 4.11 (dd, *J* = 5.5, 2.5 Hz, 4H, C*H*$_2$), 2.28 (t, *J* = 2.5 Hz, 2H, C*H*$_{Alkyne}$). Impurities: 2% dichloromethane (5.33 ppm), water from the NMR solvent (1.59 ppm).– **^{13}C NMR** (126 MHz, CD_2Cl_2 [53.8 ppm], ppm) δ = 167.3 (2C, C$_q$, *C*O), 150.6–150.4 (m, C$_q$), 139.2 (*C*H), 139.0 *C*H$_{Ar}$), 136.4–136.1 (m, *C*H$_{Ar}$), 134.9(*C*H$_{Ar}$), 134.6–133.7 (m, *C*H$_{Ar}$), 130.0 (*C*H$_{Ar}$), 123.0 (*C*H$_{Ar}$), 129.0–128.6 (m, *C*H$_{Ar}$), 127.2 (d, *J* = 8.6 Hz, *C*H$_{Ar}$), 123.8

(C_q), 80.7 (2C, C_q, *C*H*Alkyne*), 71.5 (2C, *C*H$_{Alkyne}$), 29.9 (2C, *C*H$_2$). – **^{31}P NMR** (202 MHz, CD_2Cl_2, ppm) δ = -1.79 (1P, L_{NP}), -4.07 (2P, L_P). – **MS** (ESI, DCM) *m/z* (%): 1364 (2) $[P_2(NP)_2Cu_3(CN)_2]^+$, 1192 (1) $[M + Cu]^+$, 1181 (1) $[P_3Cu_2CN]^+$, 1112 (1) $[P_2(NP)Cu]^+$, 1112 (1) $[P(NP)_2Cu_3(CN)_2]^+$, 1101 (1) $[M - CN]^+$, 838 (9) $[P_2Cu_2CN]^+$, 759 (4) $[P(NP)_2Cu_2CN]^+$, 749 (2) $[P_2Cu]^+$, 678 (91) $[(NP)_2Cu_2CN]^+$, 669 (5) $[P(NP)_2Cu]^+$, 589 (100) $[(NP)_2Cu]^+$. Exact mass of complex, 1127, not observed. HRMS (ESI, DCM, $C_{62}H_{50}Cu_2N_4O_2P_3$): calcd. 1101.1739, found 1101.1725. – **IR** (ATR, ṽ) = 3292 (w), 3053 (w), 2113 (w), 1646 (m), 1521 (m), 1482 (m), 1435 (s), 1421 (w), 1296 (m), 1094 (m), 742 (vs), 693 (vs), 630 (m), 582 (m), 509 (vs), 493 (vs), 456 (s), 422 (s), 397 (m), 375 (w) cm^{-1}. – **EA** ($C_{63}H_{50}Cu_2N_5O_2P_3$) calcd. C 67.02, H 4.46, N 6.20; found C 66.71, H 4.55, N 6.26. – **M.p.** decomp > 118 – 165 °C.

Additional information on the chemical synthesis is available *via* the Chemotion repository: https://dx.doi.org/10.14272/reaction/SA-FUHFF-UHFFFADPSC-DRERHWHJBP-UHFFFADPSC-NUHFF-NUHFF-NUHFF-ZZZ.

Additional information on the analytical data is available via: https://dx.doi.org/10.14272/DRERHWHJBPDWAA-UHFFFAOYSA-N.1.

***(2-(Diphenylphosphaneyl)pyridine)(4-(diphenylphosphino)-N-(2-propyn-1-yl)benzamide)$_2$Cu$_2$SCN$_2$* (Cu-L1-P1-SCN)**

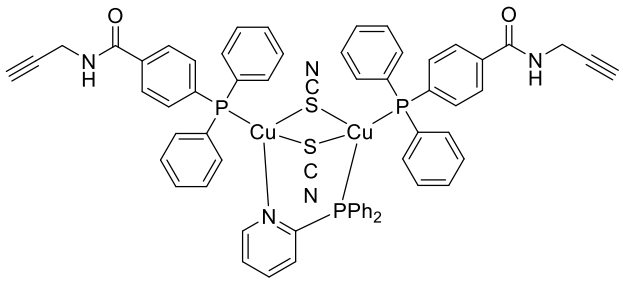

2-(Diphenylphosphaneyl)pyridine (0.0500 g, 0.190 mmol, 1.00 equiv), copper (I) thiocyanate (0.046 g, 0.380 mmol, 2.00 equiv) and 4-(diphenylphosphino)-N-(2-propyn-1-yl)benzamide (0.130 g, 0.380 mmol, 2.00 equiv) were dissolved in 5 mL of dry dichloromethane in a 10 mL crimp vial under a nitrogen atmosphere. The reaction mixture was degassed for 5 minutes with Argon and stirred for about 16 h at room temperature. The resulting complex was precipitated in 50 mL *n*-pentane, filtrated and washed with *n*-pentane (2 × 50 mL). After removing the solvent residues under removed pressure, $C_{63}H_{50}Cu_2N_5O_2P_3S_2$ (180 mg, 95% purity, 145 µmol, 76% yield) was obtained as a colorless powder.

^{1}H NMR (500 MHz, DMSO-d_6, ppm) δ = 8.99 (t, *J* = 5.6 Hz, 2H, N*H),* 7.81 (d, *J* = 8.4 Hz, 4H, C*H*$_{Ar}$), 7.50–7.25 (m, 38H, C*H*$_{Ar}$), 4.05 (dd, *J* = 5.6, 2.5 Hz, 4H, C*H*$_2$), 3.14 (t, *J* = 2.5 Hz, 2H, C*H*$_{Alkyne}$). 1% Impurities: phosphine oxide (8.0–7.97 ppm, 7.75–7.53 ppm), dichloromethane (5.76 ppm), water from solvent (3.33 ppm), ethyl acetate (1.99 ppm, 1.16 ppm), tetramethyl urea (1.26 ppm), H grease (1.24 ppm, 0.85 ppm), diethyl ether (1.09 ppm) unknown impurities

(0.66 ppm). – **^{13}C NMR (**126 MHz, DMSO-d_6 [39.5 ppm], ppm) δ = 165.3 (2C, C_q, *C*O), 136.9 (d, *J* = 26.1 Hz, C_q), 135.0 (*C*H$_{Ar}$), 133.4 (d, *J* = 14.6 Hz, *C*H$_{Ar}$), 133.0 (d, *J* = 14.2 Hz), 132.3 (d, *J* = 28.1 Hz, C_q), 131.5 (d, *J* = 10.6 Hz, C_q), 130.3 (*C*H$_{Ar}$), 130.2 (*C*H$_{Ar}$), 128.9 (d, *J* = 8.1 Hz, *C*H$_{Ar}$), 128.7 (*C*H$_{Ar}$), 127.4 (d, *J* = 7.6 Hz, *C*H$_{Ar}$), 81.1 (2C, C_q, C_{Alkyne}), 73.0 (2C, *C*H$_{Alkyne}$), 28.6 (2C, *C*H$_2$). – **^{31}P NMR** (202 MHz, DMSO-d_6, ppm) δ = -2.66 (br.s, 1P, L_{NP}), -4.61 (br.s, 2P, L_P). Impurities: Phosphine oxide (25.09 ppm). – **MS** (ESI, DCM) m/z (%): 1256 (1) [M + Cu]$^+$, 1176 (1) [$L_P(L_{NP})_2Cu_3(SCN)_2$]$^+$, 1133 (1) [M - SCN]$^+$, 1096 (1) [$(L_{NP})_3Cu_3(SCN)_2$]$^+$, 1053 (1) [$L_P(L_{NP})_2Cu_2(SCN)_2$]$^+$, 973 (6) [$(L_{NP})_3Cu_2SCN$]$^+$, 870 (1) [$(L_P)_2Cu_2SCN$]$^+$, 852 (33) [$(L_{NP})_3Cu$]$^+$, 749 (1) [$(L_P)_2Cu$]$^+$, 710 (8) [$(L_{NP})_2Cu_2SCN$]$^+$, 669 (6) [$L_P(L_{NP})Cu$]$^+$, 589 (100) [$(L_{NP})_2Cu$]$^+$. – **HRMS** (ESI, [$(L_P)_2Cu_2SCN$]$^+$): calcd. 870.0590, found. 870.0578. – **IR** (ATR, ṽ) = 3292 (w), 2099 (m), 1647 (m), 1598 (w), 1526 (m), 1482 (m), 1435 (m), 1421 (w), 1296 (m), 1184 (w), 1154 (w), 1095 (m), 987 (w), 849 (w), 742 (s), 720 (w), 693 (vs), 630 (m), 584 (m), 507 (vs), 456 (m), 422 (m), 399 (w) cm^{-1}. – **M.p.** decomp 110-160 °C.

Additional information on the chemical synthesis is available *via* the Chemotion repository: https://dx.doi.org/10.14272/reaction/SA-FUHFF-UHFFFADPSC-RXVJMWOXAL-UHFFFADPSC-NUHFF-LUHFF-NUHFF-ZZZ.

Additional information on the analytical data is available via: https://dx.doi.org/10.14272/RXVJMWOXALFAFE-UHFFFAOYSA-L.1.

***(2-(Diphenylphosphaneyl)-4-methylpyridine)(4-(diphenylphosphino)-N-(2-propyn-1-yl)benzamide)$_2$Cu$_2$I$_2$* (Cu-L5-P1-I)**

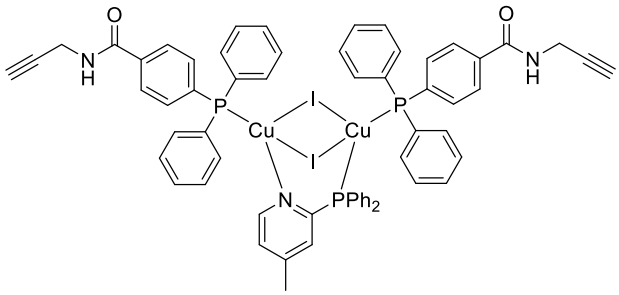

A 10 mL crimp vial was charged with 4-diphenylphosphanyl-N-prop-2-ynylbenzamide (150 mg, 0.44 mmol, 2.00 equiv), copper (I) iodide (83.2 mg, 437 µmol, 2.00 equiv) and (2-(diphenylphosphaneyl)-4-methylpyridine (60.6 mg, 218 µmol, 1.00 equiv). The substances were dissolved in 5 mL dry dichloromethane under argon and the suspension was degassed with argon for 5 minutes. The reaction mixture was stirred for 16 h at 22 °C in the dark. The reaction mixture was then poured into 10 mL *n*-pentane. The precipitate was filtered off, washed with *n*-pentane (5 mL) and diethyl ether (5 mL) and was dried in vacuum. After removing the solvent residues under reduced pressure, the complex $C_{62}H_{52}Cu_2I_2N_3O_2P_3$ (202 mg, 0.150 mmol, 69% yield) was obtained as a light-yellow solid.

^{1}H NMR (500 MHz, CD_2Cl_2 [5.32 ppm], ppm) δ = 8.40 (s, 1H, N*H*), 7.87–6.78 (m, 40H, C*H*), 6.93 (b.s., 1H, C*H*), 4.29–4.25 (br s., 4H, CH_2), 2.30 (t, *J* = 2.6 Hz, 2H, CH_{Alkyne}), 2.25 (s, 3H, CH_3). − **^{1}H NMR** (500 MHz, DMSO-d_6 [2.50 ppm], ppm) δ = 8.99 (t, *J* = 5.6 Hz, 2H, N*H*), 7.79 (d, *J* = 7.9 Hz, 4H, C*H*), 7.61–7.15 (m, 37H, C*H*), 4.07 (dd, *J* = 5.5, 2.5 Hz, 4H, CH_2), 3.15 (t, *J* = 2.5 Hz, 2H, CH_{Alkyne}), 2.25 (s, 3H, CH_3). Impurities: 3.33 ppm (water from solvent). − **^{13}C NMR** (126 MHz, CD_2Cl_2) δ = 166.5 (2C, C_q, *C*O), 151.7 (2C, C_q), 149.3 (C_q), 134.4 (br.s., *C*H_{Ar}), 133.7 (d, *J* = 14.0 Hz, *C*H_{Ar}), 133.4–133.2 (m, *C*$_q$), 130.3 (*C*H_{Ar}), 129.7 (*C*H_{Ar}), 128.5−128.4 (m, *C*H_{Ar}), 126.7 (d, *J* = 9.0 Hz, *C*H_{Ar}), 125.6 (*C*H_{Ar}), 117.6 (C_q), 80.0 (2C, C_q, C_{Alkyne}), 70.9 (2C, *C*H_{Alkyne}), 29.6 (2C, *C*H_2), 20.9 (*C*H_3). − **^{31}P NMR** (202 MHz, CD_2Cl_2) δ = - 4.67 (1P, L^{PN}), -13.29 (d, *J* = 357.4 Hz, 2P, L^{P}). − **MS** (FAB, 3-NBA) m/z (%): 1407 (1) $[M+Cu]^+$, 1344 (1) $[M+H]^+$,1216 (4) $[M-I]^+$, 873 (25) $[M-P-I]^+$, 779 (6) $[L_2Cu_2I]^+$, 721 (23) $[LCu_3I_2]^+$, 530 (88) $[LCu_2I]^+$, 340 (97) $[LCu]^+$, 154 (100). − **IR** (ATR, ṽ) = 3293 (w), 1649 (m), 1598 (w), 1523 (m), 1482 (m), 1434 (m), 1391 (w), 1351 (w), 1296 (w), 1186 (w), 1156 (w), 1095 (m), 1027 (w), 1018 (w), 999 (w), 987 (w), 847 (w), 829 (w), 744 (s), 718 (w), 693 (vs), 630 (m), 619 (w), 582 (m), 513 (vs), 497 (vs), 463 (s), 446 (m), 433 (m), 392 (w), 375 (w) cm^{-1}. **EA** ($C_{62}H_{52}Cu_2I_2N_3O_2P_3$): Calcd C 55.37; H 3.90; N 3.12. Found C 55.41; H 3.83; N 3.23.− **M.p**. 160 °C.

Additional information on the chemical synthesis is available *via* the Chemotion repository: https://dx.doi.org/10.14272/reaction/SA-FUHFF-UHFFFADPSC-DWJIVJKXKU-UHFFFADPSC-NUHFF-LUHFF-NUHFF-ZZZ.

Additional information on the analytical data is available via:. https://dx.doi.org/10.14272/DWJIVJKXKUVFBE-UHFFFAOYSA-L.1.

***(2-(Diphenylphosphaneyl)-4-methylpyridine)(4-(diphenylphosphino)-N-(2-propyn-1-yl)benzamide)$_2$Cu$_2$Br$_2$* (Cu-L5-P1-Br)**

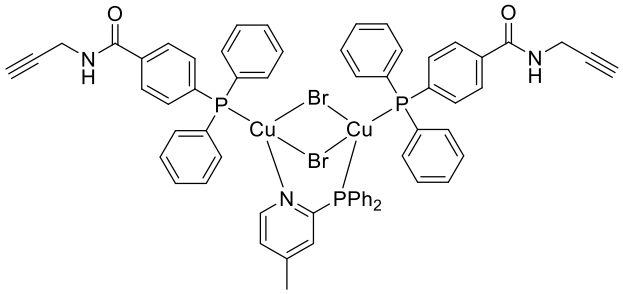

A 10 mL crimp vial was charged with 4-diphenylphosphanyl-*N*-prop-2-ynylbenzamide (150 mg, 437 µmol, 2.00 equiv), copper (I) bromide (62.7 mg, 0.430 mmol, 2.00 equiv) and 2-(diphenylphosphaneyl)-4-methylpyridine (60.6 mg, 218 µmol, 1.00 equiv). The substances were dissolved in 5 mL of dry dichloromethane under argon and the suspension was degassed with argon for 5 minutes. The reaction mixture was stirred for 16 h at 22 °C in the dark. The reaction mixture was then poured into 10 mL of *n*-pentane. The precipitate was filtered off, washed with *n*-pentane (5 mL) and

diethyl ether (5 mL) and was dried in vacuum. After removing the solvent residues under reduced pressure, the complex $C_{62}H_{52}Cu_2Br_2N_3O_2P_3$ (199 mg, 0.150 mmol, 69% yield) was obtained as a light-yellow solid.

^{1}H NMR (500 MHz, DMSO-d_6 [2.50 ppm], ppm) δ = 8.97 (t, *J* = 5.6 Hz, 2H, N*H*), 7.78 (d, *J* = 8.0 Hz, 4H), 7.44–7.21 (m, 37H), 4.06 (dd, *J* = 5.6, 2.5 Hz, 4H), 3.13 (t, *J* = 2.5 Hz, 2H), 2.22 (s, 3H). Impurities: water from solvent (3.33 ppm). *n*-pentane (1.28–1.42, 0.86 ppm). – **^{13}C NMR** (126 MHz, CD_2Cl_2 [53.8 ppm], ppm) δ = 167.0 (2C, C_q, CO), 152.1 (C_q), 149.5 (C_q), 138.6 (2C, C_q), 135.0 (C_q), 134.8–133.9 (m, CH_{Ar}), 133.2–132.6 (m, C_q), 130.5–130.0 (m, CH_{Ar}), 129.0 (d, *J* = 8.0 Hz, CH_{Ar}), 127.3 (d, *J* = 8.0 Hz, CH_{Ar}), 125.9 (CH_{Ar}), 80.3 (2C, C_q, C_{Alkyne}), 71.4 (2C, CH_{Alkyne}), 30.0 (2C, CH_2), 21.4 (1C, CH_3). Impurities: n-pentane (34.5, 22.7, 14.2 ppm). – **^{31}P NMR** (202 MHz, DMSO-d_6) δ = -4.73 (br.s, 1P, L_{NP}), - 7.51 (br.s., 2P, L_P). – **MS** (FAB, 3-NBA), m/z (%): 1169 (1) $[M\text{-}Br]^+$, 905 (11) $[M\text{-}L_P]^+$, 827 (7) $[M\text{-}Br\text{-}L_P]$, 683 (33) $[CuL_{NP}L_P]^+$, 484 (63) $[CuBrL_P]^+$, 340 (100), 278 (20) $[L_{NP}+H]^+$. Exact Mass of complex, 1248, not found. – **IR** (ATR, ṽ) = 3279 (w), 3037 (vw), 1649 (m), 1598 (w), 1523 (m), 1482 (m), 1434 (m), 1296 (m), 1095 (m), 847 (w), 744 (s), 718 (w), 693 (vs), 669 (m), 629 (m), 619 (m), 582 (m), 552 (w), 511 (vs), 465 (s), 442 (m), 435 (m), 422 (m), 411 (w), 401 (w), 388 (w), 375 (w) cm^{-1}. – **EA** ($C_{62}H_{52}Cu_2Br_2N_3O_2P_3$+$H_2O$): calcd C 58.68; H 4.29; N 3.31. found C 58.86; H 3.95; N 3.32. – **M.p**. 155 °C.

Additional information on the chemical synthesis is available *via* the Chemotion repository: https://dx.doi.org/10.14272/reaction/SA-FUHFF-UHFFFADPSC-LJDOKMYDYR-UHFFFADPSC-NUHFF-LUHFF-NUHFF-ZZZ.

Additional information on the analytical data is available via: https://dx.doi.org/10.14272/LJDOKMYDYRXCRH-UHFFFAOYSA-L.1.

(2-(Diphenylphosphaneyl)-4-methylpyridine)(4-(diphenylphosphino)-N-(2-propyn-1-yl)benzamide)$_2$Cu$_2$Cl$_2$ **(Cu-L5-P1-Cl)**

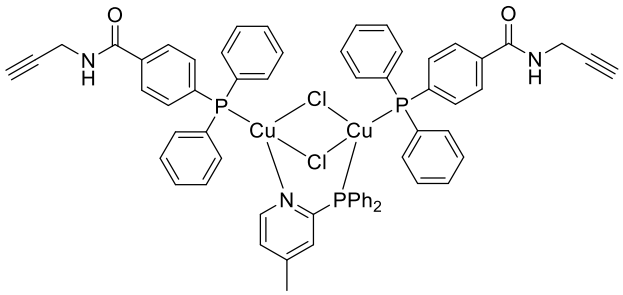

(2-(Diphenylphosphaneyl)-4-methylpyridine (60.6 mg, 218 µmol, 1.00 equiv), copper (I) chloride (43.2 mg, 437 µmol, 2.00 equiv) and 4-(diphenylphosphino)-*N*-(2-propyn-1-yl)benzamide (150 mg, 437 µmol, 2.00 equiv) were dissolved in 5.5 mL of dry dichloromethane in a 10 mL crimp vial under an argon atmosphere. The reaction mixture was degassed for 5 minutes with argon and stirred for 16 h at 22 °C. The resulting complex was

precipitated in 150 mL of *n*-pentane, filtered, and washed with *n*-pentane (2 × 50 mL) and diethyl ether (10 mL). After removing the solvent residues under reduced pressure, the complex $C_{62}H_{52}Cu_2Cl_2N_3O_2P_3$ (183 mg, 158 µmol, 72% yield) was obtained as a light-yellow solid.

^{1}H NMR (500 MHz, DMSO-d_6 [2.50 ppm], ppm) δ = 8.97 (t, *J* = 5.6 Hz, 2H, N*H*), 7.77 (d, *J* = 8.0 Hz, 4H, C*H*$_{Ar}$), 7.48–7.27 (m, 37H, C*H*$_{Ar}$), 4.06 (dd, *J* = 5.5, 2.5 Hz, 4H, C*H*$_2$), 3.14 (t, *J* = 2.4 Hz, 2H, C*H*$_{Alkyne}$), 2.20 (s, 3H, C*H*$_3$). Impurities: water from solvent (3.33 ppm). − **^{13}C NMR** (126 MHz, CD_2Cl_2 [53.8 ppm], ppm) δ = 167.0 (2C, C_q, *C*O), 151.7 (d, *J* = 11.4 Hz, 2C, *C*$_q$), 149.4 (C_q), 138.1 (d, *J* = 27.2 Hz, 2C, *C*$_q$), 135.3 (2C, C_q), 134.5 (d, *J* = 14.4 Hz, *C*H$_{Ar}$), 134.2 (d, *J* = 12.8 Hz, *C*H$_{Ar}$), 132.7 (d, *J* = 30.0 Hz, C_q), 130.5 (*C*H$_{Ar}$), 130.4 (*C*H$_{Ar}$), 129.1 (d, *J* = 8.0 Hz, *C*H$_{Ar}$), 127.4 (d, *J* = 7.8 Hz, *C*H$_{Ar}$), 80.4 (2C, C_q, *C*H$_{Alkyne}$), 71.5 (2C, *C*H$_{Alkyne}$), 29.9 (2C, *C*H$_2$), 21.39 (1C, *C*H$_3$). − **^{31}P NMR** (202 MHz, DMSO-d_6, ppm) δ = -4.42 (1P), -6.34 (2P). Impurity: phosphine oxide (22.4 ppm). − **MS** (FAB, 3-NBA), m/z (%): 1160 (1) $[M+H]^+$, 815 (15), 783 (10) $[M\text{-}Cl\text{-}P]^+$, 749 (23), 717 (41), 716 (12), 715 (33), 683 (22) $[L+P]^+$, 617 (50), 616 (2), 538 (22), 440 (57) $[Cu_2ClL]^+$, 340 (100) $[CuL]^+$, 289 (17). Exact Mass of complex, 1160, found. − **IR** (ATR, ṽ) = 3302 (w), 3293 (w), 1655 (m), 1649 (m), 1598 (w), 1527 (m), 1482 (m), 1435 (m), 1299 (w), 1096 (m), 1027 (w), 1018 (w), 999 (w), 987 (w), 849 (w), 745 (s), 718 (w), 693 (vs), 663 (m), 629 (w), 619 (w), 582 (m), 510 (vs), 465 (s), 441 (w), 421 (w), 407 (w), 398 (w), 387 (w) cm^{-1}. − **EA** ($C_{62}H_{52}Cl_2Cu_2N_3O_2P_3 + H_2O$): Calcd C 63.11 ; H 4.61; N 3.56. Found C 63.12; H 4.24; N 3.57. − **M.p.** 166 °C.

Additional information on the chemical synthesis is available *via* the Chemotion repository: https://dx.doi.org/10.14272/reaction/SA-FUHFF-UHFFFADPSC-PBBMVWNICV-UHFFFADPSC-NUHFF-LUHFF-NUHFF-ZZZ.

Additional information on the analytical data is available via: https://dx.doi.org/10.14272/PBBMVWNICVQPNS-UHFFFAOYSA-L.1.

***(2-(Diphenylphosphaneyl)pyridine)(2-(methacryloyloxy)ethyl-4-(diphenylphosphino)benzoate)$_2$Cu$_2$I$_2$* (Cu-L1-P2-I)**

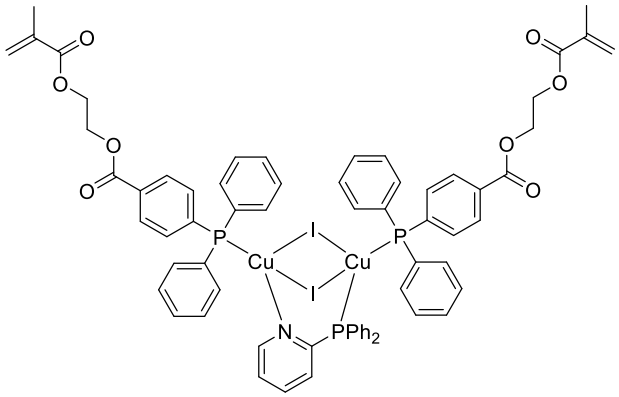

Diphenyl(pyridin-2-yl)phosphane (65.4 mg, 249 µmol, 1.00 equiv), copper (I) iodide (94.7 mg, 497 µmol, 2.00 equiv) and 2-(methacryloyloxy)ethyl-4-(diphenylphosphino)benzoate (208 mg, 497 µmol, 2.00 equiv) were dissolved in 5 mL of dry dichloromethane in a 10 mL crimp vial under an argon atmosphere. The reaction mixture was degassed for 5 minutes with argon and stirred for 16 h at 20 °C in the dark. The complex was precipitated in 50 mL *n*-pentane, filtered off, and washed with *n*-pentane (2 × 50 mL) and diethyl ether (5 mL). After removing the solvent residues under reduced pressure, the complex $C_{67}H_{66}Cu_2I_2NO_8P_3$ (298 mg, 200 µmol, 81% yield) was obtained as a light yellow powder.

^{1}H NMR (500 MHz, CD_2Cl_2 [5.32 ppm], ppm) δ = 7.90 (s, 4H, CH_{Ar}), 7.72–7.06 (m, 38H, CH_{Ar}), 6.10 (s, 2H, CH_{Alkene}), 5.57 (t, *J* = 1.7 Hz, 2H, CH_{Alkene}), 4.56 (dd, *J* = 6.0, 3.4 Hz, 4H, CH_2), 4.46 (dd, *J* = 5.9, 3.5 Hz, 4H, CH_2), 1.92 (s, 6H, CH_3). Impurity: water from solvent (1.54 ppm). − **^{13}C NMR** (126 MHz, CD_2Cl_2 [53.8 ppm], ppm) δ = 167.4 (2C, C_q, *C*O), 166.2 (2C, C_q, *C*O), 152.5 (2C, C_q), 140.1 (2C, C_q), 137.6 (2C, C_q), 136.5 (2C, C_q), 134.9 (d, *J* = 13.8 Hz, 9C, *C*H$_{Ar}$), 134.3 (d, *J* = 13.3 Hz, 9C, *C*H$_{Ar}$), 133.1 (4C, *C*H$_{Ar}$), 131.0 (2C, C_q), 130.4 (4C, *C*H$_{Ar}$), 130.2 (2C, *C*H$_{Ar}$), 129.5 (d, *J* = 8.5 Hz, 4C, *C*H$_{Ar}$), 128.9 (t, *J* = 8.7 Hz, 12C, *C*H$_{Ar}$), 126.1 (2C, *C*H$_2$, C_{Alkene}), 124.9 (1C, C_q), 63.2 (2C, *C*H$_2$), 62.8 (2C, *C*H$_2$), 18.4 (2C, *C*H$_3$). – **^{31}P NMR** (202 MHz, CD_2Cl_2, ppm) δ = -5.10 (1P), -12.86 (2P). − **MS** (ESI) m/z (%): 1544 (1) $[M+Cu]^+$, 1352 (1) $[M-I]^+$, 1234 (46) $[(L_{NP})_3Cu_3I_2]^+$, 1042 (5) $[(L_{NP})_3Cu_2I]+$, 971 (40) $[(L_{NP})_2Cu_3I_2]^+$, 934 (1) $[(L_P)_2(L_{NP})Cu_2I]^+$, 899 (1) $[(L_P)_2Cu]^+$, 779 (15) $[(L_{NP})_2Cu_2I]+$, 744 (13) $[(L_P)(L_{NP})Cu]^+$, 589 (100) $[(L_{NP})_2Cu]^+$, 264 (2) $[(L_{NP})+H]^+$. − **HRMS** (ESI, $C_{67}H_{60}Cu_2INO_8P_3$): calcd. 1352.1168, found 1352.1163. − **IR** (ATR, ṽ) = 3046 (w), 2958 (w), 1715 (vs), 1434 (m), 1394 (w), 1320 (w), 1298 (w), 1266 (vs), 1157 (s), 1123 (m), 1106 (s), 1088 (vs), 1050 (w), 1026 (w), 1017 (m), 999 (w), 942 (w), 761 (m), 742 (s), 721 (m), 691 (vs), 507 (vs), 490 (vs), 462 (m), 439 (m), 428 (m), 404 (w), 394 (w) cm^{-1}. − **EA** ($C_{67}H_{60}Cu_2I_2NO_8P_3$) calcd. C 54.34, H 4.08, N 0.95; found C 54.33, H 4.07, N 1.19. – **M.p.** 112 °C.

Additional information on the chemical synthesis is available *via* the Chemotion repository: https://dx.doi.org/10.14272/reaction/SA-FUHFF-UHFFFADPSC-PHXKCWYEIT-UHFFFADPSC-NUHFF-LUHFF-NUHFF-ZZZ.

Additional information on the analytical data is available via: https://dx.doi.org/10.14272/PHXKCWYEITUECI-UHFFFAOYSA-L.1.

***(2-(Diphenylphosphaneyl)pyridine)(2-(methacryloyloxy)ethyl-4-(diphenylphosphino)benzoate)$_2$Cu$_2$Br$_2$* (Cu-L1-P2-Br)**

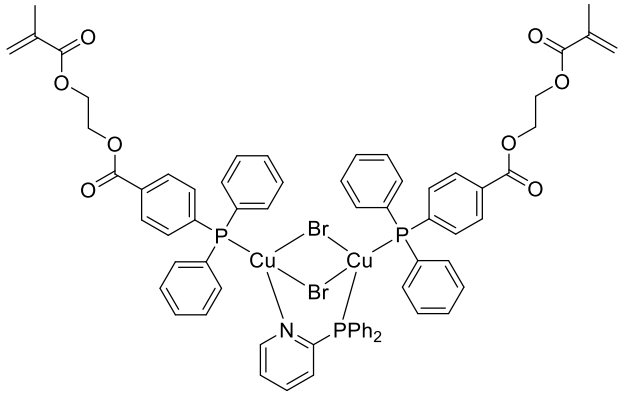

2-(Diphenylphosphaneyl)pyridine (54.0 mg, 205 µmol, 1.00 equiv), copper (I) bromide (58.8 mg, 410 µmol, 2.00 equiv) and 2-(methacryloyloxy)ethyl-4-(diphenylphosphino)benzoate (172 mg, 410 µmol, 2.00 equiv) were dissolved in 5 mL of dry dichloromethane in a 10 mL crimp vial under an argon atmosphere. The reaction mixture was degassed for 5 minutes with argon and stirred for 18 h at 20 °C in the dark. The complex was precipitated in 50 mL *n*-pentane, filtered, and washed with *n*-pentane (2 × 50 mL) and diethyl ether (5 mL). After removing the solvent residues under reduced pressure, the complex $C_{67}H_{60}Cu_2Br_2NO_8P_3$ (190 mg, 137 µmol, 67% yield) was obtained as a light-yellow powder.

^{1}H NMR (500 MHz, CD_2Cl_2 [5.32 ppm], ppm) δ = 7.88 (d, *J* = 7.8 Hz, 4H, C*H*$_{Ar}$), 7.66 (t, *J* = 7.9 Hz, 1H, C*H*$_{Ar}$), 7.62–7.34 (m, 24H, C*H*$_{Ar}$), 7.27 (dt, *J* = 27.5, 7.6 Hz, 13H, C*H*$_{Ar}$), 7.15 (s, 1, C*H*$_{Ar}$), 6.10 (t, *J* = 1.3 Hz, 2H, C*H*$_{Alkene}$), 5.56 (t, *J* = 1.6 Hz, 2H, C*H*$_{Alkene}$), 4.60–4.52 (m, 4H, C*H*$_2$), 4.49–4.42 (m, 4H, C*H*$_2$), 1.92 (t, *J* = 1.3 Hz, 6H, C*H*$_3$). Impurity: water from solvent (1.54 ppm). – **^{13}C NMR** (126 MHz, CD_2Cl_2 [53.8 ppm], ppm) δ = 167.4 (2C, C_q, *C*O), 166.2 (2C, C_q, *C*O), 152.3 (C_q), 140.1 (C_q), 137.3 (C_q), 136.5 (C_q), 134.7 (d, *J* = 13.8 Hz, *C*H$_{Ar}$), 134.4–133.7 (m, *C*H$_{Ar}$), 132.8 (C_q), 131.1 (C_q), 130.5, *C*H$_{Ar}$), 130.3, *C*H$_{Ar}$), 129.6 (d, *J* = 7.1 Hz, *C*H$_{Ar}$), 129.0 (d, *J* = 8.2 Hz, *C*H$_{Ar}$), 126.1 (2C, *C*H$_2$, C$_{Alkene}$), 124.7 (C_q), 63.2 (2C, *C*H$_2$), 62.8 (2C, *C*H$_2$), 18.4 (2C, *C*H$_3$). – **^{31}P NMR** (202 MHz, CD_2Cl_2, ppm) δ = -4.33 (br.s, 1P), -6.90 (br.s, 2P). – **MS** (ESI) m/z (%): 1304 (1) $[M\text{-}Br]^+$, 1139 (22), 996 (14), 876 (55), 733 (47) $[(L_{NP})_2Cu_2Br]^+$, 589 (100) $[(L_{NP})_2Cu]^+$. – **IR** (ATR, ṽ) = 3040 (w), 2953 (w), 1718 (vs), 1596 (w), 1480 (w), 1452 (w), 1434 (m), 1395 (w), 1320 (w), 1298 (w), 1268 (vs), 1160 (s), 1125 (m), 1108 (m), 1089 (vs), 1050 (w), 1026 (w), 1017 (m), 999 (w), 943 (w), 851 (w), 813 (w),

761 (m), 744 (s), 721 (m), 693 (vs), 509 (vs), 490 (vs), 456 (w), 429 (m), 398 (w), 392 (w), 384 (w) cm^{-1}. – **M.p.** 79 °C.

Additional information on the chemical synthesis is available *via* the Chemotion repository: https://dx.doi.org/10.14272/reaction/SA-FUHFF-UHFFFADPSC-WANKDJKJPJ-UHFFFADPSC-NUHFF-LUHFF-NUHFF-ZZZ.

Additional information on the analytical data is available via: https://dx.doi.org/10.14272/WANKDJKJPJQQAQ-UHFFFAOYSA-L.1.

***(2-(Diphenylphosphaneyl)pyridine)(2-(methacryloyloxy)ethyl-4-(diphenylphosphino)benzoate)$_2$Cu$_2$Cl$_2$* (Cu-L1-P2-Cl)**

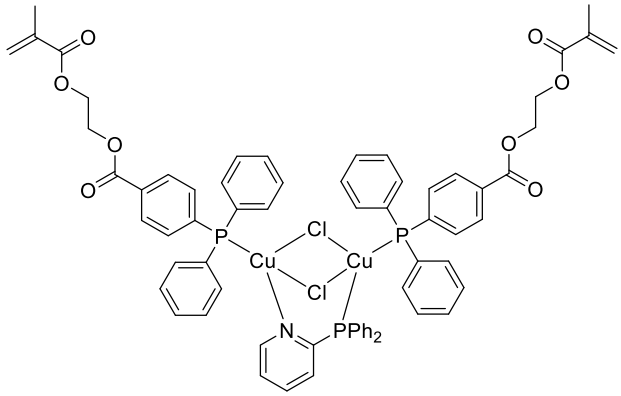

2-(Diphenylphosphaneyl)pyridine (36.6 mg, 139 µmol, 1.00 equiv), copper (I) chloride (27.5 mg, 278 µmol, 2.00 equiv) and 2-(methacryloyloxy)ethyl-4-(diphenylphosphino)benzoate (116 mg, 278 µmol, 2.00 equiv) were dissolved in 5 mL of dry dichloromethane in a 10 mL crimp vial under an argon atmosphere. The reaction mixture was degassed for 5 minutes with argon and stirred for 18 h at 20 °C in the dark. The complex was precipitated in 50 mL *n*-pentane, filtered, and washed with *n*-pentane (2 × 50 mL) and diethyl ether (5 mL). After removing the solvent residues under reduced pressure, the complex $C_{67}H_{60}Cu_2Cl_2NO_8P_3$ (66.0 mg, 50.8 µmol, 37% yield) was obtained as a light-yellow powder.

^{1}H NMR (500 MHz, CD_2Cl_2 [5.32 ppm], ppm) δ = 8.71 (s, 1H, CH_{Ar}), 7.86 (d, *J* = 8.0 Hz, 3H, CH_{Ar}), 7.65 (d, *J* = 8.0 Hz, 1H, CH_{Ar}), 7.55–7.31 (m, 23H, CH_{Ar}), 7.26 (dt, *J* = 24.5, 7.6 Hz, 14H, CH_{Ar}), 6.09 (s, 2H, CH_{Alkene}), 5.56 (d, *J* = 2.2 Hz, 2H, CH_{Alkene}), 4.58–4.51 (m, 4H, CH_2), 4.50–4.40 (m, 4H, CH_2), 1.91 (s, 6H, CH_3). Impurity: water from solvent (1.54 ppm).– **^{13}C NMR** (126 MHz, CD_2Cl_2 [53.8 ppm], ppm) δ = 167.4 (2C, C_q, *C*O), 166.1 (2C, C_q, *C*O), 152.1 (C_q), 139.9 (C_q), 137.3 (C_q), 136.5 (C_q), 134.52 (d, *J* = 13.8 Hz, *C*H$_{Ar}$), 134.32 (d, *J* = 13.3 Hz, *C*H$_{Ar}$), 133.97 (d, *J* = 12.9 Hz, *C*H$_{Ar}$), 132.47 (d, *J* = 30.8 Hz), 131.3 (C_q), 130.55 (d, *J* = 6.2 Hz, *C*H$_{Ar}$), 129.70 (d, *J* = 7.1 Hz, *C*H$_{Ar}$), 129.1 (*C*H$_{Ar}$), 126.1 (2C, *C*H$_2$, C_{Alkene}), 124.8 (C_q), 63.2 (2C, *C*H$_2$), 62.8 (2C, *C*H$_2$), 18.4 (2C, *C*H$_3$) – **^{31}P NMR** (202 MHz, CD_2Cl_2, ppm) δ = -3.68 (br.s, 1P), -4.60 (br.s, 2P). – **MS** (ESI) m/z (%): 1260 (1) $[M\text{-}Cl]^+$, 952 (33), 842 (7) $[(L_{NP})(L_P)Cu_2Cl]^+$, 787 (51), 687 (46) $[(L_{NP})_2Cu_2Cl]^+$, 589 (100) $[(L_{NP})_2Cu]^+$. – **IR** (ATR, $\tilde{\nu}$) =

3053 (w), 2946 (w), 1718 (vs), 1598 (w), 1435 (m), 1269 (vs), 1162 (s), 1108 (m), 1091 (s), 1021 (w), 744 (s), 694 (vs), 509 (vs) cm^{-1}. – **M.p:** 67 °C.

Additional information on the chemical synthesis is available *via* the Chemotion repository: https://dx.doi.org/10.14272/reaction/SA-FUHFF-UHFFFADPSC-NNVAPXZJEN-UHFFFADPSC-NUHFF-LUHFF-NUHFF-ZZZ.

Additional information on the analytical data is available via: https://dx.doi.org/10.14272/NNVAPXZJENJQAN-UHFFFAOYSA-L.1.

***(2-(Diphenylphosphaneyl)pyridine)(2-(methacryloyloxy)ethyl-4-(diphenylphosphino)benzoate)$_2$Cu$_2$(CN)$_2$* (Cu-L1-P2-CN)**

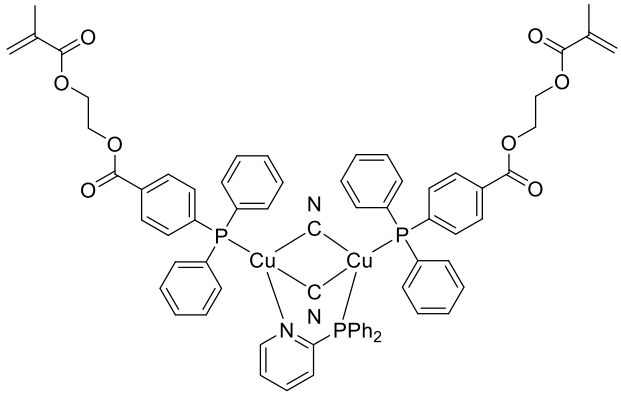

2-(Diphenylphosphaneyl)pyridine (0.0400 g, 0.152 mmol, 1.00 equiv), copper (I) cyanide (0.0290 g, 0.304 mmol, 2.00 equiv) and 2-(methacryloyloxy)ethyl-4-(diphenylphosphino)benzoate (0.127 g, 0.304 mmol, 2.00 equiv) were dissolved in 5 mL of dry dichloromethane in a 10 mL crimp vial under an argon atmosphere. The reaction mixture was degassed for 5 minutes with Argon and stirred for about 16 h at 20 °C in the dark. The resulting complex was precipitated in 50 mL of *n*-pentane, filtered off and washed with *n*-pentane (2 × 50 mL) and diethyl ether (10 mL). After removing the solvent residues under removed pressure, $C_{69}H_{60}Cu_2N_3O_8P_3$ (28.5 mg, 95% purity, 22.3 µmol, 14% yield) was obtained as a light yellow solid.

^{1}H NMR (500 MHz, DMSO-d_6, ppm) δ = 8.47 (d, *J* = 4.7 Hz, 1H), 7.60 (d, *J* = 7.9 Hz, 4H, C*H*$_{Ar}$), 7.43–7.23 (m, 24H, C*H*$_{Ar}$), 7.19–7.09 (m, 13H, C*H*$_{Ar}$), 5.97 (t, *J* = 1.2 Hz, 2H, C*H*$_{Alkene}$), 5.60 (t, *J* = 1.7 Hz, 2H, C*H*$_{Alkene}$), 4.53–4.43 (m, 4H, C*H*$_2$), 4.43–4.33 (m, 4H, C*H*$_2$), 1.79 (s, 6H, C*H*$_3$). Impurities: 5% diethyl ether (3.38, 1.09 ppm), water from the NMR solvent (3.33 ppm). – **^{13}C NMR** (126 MHz, DMSO-d_6 [39.52 ppm], ppm) δ = 166.4 (2C, C_q, *C*O), 165.1 (2C, C_q, *C*O), 150.0 (d, *J* = 11.3 Hz, 2C, C_q), 135.9 (d, *J* = 8.0 Hz, C_q), 135.5 (C_q), 133.7 (d, *J* = 15.1 Hz, *C*H$_{Ar}$), 133.5 (d, *J* = 14.9 Hz, *C*H$_{Ar}$), 132.9 (d, *J* = 14.3 Hz, *C*H$_{Ar}$), 129.9 (d, *J* = 5.3 Hz, *C*H$_{Ar}$), 129.5, 128.8 (d, *J* = 7.4 Hz), 128.6 (d, *J* = 7.8 Hz, *C*H$_{Ar}$), 128.2 (d, *J* = 8.5 Hz, *C*H$_{Ar}$), 126.1 (2C, *C*H$_2$, C$_{Alkene}$), 123.5 (*C*H$_{Ar}$), 62.8 (2C, *C*H$_2$), 62.5 (2C, *C*H$_2$), 17.9 (2C, *C*H$_3$). Missing signals (2C, CN, due to peak broadening). Impurities: diethyl ether (64.9, 15.2 ppm). – **^{31}P NMR** (202 MHz, DMSO-d_6, ppm) δ = -2.87 (1P, L^{NP}), -4.36 (2P, L^{P}). Impurities:

phosphine oxide at 25.02 ppm and 18.48 ppm. − **MS** (ESI) m/z (%): 1359 (4) $[L_P(L_{NP})_3Cu_2CN]^+$, 1342 (6) $[M+Cu]^+$, 1251 (7) $[M-CN]^+$, 1187 (4) $[L_P(L_{NP})_2Cu_3(CN)_2]^+$, 1096 (10) $[L_P(L_{NP})_2Cu_2CN]^+$, 988 (88) $[(L_P)_2Cu_2(CN)_2]^+$, 924 (32) $[L_P(L_{NP})Cu_3(CN)_2]^+$, 833 (43) $[L_P(L_{NP})Cu_2CN]^+$, 769 (46) $[(L_{NP})_2Cu_3(CN)_2]^+$, 744 (20) $[L_P(L_{NP})Cu]^+$, 678 (100) $[(L_{NP})_2Cu_2CN]^+$. Exact mass of complex, 1277, not observed. − **HRMS** (ESI, $C_{68}H_{60}Cu_2N_2O_8P_3$): calcd. 1251.2149, found 1251.2142. − **IR** (ATR, $\tilde{\nu}$) = 3051 (w), 2951 (w), 2113 (w), 1717 (s), 1434 (m), 1265 (s), 1157 (s), 1088 (vs), 1047 (m), 1016 (s), 999 (m), 943 (m), 847 (m), 761 (m), 741 (s), 721 (m), 691 (vs), 506 (vs), 492 (vs), 441 (m), 419 (s), 394 (m), 375 (m) cm^{-1}. − **M.p.** decomp > 120 °C.

Additional information on the chemical synthesis is available *via* the Chemotion repository:

https://dx.doi.org/10.14272/reaction/SA-FUHFF-UHFFFADPSC-KHNBAYNAGL-UHFFFADPSC-NUHFF-NUHFF-NUHFF-ZZZ.

Additional information on the analytical data is available via:
https://dx.doi.org/10.14272/KHNBAYNAGLATKF-UHFFFAOYSA-N.1.

(2-(Diphenylphosphaneyl)pyridine)(2-(methacryloyloxy)ethyl-4-(diphenylphosphino)benzoate)$_2$Cu$_2$(SCN)$_2$ **(Cu-L1-P2-SCN)**

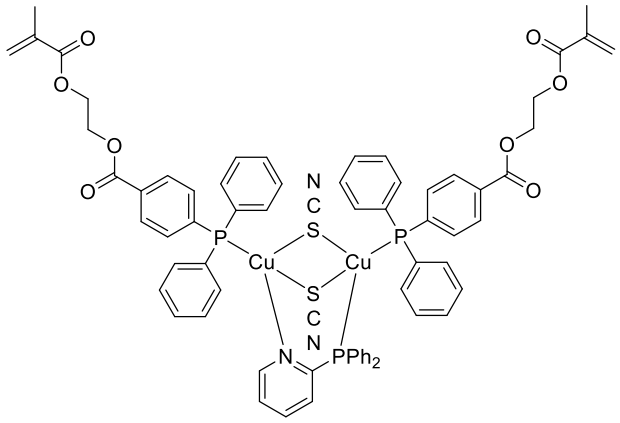

2-(Diphenylphosphaneyl)pyridine (44.4 mg, 168 µmol, 0.500 equiv), copper (I) thiocyanate (41.0 mg, 337 µmol, 1.00 equiv) and 2-(methacryloyloxy)ethyl-4-(diphenylphosphino)benzoate (141 mg, 337 µmol, 1.00 equiv) were dissolved in 5 mL of dry dichloromethane in a 10 mL crimp vial under an argon atmosphere. The reaction mixture was degassed for 5 minutes with Argon and stirred for about 16 h at room temperature in the dark. The resulting complex was precipitated in 50 mL of *n*-pentane, filtered and washed with *n*-pentane (2 × 50 mL) and diethyl ether (10 mL). After removing the solvent residues under removed pressure, $C_{69}H_{60}Cu_2N_3O_8P_3S_2$ (125 mg, 74.0 µmol, 44% yield)was obtained as a light yellow solid.

^{1}H NMR (500 MHz, DMSO-d_6 [2.50 ppm], ppm) δ = 7.84 (d, J = 8.2 Hz, 4H, CH_{Ar}), 7.48–7.29 (m, 38H, CH_{Ar}), 6.02 (t, *J* = 1.4 Hz, 2H, 2H, CH_{Alkene}), 5.67 (p, *J* = 1.7 Hz, 2H, 2H, CH_{Alkene}), 4.56–4.51 (m, 4H, CH_2), 4.44–4.41 (m, 4H, CH_2), 1.85 (t, *J* = 1.3 Hz, 6H, CH_3). Impurities: 3% dichloromethane (5.76 ppm), water from solvent (3.33 ppm), unknown (1.26, 0.65 ppm). – **^{13}C**

NMR (126 MHz, DMSO-d_6 [39.5 ppm], ppm) δ = 166.4 (2C, C_q, *C*O), 165.1 (2C, C_q, *C*O), 139.6 (d, *J* = 23.7 Hz, C_q), 135.6 (C_q), 133.6 (d, *J* = 15.1 Hz, *C*H_{Ar}), 133.1 (d, *J* = 14.1 Hz, *C*H_{Ar}), 132.1 (d, *J* = 27.0 Hz, C_q), 130.3 (d, *J* = 2.1 Hz, *C*H_{Ar}), 130.1 (C_q), 129.1 (d, *J* = 7.7 Hz, *C*H_{Ar}), 128.9 (d, *J* = 8.2 Hz, *C*H_{Ar}), 128.6 (*C*H_{Ar}), 126.2 (2C, *C*H_2, C_{Alkene}), 62.9 (2C, *C*H_2), 62.4 (2C, *C*H_2), *J* = 114.0 Hz), 17.9 (2C, *C*H_3). Impurities: dichloromethane (54.9 ppm), unknown (21.2, 20.3 ppm). – **^{31}P NMR** (202 MHz, DMSO-d_6, ppm) δ = -2.98 (br.s, 1P, L_{NP}), -4.44 (br.s, 2P, L_P). Impurities: phosphine oxides (25.03, 18.59 ppm). – **MS (ESI) m/z (%):** 1406 (1) $[M+Cu]^+$, 1283 (1) $[M-SCN]^+$, 899 (3) $[L^2{}_2Cu]^+$, 852 (28), 833 (4), 744 (16) $[L_PL_{NP}Cu]^+$, 589 (100) $[(L_{NP})_2Cu]^+$, 326 (1) $[L_{NP}Cu]^+$. **HRMS** (ESI, $C_{68}H_{60}Cu_2N_2O_8P_3S$): calcd. 1283.1870, found 1251.1862. – **IR** (ATR, ṽ) = 3051 (w), 2953 (w), 2096 (m), 1717 (vs), 1636 (w), 1596 (w), 1571 (w), 1480 (w), 1451 (w), 1434 (m), 1394 (w), 1367 (w), 1320 (w), 1265 (vs), 1157 (s), 1088 (vs), 1047 (m), 1016 (m), 999 (m), 942 (w), 895 (w), 850 (w), 813 (w), 761 (m), 741 (vs), 721 (m), 691 (vs), 632 (w), 618 (w), 506 (vs), 422 (m), 401 (m) cm^{-1}. –
M.p. 103 °C.

Additional information on the chemical synthesis is available *via* the Chemotion repository:

https://dx.doi.org/10.14272/reaction/SA-FUHFF-UHFFFADPSC-VYXBTVGWRJ-UHFFFADPSC-NUHFF-LUHFF-NUHFF-ZZZ.

Additional information on the analytical data is available via:
https://dx.doi.org/10.14272/VYXBTVGWRJZSHK-UHFFFAOYSA-L.1.

***(2-(Diphenylphosphaneyl)-4-methylpyridine)(2-(methacryloyloxy)ethyl-4-(diphenylphosphino)benzoate)$_2$Cu$_2$(I)$_2$* (Cu-L5-P2-I)**

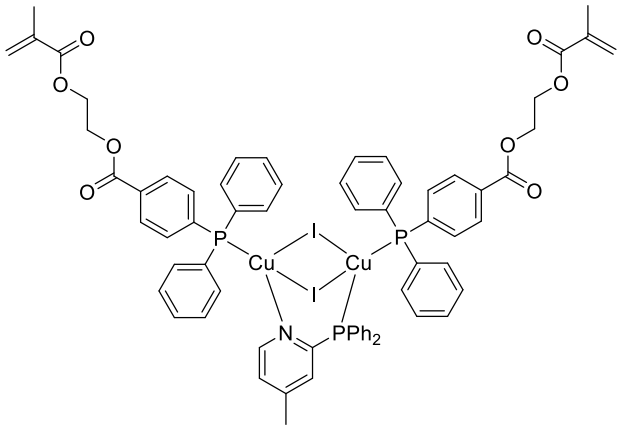

(2-(Diphenylphosphaneyl)-4-methylpyridine (71.0 mg, 256 µmol, 0.500 equiv), copper (I) iodide (97.5 mg, 512 µmol, 1.00 equiv) and 2-(methacryloyloxy)ethyl-4-(diphenylphosphino)benzoate (214 mg, 512 µmol, 1.00 equiv) were dissolved in 6 mL of dry dichloromethane in a 10 mL crimp vial under nitrogen atmosphere. The reaction mixture was degassed for 5 minutes with argon and stirred for about 16 h at 20 °C in the dark. The resulting complex was precipitated in 50 mL of *n*-pentane, filtered and washed with *n*-pentane (2 × 50 mL) and diethyl ether (10 mL).

After removing the solvent residues under removed pressure, $C_{68}H_{62}Cu_2I_2NO_8P_3$ (295 mg, 198 µmol, 77% yield) was obtained as a light yellow solid.

^{1}H NMR (500 MHz, CD_2Cl_2 [5.32 ppm], ppm) δ = 8.33 (s, 1H, C*H*$_{Ar}$), 7.90 (s, 4H, C*H*$_{Ar}$), 7.70–7.17 (m, 35H, C*H*$_{Ar}$), 6.90 (s, 1H, C*H*$_{Ar}$), 6.11 (s, 2H, C*H*$_{Alkene}$), 5.57 (s, 2H, C*H*$_{Alkene}$), 4.56 (t, *J* = 4.6 Hz, 4H, C*H*$_2$), 4.46 (dd, *J* = 5.9, 3.6 Hz, 4H, C*H*$_2$), 2.24 (s, 3H, C*H*$_3$), 1.92 (s, 6H, C*H*$_3$). Impurities: water from solvent (1.54 ppm). − **^{13}C NMR** (126 MHz, CD_2Cl_2 [53.8 ppm], ppm) δ = 167.4 (2C, C_q, *C*O), 166.2 (2C, C_q, *C*O), 152.1 (C_q), 149.7 (C_q), 136.5 (C_q), 134.9 (d, *J* = 13.9 Hz ,9C, *C*H$_{Ar}$), 134.5–133.9 (m, 9C, *C*H$_{Ar}$), 133.1 (C_q), 131.1 (C_q), 130.4 (*C*H$_{Ar}$), 130.1 (*C*H$_{Ar}$), 129.5 (d, *J* = 8.4 Hz, C_q), 129.1–128.6 (m, *C*H$_{Ar}$), 126.1 (2C, *C*H$_2$, C_{Alkene}), 63.2 (2C, *C*H$_2$), 62.8 (2C, *C*H$_2$), 21.3 (1C, *C*H$_3$), 18.4 (2C, *C*H$_3$). − **^{31}P NMR** (202 MHz, CD_2Cl_2, ppm) δ = -5.05 (1P, L^{NP}), -12.73 (2P, L^{P}). − **MS** (FAB, 3-NBA), m/z (%): 1557 (1) $[M+Cu]^+$, 1368 (1) $[M-I]^+$, 948 (13) $[M-I-L^P]$, 758 (48) $[CuL^P\ L^{NP}]^+$, 722 (51), 530 (84) $[Cu_2IL^PL^{NP}]^+$, 340 (100) $[CuL^{NP}]^+$. − **IR** (ATR, ṽ) = 3050 (w), 2961 (w), 1718 (vs), 1596 (w), 1480 (w), 1451 (w), 1434 (m), 1394 (w), 1368 (w), 1320 (w), 1298 (w), 1268 (vs), 1160 (s), 1123 (m), 1108 (s), 1089 (vs), 1048 (w), 1027 (w), 1017 (m), 1000 (w), 943 (w), 894 (w), 850 (w), 815 (w), 761 (m), 744 (s), 721 (m), 693 (vs), 633 (w), 618 (w), 510 (vs), 496 (vs), 465 (s), 441 (m), 432 (m), 411 (w), 391 (w), 382 (w) cm^{-1}. − **M.p.** 95 °C.

Additional information on the chemical synthesis is available *via* the Chemotion repository: https://dx.doi.org/10.14272/reaction/SA-FUHFF-UHFFFADPSC-YVJKICWCHF-UHFFFADPSC-NUHFF-LUHFF-NUHFF-ZZZ.

Additional information on the analytical data is available via: https://dx.doi.org/10.14272/YVJKICWCHFTALT-UHFFFAOYSA-L.1.

***(2-(Diphenylphosphaneyl)-4-methylpyridine)(2-(methacryloyloxy)ethyl-4-(diphenylphosphino)benzoate)$_2$Cu$_2$(Br)$_2$* (Cu-L5-P2-Br)**

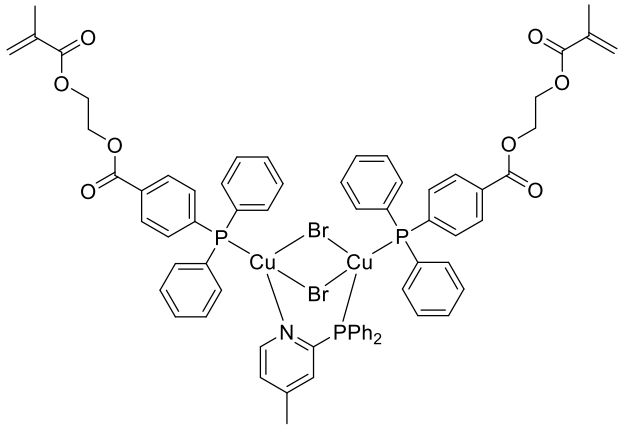

2-(Diphenylphosphaneyl)-4-methylpyridine (56.0 mg, 202 µmol, 0.500 equiv), copper bromide (58.0 mg, 404 µmol, 1.00 equiv) and 2-(methacryloyloxy)ethyl-4-(diphenylphosphino)benzoate (169 mg, 404 µmol, 1.00 equiv) were dissolved in 5 mL of dry dichloromethane in a 10 mL crimp vial under argon atmosphere. The reaction mixture was degassed for 5 minutes with argon and stirred for about 16 h at 20 °C in the dark. The resulting complex was precipitated in 50 mL of *n*-pentane, filtered and washed

with *n*-pentane (2 × 50 mL) and diethyl ether (10 mL). After removing the solvent residues under reduced pressure, $C_{68}H_{62}Cu_2Br_2NO_8P_3$ (196 mg, 140 µmol, 35% yield) was obtained as a light yellow solid.

^{1}H NMR (500 MHz, CD_2Cl_2 [5.32 ppm], ppm) δ = 7.88 (d, *J* = 7.8 Hz, 4H, C*H*$_{Ar}$), 7.53 (s, 12H, C*H*$_{Ar}$), 7.44–7.34 (m, 11H, C*H*$_{Ar}$), 7.26 (dt, *J* = 28.5, 7.7 Hz, 13H, C*H*$_{Ar}$), 6.99 (br. s, 1H, C*H*$_{Ar}$), 6.10 (t, *J* = 1.3 Hz, 2H, C*H*$_{Alkene}$), 5.56 (t, *J* = 1.6 Hz, 2H, C*H*$_{Alkene}$), 4.57–4.54 (m, 4H, C*H*$_2$), 4.48–4.43 (m, 4H, C*H*$_2$), 2.23 (s, 3H, C*H*$_3$), 1.91 (t, *J* = 1.3 Hz, 6H, C*H*$_3$). Impurities: water from solvent (1.54 ppm).– **^{13}C NMR** (126 MHz, CD_2Cl_2 [53.8 ppm], ppm) δ = 167.4 (2C, C_q, *C*O), 166.2 (2C, C_q, *C*O), 136.5 (C_q), 134.7 (d, *J* = 13.1 Hz, *C*H$_{Ar}$), 134.4–33.9 (m, *C*H$_{Ar}$), 132.7 (C_q), 131.2 (C_q), 130.5 (*C*H$_{Ar}$), 129.61 (d, *J* = 7.2 Hz, *C*H$_{Ar}$), 129.03 (d, *J* = 7.2 Hz, *C*H$_{Ar}$), 126.1 (2C, *C*H$_2$, C_{Alkene}), 63.2 (2C, *C*H$_2$), 62.8 (2C, *C*H$_2$), 21.3 (1C, *C*H$_3$), 18.4 (2C, *C*H$_3$). – **^{31}P NMR** (202 MHz, CD_2Cl_2, ppm) δ = -4.15 (1P, L_{NP}), -6.30 (br. s, 2P, L_P). – **MS** (FAB, 3-NBA), m/z (%): 1320 (1) $[M\text{-}I]^+$, 900 (42) $[M\text{-}I\text{-}L_P]$, 758 (44) $[CuL_P\,L_{NP}]^+$, 484 (84) $[Cu_2BrL_PL_{NP}]^+$, 418 (82), 340 (100) $[CuL^{NP}]^+$, 154 (100). Exact mass of complex, 1397, not found. – **IR** (ATR, $\tilde{\nu}$) = 3050 (vw), 1718 (vs), 1636 (w), 1596 (w), 1480 (w), 1451 (w), 1435 (m), 1395 (w), 1368 (w), 1320 (w), 1298 (w), 1268 (vs), 1163 (s), 1125 (m), 1108 (m), 1091 (s), 1048 (w), 1026 (w), 1017 (w), 999 (w), 945 (w), 895 (w), 851 (w), 815 (w), 762 (w), 744 (s), 721 (w), 693 (vs), 656 (w), 632 (w), 618 (w), 510 (vs), 497 (s), 465 (s), 441 (w), 436 (w), 394 (w), 381 (w) cm^{-1}. – **M.p.** 93 °C.

Additional information on the chemical synthesis is available *via* the Chemotion repository: https://dx.doi.org/10.14272/reaction/SA-FUHFF-UHFFFADPSC-PPWGUNNXQM-UHFFFADPSC-NUHFF-LUHFF-NUHFF-ZZZ.

Additional information on the analytical data is available via: https://dx.doi.org/10.14272/PPWGUNNXQMXPQL-UHFFFAOYSA-L.1.

***(2-(Diphenylphosphaneyl)-4-methylpyridine)(2-(methacryloyloxy)ethyl-4-(diphenylphosphino)benzoate)$_2$Cu$_2$(Cl)$_2$* (Cu-L5-P2-Cl)**

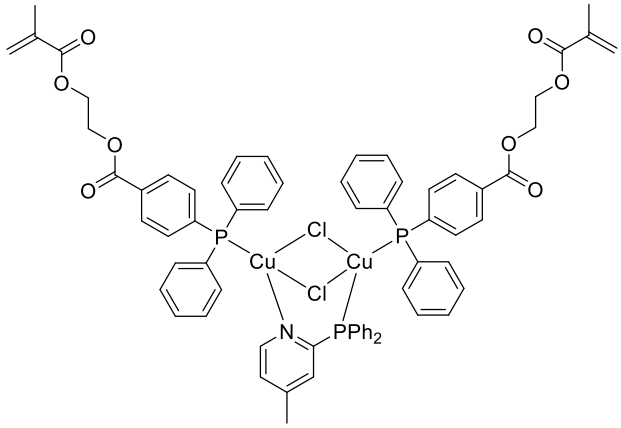

2-(Diphenylphosphaneyl)-4-methylpyridine (54.9 mg, 198 µmol, 0.500 equiv), copper (I) chloride (39.2 mg, 396 µmol, 1.00 equiv) and 2-(methacryloyloxy)ethyl-4-(diphenylphosphino)benzoate (166 mg, 396 µmol, 1.00 equiv) were dissolved in 5 mL of dry dichloromethane in a 10 mL crimp vial under argon atmosphere. The

reaction mixture was degassed for 5 minutes with argon and stirred for about 16 h at 20 °C in the dark. The resulting complex was precipitated in 50 mL of *n*-pentane, filtered and washed with *n*-pentane (2 × 50 mL) and diethyl ether (10 mL). After removing the solvent residues under removed pressure, $C_{68}H_{62}Cu_2Cl_2NO_8P_3$ (196 mg, 140 μmol, 35% yield) was obtained as a light yellow solid.

^{1}H NMR (500 MHz, CD_2Cl_2 [5.32 ppm], ppm) δ = 8.54 (br.s, 1H), 7.87 (d, *J* = 7.9 Hz, 4H, C*H*$_{Ar}$), 7.53–7.45 (m, 13H, C*H*$_{Ar}$), 7.43–7.33 (m, 10H, C*H*$_{Ar}$), 7.28 (t, *J* = 7.6 Hz, 8H, C*H*$_{Ar}$), 7.22 (t, *J* = 7.5 Hz, 4H, C*H*$_{Ar}$), 7.16–7.04 (m, 1H, C*H*$_{Ar}$), 6.10 (d, *J* = 1.9 Hz, 2H, C*H*$_{Alkene}$), 5.56 (q, *J* = 1.6 Hz, 2H, C*H*$_{Alkene}$), 4.59–4.52 (m, 4H, C*H*$_2$), 4.48–4.40 (m, 4H, C*H*$_2$), 2.22 (s, 3H, C*H*$_3$), 1.92 (t, *J* = 1.4 Hz, 6H, C*H*$_3$). Impurities: water from solvent (1.54 ppm). – **^{13}C NMR** (126 MHz, CD_2Cl_2 [53.8 ppm], ppm) δ = 167.4 (2C, C_q, *C*O), 166.1 (2C, C_q, *C*O), 151.7 (d, *J* = 13.3 Hz, C_q), 149.4 (C_q), 139.85 (d, *J* = 27.6 Hz, C_q), 136.5 (C_q), 134.5 (d, *J* = 14.3 Hz, *C*H$_{Ar}$), 134.3 (d, *J* = 12.8 Hz, *C*H$_{Ar}$), 134.0 (d, *J* = 13.5 Hz, *C*H$_{Ar}$), 132.6 (d, *J* = 30.1 Hz, C_q), 131.3 (C_q), 130.5 (*C*H$_{Ar}$), 130.4 (*C*H$_{Ar}$), 129.69 (d, *J* = 7.5 Hz, *C*H$_{Ar}$), 129.28–128.88 (m, *C*H$_{Ar}$), 126.0 (2C, *C*H$_2$, C$_{Alkene}$), 63.2 (2C, *C*H$_2$), 62.8 (2C, *C*H$_2$), 21.4 (1C, *C*H$_3$), 18.4 (2C, *C*H$_3$). – **^{31}P NMR** (202 MHz, CD_2Cl_2, ppm) δ = -4.80–-5.46 (m, 3P). – **MS** (FAB, 3-NBA), m/z (%): 1274 (1) [M-Cl]$^+$, 999 (17) [M-Cl-L$_{NP}$], 758 (32) [CuL$_P$L$_{NP}$]$^+$, 581 (28) [Cu$_2$ClL$_P$], 340 (100) [CuL^{NP}]$^+$, 154 (54). Exact mass of complex, 1309, not found. – **IR** (ATR, $\tilde{\nu}$) = 3051 (w), 2955 (vw), 1717 (vs), 1636 (w), 1596 (w), 1480 (w), 1451 (w), 1435 (s), 1395 (w), 1368 (w), 1320 (w), 1298 (m), 1268 (vs), 1162 (s), 1125 (m), 1108 (s), 1091 (vs), 1048 (w), 1027 (w), 1017 (m), 999 (w), 943 (w), 894 (w), 851 (w), 815 (w), 761 (m), 744 (s), 721 (m), 693 (vs), 659 (w), 633 (w), 618 (w), 599 (w), 509 (vs), 497 (vs), 465 (s), 439 (m), 431 (m), 398 (w), 388 (w) cm^{-1}. – **M.p.** 72 °C

Additional information on the chemical synthesis is available *via* the Chemotion repository: https://dx.doi.org/10.14272/reaction/SA-FUHFF-UHFFFADPSC-QKZIUBSUIS-UHFFFADPSC-NUHFF-LUHFF-NUHFF-ZZZ.

Additional information on the analytical data is available via: https://dx.doi.org/10.14272/QKZIUBSUISMKMH-UHFFFAOYSA-L.1.

***(2-(Diphenylphosphaneyl)pyridine)(4-(diphenylphosphaneyl)-N-(4-ethynylphenyl)benzamide)$_2$Cu$_2$(I)$_2$* (Cu-L1-P3-I)**

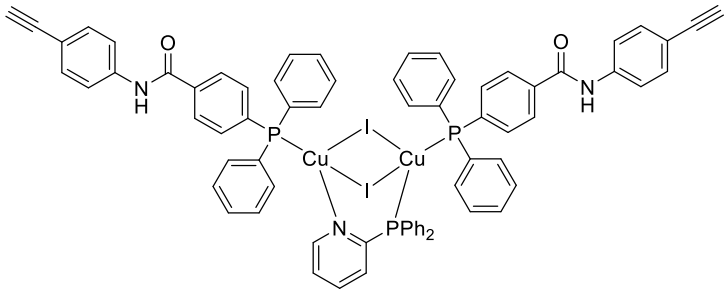

A 10 mL crimp vial was charged with 4-(diphenylphosphaneyl)-*N*-(4-ethynylphenyl)benzamide (308 mg, 760 µmol, 2.00 equiv), copper (I) iodide (145 mg, 760 µmol, 2.00 equiv) and 2-(diphenylphosphaneyl)pyridine (100 mg, 380 µmol, 1.00 equiv). The substances were dissolved in 6 mL of dry dichloromethane under argon and the suspension was degassed with argon for 5 minutes. The reaction mixture was stirred for 16 h at 22 °C in the dark. The reaction mixture was then poured into 10 mL of *n*-pentane. The precipitate was filtered off, washed with *n*-pentane (5 mL) and diethyl ether (5 mL) and was dried in vacuum to obtain $C_{71}H_{54}Cu_2I_2N_3O_2P_3$ (539 mg, 370 µmol, 97% yield) as a light yellow solid.

^{1}H NMR (500 MHz, DMSO-d_6 [2.50 ppm]) δ = 10.45 (s, 2H, N*H*), 7.87 (d, *J* = 8.0 Hz, 4H, C*H*$_{Ar}$), 7.85–7.74 (m, 4H, C*H*$_{Ar}$), 7.64–7.26 (m, 42H, C*H*$_{Ar}$), 4.11 (s, 2H, C*H*$_{Alkyne}$). Impurities: phosphine oxide (10.56, 8.06–8.04), water from the NMR solvent (3.33 ppm). – **^{13}C NMR** (126 MHz, DMSO-d_6 [39.5 ppm], ppm) δ = 165.3 (2C, C_q, *C*O), 139.6 (C_q), 137.5 (d, *J* = 24.6 Hz, C_q), 135.8 (C_q), 133.8 (d, *J* = 14.1 Hz), 133.4 (d, *J* = 13.6 Hz), 132.6 (d, *J* = 27.6 Hz), 132.3 (*C*H$_{Ar}$), 131.5 (d, *J* = 9.8 Hz, C_q) 130.1 (*C*H$_{Ar}$), 123.0 (*C*H$_{Ar}$), 128.6 (d, *J* = 8.7 Hz, *C*H$_{Ar}$), 127.6 (d, *J* = 7.9 Hz, C_q), 120.0 (*C*H$_{Ar}$), 116.6 (C_q), 83.5 (*C*H$_{Alkyne}$), 80.1 (*C*H$_{Alkyne}$). – **^{31}P NMR** (202 MHz, DMSO-d_6) δ = -5.30 (1P), -9.71 (2P). Impurities: 1% Phosphine oxide (25.08 ppm,18.39 ppm), unknown (12.58 ppm). – **MS** (FAB, 3-NBA), m/z (%): 1517 (1) $[M+Cu]^+$, 1456 (1) $[M+H]^+$, 1328 (1) $[M-I]^+$, 971 (5), 873 (3) $[(L_p)_2Cu]$, 708 (8), 518 (22), 326 (31), 154 (100). – **IR** (ATR, ṽ) = 3055 (vw), 1673 (w), 1656 (w), 1595 (w), 1587 (w), 1510 (vs), 1482 (m), 1435 (m), 1402 (w), 1315 (s), 1293 (w), 1241 (w), 1094 (w), 836 (m), 742 (vs), 693 (vs), 656 (w), 642 (w), 632 (w), 618 (w), 538 (m), 509 (vs), 489 (s), 431 (w), 411 (w), 404 (w), 397 (w) cm^{-1}. – **M.p.** 170 °C.

Additional information on the chemical synthesis is available *via* the Chemotion repository: https://dx.doi.org/10.14272/reaction/SA-FUHFF-UHFFFADPSC-HLNFWRSQTW-UHFFFADPSC-NUHFF-LUHFF-NUHFF-ZZZ.

Additional information on the analytical data is available via: https://dx.doi.org/10.14272/HLNFWRSQTWJZME-UHFFFAOYSA-L.1.

***(2-(Diphenylphosphaneyl)-4-methylpyridine)(4-(diphenylphosphaneyl)-N-(4-ethynylphenyl)benzamide)$_2$Cu$_2$(I)$_2$* (Cu-L5-P3-I)**

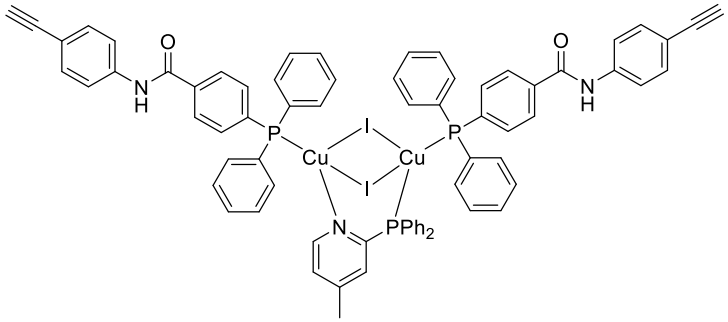

A 10 mL crimp vial was charged with 4-(diphenylphosphaneyl)-*N*-(4-ethynylphenyl)benzamide (292 mg, 721 µmol, 2.00 equiv), copper (I) iodide (137 mg, 721 µmol, 2.00 equiv) and 2-(Diphenylphosphaneyl)-4-methylpyridine (100 mg, 361 µmol, 1.00 equiv). The substances were dissolved in 6 mL of dry dichloromethane under argon and the suspension was degassed with argon for 5 minutes. The reaction mixture was stirred for 18 h at 22 °C in the dark. The reaction mixture was then poured into 10 mL of *n*-pentane. The precipitate was filtered off, washed with *n*-pentane (5 mL) and diethyl ether (5 mL) and was dried in vacuum to obtain $C_{72}H_{56}Cu_2I_2N_3O_2P_3$ (458 mg, 99% purity, 309 µmol, 86% yield) as a light yellow solid.

^{1}H NMR (500 MHz, DMSO-d_6 [2.50 ppm], ppm) δ = 10.46 (s, 2H, N*H*), 7.87 (d, *J* = 7.8 Hz, 4H, C*H*$_{Ar}$), 7.79 (d, *J* = 8.6 Hz, 4H, C*H*$_{Ar}$), 7.63–7.23 (m, 41H, C*H*$_{Ar}$), 4.11 (s, 2H, C*H*$_{Alkyne}$), 2.26 (s, 3H, CH_3). Impurities: phosphine oxide (10.56, 8.06–8.04), water from solvent (3.33 ppm). – **^{13}C NMR** (126 MHz, DMSO-d_6 [39.5 ppm], ppm) δ = 165.3 (2C, C_q, *C*O), 139.6 (C_q), 137.6 (d, *J* = 25.7 Hz), 135.8 (C_q), 133.9 (d, *J* = 13.9 Hz, *C*H$_{Ar}$), 133.4 (d, *J* = 13.2 Hz, *C*H$_{Ar}$), 132.6 (d, *J* = 27.7 Hz), 132.3 (*C*H$_{Ar}$), 131.5 (d, *J* = 9.6 Hz, C_q), 130.1 (*C*H$_{Ar}$), 129.9, 128.9 (d, *J* = 11.8 Hz, C_q), 128.7–128.4 (m, *C*H$_{Ar}$), 127.6 (d, *J* = 8.2 Hz), 120.0 (*C*H$_{Ar}$), 116.6 (C_q), 83.6 (*C*H$_{Alkyne}$), 80.1 (*C*H$_{Alkyne}$), 20.6 (1C, CH_3). – **^{31}P NMR** (202 MHz, DMSO-d_6) δ = -4.98 (1P), -10.84 (2P). Impurities: Phosphine oxide (25.11 ppm,18.66 ppm, 18.42 ppm). – **MS** (FAB, 3-NBA), m/z (%): 1467 (1) $[M]^+$, 1340 (1) $[M\text{-}I]^+$, 998 (18), 745 (18), 721 (29), 617 (29), 530 (67), 349 (100) $[C_{18}H_{16}CuNP]^+$. – **IR** (ATR, ṽ) = 3299 (vw), 3053 (vw), 1674 (w), 1657 (w), 1595 (m), 1588 (m), 1510 (vs), 1482 (m), 1435 (m), 1402 (w), 1315 (s), 1293 (w), 1241 (w), 1186 (w), 1176 (w), 1095 (w), 1017 (w), 834 (m), 742 (s), 693 (vs), 656 (w), 642 (w), 632 (w), 618 (w), 611 (w), 538 (s), 510 (vs), 496 (s), 465 (m), 439 (w), 432 (w), 407 (w), 384 (w) cm^{-1}. – **M.p**. 234 °C.

Additional information on the chemical synthesis is available *via* the Chemotion repository: https://dx.doi.org/10.14272/reaction/SA-FUHFF-UHFFFADPSC-MQXGYJDCOR-UHFFFADPSC-NUHFF-LUHFF-NUHFF-ZZZ.

Additional information on the analytical data is available via: https://dx.doi.org/10.14272/MQXGYJDCORDNCG-UHFFFAOYSA-L.1.

***(2-(Di-p-tolylphosphaneyl)pyridine)(4-(diphenylphosphaneyl)-N-(4-ethynylphenyl)benzamide)$_2$Cu$_2$(I)$_2$* (Cu-L6-P3-I)**

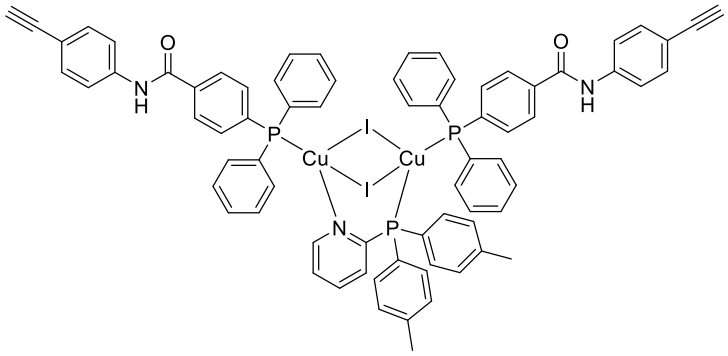

A 10 mL crimp vial was charged with 4-(diphenylphosphaneyl)-*N*-(4-ethynylphenyl)benzamide (278 mg, 687 µmol, 2.00 equiv), copper (I) iodide (131 mg, 687 µmol, 2.00 equiv) and 2-(di-p-tolylphosphaneyl)pyridine (100 mg, 343 µmol, 1.00 equiv). The substances were dissolved in 7 mL of dry dichloromethane under argon and the suspension was degassed with argon for 5 minutes. The reaction mixture was stirred for 18 h at 22 °C in the dark. The reaction mixture was then poured into 10 mL of n-pentane. The precipitate was filtered off, washed with n-pentane (5 mL) and diethyl ether (5 mL) and was dried in vacuum to obtain $C_{73}H_{58}Cu_2I_2N_3O_2P_3$ (303 mg, 98% purity, 204 µmol, 59% yield) as a light yellow solid.

^{1}H NMR (500 MHz, DMSO-d_6 [2.50 ppm], ppm) δ = 10.45 (s, 2H, N*H*), 7.87 (d, *J* = 7.8 Hz, 4H, C*H*$_{Ar}$), 7.80 (d, *J* = 8.3 Hz, 4H, C*H*$_{Ar}$), 7.60–7.35 (m, 33H, C*H*$_{Ar}$), 7.22 (s, 3H, C*H*$_{Ar}$), 7.09 (d, *J* = 7.7 Hz, 4H, C*H*$_{Ar}$), 4.11 (s, 2H, C*H*$_{Alkyne}$), 2.28 (s, 6H, CH_3). 5% of impurities: phosphine oxide (10.55 ppm, 8.77–8.65 ppm, 8.09–7.96ppm, 7.70–7.61 ppm, 7.33–7.29 ppm, 2.34 ppm), water from the solvent (3.33 ppm), cyclohexane (1.47 ppm), n-pentane (1.30–1.21 ppm, 0.87–0.84 ppm). – **^{13}C NMR** (126 MHz, DMSO-d_6 [39.5 ppm], ppm) δ = 165.3 (2C, C_q, *C*O), 139.8 (C_q), 139.6 (C_q), 137.5 (d, *J* = 25.6 Hz, C_q), 135.8 (C_q), 133.9 (d, *J* = 14.0 Hz, *C*H$_{Ar}$), 133.4 (d, *J* = 13.5 Hz, *C*H$_{Ar}$), 132.6 (d, *J* = 27.9 Hz), 132.3 (*C*H$_{Ar}$), 131.6–131.5 (m, C_q), 130.1 (*C*H$_{Ar}$), 129.2 (d, *J* = 8.6 Hz, *C*H$_{Ar}$), 129.0 (d, *J* = 18.3 Hz, C_q), 128.6 (d, *J* = 8.4 Hz, *C*H$_{Ar}$), 127.6 (d, *J* = 8.1 Hz), 120.0 (*C*H$_{Ar}$), 116.6 (C_q), 83.5 (1C, *C*H$_{Alkyne}$), 80.0 (1C, *C*H$_{Alkyne}$), 33.4 (C_q), 20.9 (2C, *C*H$_3$). Impurities: phosphine oxide (139.7, 131.6–131.5, 21.1 ppm), pentane (21.7 ppm, 13.9). – **^{31}P NMR** (202 MHz, DMSO-d_6) δ = -5.98 (1P), -10.24 (2P). Impurities: Phosphine oxide (25.09 ppm, 19.27 ppm). – **MS** (ESI, DCM), m/z (%): 1318 (84) $[(L_{NP})_3Cu_3I_2]^+$, 1037 (100) $[(L_{NP})_2Cu_3I_2]^+$, 834 (23) $[(L_{NP})_2Cu_2I]^+$, 645 (65) $[(L_{NP})_2Cu]^+$. Exact mass of complex, 1483, not observed. – **IR** (ATR, ṽ) = 3286 (vs), 3049 (vs), 1676 (s), 1596 (vs), 1509 (vs), 1482 (vs), 1314 (vs), 1092 (s), 842 (m), 741 (s), 689 (s), 508 (s) cm^{-1}. – **M.p.** 171 °C.

Additional information on the chemical synthesis is available *via* the Chemotion repository: https://dx.doi.org/10.14272/reaction/SA-FUHFF-UHFFFADPSC-DXEQAPIKVI-UHFFFADPSC-NUHFF-LUHFF-NUHFF-ZZZ.

Additional information on the analytical data is available via: https://dx.doi.org/10.14272/DXEQAPIKVIVHPH-UHFFFAOYSA-L.1.

5.2.3.4 Tetranuclear complexes

***(4-(Diphenylphosphino)-N-(2-propyn-1-yl)benzamide)$_4$Cu$_4$I$_4$* (Cu-4-P1)**

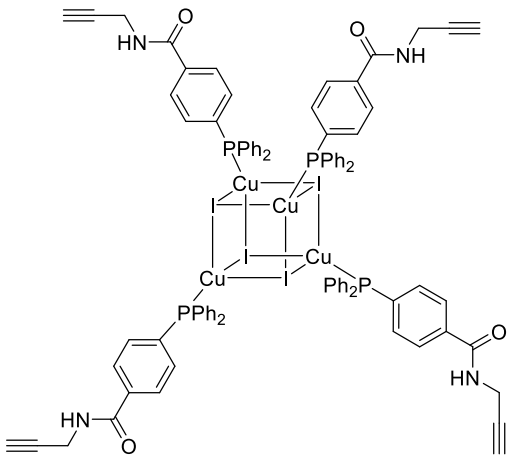

Copper (I) iodide (0.0830 g, 0.440 mmol, 4.00 equiv) and 4-(diphenylphosphino)-*N*-(2-propyn-1-yl)benzamide (0.150 g, 0.440 mmol, 4.00 equiv) were dissolved in 5 mL of dry dichloromethane in a 10 mL crimp vial under a nitrogen atmosphere. The reaction mixture was degassed for 5 minutes with argon and stirred for 16 h at 19 °C. The resulting complex was precipitated in 150 mL of *n*-pentane, filtered and washed with *n*-pentane (2 × 50 mL) and diethyl ether (15 mL). After removing the solvent residues under removed pressure, the complex $C_{88}H_{76}Cu_4I_4N_4O_4P_4$ (167 mg, 99% purity, 0.78 mmol, 71% yield) was obtained as a colorless solid.

^{1}H NMR (400 MHz, DMSO-d_6 [2.50 ppm], ppm) δ = 8.99 (t, *J* = 5.6 Hz, 4H, N*H)*, 7.84 (d, *J* = 7.9 Hz, 8H, C*H*), 7.55–7.37 (m, 48H, C*H*), 4.06 (dd, *J* = 5.6, 2.5 Hz, 8H, CH_2), 3.13 (t, *J* = 2.4 Hz, 4H, CH_{Alkyne}). Impurities: 7.70–7.56 (unknown), 3.33 (water from solvent), 1.27 ppm (tetramethyl urea) and 0.66 ppm (unknown). − **^{13}C NMR** (126 MHz, CD_2Cl_2 [53.84 ppm] ppm) δ = 166.9 (4C, C_q, *C*O), 138.3 (d, *J* = 27.9 Hz, 4C, C_q), 134.9 (4C, C_q), 134.7 (d, *J* = 13.8 Hz, 16C, *C*H), 134.6 (d, *J* = 13.2 Hz, 8C, *C*H), 132.7 (d, *J* = 29.7 Hz, 8C, C_q), 130.4 (8C, *C*H), 129.0 (d, *J* = 9.2 Hz, 16C, *C*H), 127.3 (d, *J* = 9.1 Hz, 8C, *C*H), 80.3 (4C, C_q, C_{Alkyne}), 71.3 (4C, *C*H), 30.0 (4C, *C*H_2). Impurities: 21.0 ppm (tetramethyl urea), 132.3, 43.4 ppm and 22.4 ppm (unknown). − **^{31}P NMR** (162 MHz, DMSO-d_6, ppm) δ = -8.47 (s, 4P). − **MS** (FAB, 3-NBA) *m/z* (%): 2007 (1) $[M\text{-}I]^+$, 1665 (1) $[M\text{-}L_P\text{-}I]^+$, 788 (6) $[L_P\ Cu_3I_2]^+$, 749 (31) $[(L_P)_2Cu]^+$, 596 (8) $[L_PCu_2I]^+$, 344 (22) $[L_P]^+$. − **HRMS** (FAB, 3-NBA, $C_{17}H_{14}CuNP$): calcd. 344.1204, found 344.1211. − **MS** (ESI, DCM) *m/z* (%): 2479 (1) $[M+P1]^+$, 2132(8) $[M+H]^+$, 2007 (1) $[M\text{-}I]^+$, 1410 (10) $[(P1)_3Cu_2I_2]^+$, 1067 (13) $[(P1)_2Cu_2I_2]^+$, 939 (3) $[(P1)_2Cu_2I]$+, 766 (32) $[(P1)_2CuNH_3]^+$, 765 (67) $[(P1)_2CuNH_2]^+$, 749 (57) $[(P1)_2Cu]^+$, 704 (45) $[(P1)_2NH_4]^+$, 703 (100) $[(P1)_2NH_3]^+$, 687 (64) $[(P1)_2]^+$, 344 (16) $[P1]^+$. − **HRMS** (ESI, DCM, $C_{88}H_{73}Cu_4I_4N_4O_4P_4$): calcd. 2134.7927, found 2134.7957. − **IR** (ATR, ṽ) = 3301 (w), 3053 (w), 1647 (s), 1642 (s),

1523 (s), 1482 (s), 1434 (s), 1293 (m), 1095 (s), 853 (w), 744 (s), 693 (vs), 671 (s), 663 (s), 654 (m), 640 (m), 630 (m), 619 (m), 582 (m), 510 (vs), 489 (s) cm^{-1}. – **M.p.** decomposition between 135–218 °C.

Additional information on the chemical synthesis is available *via* the Chemotion repository: https://dx.doi.org/10.14272/reaction/SA-FUHFF-UHFFFADPSC-VLYAVFNFWZ-UHFFFADPSC-NUHFF-NUHFF-NUHFF-ZZZ.

Additional information on the analytical data is available via: https://dx.doi.org/10.14272/VLYAVFNFWZYYKO-UHFFFAOYSA-N.1.

***(4-(Diphenylphosphaneyl)-N-(4-ethynylphenyl)benzamide)$_4$Cu$_4$I$_4$* (Cu-4-P3)**

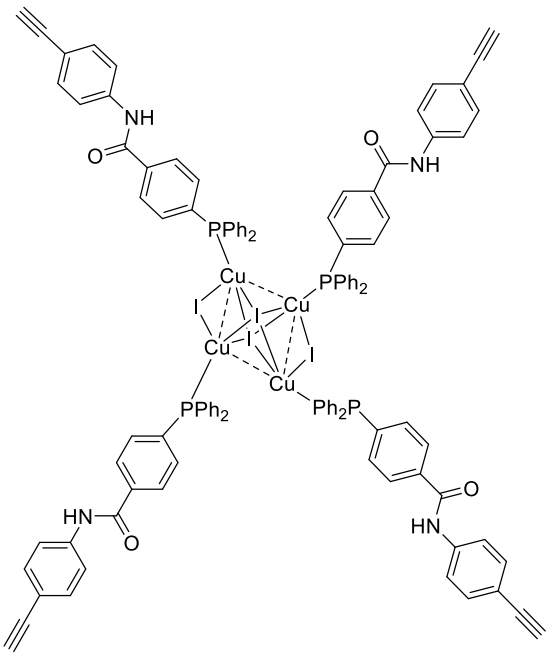

Copper (I) iodide (80.0 mg, 420 µmol, 1.00 equiv) and 4-(diphenylphosphaneyl)-*N*-(4-ethynylphenyl)benzamide (170 mg, 420 µmol, 1.00 equiv) were dissolved in 5 mL dry dichloromethane in a 10 mL crimp vial under an argon atmosphere. The reaction mixture was degassed for 5 minutes with argon and stirred for 18 h at 23 °C. The resulting complex was precipitated in 150 mL *n*-pentane, filtrated, and washed with *n*-pentane (2 × 50 mL) and diethyl ether (15 mL). After removing the solvent residues under reduced pressure, the complex $C_{108}H_{80}Cu_4I_4N_4O_4P_4$ (119 mg, 49.9 µmol, 48% yield) was obtained as a yellow powder.

^{1}H NMR (500 MHz, DMSO-d_6 [2.50 ppm], ppm) δ = 10.46 (s, 4H, N*H*), 7.92 (d, *J* = 7.9 Hz, 8H, CH_{Ar}), 7.83–7.75 (m, 8H, CH_{Ar}), 7.66–7.39 (m, 56H, CH_{Ar}), 4.11 (s, 4H, CH_{Alkyne}). Impurities: water from solvent at 3.33 ppm. – **^{13}C NMR** (126 MHz, DMSO-d_6 [39.5 ppm], ppm) δ = 165.8 (4C, *C*O, C_q), 140.1 (4C, C_q), 137.6 (d, 8C, C_q), 136.5 (4C, C_q), 134.2 (d, *J* = 14.6 Hz, 16C, *C*H$_{Ar}$), 133.9 (d, *J* = 14.4 Hz, 8C, *C*H$_{Ar}$), 132.9–132.5 (m, 8C), 130.8 (4C, Cq), 129.3 (d, *J* = 9.0 Hz, 24C, *C*H$_{Ar}$), 128.3 (d, *J* = 8.9 Hz, 8C, *C*H$_{Ar}$), 120.5 (8C, *C*H$_{Ar}$), 117.1 (4C, Cq), 84.0 (4C, C_q, C_{Alkyne}), 80.6 (4C, *C*H$_{Alkyne}$). − **^{31}P NMR** (202 MHz, ppm) δ = -8.10 (b.s., 4P). Impurities: 25.09 ppm (phosphine oxide). − **MS** (ESI, DCM), m/z (%): 2383 (11) $[M]^+$, 2256 (15) $[M\text{-}I]^+$, 2034 (100), 2019 (38). MS (ESI, DCM), m/z (%): 2383 (11) $[M]^+$, 2256 (15) $[M\text{-}I]^+$, 2034 (100), 2019 (38). − **IR** (ATR, $\tilde{\nu}$) = 3279 (w), 3060 (w), 1659 (m), 1653 (m), 1595 (m), 1587 (m), 1509 (vs), 1483 (s), 1435 (m), 1402 (m), 1315 (s), 1293 (m), 1239 (m), 1187

(w), 1176 (w), 1095 (m), 1016 (w), 833 (s), 742 (vs), 691 (vs), 654 (m), 642 (m), 630 (m), 618 (m), 609 (m), 575 (w), 537 (vs), 510 (vs), 487 (vs), 449 (m), 442 (m), 429 (m), 416 (m), 408 (m), 392 (w), 388 (m), 380 (w) cm^{-1}. − **EA** ($C_{108}H_{80}Cu_4I_4N_4O_4P_4$): Calcd C 54.42; H 3.38; N 2.35. Found C 54.37; H 3.20; N 2.50. − **M.p.** 175 °C.

Additional information on the chemical synthesis is available *via* the Chemotion repository: https://dx.doi.org/10.14272/reaction/SA-FUHFF-UHFFFADPSC-YBSGBAJLEN-UHFFFADPSC-NUHFF-JUHFF-NUHFF-ZZZ.

Additional information on the analytical data is available via: https://dx.doi.org/10.14272/YBSGBAJLENAMLM-UHFFFAOYSA-J.1.

5.2.4 Crosslinking Experiments

The crosslinking reactions between an alkyne copper(I) complex and azides or thiols were conducted following the general procedure of Volz.[132] For the attachment of a copper complex to an azide-/thiol substituted reagent equimolar amounts of the alkyne substituted complex and the azide-substituted reagent (calculated according to the number of alkyne-containing ligands attached to the complex) were weighted in a flask equipped under argon with a stirring bar and dissolved in dry dichloromethane (10 mL per 1 g of complex). The mixture was stirred at 22 °C for 6 to 24 h, the precipitated product was filtered off and washed with 50 mL of pentane, methanol and dichloromethane, subsequently, and the resulting precipitate was dried under vacuum.

53a Cu-L1-P1-I + benzylazide

Cu-L1-P1-I (150 mg, 113 µmol, 1.00 equiv) and benzylazide (30.9 mg, 29.0 µL, 225 µmol, 2.00 equiv) were reacted following the general procedure, to yield 53a.

IR (ATR, ṽ) = 3259 (m), 3055 (m), 2093 (w), 1655 (s), 1649 (s), 1528 (m), 1482 (w), 1435 (vs), 1311 (w), 1176 (s), 1113 (vs), 1068 (w), 1016 (w), 995 (w), 722 (vs), 691 (vs), 562 (s), 539 (s), 522 (s) cm^{-1}. − **EA** ($C_{75}H_{64}Cu_2I_2N_9O_2P_3$): calcd. C 56.49, N 7.89, H 4.04; found C 55.83, N 8.19, H 4.34

53b Cu-L1-P1-I + diazidobenzene

Cu-L1-P1-I (100 mg, 75.1 µmol, 1.00 equiv) and 1,4-diazidobenzene (12.4 mg, 11.6 µL, 75.1 µmol, 1.00 equiv) were reacted following the general procedure, to yield 53b.

IR (ATR, ṽ) = 3050 (m), 3046 (m), 2980 (s), 2971 (s), 1657 (m), 1650 (m), 1645 (m), 1519 (s), 1510 (s), 1481 (s), 1433 (s), 1423 (m), 1418 (m), 1391 (m), 1386 (m), 1289 (m), 1283 (m), 1273

(m), 1266 (m), 1093 (m), 1040 (m), 985 (m), 741 (m), 691 (m), 514 (m), 512 (m), 507 (m), 501 (m), 488 (m), 475 (m), 467 (m), 458 (m), 419 (m), 413 (m), 406 (vs) cm^{-1}. − **EA** ($C_{67}H_{54}Cu_2I_2N_9O_2P_3$): calcd. C 53.97 N 8.45, H 3.65; found C 49.93, N 8.30, H 3.49.

55a Cu-L1-P1-I + dithioethane

Cu-L1-P1-I (60.0 mg, 45.1 µmol, 1.00 equiv) and (4.25 mg, 3.35 µL, 45.1 µmol, 1.00 equiv) were reacted following the general procedure, to yield 55a.

IR (ATR, ṽ) = 3292 (vs), 3285 (vs), 3050 (vs), 2904 (vs), 1654 (vs), 1648 (vs), 1598 (s), 1550 (w), 1522 (vs), 1481 (s), 1434 (vs), 1406 (s), 1294 (m), 1275 (m), 1246 (m), 1185 (m), 1158 (w), 1143 (w), 1136 (w), 1095 (vs), 1071 (w), 1011 (w), 836 (w), 744 (m), 717 (w), 692 (vs), 647 (w), 506 (m) cm^{-1}. − **EA** ($C_{63}H_{56}Cu_2I_2N_3O_2P_3S_2$): calcd. C 53.10 N 2.95, H 3.96 S 4.50; found C 52.55, N 3.06, H 3.85, S 2.86.

55b Cu-L1-P1-Br + benzene-1,4-dithiol

Cu-L1-P1-Br (30.0 mg, 24.3 µmol, 1.00 equiv) and benzene-1,4-dithiol (3.45 mg, 24.3 µmol, 1.00 equiv) were reacted following the general procedure, to yield 55b.

IR (ATR, ṽ) = 3273 (s), 3267 (s), 3259 (s), 3050 (s), 3046 (s), 3029 (m), 2913 (m), 1656 (vs), 1649 (vs), 1527 (vs), 1480 (s), 1471 (s), 1435 (vs), 1388 (m), 1297 (s), 1179 (s), 1110 (vs), 1096 (vs), 1073 (m), 1032 (m), 1006 (s), 998 (m), 745 (s), 725 (vs), 692 (vs), 644 (m), 562 (s), 552 (m), 538 (s), 521 (s), 511 (s), 506 (s), 491 (s), 418 (s), 407 (m), 401 (m) cm^{-1}. − **EA** ($C_{67}H_{56}Cu_2I_2N_3O_2P_3S_2$): calcd. C 58.35 N 3.05, H 4.09 S 4.65; found C 59.19, N 2.82, H 5.11, S 2.92.

57a Polymerization of Cu-L1-P1-I

Cu-L1-P1-I (50.0 mg, 33.8 µmol, 1.00 equiv) was dissolved under argon in 0.50 ml dry, degassed DCM and was irradiated for 30 minutes with UV light (254 nm).

EA ($C_{67}H_{60}Cu_2I_2NO_8P$): calcd. C 54.34 N 0.95, H 4.08; found C 51.64, N 0.89, H 4.01.

5.2.5 Crystallographic data

Crystal structures in this section were measured and solved by Dr. Martin Nieger at the University of Helsinki or Dr. Olaf Fuhr from the KIT.

Table 19. Overview of the numbering and sample code of crystals.

Entry	Numbering in this thesis	Sample code used by crystallographer
1	Cu-4-L2-I in pyridine	SB1491_HY
2	Cu-4-L2-Br in pyridine	SB1498_HY
3	Cu-L2-I	SB1511_HY
4	Cu-L2-Br	SB1509_HY
5	Cu-L2-Cl	CRA89-1a
6	Cu-L2-I-a	CRA105mf
	Cu-L2-I-b	CRA105-1
7	Ag-L2-I	CRA142mf-K
8	Ag-L2-Br	CRA141mf
9	Cu-L4-I	CRA132c
10	Cu-L4i-I	CRA124c
11	Cu-1-P3-I	PJS30-1

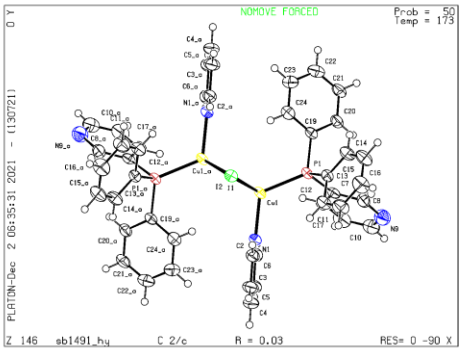

SB1491_HY

Cu-4-L2-I in pyridine

$L_2Cu_2I_2(pyridine)_2$

Crystal Data

$C_{44}H_{38}Cu_2I_2N_4P_2$	$F(000)$ = 2096
M_r = 1065.60	D_x = 1.712 Mg m^{-3}
Monoclinic, *C*2/*c* *(no.15)*	Cu *K*α radiation, λ = 1.54178 Å
a = 26.0165 (8) Å	Cell parameters from 9502 reflections
b = 14.3362 (4) Å	θ = 3.5–72.3°
c = 11.1495 (3) Å	μ = 14.01 mm^{-1}
β = 96.226 (1)°	*T* = 173 K
V = 4134.0 (2) Å^3	Blocks, colorless
Z = 4	0.16 × 0.08 × 0.04 mm

Data collection

Bruker D8 diffractometer VENTURE with PhotonII CPAD detector	3869 reflections with $I > 2\sigma(I)$
Radiation source: INCOATEC microfocus sealed tube	R_{int} = 0.057
rotation in ϕ and ω, 1°, shutterless scans	θ_{max} = 72.3°, θ_{min} = 3.5°
Absorption correction: multi-scan *SADABS* (Sheldrick, 2014)	*h* = -32→32
T_{min} = 0.283, T_{max} = 0.586	*k* = -17→17
25026 measured reflections	*l* = -12→13
4081 independent reflections	

Refinement

Refinement on F^2	Secondary atom site location: difference Fourier map
Least-squares matrix: full	Hydrogen site location: difference Fourier map
$R[F^2 > 2\sigma(F^2)]$ = 0.029	H-atom parameters constrained
$wR(F^2)$ = 0.079	$w = 1/[\sigma^2(F_o^2) + (0.0377P)^2 + 5.6201P]$ where $P = (F_o^2 + 2F_c^2)/3$
S = 1.05	$(\Delta/\sigma)_{max}$ = 0.001
4081 reflections	$\Delta\rangle_{max}$ = 0.79 e Å^{-3}
246 parameters	$\Delta\rangle_{min}$ = -0.68 e Å^{-3}
0 restraints	Extinction correction: *SHELXL2014*/7 (Sheldrick 2014), $Fc^*=kFc[1+0.001xFc^2\lambda^3/\sin(2\theta)]^{-1/4}$
Primary atom site location: dual	Extinction coefficient: 0.00021 (2)

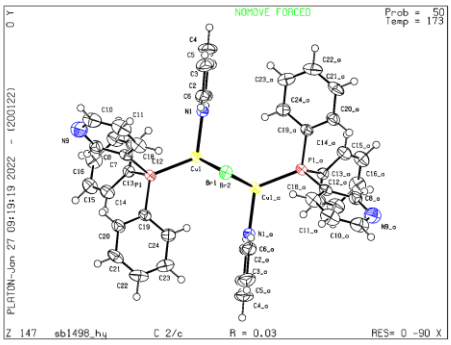

SB1498_HY

Cu-4-L2-Br in pyridine

***L*$_2$*Cu*$_2$*Br*$_2$*(pyridine)*$_2$**

Crystal Data

$C_{44}H_{38}Br_2Cu_2N_4P_2$	$F(000)$ = 1952
M_r = 971.62	D_x = 1.598 Mg m^{-3}
Monoclinic, *C*2/*c* *(no.15)*	Mo *K*α radiation, λ = 0.71073 Å
a = 26.2253 (10) Å	Cell parameters from 9949 reflections
b = 14.0114 (5) Å	θ = 2.4–27.4°
c = 11.0387 (4) Å	μ = 3.15 mm^{-1}
β = 95.375 (2)°	*T* = 173 K
V = 4038.4 (3) Å^3	Blocks, colorless
Z = 4	0.18 × 0.12 × 0.06 mm

Data collection

Bruker D8 VENTURE diffractometer with PhotonII CPAD detector	3929 reflections with $I > 2\sigma(I)$
Radiation source: INCOATEC microfocus sealed tube	R_{int} = 0.055
rotation in ϕ and ω, 1°, shutterless scans	θ_{max} = 27.5°, θ_{min} = 2.4°
Absorption correction: multi-scan *SADABS* (Sheldrick, 2014)	*h* = -34→34
T_{min} = 0.526, T_{max} = 0.837	*k* = -18→18
31013 measured reflections	*l* = -14→14
4642 independent reflections	

Refinement

Refinement on F^2	Primary atom site location: dual
Least-squares matrix: full	Secondary atom site location: difference Fourier map
$R[F^2 > 2\sigma(F^2)]$ = 0.028	Hydrogen site location: difference Fourier map
$wR(F^2)$ = 0.075	H-atom parameters constrained
S = 1.03	$w = 1/[\sigma^2(F_o^2) + (0.0204P)^2 + 5.8014P]$ where $P = (F_o^2 + 2F_c^2)/3$
4642 reflections	$(\Delta/\sigma)_{max}$ = 0.002
245 parameters	$\Delta\rangle_{max}$ = 0.38 e Å^{-3}
0 restraints	$\Delta\rangle_{min}$ = -0.38 e Å^{-3}

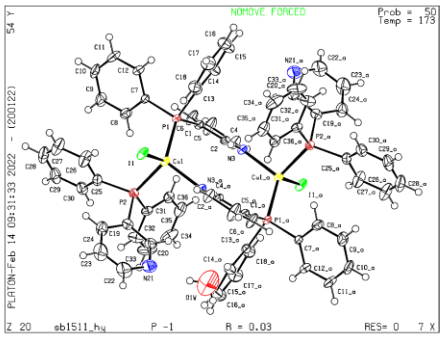

SB1511_HY

Cu-L2-I

traces of water (from SQUEEZE data: less than 1 water/unit cell or 0.5 water per void)

Crystal data

$C_{68}H_{56}Cu_2I_2N_4P_4 \cdot H_2O$	Z = 1
M_r = 1451.94	$F(000)$ = 726
Triclinic, *P*-1 (no.2)	D_x = 1.588 Mg m^{-3}
a = 9.6616 (5) Å	Mo $K\alpha$ radiation, λ = 0.71073 Å
b = 13.1995 (6) Å	Cell parameters from 9901 reflections
c = 13.8626 (6) Å	θ = 2.3–27.5°
α = 69.848 (2)°	μ = 1.87 mm^{-1}
β = 72.632 (2)°	T = 173 K
γ = 69.014 (2)°	Blocks, colorless
V = 1518.32 (13) Å^3	0.18 × 0.12 × 0.04 mm

Data collection

Bruker D8 VENTURE diffractometer with PhotonII CPAD detector	6174 reflections with $I > 2\sigma(I)$
Radiation source: INCOATEC microfocus sealed tube	R_{int} = 0.063
rotation in ϕ and ω, 1°, shutterless scans	θ_{max} = 27.6°, θ_{min} = 2.0°
Absorption correction: multi-scan *SADABS* (Sheldrick, 2014)	h = -12→12
T_{min} = 0.608, T_{max} = 0.942	k = -17→17
46094 measured reflections	l = -18→17
6997 independent reflections	

Refinement

Refinement on F^2	Primary atom site location: dual
Least-squares matrix: full	Secondary atom site location: difference Fourier map
$R[F^2 > 2\sigma(F^2)]$ = 0.029	Hydrogen site location: mixed
$wR(F^2)$ = 0.076	H atoms treated by a mixture of independent and constrained refinement
S = 1.04	$w = 1/[\sigma^2(F_o^2) + (0.0304P)^2 + 1.4659P]$ where $P = (F_o^2 + 2F_c^2)/3$
6997 reflections	$(\Delta/\sigma)_{max}$ = 0.002
376 parameters	$\Delta\rangle_{max}$ = 0.51 e Å^{-3}
9 restraints	$\Delta\rangle_{min}$ = -0.66 e Å^{-3}

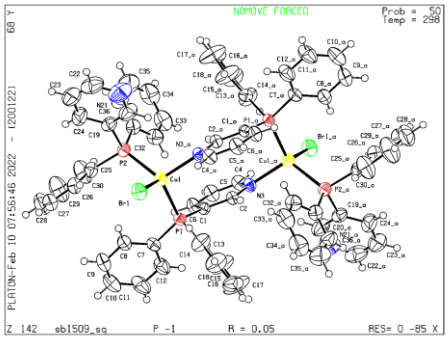

SB1509_HY

Cu-L2-Br

unknown solvent (pentane or water) squeezed out

Crystal data

$C_{68}H_{56}Br_2Cu_2N_4P_4$	Z = 1
M_r = 1339.94	F(000) = 680
Triclinic, P-1 (no.2)	D_x = 1.382 Mg m^{-3}
a = 10.3857 (6) Å	Cu $K\alpha$ radiation, λ = 1.54178 Å
b = 12.7076 (7) Å	Cell parameters from 9469 reflections
c = 13.1936 (8) Å	θ = 3.5–72.4°
α = 72.180 (2)°	μ = 3.53 mm^{-1}
β = 79.856 (2)°	T = 298 K
γ = 78.092 (2)°	Plates, colorless
V = 1610.07 (16) Å^3	0.16 × 0.06 × 0.02 mm

Data collection

Bruker D8 VENTURE diffractometer with PhotonII CPAD detector	5821 reflections with $I > 2\sigma(I)$
Radiation source: INCOATEC microfocus sealed tube	R_{int} = 0.068
rotation in ϕ and ω, 1°, shutterless scans	θ_{max} = 72.4°, θ_{min} = 3.6°
Absorption correction: multi-scan *SADABS* (Sheldrick, 2014)	h = -12→12
T_{min} = 0.569, T_{max} = 0.841	k = -14→15
24359 measured reflections	l = -16→16
6347 independent reflections	

Refinement

Refinement on F^2	Secondary atom site location: difference Fourier map
Least-squares matrix: full	Hydrogen site location: inferred from neighbouring sites
$R[F^2 > 2\sigma(F^2)]$ = 0.049	H-atom parameters constrained
$wR(F^2)$ = 0.140	$w = 1/[\sigma^2(F_o^2) + (0.099P)^2 + 0.2658P]$ where $P = (F_o^2 + 2F_c^2)/3$
S = 1.03	$(\Delta/\sigma)_{max}$ = 0.001
6347 reflections	$\Delta\rangle_{max}$ = 0.77 e Å^{-3}
362 parameters	$\Delta\rangle_{min}$ = -0.55 e Å^{-3}
324 restraints	Extinction correction: *SHELXL2014/7* (Sheldrick 2014), $Fc^*=kFc[1+0.001xFc^2\lambda^3/\sin(2\theta)]^{-1/4}$
Primary atom site location: dual	Extinction coefficient: 0.0013 (3)

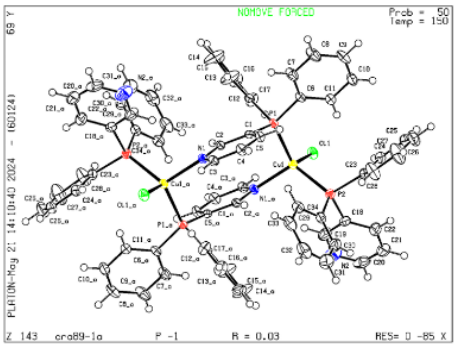

CRA89-1a

Cu-L2-Cl

Crystallizes with one molecule CH_2Cl_2

Identification code	CRA89-1a
Empirical formula	$C_{69}H_{58}Cl_4Cu_2N_4P_4$
Formula weight	1335.95
Temperature/K	150
Crystal system	triclinic
Space group	P-1
a/Å	10.1259(3)
b/Å	12.6077(4)
c/Å	13.1303(5)
α/°	72.157(3)
β/°	79.874(3)
γ/°	77.823(3)
Volume/Å^3	1548.57(10)
Z	1
ρ_{calc}g/cm^3	1.433
μ/mm^{-1}	5.614
F(000)	686.0
Crystal size/mm^3	0.14 × 0.13 × 0.12
Radiation	Ga Kα (λ = 1.34143)
2Θ range for data collection/°	6.196 to 115.02
Index ranges	-6 ≤ h ≤ 12, -15 ≤ k ≤ 15, -16 ≤ l ≤ 16
Reflections collected	15985
Independent reflections	6334 [R_{int} = 0.0157, R_{sigma} = 0.0162]
Data/restraints/parameters	6334/0/361
Goodness-of-fit on F^2	1.055
Final R indexes [I>=2σ (I)]	R_1 = 0.0326, wR_2 = 0.0813
Final R indexes [all data]	R_1 = 0.0350, wR_2 = 0.0826
Largest diff. peak/hole / e Å^{-3}	0.32/-0.51

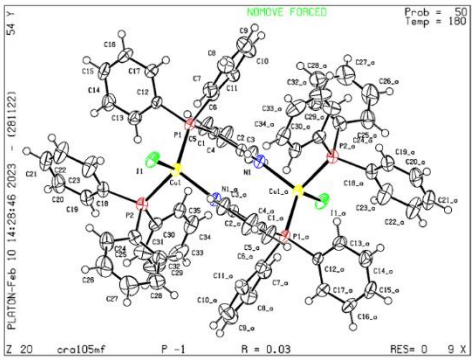

CRA105mf

Cu-L2-I-a

Identification code	CRA105mf
Empirical formula	$C_{70}H_{58}Cu_2I_2N_2P_4$
Formula weight	1431.94
Temperature/K	180
Crystal system	triclinic
Space group	P-1
a/Å	9.6604(8)
b/Å	13.2725(10)
c/Å	13.8030(8)
α/°	69.956(5)
β/°	72.582(6)
γ/°	69.150(6)
Volume/Å^3	1521.7(2)
Z	1
ρ_{calc}g/cm^3	1.563
μ/mm^{-1}	9.981
F(000)	716.0
Crystal size/mm^3	0.12 × 0.1 × 0.08
Radiation	GaKα (λ = 1.34143)
2Θ range for data collection/°	6.054 to 125.026
Index ranges	-12 ≤ h ≤ 9, -16 ≤ k ≤ 17, -18 ≤ l ≤ 18
Reflections collected	24148
Independent reflections	7294 [R_{int} = 0.0285, R_{sigma} = 0.0239]
Data/restraints/parameters	7294/0/361
Goodness-of-fit on F^2	1.038
Final R indexes [I>=2σ (I)]	R_1 = 0.0327, wR_2 = 0.0881
Final R indexes [all data]	R_1 = 0.0380, wR_2 = 0.0912
Largest diff. peak/hole / e Å^{-3}	0.72/-0.95

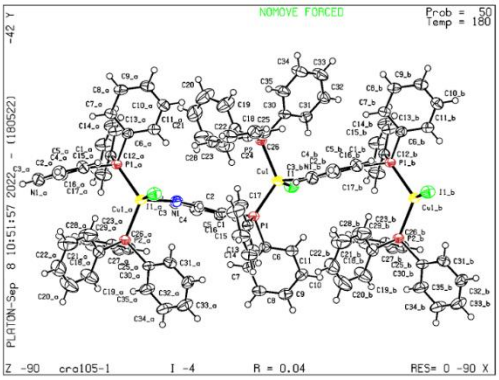

CRA105-1

Cu-L2-Ib

Identification code	CRA105-1
Empirical formula	$C_{35}H_{29}CuINP_2$
Formula weight	715.97
Temperature/K	180
Crystal system	tetragonal
Space group	I-4
a/Å	21.9276(4)
b/Å	21.9276(4)
c/Å	14.0993(3)
α/°	90
β/°	90
γ/°	90
Volume/Å^3	6779.2(3)
Z	8
ρ_{calc}g/cm^3	1.403
μ/mm^{-1}	8.961
F(000)	2864.0
Crystal size/mm^3	0.18 × 0.16 × 0.03
Radiation	GaKα (λ = 1.34143)
2Θ range for data collection/°	6.484 to 114.97
Index ranges	-27 ≤ h ≤ 27, -14 ≤ k ≤ 27, -17 ≤ l ≤ 17
Reflections collected	28942
Independent reflections	6998 [R_{int} = 0.0339, R_{sigma} = 0.0295]
Data/restraints/parameters	6998/0/361
Goodness-of-fit on F^2	1.019
Final R indexes [I>=2σ (I)]	R_1 = 0.0427, wR_2 = 0.1090
Final R indexes [all data]	R_1 = 0.0474, wR_2 = 0.1112
Largest diff. peak/hole / e Å^{-3}	0.62/-0.58
Flack parameter	-0.001(5)

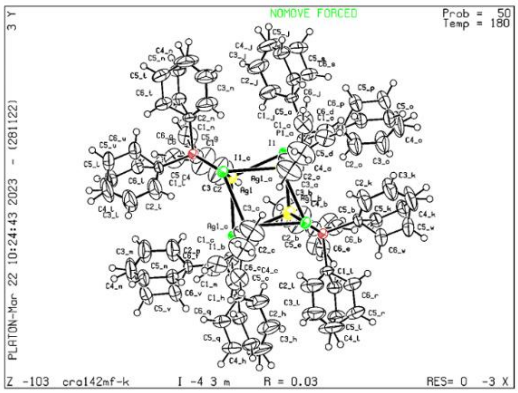

CRA142mf-K

Ag-L2-I

Identification code	CRA142mf-K
Empirical formula	$C_{72}H_{60}Ag_4I_4P_4$
Formula weight	1988.16
Temperature/K	180
Crystal system	cubic
Space group	I-43m
a/Å	15.1097(4)
b/Å	15.1097(4)
c/Å	15.1097(4)
α/°	90
β/°	90
γ/°	90
Volume/Å^3	3449.6(3)
Z	2
ρ_{calc}g/cm^3	1.914
μ/mm^{-1}	16.214
F(000)	1904.0
Crystal size/mm^3	0.15 × 0.117 × 0.1
Radiation	GaKα (λ = 1.34143)
2Θ range for data collection/°	7.198 to 119.318
Index ranges	-19 ≤ h ≤ 16, -19 ≤ k ≤ 19, -13 ≤ l ≤ 19
Reflections collected	20368
Independent reflections	759 [R_{int} = 0.0843, R_{sigma} = 0.0226]
Data/restraints/parameters	759/6/52
Goodness-of-fit on F^2	1.179
Final R indexes [I>=2σ (I)]	R_1 = 0.0349, wR_2 = 0.0962
Final R indexes [all data]	R_1 = 0.0353, wR_2 = 0.0964
Largest diff. peak/hole / e Å^{-3}	0.37/-0.59
Flack parameter	0.01(3)

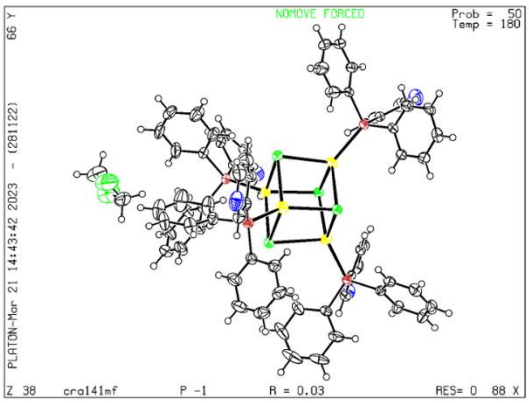

CRA141mf

Ag-L2-Br

Identification code	CRA141mf
Empirical formula	$C_{69}H_{58}Ag_4Br_4Cl_2N_4P_4$
Formula weight	1889.09
Temperature/K	180
Crystal system	triclinic
Space group	P-1
a/Å	14.0453(10)
b/Å	15.8344(14)
c/Å	16.5446(9)
α/°	87.124(6)
β/°	67.954(5)
γ/°	81.752(6)
Volume/Å^3	3375.2(4)
Z	2
ρ_{calc}g/cm^3	1.859
μ/mm^{-1}	9.370
F(000)	1844.0
Crystal size/mm^3	0.12 × 0.1 × 0.05
Radiation	GaKα (λ = 1.34143)
2Θ range for data collection/°	4.906 to 125.446
Index ranges	$-9 \le h \le 18$, $-20 \le k \le 20$, $-21 \le l \le 21$
Reflections collected	58028
Independent reflections	16053 [R_{int} = 0.0516, R_{sigma} = 0.0715]
Data/restraints/parameters	16053/0/793
Goodness-of-fit on F^2	0.831
Final R indexes [I>=2σ (I)]	R_1 = 0.0329, wR_2 = 0.0695
Final R indexes [all data]	R_1 = 0.0520, wR_2 = 0.0713
Largest diff. peak/hole / e Å^{-3}	1.18/-0.91

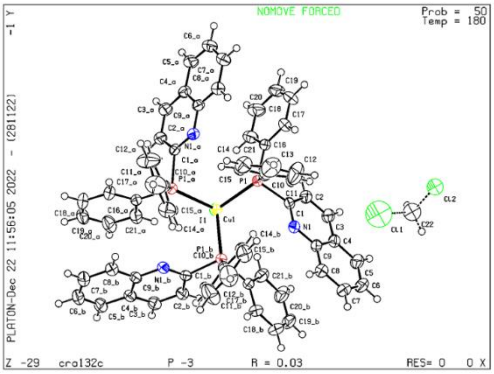

CRA132c

Cu-L4-I

Crystallizes with one molecule CH_2Cl_2

Identification code	CRA132c
Empirical formula	$C_{64}H_{50}Cl_2CuIN_3P_3$
Formula weight	1215.32
Temperature/K	180
Crystal system	trigonal
Space group	P-3
a/Å	14.7202(4)
b/Å	14.7202(4)
c/Å	15.9759(4)
α/°	90
β/°	90
γ/°	120
Volume/Å^3	2997.94(18)
Z	2
ρ_{calc}g/cm^3	1.346
μ/mm^{-1}	5.917
F(000)	1232.0
Crystal size/mm^3	0.12 × 0.1 × 0.08
Radiation	GaKα (λ = 1.34143)
2Θ range for data collection/°	6.032 to 114.984
Index ranges	-18 ≤ h ≤ 16, -17 ≤ k ≤ 18, -20 ≤ l ≤ 13
Reflections collected	37199
Independent reflections	4163 [R_{int} = 0.0232, R_{sigma} = 0.0115]
Data/restraints/parameters	4163/2/226
Goodness-of-fit on F^2	1.044
Final R indexes [I>=2σ (I)]	R_1 = 0.0301, wR_2 = 0.0793
Final R indexes [all data]	R_1 = 0.0332, wR_2 = 0.0810
Largest diff. peak/hole / e Å^{-3}	0.80/-0.79

CRA124C

Cu-L4i-I

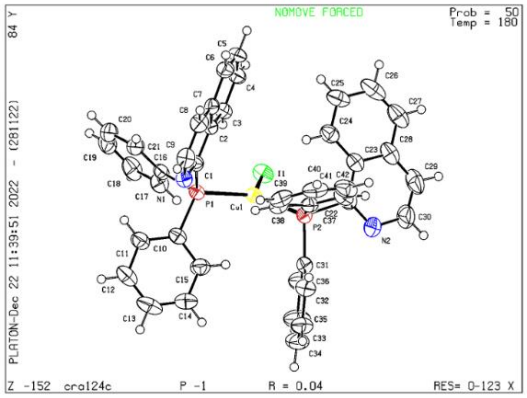

Identification code	CRA124C
Empirical formula	$C_{42}H_{32}CuIN_2P_2$
Formula weight	817.07
Temperature/K	180
Crystal system	triclinic
Space group	P-1
a/Å	10.5752(7)
b/Å	12.0121(10)
c/Å	16.2449(12)
α/°	77.769(6)
β/°	86.285(6)
γ/°	68.740(6)
Volume/Å^3	1879.3(3)
Z	2
ρ_{calc}g/cm^3	1.444
μ/mm^{-1}	8.137
F(000)	820.0
Crystal size/mm^3	0.12 × 0.04 × 0.03
Radiation	GaKα (λ = 1.34143)
2Θ range for data collection/°	4.842 to 115.1
Index ranges	-13 ≤ h ≤ 12, -14 ≤ k ≤ 7, -20 ≤ l ≤ 19
Reflections collected	24095
Independent reflections	7727 [R_{int} = 0.0325, R_{sigma} = 0.0415]
Data/restraints/parameters	7727/0/433
Goodness-of-fit on F^2	0.949
Final R indexes [I>=2σ (I)]	R_1 = 0.0378, wR_2 = 0.0958
Final R indexes [all data]	R_1 = 0.0549, wR_2 = 0.1008
Largest diff. peak/hole / e Å^{-3}	1.28/-0.99

PJS-30-1

Cu-1-L8-I

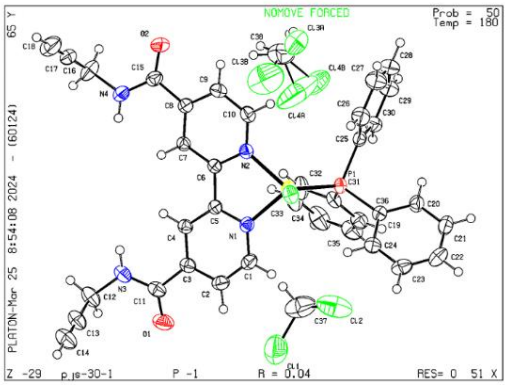

Crystallizes with CH_2Cl_2

Identification code	PJS-30-1
Empirical formula	$C_{38}H_{33}Cl_4CuIN_4O_2P$
Formula weight	940.89
Temperature/K	180
Crystal system	triclinic
Space group	P-1
a/Å	9.0817(2)
b/Å	13.6863(3)
c/Å	17.4599(4)
α/°	70.878(2)
β/°	80.431(2)
γ/°	80.775(2)
Volume/Å^3	2008.81(8)
Z	2
ρ_{calc}g/cm^3	1.556
μ/mm^{-1}	9.164
F(000)	940.0
Crystal size/mm^3	0.14 × 0.12 × 0.1
Radiation	Ga Kα (λ = 1.34143)
2Θ range for data collection/°	5.986 to 124.972
Index ranges	$-11 \leq h \leq 5$, $-18 \leq k \leq 16$, $-23 \leq l \leq 22$
Reflections collected	27630
Independent reflections	9501 [R_{int} = 0.0189, R_{sigma} = 0.0166]
Data/restraints/parameters	9501/0/478
Goodness-of-fit on F^2	1.028
Final R indexes [I>=2σ (I)]	R_1 = 0.0367, wR_2 = 0.0993
Final R indexes [all data]	R_1 = 0.0408, wR_2 = 0.1022
Largest diff. peak/hole / e Å^{-3}	1.95/-1.07

5.2.6 Theoretical Calculations

The following results were provided by Anna Mauri (KIT, INT).

Table 20. Overview of the numbering and sample code for calculations of chapter 3.1.

Entry	Numbering in this thesis	Sample code used by the calculator
1	Cu-L2-I	Cu-1
2	Cu-L2-Br	Cu-2
3	Cu-L2-Cl	Cu-3
4	Cu-L2-CN	Cu-4
5	Cu-L2-SCN	Cu-5

Table 21. Energies (in eV) of the highest occupied molecular orbital (HOMO) and lowest unoccupied molecular orbital (LUMO) of the optimized ground state geometry of **Cu-L2-I, Cu-L2-Br, Cu-L2-Cl, Cu-L2-CN, Cu-L2-SCN (Cu-1-5)** in gas phase. Data are computed with B3LYP-D3(BJ)/def2-TZVP including LANL2DZ for iodine.[237-242] The fundamental gap refers to the difference between HOMO and LUMO while the optical gap refers to the energy of the lowest electronic singlet state S_1 of **Table 22**.[253]

	HOMO	LUMO	Fundamental gap	Optical gap
Cu-1	-5.18	-1.80	3.38	2.92
Cu-2	-5.42	-1.86	3.55	3.06
Cu-3	-5.38	-1.82	3.76	3.10
Cu-4	-5.89	-1.90	3.99	3.32
Cu-5	-5.20	-1.86	3.34	2.83

Table 22. First ten singlet vertical excitation energies for **Cu-1**–**5** in gas phase. Data arecomputed with B3LYP-D3(BJ)/def2-TZVP including LANL2DZ for iodine.

	Cu-1		Cu-2		Cu-3		Cu-4		Cu-5	
	eV	f	eV	f	eV	f	eV	f	eV	f
S_1	2.92	0.00	3.06	0.00	3.10	0.00	3.32	0.00	2.83	0.00
S_2	2.94	0.01	3.08	0.02	3.12	0.03	3.33	0.03	2.87	0.01
S_3	3.04	0.00	3.21	0.01	3.24	0.00	3.43	0.00	2.94	0.00
S_4	3.04	0.00	3.22	0.00	3.26	0.00	3.46	0.00	2.95	0.00
S_5	3.07	0.01	3.24	0.00	3.27	0.00	3.48	0.01	2.95	0.00
S_6	3.09	0.00	3.26	0.00	3.29	0.01	3.49	0.00	2.98	0.00
S_7	3.12	0.00	3.27	0.01	3.33	0.03	3.52	0.00	3.02	0.01
S_8	3.14	0.00	3.27	0.00	3.33	0.00	3.51	0.02	3.03	0.01
S_9	3.18	0.00	3.31	0.03	3.35	0.01	3.55	0.00	3.05	0.00
S_{10}	3.19	0.01	3.31	0.00	3.36	0.00	3.55	0.03	3.09	0.00

Table 23. First ten triplet vertical excitation energies (in eV) for **Cu-1**–**5** in gas phase. Data are computed with B3LYP-D3(BJ)/def2-TZVP including LANL2DZ for iodine.

	Cu-1	**Cu-2**	**Cu-3**	**Cu-4**	**Cu-5**
T_1	2.89	3.00	3.02	3.21	2.81
T_2	2.90	3.00	3.02	3.21	2.84
T_3	2.99	3.10	3.13	3.30	2.91
T_4	2.99	3.10	3.13	3.30	2.92
T_5	3.01	3.16	3.17	3.36	2.92
T_6	3.01	3.17	3.19	3.36	2.95
T_7	3.06	3.19	3.20	3.37	2.97
T_8	3.06	3.19	3.20	3.37	3.00
T_9	3.11	3.21	3.25	3.40	3.04
T_{10}	3.12	3.21	3.25	3.40	3.07

Table 24. Energy gap between the first singlet state (S_1) and the first five triplets (T_1-T_5). Data are computed from the vertical excitation energies for **Cu-1**–**5** calculated with B3LYP-D3(BJ)/def2-TZVP in gas phase including LANL2DZ for iodine.

ΔS_1-	**Cu-1**	**Cu-2**	**Cu-3**	**Cu-4**	**Cu-5**
T_1	0.03	0.06	0.09	0.11	0.02
T_2	0.02	0.06	0.07	0.11	-0.01
T_3	-0.07	-0.04	-0.04	0.02	-0.07
T_4	-0.07	-0.04	-0.04	0.02	-0.08
T_5	-0.09	-0.10	-0.07	-0.04	-0.09

The following calculations were made, to investigate the influence considering different functionals and solvent effects. The data were computed employing B3LYP-D3(BJ)/def2-TZVP and CAM-B3LYP-D3(BJ)/def2-TZVP in dichloromethane (DCM) using polarizable continuum model (PCM) including LANL2DZ for iodine.[245] Results are reported in **Table 25** to **Table 30**

Table 25. First ten singlet vertical excitation energies for **Cu-1**–**5** in DCM**.** Data are computed with B3LYP-D3(BJ)/def2-TZVP (PCM model) including LANL2DZ for iodine.[244]

	Cu-1		**Cu-2**		**Cu-3**		**Cu-4**		**Cu-5**	
	eV	f	eV	f	eV	f	eV	f	eV	f
S_1	3.23	0.00	3.25	0.00	3.27	0.00	3.43	0.00	3.25	0.01
S_2	3.24	0.03	3.28	0.05	3.29	0.05	3.45	0.04	3.27	0.03
S_3	3.34	0.01	3.38	0.03	3.41	0.02	3.57	0.02	3.39	0.01
S_4	3.34	0.00	3.40	0.00	3.43	0.00	3.60	0.00	3.42	0.01
S_5	3.40	0.02	3.46	0.02	3.47	0.00	3.62	0.03	3.44	0.00
S_6	3.41	0.00	3.47	0.00	3.49	0.01	3.63	0.00	3.46	0.01
S_7	3.45	0.00	3.48	0.00	3.50	0.03	3.67	0.00	3.47	0.01
S_8	3.46	0.01	3.50	0.01	3.51	0.00	3.68	0.01	3.48	0.00
S_9	3.49	0.00	3.56	0.05	3.53	0.05	3.70	0.00	3.51	0.02
S_{10}	3.51	0.01	3.57	0.00	3.54	0.00	3.71	0.05	3.52	0.03

Table 26. First ten triplet vertical excitation energies for **Cu-1**–**5** in DCM. Data are computed with B3LYP-D3(BJ)/def2-TZVP (PCM model) including LANL2DZ for iodine.

	Cu-1	**Cu-2**	**Cu-3**	**Cu-4**	**Cu-5**
T_1	3.15	3.15	3.16	3.30	3.17
T_2	3.16	3.15	3.16	3.30	3.19
T_3	3.24	3.23	3.26	3.37	3.28
T_4	3.25	3.24	3.26	3.39	3.29
T_5	3.27	3.33	3.32	3.43	3.33
T_6	3.29	3.33	3.34	3.46	3.35
T_7	3.36	3.37	3.36	3.48	3.35
T_8	3.36	3.39	3.37	3.48	3.36
T_9	3.38	3.40	3.39	3.51	3.37
T_{10}	3.39	3.40	3.40	3.51	3.39

Table 27. The energy gap between the first singlet state (S_1) and the first five triplet states (T_1-T_5). Data are computed from the vertical excitation energies for **Cu-1**–**5** calculated with B3LYP-D3(BJ)/def2-TZVP in DCM (PCM model) including LANL2DZ for iodine.

ΔS_1-	**Cu-1**	**Cu-2**	**Cu-3**	**Cu-4**	**Cu-5**
T_1	0.07	0.10	0.11	0.14	0.08
T_2	0.06	0.10	0.10	0.13	0.07
T_3	-0.03	0.02	0.01	0.06	-0.03
T_4	-0.04	0.01	0.00	0.04	-0.04
T_5	-0.05	-0.08	-0.06	-0.00	-0.08

Table 28. First ten singlet vertical excitation energies for **Cu-1**–**5** in DCM**.** Data are computed with CAM-B3LYP-D3(BJ)/def2-TZVP (PCM model) including LANL2DZ for iodine.

	Cu-1		**Cu-2**		**Cu-3**		**Cu-4**		**Cu-5**	
	eV	f	eV	f	eV	f	eV	f	eV	f
S_1	4.38	0.00	4.15	0.00	4.36	0.00	4.50	0.00	4.41	0.00
S_2	4.39	0.04	4.16	0.04	4.37	0.05	4.51	0.04	4.424	0.06
S_3	4.45	0.09	4.31	0.00	4.48	0.10	4.59	0.09	4.52	0.05
S_4	4.49	0.00	4.32	0.03	4.51	0.00	4.63	0.00	4.53	0.04
S_5	4.55	0.00	4.34	0.08	4.53	0.11	4.65	0.13	4.55	0.10
S_6	4.57	0.12	4.35	0.00	4.53	0.00	4.68	0.00	4.57	0.00
S_7	4.57	0.00	4.36	0.00	4.55	0.00	4.69	0.00	4.61	0.17
S_8	4.58	0.00	4.38	0.05	4.57	0.21	4.71	0.00	4.62	0.00
S_9	4.59	0.06	4.43	0.00	4.59	0.00	4.72	0.37	4.63	0.07
S_{10}	4.62	0.16	4.43	0.05	4.60	0.11	4.73	0.07	4.67	0.10

Table 29. First ten triplet vertical excitation energies for **Cu-1**–**5** in DCM**.** Data are computed with CAM-B3LYP-D3(BJ)/def2-TZVP (PCM model) including LANL2DZ for iodine.

	Cu-1	**Cu-2**	**Cu-3**	**Cu-4**	**Cu-5**
T_1	3.52	3.45	3.52	3.52	3.52
T_2	3.52	3.45	3.52	3.52	3.53

T_3	3.52	3.46	3.52	3.53	3.53
T_4	3.52	3.46	3.53	3.53	3.53
T_5	3.54	3.46	3.53	3.54	3.54
T_6	3.54	3.46	3.53	3.54	3.54
T_7	3.54	3.48	3.54	3.55	3.55
T_8	3.54	3.48	3.54	3.55	3.55
T_9	3.57	3.51	3.56	3.57	3.56
T_{10}	3.57	3.51	3.56	3.57	3.57

Table 30. The energy gap between the first singlet state (S_1) and the first triplets (T_1-T_5). Data are computed from the vertical excitation energies for **Cu-1**–**5** calculated with CAM-B3LYP-D3(BJ)/def2-TZVP in DCM (PCM model) including LANL2DZ for iodine.

ΔS_1-	**Cu-1**	**Cu-2**	**Cu-3**	**Cu-4**	**Cu-5**
T_1	0.86	0.72	0.84	0.97	0.89
T_2	0.86	0.71	0.84	0.97	0.89
T_3	0.86	0.70	0.83	0.97	0.89
T_4	0.86	0.70	0.83	0.97	0.88
T_5	0.85	0.70	0.82	0.96	0.88

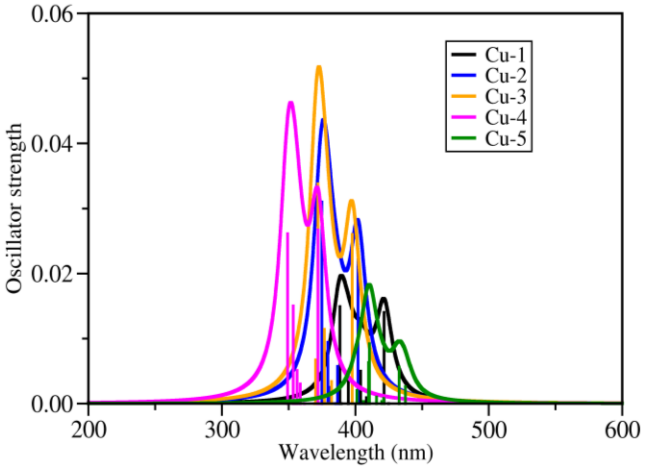

Figure 89. Computed absorption spectra for **Cu-1** to **Cu-5** in gas-phase**.** Calculated in B3LYP-D3(BJ)/def2-TZVP (including LANL2DZ for I_2). Spectra were plotted using HWHM as 0.1 eV and Lorentzian type broadening function.

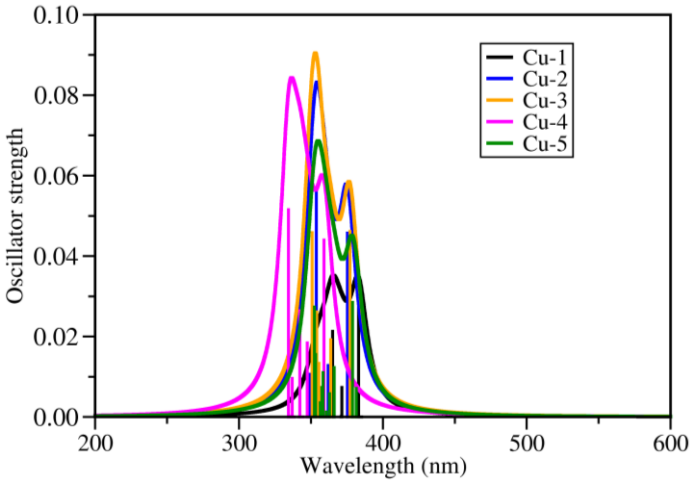

Figure 90. Theoretical absorption spectra of **Cu-1**–**5** in DCM**.** Computed in B3LYP-D3(BJ)/def2-TZVP (including LANL2DZ for I_2) (PCM model). Spectra were plotted using HWHM as 0.1 eV and Lorentzian type broadening function.

Table 31. List atom contribution in % to the hole region (HOMO) upon $S_0 \rightarrow S_1$ transition for **Cu-1**–**5** in gas-phase. Data are computed with B3LYP-D3(BJ)/def2-TZVP (including LANL2DZ for I_2) and by employing Multiwfn analyzer (version 3.6).[246]

Hole (%)		
	M (%)	X (%)
Cu-1	Cu(3) 6.90 Cu(4) 8.25	I(1) 29.31 I(2) 35.30
Cu-2	Cu(3) 14.22 Cu(4) 14.28	Br(1) 18.42 Br(2) 18.50
Cu-3	Cu(1) 17.70 Cu(2) 17.88	Cl(3) 10.83 Cl(4) 10.94
Cu-4	Cu(14) 19.23 Cu(36) 18.97	P(7) 10.77 P(37) 10.62
Cu-5	Cu(1) 11.87 Cu(2) 0.01	N(135) 17.62 C(136) 2.32 S(137) 56.60

5.2.7 Photophysical Data

5.2.7.1 Chapter 3.1

Table 32: Numbering schmeme for the phtophysical data that were provided by Daniel Marhöfer.

Entry	Numbering in this thesis	Sample code used for photophysical measurements
1	Cu-L2-I	Cu-1
2	Cu-L2-Br	Cu-2
3	Cu-L2-Cl	Cu-3
4	Cu-L2-CN	Cu-4
4	Cu-L2-SCN	Cu-5

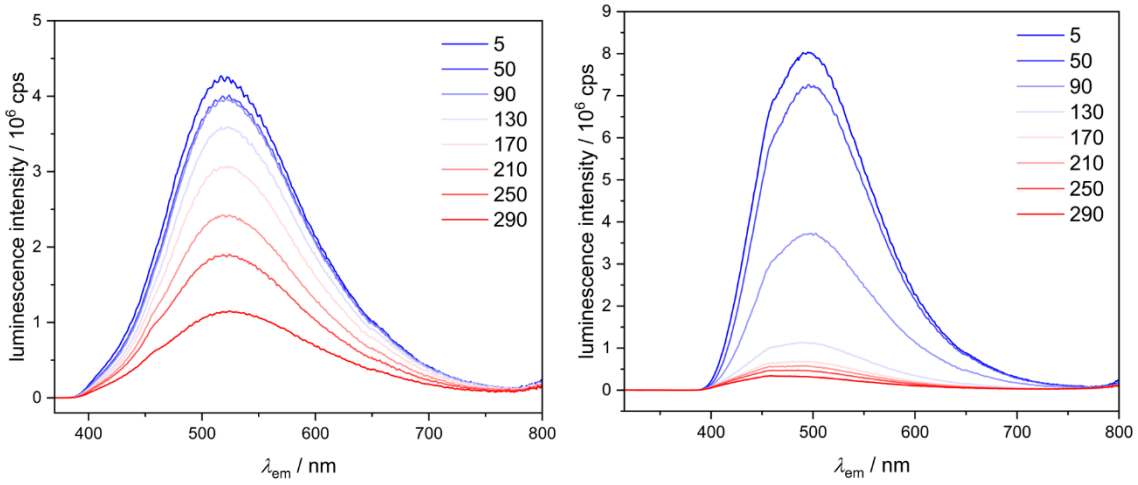

Figure 91. Luminescence spectra of **L2** at λ_{ex}= 355 (left) and λ_{ex}= 300 nm (right) in a sintered KBr pellet between 5 and 290 K. Results provided by Daniel Marhöfer (RPTU).

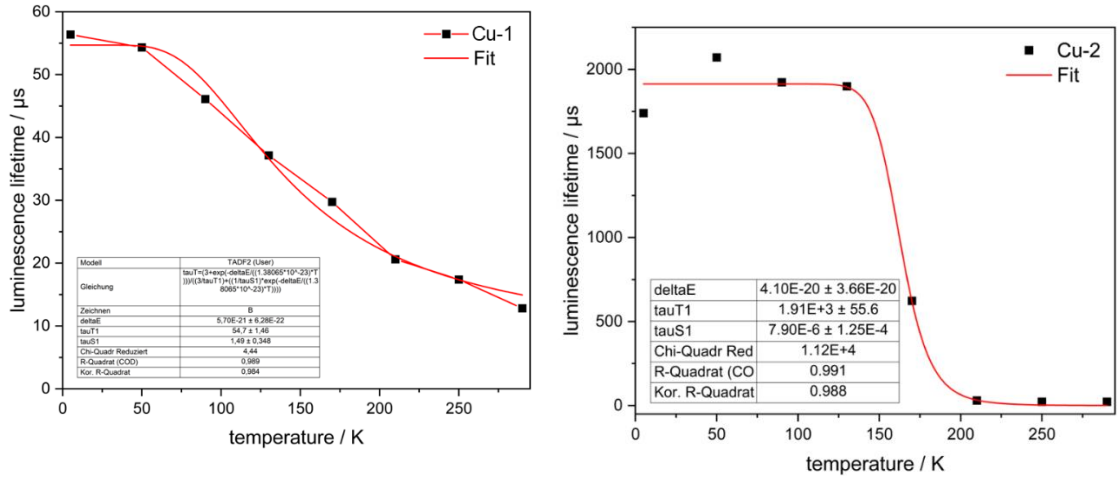

Figure 92. TADF fits of the measured lifetimes for Cu-1 (left) and Cu-2 (right). Energy given in J. Results provided by Daniel Marhöfer (RPTU).

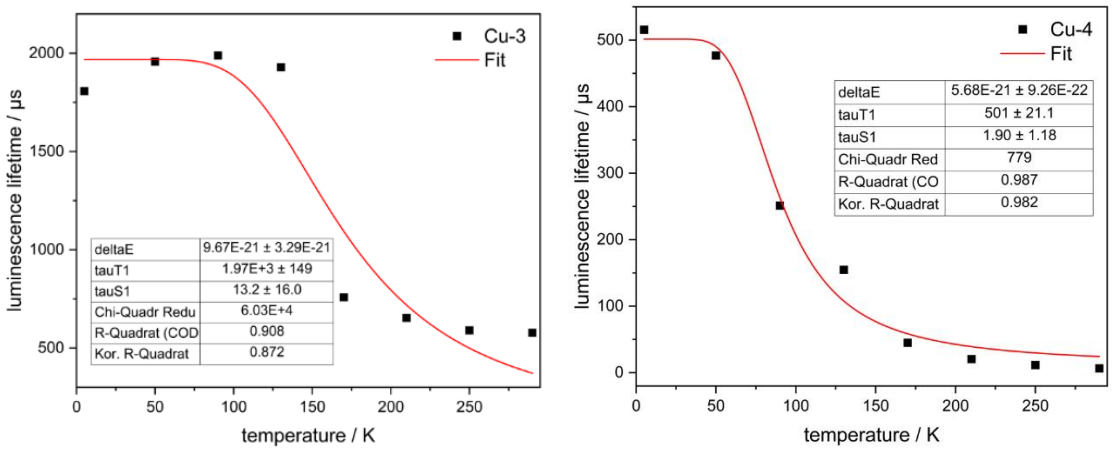

Figure 93. TADF fits of the measured lifetimes for Cu-3 (left) and Cu-4 (right). The energy is given in J. Results provided by Daniel Marhöfer (RPTU).

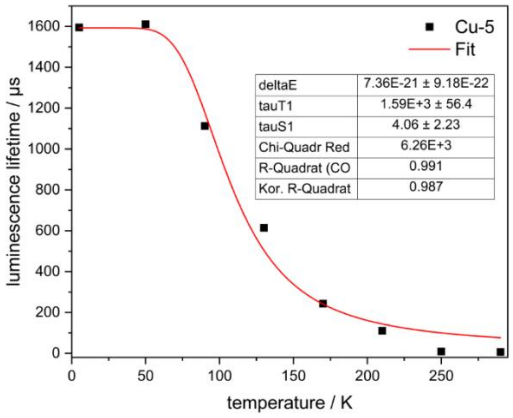

Figure 94. TADF fits of the measured lifetimes for Cu-5. The energy is given in J. Results provided by Daniel Marhöfer (RPTU).

5.2.7.2 Chapter 3.3.

5.2.7.2.1 Steady-state photoluminescence.

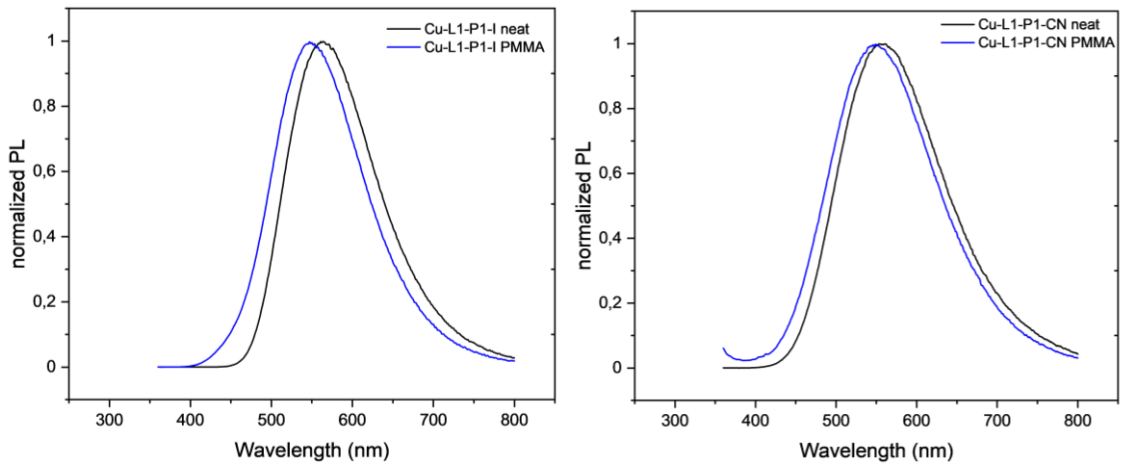

Figure 95. Comparison of photoluminescence spectra of a neat film and a film with 1 wt% emitter in PMMA for **Cu-L1-P1-I** and **Cu-L1-P1-CN**. Films were prepared by drop-casting and measured in air at room temperature.

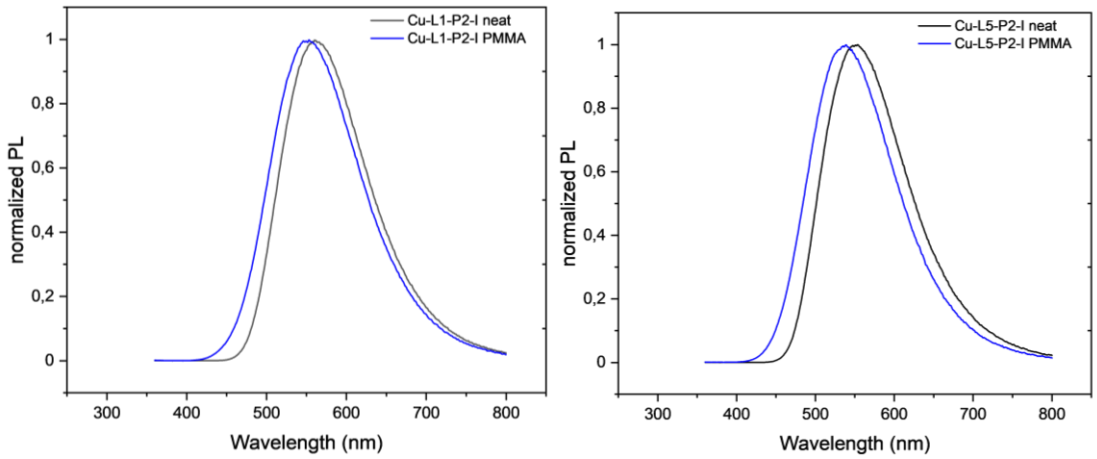

Figure 96. Comparison of photoluminescence spectra of a neat film and a film with 1 wt% emitter in PMMA for **Cu-L1-P2-I** and **Cu-L5-P2-I**. Films were prepared by drop-casting and measured in air at room temperature.

5.2.7.2.2 Time-resolved measurements (iCCD)

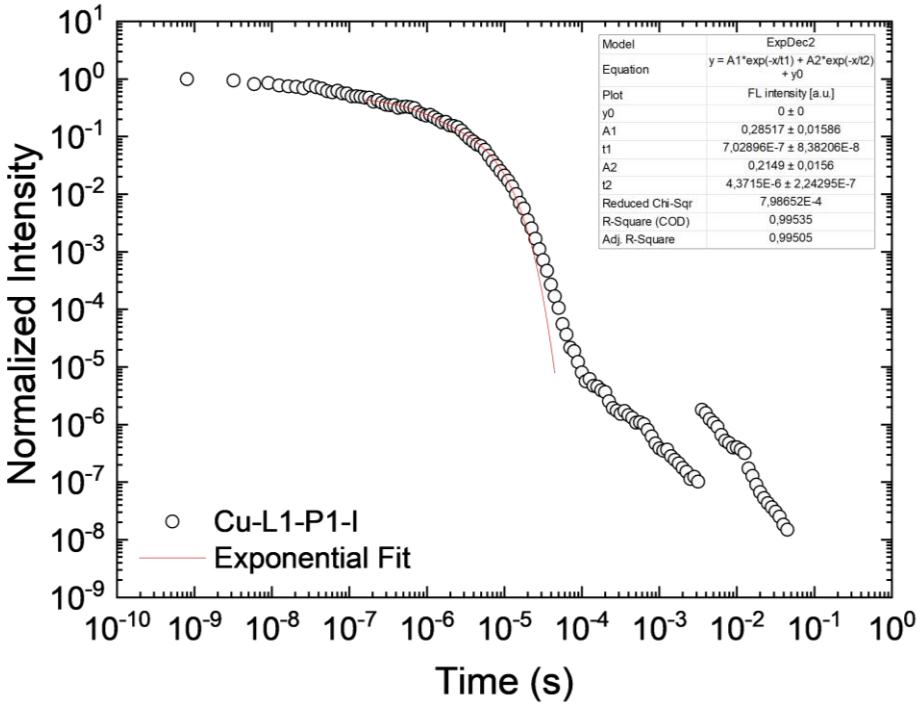

Figure 97. Decay fit of the iCCD measured lifetimes for **Cu-L1-P1-I** at room temperature.

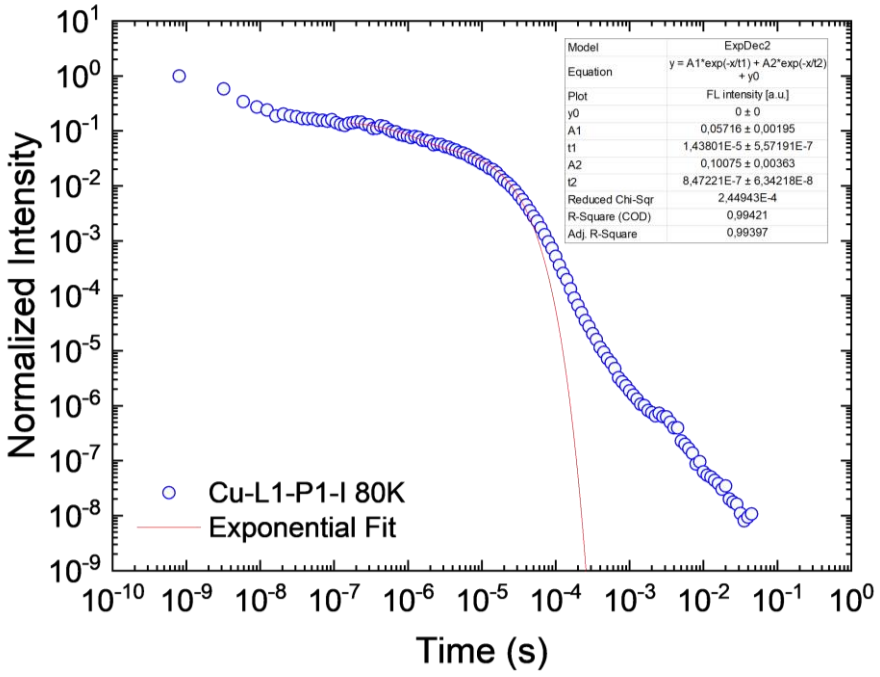

Figure 98. Decay fit of the iCCD measured lifetimes for **Cu-L1-P1-I** at 80 K.

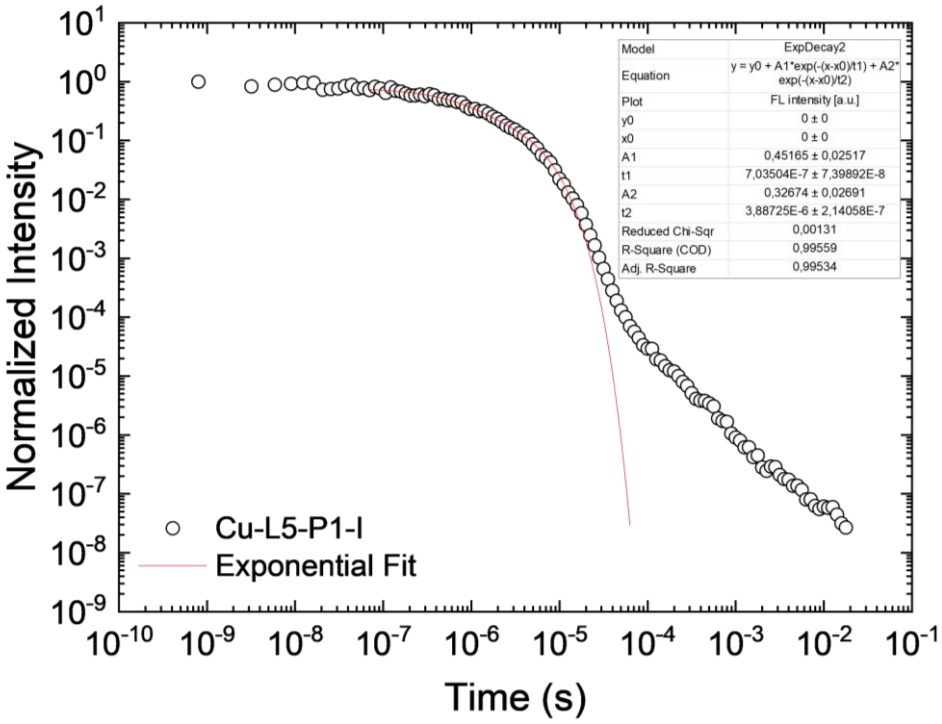

Figure 99. Decay fit of the iCCD measured lifetimes for **Cu-L5-P1-I** at room temperature.

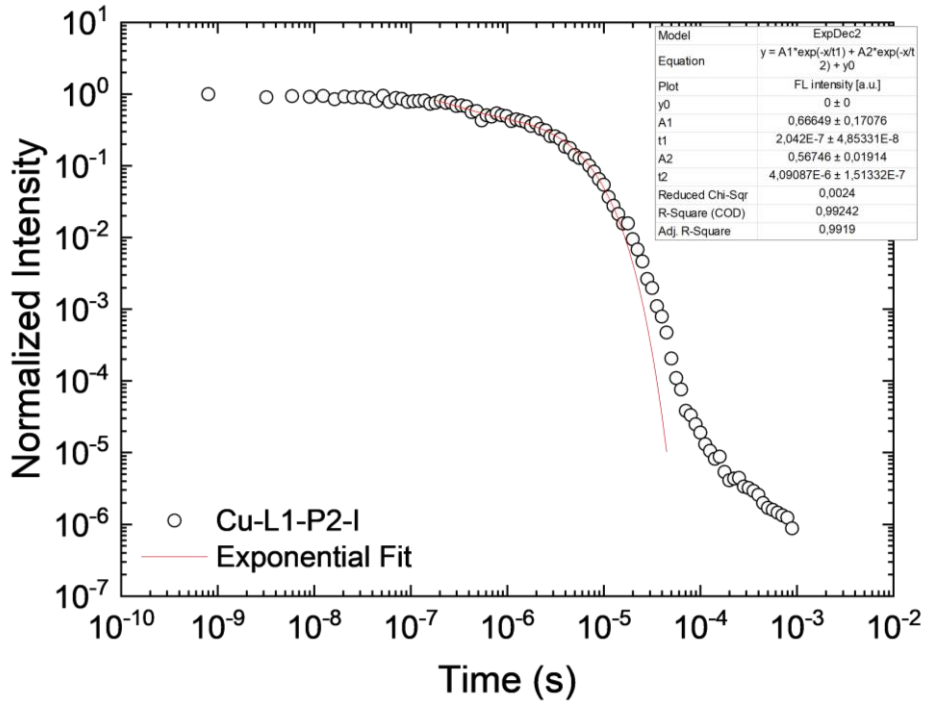

Figure 100. Decay fit of the iCCD measured lifetimes for **Cu-L1-P2-I** at room temperature.

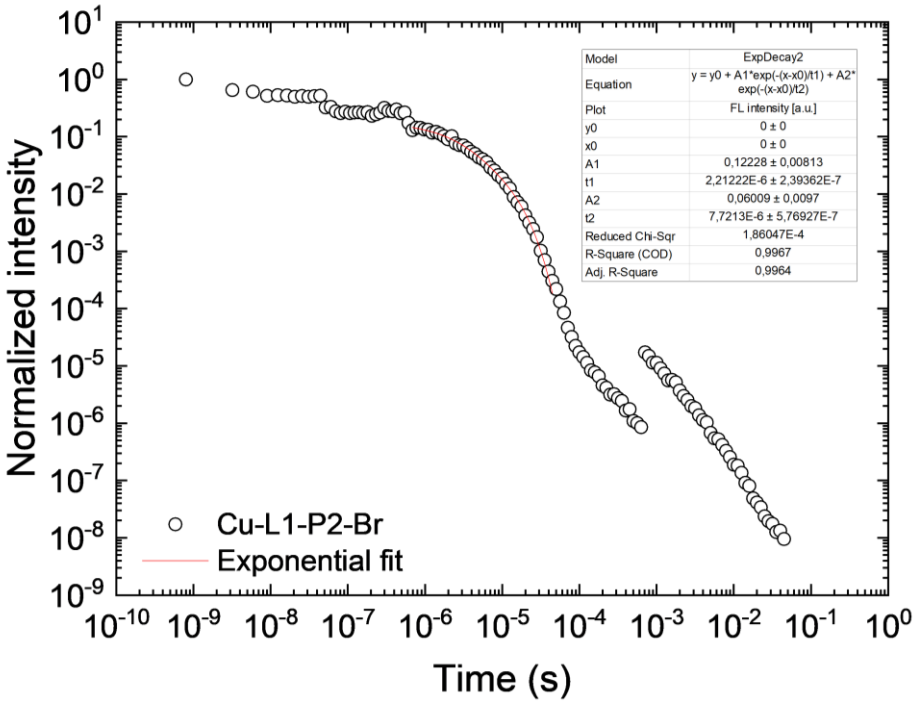

Figure 101. Decay fit of the iCCD measured lifetimes for **Cu-L1-P2-Br** at room temperature.

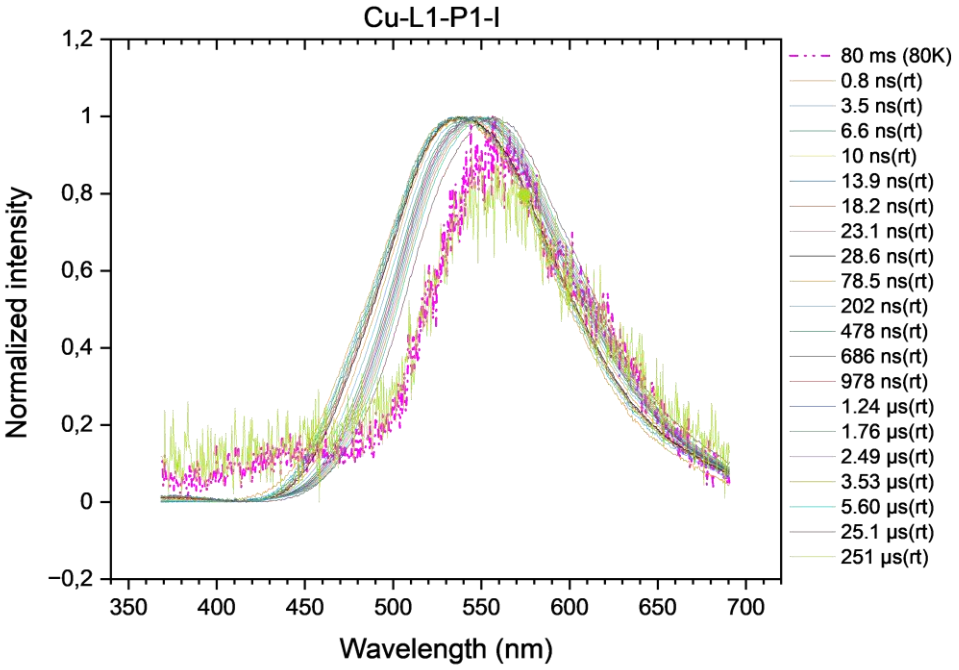

Figure 102. Comparison of normalized time-resolved photoluminescence spectra (λ_{exc} = 355 nm) of **Cu-L1-P1-I** in 1 wt% doped zeonex film at room-temperature and 80 K.

5.2.8 OLED devices

Table 33. Overview of fabricated OLED devices in *Set 1*. If not noted otherwise dynamic spin coating was performed with 2500 rpm and a concentration of 10mg/ml

OLED No.	**File No.**	**Compounds**	**Host**	**Processing details**	**Device Structure**	**EQE_{max} [%]**
OLED 1.1	2.dev4	Cu-L1-P1-I 50 wt%	mCP	2500 rpm chlorobenzene	ITO | PEDOT:PSS (40) | Cu-L1-P1-I:mCB50| T2T (5) | TPBi (40) | LiF (1) | Al 100)	2.2
OLED 1.2	2.dev5	Cu-L1-P1-I 20 wt%	mCP	2500 rpm chlorobenzene	ITO | PEDOT:PSS | Cu-L1-P1-I:mCP20 | T2T (5) | TPBi (40) | LiF (1) | Al 100)	2.8
OLED 1.3	3.dev3	Cu-L1-P1-I 50 wt%	mCP	Static 2500 rpm chlorobenzene	ITO | PEDOT:PSS (40) | Cu-L1-P1-I:mCP50 (40)| T2T (5) | TPBi (40) | LiF (1) | Al 100)	3.6
OLED 1.4	2.dev6	Cu-L1-P1-I 20 wt%	PVK	2500 rpm chlorobenzene	ITO | PEDOT:PSS (40) | Cu-L1-P1-I:PVK20 | T2T (5) | TPBi (40) | LiF (1) |	0.8
OLED 1.5	3.dev5	Cu-L1-P1-I 20 wt%	PVK (1 Mio.)	2500 rpm	ITO | PEDOT:PSS (40) | Cu-L1-P1-I:PVK20 (40)| T2T (5) | TPBi (40) | LiF (1) | Al 100)	-
OLED 1.6	3.dev4	Cu-L1-P2-Br 50 wt%	mCP	3000 rpm	ITO | PEDOT:PSS (40) | Br:mCP50 (40)| T2T (5) | TPBi (40) | LiF (1) | Al 100)	1.6
OLED 1.7	3.dev6	Cu-L1-P2-Br 20 wt%	PVK (1 Mio.)	2500 rpm	ITO | PEDOT:PSS (40) | Br:PVK20 (40)| T2T (5) | TPBi (40) | LiF (1) | Al 100)	<1
OLED 1.8	4.1	Cu-L1-P2-I neat	-	Curing at 120°C 2500	ITO | PEDOT:PSS (40) | Acryl neat (40) | T2T (5) | TPBi (40) | LiF (1) | Al 100	2

Table 34. Overview of fabricated OLED devices in *Set 2*. If not noted otherwise dynamic spin coating was performed with 2500 rpm and a concentration of 10 mg/ml

OLED No.	**File No.**	**Compounds**	**Host**	**Processing details**	**Device Structure**	**EQE_{max} [%]**
OLED 2.1	4.3	Cu-L1-P1-I 50 wt%	mCP	No T2T 2500 rpm	ITO | PEDOT:PSS (40) | Cu-L1-P1-I:mCP 50 (40) | TPBi (40) | LiF (1) | Al 100	3.1
OLED 2.2	5.1	Cu-L1-P1-I 50 wt%	mCP	DCM	ITO | PEDOT:PSS (40) | Cu-L1-P1-I:mCP (50) DCM (40) | TPBi (40) | LiF (1) | Al 100	6.7
OLED 2.3	6.2	Cu-L1-P1-I 50 wt%	mCP	3000 rpm, DCM No DPEPO	ITO | PEDOT:PSS (40) | Cu-L1-P1-I:mCP50 | TPBi (40) | LiF (1) | Al (100)	5.1
OLED 2.4	6.4	Cu-L1-P1-I 50 wt%	mCP	half conc 3000 rpm	ITO | PEDOT:PSS (40) | Cu-L1-P1-I:mCP50 | TPBi (40) | LiF (1) | Al (100)	1.6
OLED 2.5	4.2	Cu-L1-P2-I neat	-	UV 30 min 2500 rpm	ITO | PEDOT:PSS (40) | Cu-L1-P2-I | T2T (5) | TPBi (40) | LiF (1)	--
OLED 2.6	5.2	Cu-L1-P2-I neat	-	DCM, UV 2x15s	ITO | PEDOT:PSS (40) | Cu-L1-P2-I | TPBi (40) | LiF (1) | Al 100	<1
OLED 2.7	5.3	Cu-L1-P2-I neat	-	Toluene	ITO | PEDOT:PSS (40) | Cu-L1-P2-I | TPBi (40) | LiF (1) | Al 100	3.2
OLED 2.8	5.4	Cu-L1-P2-I neat	-	DCM	ITO | PEDOT:PSS (40) | Cu-L1-P2-I | TPBi (40) | LiF (1) | Al 100	2.9

Table 35. Overview of fabricated OLED devices in *Set 3*. If not noted otherwise dynamic spin coating was performed with 2500 rpm and a concentration of 10 mg/ml

OLED No.	**File No.**	**Compounds**	**Host**	**Processing details**	**Device Structure**	**EQE_{max} [%]**
OLED 3.1	6.1	Cu-L1-P1-I 50 wt%	mCP	3000 rpm, DCM +DPEPO	ITO | PEDOT:PSS (40) | Cu-L1-P1-I:mCP50 | DPEPO (10) | TPBi (40) | LiF (1) | Al (100)	6.8
OLED 3.2	6.3	Cu-L1-P1-I 50 wt%	mCP	3000 rpm, DCM + DPEPO Annealed 5min 70°C	ITO | PEDOT:PSS (40) | Cu-L1-P1-I:mCP50 | DPEPO (10) | TPBi (40) | LiF (1) | Al (100)	8.9
OLED 3.3	7.1	Cu-L1-P1-I 10 wt%	mCP	DCM, 3000 rpm Annealed 5 min 70°C	ITO | PEDOT:PSS (40) | Cu-L1-P1-I:mCP10 | DPEPO (10) | TPBi (40) | LiF (1) | Al (100)	6
OLED 3.4	7.2	Cu-L1-P1-I 3 wt%	mCP	DCM, 3000 rpm Annealed 5 min 70°C	ITO | PEDOT:PSS (40) | Cu-L1-P1-I:mCP3 | DPEPO (10) | TPBi (40) | LiF (1) | Al (100)	6.1
OLED 3.5	7.5	Cu-L1-P1-I 50 wt%	mCP	Dcm, 4000 rpm, anneal 5min, 70°C	ITO | PEDOT:PSS (40) | Cu-L1-P1-I:mCP50 | DPEPO (10) | TPBi (40) | LiF (1) | Al (100)	3.0
OLED 3.6	7.6	Cu-L1-P1-I 50 wt%	mCP	Dcm, 3000 rpm, anneal 20min	ITO | PEDOT:PSS (40) | Cu-L1-P1-I:mCP50 | DPEPO (10) | TPBi (40) | LiF (1) | Al (100)	3.6
OLED 3.7	7.9	Cu-L1-P1-I 50 wt%	mCP	Dcm, 3000 rpm, anneal 10 min	ITO | PEDOT:PSS (40) | Cu-L1-P1-I:mCP50 | DPEPO (10) | TPBi (40) | LiF (1) | Al (100)	3.0
OLED 3.7	8.1	Cu-L1-P1-I 50 wt%	mCP	DPEPO 5nm, Dcm, 3000 rpm,5 min 70°C	ITO | PEDOT:PSS (40) | Cu-L1-P1-I:mCP50 | DPEPO (5) | TPBi (40) | LiF (1) | Al (100)	6.4
OLED 3.8	8.2	Cu-L1-P1-I 50 wt%	mCP	DPEPO 10 nm, Dcm, 3000,5 min 70°C	ITO | PEDOT:PSS (40) | Cu-L1-P1-I:mCP50 | DPEPO (10) | TPBi (40) | LiF (1) | Al (100)	5.9
OLED 3.9	8.3	Cu-L1-P1-I 50 wt%	mCP	DPEPO 15 nm, Dcm, 3000 rpm,5 min 70°C	ITO | PEDOT:PSS (40) | Cu-L1-P1-I:mCP50 | DPEPO (15) | TPBi (40) | LiF (1) | Al (100)	5.4
OLED 3.10	9.1	Cu-L1-P1-I 20 wt%	mCP	$CHCl_3$, 3000 rpm, 5min, 70°C	ITO | PEDOT:PSS (40) | Cu-L1-P1-I:mCP20 | DPEPO (10) | TPBi (40) | LiF (1) | Al (100)	6.7
OLED 3.11	9.2	Cu-L1-P1-I 50 wt%	mCP	$CHCl_3$,70°C, 5 min, 3000 rpm	ITO | PEDOT:PSS (40) | Cu-L1-P1-I:mCP50| DPEPO (10) | TPBi (40) | LiF (1) | Al (100)	2.7

OLED No.	File No.	Compounds	Host	Processing details	Device Structure	EQE_{max} [%]
OLED 3.12	9.3	Cu-L1-P1-I 50 wt%	mCP	$CHCl_3$:Chlorobenzene 90:10, 100°C, 5min 3000 rpm	ITO | PEDOT:PSS (40) | Cu-L1-P1-I:mCP50 | DPEPO (10) | TPBi (40) | LiF (1) | Al (100)	3.2
OLED 3.13	7.8	Cu-L1-P1-I 10 wt%	PVK	Dcm, 3000 rpm	ITO | PEDOT:PSS (40) | Cu-L1-P1-I:PVK10| DPEPO (10) | TPBi (40) | LiF (1) | Al (100)	--
OLED 3.14	7.3	Cu-L1-P2-I neat	-	DCM, Annealed 5 min 70°C, 3000 rpm	ITO | PEDOT:PSS (40) | Cu-L1-P2-I | DPEPO (10) | TPBi (40) | LiF (1) | Al (100)	5
OLED 3.14	7.4	Cu-L1-P2-I neat	-	Toluene, Annealed 5 min 70 °C, 3000 rpm	ITO | PEDOT:PSS (40) Cu-L1-P2-I | DPEPO (10) | TPBi (40) | LiF (1) | Al (100)	3.2
OLED 3.15	7.7	Cu-L1-P2-I 20 wt%	mCP	Dcm, 3000 rpm	ITO | PEDOT:PSS (40) | Cu-L1-P2-I:mCP | DPEPO (10) | TPBi (40) | LiF (1) | Al (100)	8.5
OLED 3.16	9.4	Cu-L1-P2-I 20 wt%	mCP	Toluene, 70 °C, 5min 3000 rpm	ITO | PEDOT:PSS (40) | Cu-L1-P2-I _mCP | DPEPO (10) | TPBi (40) | LiF (1) | Al (100)	6.4
OLED 3.17	10.1	Cu-L1-P2-I neat	-	20 mg/ml, Toluene, UV 15 s, 2000 rpm	ITO | PEDOT:PSS (40) | Cu-L1-P2-I | DPEPO (10) | TPBi (40) | LiF (1) | Al (100)	2.6
OLED 3.18	10.2	Cu-L1-P2-I neat	-	20 mg/ml, $CHCl_3$, UV 15 s, 2000 rpm	ITO | PEDOT:PSS (40) | Cu-L1-P2-I | DPEPO (10) | TPBi (40) | LiF (1) | Al (100)	--
OLED 3.19	10.3	Cu-L1-P2-I neat	-	20mg/ml, $CHCl_3$, no UV, 2000rpm	ITO | PEDOT:PSS (40) | Cu-L1-P2-I | DPEPO (10) | TPBi (40) | LiF (1) | Al (100)	4
OLED 3.20	10.4	Cu-L1-P2-I neat	-	20 mg/ml, Toluene, UV 15 s, 2000 rpm	ITO | PEDOT:PSS (40) | Cu-L1-P2-I | DPEPO (10) | TPBi (40) | LiF (1) | Al (100)	1-2
OLED 3.21	10.5	Cu-L1-P2-Br 50 wt%	PVK	Dcm, 3000 rpm	ITO | PEDOT:PSS (40) | Cu-L1-P2-Br:PVK50 | DPEPO (10) | TPBi (40) | LiF (1) | Al (100)	--
OLED 3.22	10.6	Cu-L1-P2-Br 10 wt%	PVK	Dcm, 3000 rpm	ITO | PEDOT:PSS (40) | Cu-L1-P2-Br:PVK10 | DPEPO (10) | TPBi (40) | LiF (1) | Al (100)	< 1
OLED 3.23	11.1	Cu-L1-P2-Br 20 wt%	mCP	DCM, 3000 rpm, 2 min, 70 °C	ITO | PEDOT:PSS (40) | Cu-L1-P2-Br:mCP20 | DPEPO (10) | TPBi (40) | LiF (1) | Al (100)	3.3
OLED 3.24	11.2	Cu-L1-P2-Br 50 wt%	mCP	DCM, 3000 rpm, 2 min, 70 °C	ITO | PEDOT:PSS (40) | Cu-L1-P2-Br:mCP50 | DPEPO (10) | TPBi (40) | LiF (1) | Al (100)	2.5

OLED No.	**File No.**	**Compounds**	**Host**	**Processing details**	**Device Structure**	**EQE_{max} [%]**
OLED 3.25	11.3	Cu-L5-P1-I 20 wt%	mCP	DCM, 3000 rpm, 2 min, 70 °C	ITO | PEDOT:PSS (40) | Cu-L5-P1-I:mCP20 | DPEPO (10) | TPBi (40) | LiF (1) | Al (100)	6.4
OLED 3.26	11.4	Cu-L5-P1-I 50 wt%	mCP	DCM, 3000 rpm, 2 min, 70 °C	ITO | PEDOT:PSS (40) | Cu-L5-P1-I:mCP50 | DPEPO (10) | TPBi (40) | LiF (1) | Al (100)	1.7

6 List of abbreviations

%	percentage
A	ampere
Å	angström (10^{-10} m)
Alq_3	8-hydroxyquinoline aluminum
ATR	attenuated total reflection (IR)
a.u.	arbitrary unit
bipy	bipyridine
BJ	binder jetting
Bn	benzyl
br.s	broad singulett (NMR)
BPhen	bathophenanthroline
°	degree
°C	degree celsius
CAAC	cyclic alkyl amino carbene
Calcd.	calculated
CBP	4,4′-bis(N-carbazolyl)-1,1′-biphenyl
CC	cluster-centered
Cd	candela
$CDCl_3$	deuterated chloroforme
CD_2Cl	deuterated dichloromethane
cHec	cyclohexane
CIE	commission internationale de l'éclairage
COSY	correlated pectroscopy experiment (NMR)
cps	counts per second
CT	charge transfer
CuAAc	copper catalyzed alkyne-azide click reaction
CVD	chemical vapor deposition
Cz	9H-carbazole
4CzIPN	carbazole phenyl triazine
brine	saturated aqueous NaCl solution

d	dublett (NMR)
DCM	dichloromethan
Δ	difference
DEPT	distortionless enhancement by polarization transfer (NMR)
DFT	density functional theory
DIC	N,N'-diisopropylcarbodiimide
DIPEA	diisopropylethylamine
DLP	digital light processing
DLW	direct laser writing
DMAC	*N*,*N*-dimethyl acetamide
DMAP	dimethyl aminopyridine
DMF	*N*,*N*-dimethylformamide
DMSO	dimethyl sulfoxid
DMSO-d_6	deuterated dimethyl sulfoxid
DPEphos	bis[(2-diphenylphosphino)phenyl] ether
DPEPO	bis(2-(diphenylphosphino)phenyl)ether oxide
dppb	1,2-(bis(diphenylphosphino)benzene
E	energy
EA	elemental analysis
EBL	electron blocking layer
EDC	1-ethyl-3-(3-dimethylaminopropyl)carbodiimide hydrochloride
EtOAc	ethyl acetate
Et_2O	diethyl ether
EI	electron ionisation
EIL	electron injectionl layer
EML	emissive layer
equiv.	equivalent(s)
EQE	external quantum efficiency
EQE_{max}	maximum external quantum efficiency
ESI	electrospray ionisation
et al.	et alia (lat. and others)
ETL	electron transport layer
eV	electron-Volt

f	oscillator strength
FAB	fast atom bombardment
FFF	fused filament fabrication
g	gram; dissymmetry factor
h	hours
HBL	hole blocking layer
HIL	hole injection layer
HMBC	heteronuclear multiple bond correlation (NMR)
HOBt	1-hydroxybenzotriazole hydrate
HOMO	highest occupied molecular orbital
HRMS	high resolution mass spectrometry (NMR)
HSQC	heteronuclear single quantum coherence (NMR)
HTL	hole transport layer
Hz	hertz
IC	internal conversion
iCCD	intensified charge-coupled device camera
IFG	Institute of Functional Interfaces, KIT
INT	Institute of Nanotechnology, KIT
IR	infrared
$Ir(ppy)_3$	tris(2-phenylpyridine)iridium
ISC	intersystem crossing
ITO	indium tin oxide
IQE	internal quantum efficiency
J	coupling constant (NMR); exchange integral
JVL	current density-voltage-luminance curve
K	kelvin
k_B	Boltzmann Konstante
KHYS	Karlsruhe House of Young Scientists
KIT	Karlsruhe Institute of Technologie
konz.	Konzentriert
k_{ISC}	rate constant of ISC
k_{nr}	rate constant of non-radiative decay
k_r	rate constant of radiative decay

k_{RISC}	rate constant of RISC
KSOP	Karlsruhe School of Optics & Photonics
L	liter, ligand, luminance
LC	ligand-centered
L_{NP}	NP-bridging ligand
L_P	ancillary phosphine ligand
L_{max}	maximum Luminance
λ	wavelength
LCD	liquid crystal display
LED	Light-Emitting Diode
LTI	Light Technology Institute, KIT
LUMO	lowest unoccupied molecular orbital
M	molarity
m	mass; multiplett (NMR); medium, (IR)
MAC	monoamido amino carbene
max.	maximum
MC	metal-centered
mCP	1,3-di(9H-carbazol-9-yl)benzole
Me	methyl
MeCN	acetonitrile
meV	millielectronvolt
mg	milligramm
MHz	megahertz
MR	multi-resonance
MS	mass spectrometry
MO	molecular orbital
µm	mikrometer
µs	mikrosekunde(n)
mA	milliampere
min	minuten
mL	milliliter
µm	microliter
MLCT	metal-to-ligand charge transfer

mm	millimeter
mmol	millimol
µm	micromol
MS	mass spectrometry
m/z	mass-to-charge-ratio
3-NBA	3-nitrobenzylalcohol
nBuLi	n-Butyllithium
NHC	*N*-heterocyclic carben
NHetPhos	*N*-heteroaromatic phosphine ligand
nm	nanometer
NMR	nuclear magnetic resonance
NR	non radiate decay
ns	nanosecond
NTO	natural transition orbital
M.p.	melting point
OLED	organic light emitting diode
PEDOT	poly-3,4-ethylenedioxythiophen
PETA	pentaerythritol triacrylate
Ph	phenyl
Phen	1,10-phenantroline
PI	photoinitiator
PL	photoluminescence
PLQY	photoluminescence quantum yield
PMMA	polymethylmethacrylat
ppm	parts per million, 10^{-6}
PSS	polystyrolsulfonate
PVK	poly(9-vinyl carbazole)
PYD-2Cz	2,6-bis(9H-carbazol-9-yl)pyridine
Pyr	pyridine
2-PyrPhos	2-pyridylphosphine
3-PyrPhos	3-pyridylphosphine
q	quartett (NMR), quaternary (NMR)
quin	quintett (NMR)

R_f	retention factor
RISC	reverse intersystem crossing
rpm	rounds per minute
RT	room temperature
RPTU	Rheinland-pfälzische technische Universität
s	singulett (NMR); strong, (IR); second
SEM	scanning electron microscopy
SLA	stereolithography
SLS	selective laser sintering
SP	solution-processed
S_n	singulett state n
SOC	spin–orbit coupling
SOLED	solution-processed OLED
T	temperature
t	triplett (NMR)
TADF	thermally activated delayed fluorescence
TCSPC	time-correlated single-photon counting
TcTa	4,4′,4″tris(carbazol-9-yl)triphenylamine
td	triplett vom Dublett (NMR)
TFP	Institute of Theoretical Solid State Physics, KIT
T2T	2,4,6-tris(biphenyl-3-yl)-1,3,5-triazine
TD-DFT	time-dependent density functional theory
THF	tetrahydrofuran
T_n	triplett state n
TMPTA	trimethylolpropane triacrylate
TPA	two-photon absorption
TSA	two-step absorption
TPBi	2,2′,2"-benzol-1,3,5-triyltris(1-phenyl-1-H benzimidazole
UK	United Kingdom
UV	ultraviolett
UV-Vis	ultraviolet-visible
$\tilde{\nu}$	wavenumber [cm^{-1}]
V	volt

V_{on}	turn-on voltage
VR	vibrational relaxation
vs	very strong, IR
vw	very weak, IR
W	watt
w	weak, IR
wt%	weight percent
X	halogen ligand/substituent
XLCT	halide-to-Ligand Charge Transfer
ΔE_{ST}	singlet-triplet energy gap
δ (NMR)	chemical shift
η_{out}	light-outcoupling factor
η_r	radiative exciton fraction
Φ_{PL}	photoluminescence quantum
λ_{exc}	excitation wavelength
$\lambda_{max,PL}$	maximum emission wavelength
ξ	spin orbit coupling constant
τ	lifetime

7 Bibliography

[1] M. Bouzrati-Zerelli, N. Guillaume, F. Goubard, T.-T. Bui, S. Villotte, C. Dietlin, F. Morlet-Savary, D. Gigmes, J. P. Fouassier, F. Dumur, J. Lalevée, *New J. Chem.* **2018**, *42*, 8261-8270.

[2] Y. Shao, X. He, Y. Xin, Y. Zhang, D. Zhang, L. Duan, Y. Zou, *ACS Appl. Mater. Interfaces.* **2024**, *16*, 30344-30354.

[3] G. Hong, X. Gan, C. Leonhardt, Z. Zhang, J. Seibert, J. M. Busch, S. Bräse, *Adv. Mater.* **2021**, *33*, 2005630.

[4] H. Yersin, *Highly efficient OLEDs: Materials based on thermally activated delayed fluorescence*, John Wiley & Sons, **2019**.

[5] Z. Guo, S. Park, J. Yoon, I. Shin, *Chem. Soc. Rev.* **2014**, *43*, 16-29.

[6] Y. Yang, Q. Zhao, W. Feng, F. Li, *Chem. Rev.* **2013**, *113*, 192-270.

[7] S. Xu, L.-L. Wu, X. Wang, H.-Y. Hu, *Trends Analyt. Chem.* **2023**, *169*, 117356.

[8] Y. Meng, J. Zhang, C. Liu, K. Zheng, L. Xie, S. Bu, B. Han, R. Cao, X. Yin, C. Liu, Z. Ge, *Adv. Funct. Mater.* **2023**, *33*, 2210600.

[9] R. Hao, H. Xia, X. Wang, H. Wei, J. Huang, F. Wang, Y. Zhang, H. Tan, M. Zhu, X. Song, Q. Fan, W. Zhu, *Chem. Eng. J.* **2024**, *488*, 151067.

[10] X. Chen, J. Zhang, C. Liu, Q. Lou, K. Zheng, X. Yin, L. Xie, P. Wen, C. Liu, Z. Ge, *ACS Appl. Energy Mater.* **2021**, *4*, 11112-11120.

[11] C. Si, T. Wang, Y. Xu, D. Lin, D. Sun, E. Zysman-Colman, *Nat. Commun.* **2024**, *15*, 7439.

[12] G.-L. Yang, X.-L. Jiang, H. Xu, B. Zhao, *Small* **2021**, *17*, 2005327.

[13] H. Yersin, R. Czerwieniec, M. Z. Shafikov, A. F. Suleymanova, in *Highly Efficient OLEDs*, **2018**, pp. 1-60.

[14] S. E. Braslavsky, *Pure Appl. Chem.* **2007**, *79*, 293-465.

[15] J. Franck, E. Dymond, *Trans. Faraday Society* **1926**, *21*, 536-542.

[16] E. Condon, *Phys. Rev.* **1926**, *28*, 1182.

[17] S. E. Schwartz, *J. Chem. Educ.* **1973**, *50*, 608.

[18] A. Köhler, H. Bässler, *Electronic processes in organic semiconductors: An introduction*, John Wiley & Sons, **2015**.

[19] P. W. Atkins, *Physikalische Chemie, Vol. 5.Edition*, Wiley-VCH, Weinheim, **2013**.

[20] B. Valeur, M. N. Berberan-Santos, *Molecular fluorescence: principles and applications*, John Wiley & Sons, **2013**.

[21] S. Rajamanickam, B. K. Patel, in *Green Chemistry-New Perspectives*, IntechOpen, **2022**.

[22] M. A. Bryden, E. Zysman-Colman, *Chem. Soc. Rev.* **2021**, *50*, 7587-7680.

[23] M. Kasha, *Discuss. Faraday Soc.* **1950**, *9*, 14-19.

[24] V. Balzani, P. Ceroni, A. Juris, *Photochemistry and photophysics: concepts, research, applications*, John Wiley & Sons, **2014**.

[25] D. G. Fedorov, S. Koseki, M. W. Schmidt, M. S. Gordon, *Int. Rev. Phys. Chem.* **2003**, *22*, 551-592.

[26] R. Czerwieniec, M. J. Leitl, H. H. H. Homeier, H. Yersin, *Coord. Chem. Rev.* **2016**, *325*, 2-28.

[27] R. Ishimatsu, S. Matsunami, K. Shizu, C. Adachi, K. Nakano, T. Imato, *J. Phys. Chem. A* **2013**, *117*, 5607-5612.

[28] Y. X. Hu, J. Miao, T. Hua, Z. Huang, Y. Qi, Y. Zou, Y. Qiu, H. Xia, H. Liu, X. Cao, *Nat. Photonics* **2022**, *16*, 803-810.

[29] M. Cai, M. Auffray, D. Zhang, Y. Zhang, R. Nagata, Z. Lin, X. Tang, C.-Y. Chan, Y.-T. Lee, T. Huang, *Chem. Eng. J.* **2021**, *420*, 127591.

[30] M. Osawa, M. Hoshino, *Highly Efficient OLEDs: Materials Based on Thermally Activated Delayed Fluorescence* **2018**, 119-176.

[31] F. B. Dias, T. J. Penfold, A. P. Monkman, *Methods and applications in fluorescence* **2017**, *5*, 012001.

[32] J. C. Lima, L. Rodríguez, *Inorg.* **2019**, *7*, 124.

[33] D. Zhou, G. Cheng, G. S. M. Tong, C.-M. Che, *Chem. Eur. J.* **2020**, *26*, 15718-15726.

[34] W.-P. To, G. Cheng, G. S. M. Tong, D. Zhou, C.-M. Che, *Front. Chem.* **2020**, *8*.

[35] M. Osawa, M. Hashimoto, I. Kawata, M. Hoshino, *Dalton Trans.* **2017**, *46*, 12446-12455.

[36] H. Nakanotani, Y. Tsuchiya, C. Adachi, *Chem. Lett.* **2021**, *50*, 938-948.

[37] M. Deußen, H. Bässler, *Chem. unserer Zeit* **1997**, *31*, 76-86.

[38] T. D. Schmidt, W. Brütting, *Highly Efficient OLEDs: Materials Based on Thermally Activated Delayed Fluorescence* **2018**, 199-228.

[39] H. Yersin, A. F. Rausch, R. Czerwieniec, T. Hofbeck, T. Fischer, *Coord. Chem. Rev.* **2011**, *255*, 2622-2652.

[40] H. Yersin, in *Transition Metal and Rare Earth Compounds: Excited States, Transitions, Interactions III* (Ed.: Yersin, H.), Springer Berlin Heidelberg, Berlin, Heidelberg, **2004**, pp. 1-26.

[41] J. M. Busch, *Synthese von Kupfer (I)-und Silber (I)-Komplexen zur Untersuchung kooperativer Effekte und Anwendung in OLEDs*, Logos Berlin, **2020**.

[42] D. Volz, *Zweikernige Kupfer (I)-Komplexe als OLED-Leuchtstoffe: Synthese, Eigenschaften und neue Konzepte*, *Vol. 49*, Logos Verlag Berlin GmbH, **2014**.

[43] D. L. Dexter, *J. Chem. Phys.* **1953**, *21*, 836-850.

[44] T. Förster, *Ann. Phys.* **1948**, *437*, 55-75.

[45] C. W. Tang, S. A. VanSlyke, *Appl. Phys. Lett.* **1987**, *51*, 913-915.

[46] J. Bauri, R. B. Choudhary, G. Mandal, *J. Mater. Sci.* **2021**, *56*, 18837-18866.

[47] Y.-L. Loo, I. McCulloch, *MRS Bull.* **2008**, *33*, 653-662.

[48] D. Volz, M. Wallesch, C. Fléchon, M. Danz, A. Verma, J. Navarro, D. Zink, S. Bräse, T. Baumann, *Green Chem.* **2015**, *17*, 1988-2011.

[49] D. J. Gaspar, E. Polikarpov, *OLED fundamentals: materials, devices, and processing of organic light-emitting diodes*, CRC press, **2015**.

[50] V. I. Adamovich, S. R. Cordero, P. I. Djurovich, A. Tamayo, M. E. Thompson, B. W. D'Andrade, S. R. Forrest, *Org. Electron.* **2003**, *4*, 77-87.

[51] S. Negi, P. Mittal, B. Kumar, *Microsyst. Technol.* **2018**, *24*, 4981-4989.

[52] L. Bergmann, *New emitters for OLEDs: The coordination-and photo-chemistry of mononuclear neutral copper (I) complexes, Vol. 57*, Logos Verlag Berlin GmbH, **2016**.

[53] R. A. Hatton, M. R. Willis, M. A. Chesters, D. Briggs, *J. Mater. Chem.* **2003**, *13*, 722-726.

[54] Z. Fan, J. Ouyang, *Adv. Electron. Mater.* **2019**, *5*, 1800769.

[55] W.-Y. Hung, P.-Y. Chiang, S.-W. Lin, W.-C. Tang, Y.-T. Chen, S.-H. Liu, P.-T. Chou, Y.-T. Hung, K.-T. Wong, *ACS Appl. Mater. Interfaces.* **2016**, *8*, 4811-4818.

[56] M.-S. Gong, J.-R. Cha, C. W. Lee, *Org. Electron.* **2017**, *42*, 66-74.

[57] S. I. Ahn, W. K. Kim, S. H. Ryu, K. J. Kim, S. E. Lee, S.-H. Kim, J.-C. Park, K. C. Choi, *Org. Electron.* **2012**, *13*, 980-984.

[58] D. Volz, Y. Chen, M. Wallesch, R. Liu, C. Fléchon, D. M. Zink, J. Friedrichs, H. Flügge, R. Steininger, J. Göttlicher, C. Heske, L. Weinhardt, S. Bräse, F. So, T. Baumann, *Adv. Mater.* **2015**, *27*, 2538-2543.

[59] T. Teng, J. Xiong, G. Cheng, C. Zhou, X. Lv, K. Li, *Molecules* **2021**, *26*, 1125.

[60] V. K.-M. Au, *Energy Fuels* **2021**, *35*, 18982-18999.

[61] M. J. Leitl, D. M. Zink, A. Schinabeck, T. Baumann, D. Volz, H. Yersin, *Top. Curr. Chem.* **2016**, *374*, 25.

[62] M. Hashimoto, S. Igawa, M. Yashima, I. Kawata, M. Hoshino, M. Osawa, *J. Am. Chem. Soc.* **2011**, *133*, 10348-10351.

[63] J. M. Busch, D. S. Koshelev, A. A. Vashchenko, O. Fuhr, M. Nieger, V. V. Utochnikova, S. Bräse, *Inorg. Chem.* **2021**, *60*, 2315-2332.

[64] https://www.ossila.com/, **visited 20.10.2024**.

[65] H.-s. Yang, *Optoelectron. Lett.* **2013**, *9*, 250-253.

[66] D. H. Ahn, J. S. Moon, S. W. Kim, S. Y. Lee, D. Karthik, J. Y. Lee, J. H. Kwon, *Org. Electron.* **2018**, *59*, 39-44.

[67] Y. Wang, B. Li, C. Jiang, Y. Fang, P. Bai, Y. Wang, *J. Phys. Chem. C* **2021**, *125*, 16753-16758.

[68] K.-S. Lee, R. H. Kim, D.-Y. Yang, S. H. Park, *Prog. Polym. Sci.* **2008**, *33*, 631-681.

[69] H.-F. Chen, S.-J. Yang, Z.-H. Tsai, W.-Y. Hung, T.-C. Wang, K.-T. Wong, *J. Mater. Chem.* **2009**, *19*, 8112-8118.

[70] J. Y. Woo, M.-H. Park, S.-H. Jeong, Y.-H. Kim, B. Kim, T.-W. Lee, T.-H. Han, *Adv. Mater.* **2023**, *35*, 2207454.

[71] R. Shinar, J. Shinar, *J. Phys. Photonics* **2022**, *4*, 032002.

[72] W. Brütting, J. Frischeisen, T. D. Schmidt, B. J. Scholz, C. Mayr, *physica status solidi (a)* **2013**, *210*, 44-65.

[73] Z. Xu, B. Z. Tang, Y. Wang, D. Ma, *J. Mater. Chem. C* **2020**, *8*, 2614-2642.

[74] F.-I. Wu, P.-I. Shih, Y.-H. Tseng, G.-Y. Chen, C.-H. Chien, C.-F. Shu, Y.-L. Tung, Y. Chi, A. K. Y. Jen, *J. Phys. Chem. B* **2005**, *109*, 14000-14005.

[75] P. T. Chou, Y. Chi, *Eur. J. Inorg. Chem.* **2006**, *2006*, 3319-3332.

[76] J. Lu, Y. Tao, Y. Chi, Y. Tung, *Synth. Met.* **2005**, *155*, 56-62.

[77] J. M. Ha, S. H. Hur, A. Pathak, J.-E. Jeong, H. Y. Woo, *NPG Asia Mater.* **2021**, *13*, 53.

[78] C. Adachi, R. C. Kwong, P. Djurovich, V. Adamovich, M. A. Baldo, M. E. Thompson, S. R. Forrest, *Appl. Phys. Lett.* **2001**, *79*, 2082-2084.

[79] L. Wang, J. Miao, Y. Zhang, C. Wu, H. Huang, X. Wang, C. Yang, *Adv. Mat.* **2023**, *35*, 2303066.

[80] J. Sun, H. Ahn, S. Kang, S.-B. Ko, D. Song, H. A. Um, S. Kim, Y. Lee, P. Jeon, S.-H. Hwang, *Nat. Photonics* **2022**, *16*, 212-218.

[81] C. Adachi, M. A. Baldo, S. R. Forrest, M. E. Thompson, *Appl. Phys. Lett.* **2000**, *77*, 904-906.

[82] T. P. Saragi, T. Spehr, A. Siebert, T. Fuhrmann-Lieker, J. Salbeck, *Chem. Rev.* **2007**, *107*, 1011-1065.

[83] X. Liang, Z. L. Tu, Y. X. Zheng, *Chem. Eur. J.* **2019**, *25*, 5623-5642.

[84] J. Han, Z. Huang, X. Lv, J. Miao, Y. Qiu, X. Cao, C. Yang, *Adv. Opt. Mater.* **2022**, *10*, 2102092.

[85] H. Uoyama, K. Goushi, K. Shizu, H. Nomura, C. Adachi, *Nat.* **2012**, *492*, 234-238.

[86] D. R. Lee, B. S. Kim, C. W. Lee, Y. Im, K. S. Yook, S.-H. Hwang, J. Y. Lee, *ACS Appl. Mater. Interfaces.* **2015**, *7*, 9625-9629.

[87] R. Czerwieniec, J. Yu, H. Yersin, *Inorg. Chem.* **2011**, *50*, 8293-8301.

[88] G. Blasse, D. R. McMillin, *Chem. Phys. Let.* **1980**, *70*, 1-3.

[89] C. Kant, A. Shukla, S. K. M. McGregor, S.-C. Lo, E. B. Namdas, M. Katiyar, *Nat. Commun.* **2023**, *14*, 7220.

[90] L. Lan, J. Zou, C. Jiang, B. Liu, L. Wang, J. Peng, *Front. Optoelectron.* **2017**, *10*, 329-352.

[91] L. E. Scriven, *MRS Online Proceedings Library* **1988**, *121*, 717-729.

[92] N. Li, Z. Chen, C. Zhou, F. Ni, Z. Huang, X. Cao, C. Yang, *Adv. Mater.* **2023**, *35*, 2300510.

[93] M. Hengge, P. Hänsch, D. Ehjeij, F. S. Benneckendorf, J. Freudenberg, U. H. F. Bunz, K. Müllen, E. J. W. List-Kratochvil, F. Hermerschmidt, *J. Polym. Sci.* **2022**, *60*, 1878-1886.

[94] S. C. Gauci, A. Vranic, E. Blasco, S. Bräse, M. Wegener, C. Barner-Kowollik, *Adv. Mater.* **2024**, *36*, 2306468.

[95] J. Fischer, M. Wegener, *Laser Photonics Rev.* **2013**, *7*, 22-44.

[96] A. A. Elhadad, A. Rosa-Sainz, R. Cañete, E. Peralta, B. Begines, M. Balbuena, A. Alcudia, Y. Torres, *Mater Sci Eng R: Rep.* **2023**, *156*, 100760.

[97] V. Ferraro, C. R. Adam, A. Vranic, S. Bräse, *Adv. Funct. Mater.* **2024**, *34*, 2302157.

[98] V. Hahn, N. M. Bojanowski, P. Rietz, F. Feist, M. Kozlowska, W. Wenzel, E. Blasco, S. Bräse, C. Barner-Kowollik, M. Wegener, *ACS Photonics* **2023**, *10*, 24-33.

[99] L. Florea, E. Blasco, V. Mattoli, *Adv. Funct. Mater.* **2023**, *33*, 2305697.

[100] V. Hahn, T. Messer, N. M. Bojanowski, E. R. Curticean, I. Wacker, R. R. Schröder, E. Blasco, M. Wegener, *Nat. Photonics* **2021**, *15*, 932-938.

[101] N. M. Bojanowski, A. Vranic, V. Hahn, P. Rietz, T. Messer, J. Brückel, C. Barner-Kowollik, E. Blasco, S. Bräse, M. Wegener, *Adv. Funct. Mater.* **2023**, *33*, 2212482.

[102] G. Vicentini, L. B. Zinner, J. Zukerman-Schpector, K. Zinner, *Coord. Chem. Rev.* **2000**, *196*, 353-382.

[103] Y. Ma, Y. Wang, *Coord. Chem. Rev.* **2010**, *254*, 972-990.

[104] H. Wang, P. He, H. Yan, J. Shi, M. Gong, *Inorg. Chem. Comm.* **2011**, *14*, 1183-1185.

[105] R. Ilmi, X. Li, N. K. Al Rasbi, L. Zhou, W.-Y. Wong, P. R. Raithby, M. S. Khan, *Dalton Trans.* **2023**, *52*, 12885-12891.

[106] C. Adachi, M. A. Baldo, M. E. Thompson, S. R. Forrest, *J. Appl. Phys.* **2001**, *90*, 5048-5051.

[107] D. Kourkoulos, C. Karakus, D. Hertel, R. Alle, S. Schmeding, J. Hummel, N. Risch, E. Holder, K. Meerholz, *Dalton Trans.* **2013**, *42*, 13612-13621.

[108] P. L. dos Santos, P. Stachelek, Y. Takeda, P. H. Pander, *Mater. Chem. Front.* **2024**.

[109] https://www.finanzen.net/rohstoffe/kupferpreis, **accessed 09/10/2024**.

[110] https://www.gold.de/kurse/iridiumpreis/, **accessed 09/10/2024**.

[111] J. Beaudelot, S. Oger, S. Peruško, T.-A. Phan, T. Teunens, C. Moucheron, G. Evano, *Chem. Rev.* **2022**, *122*, 16365-16609.

[112] P. C. Ford, *Chem. Sci.* **2016**, *7*, 2964-2986.

[113] C. Förster, K. Heinze, *Chem. Soc. Rev.* **2020**, *49*, 1057-1070.

[114] C. Förster, K. Heinze, *Chem. Phys. Rev.* **2022**, *3*, 041302.

[115] P. S. Wagenknecht, P. C. Ford, *Coord. Chem. Rev.* **2011**, *255*, 591-616.

[116] S. Fraga, J. Karwowski, K. M. S. Saxena, *Handbook of atomic data*, Elsevier Scientific Publishing Company,New York, NY, United States, **1976**.

[117] M. Iwamura, S. Takeuchi, T. Tahara, *Acc. Chem. Res.* **2015**, *48*, 782-791.

[118] Y. Zhang, M. Schulz, M. Wächtler, M. Karnahl, B. Dietzek, *Coord. Chem. Rev.* **2018**, *356*, 127-146.

[119] C. E. McCusker, F. N. Castellano, *Inorg. Chem.* **2013**, *52*, 8114-8120.

[120] N. Armaroli, H. J. Bolink, *Photoluminescent materials and electroluminescent devices, Vol. 374*, Springer, **2017**.

[121] M. Wallesch, D. Volz, D. M. Zink, U. Schepers, M. Nieger, T. Baumann, S. Bräse, *Chem. Eur. J.* **2014**, *20*, 6578-6590.

[122] L. Bergmann, D. M. Zink, S. Bräse, T. Baumann, D. Volz, *Photoluminescent Materials and Electroluminescent Devices* **2017**, 201-239.

[123] C. Sandoval-Pauker, M. Santander-Nelli, P. Dreyse, *RSC Adv.* **2022**, *12*, 10653-10674.

[124] R. Czerwieniec, H. Yersin, *Inorg. Chem.* **2015**, *54*, 4322-4327.

[125] J. Li, L. Wang, Z. Zhao, X. Li, X. Yu, P. Huo, Q. Jin, Z. Liu, Z. Bian, C. Huang, *Angew. Chem. Int. Ed.* **2020**, *59*, 8210-8217.

[126] R. Wang, S. Liu, H. Chen, X. Wu, H. Ding, S. Xu, Y. Wu, Y. Wang, F. Zhao, *J. Mol. Struct.* **2023**, *1285*, 135504.

[127] R. Hamze, S. Shi, S. C. Kapper, D. S. Muthiah Ravinson, L. Estergreen, M.-C. Jung, A. C. Tadle, R. Haiges, P. I. Djurovich, J. L. Peltier, R. Jazzar, G. Bertrand, S. E. Bradforth, M. E. Thompson, *J. Am. Chem. Soc.* **2019**, *141*, 8616-8626.

[128] A. Ying, Y. Tan, S. Gong, *Adv. Opt. Mat.* **2024**, *12*, 2303333.

[129] R. Hamze, J. L. Peltier, D. Sylvinson, M. Jung, J. Cardenas, R. Haiges, M. Soleilhavoup, R. Jazzar, P. I. Djurovich, G. Bertrand, M. E. Thompson, *Sci.* **2019**, *363*, 601-606.

[130] A. A. Danopoulos, T. Simler, P. Braunstein, *Chem. Rev.* **2019**, *119*, 3730-3961.

[131] S. Shi, M. C. Jung, C. Coburn, A. Tadle, D. Sylvinson M. R, P. I. Djurovich, S. R. Forrest, M. E. Thompson, *J. Am. Chem. Soc.* **2019**, *141*, 3576-3588.

[132] D. Volz, T. Baumann, H. Flügge, M. Mydlak, T. Grab, M. Bächle, C. Barner-Kowollik, S. Bräse, *J. Mater. Chem.* **2012**, *22*, 20786-20790.

[133] A. Tsuboyama, K. Kuge, M. Furugori, S. Okada, M. Hoshino, K. Ueno, *Inorg. Chem.* **2007**, *46*, 1992-2001.

[134] X. Hong, B. Wang, L. Liu, X.-X. Zhong, F.-B. Li, L. Wang, W.-Y. Wong, H.-M. Qin, Y. H. Lo, *JLum* **2016**, *180*, 64-72.

[135] Y. Okano, H. Ohara, A. Kobayashi, M. Yoshida, M. Kato, *Inorg. Chem.* **2016**, *55*, 5227-5236.

[136] M. J. Leitl, F.-R. Küchle, H. A. Mayer, L. Wesemann, H. Yersin, *J. Phys. Chem. A* **2013**, *117*, 11823-11836.

[137] D. M. Zink, D. Volz, T. Baumann, M. Mydlak, H. Flügge, J. Friedrichs, M. Nieger, S. Bräse, *Chem. Mater.* **2013**, *25*, 4471-4486.

[138] J. M. Busch, D. M. Zink, P. Di Martino-Fumo, F. R. Rehak, P. Boden, S. Steiger, O. Fuhr, M. Nieger, W. Klopper, M. Gerhards, S. Bräse, *Dalton Trans.* **2019**, *48*, 15687-15698.

[139] P. C. Ford, E. Cariati, J. Bourassa, *Chem. Rev.* **1999**, *99*, 3625-3648.

[140] Y.-D. Yu, L.-B. Meng, Q.-C. Chen, G.-H. Chen, X.-C. Huang, *New J. Chem.* **2018**, *42*, 8426-8437.

[141] K. R. Kyle, C. K. Ryu, P. C. Ford, J. A. DiBenedetto, *J. Am. Chem. Soc.* **1991**, *113*, 2954-2965.

[142] H. Kitagawa, Y. Ozawa, K. Toriumi, *Chem. comm.* **2010**, *46*, 6302-6304.

[143] S. Perruchas, C. Tard, X. F. Le Goff, A. Fargues, A. Garcia, S. Kahlal, J.-Y. Saillard, T. Gacoin, J.-P. Boilot, *Inorg. Chem.* **2011**, *50*, 10682-10692.

[144] Z. Liu, P. I. Djurovich, M. T. Whited, M. E. Thompson, *Inorg. Chem.* **2012**, *51*, 230-236.

[145] K. Chen, J. Shearer, V. J. Catalano, *Inorg. Chem.* **2015**, *54*, 6245-6256.

[146] L. Maini, P. P. Mazzeo, F. Farinella, V. Fattori, D. Braga, *Faraday Discuss.* **2014**, *170*, 93-107.

[147] L. Zhang, B. Li, *J. Electrochem. Soc.* **2009**, *156*, J174.

[148] M. W. Blaskie, D. R. McMillin, *Inorg. Chem.* **1980**, *19*, 3519-3522.

[149] J. R. Kirchhoff, R. E. Gamache Jr, M. W. Blaskie, A. A. Del Paggio, R. K. Lengel, D. R. McMillin, *Inorg. Chem.* **1983**, *22*, 2380-2384.

[150] W. J. Finkenzeller, H. Yersin, *Chem. Phys. Lett.* **2003**, *377*, 299-305.

[151] Y. Gou, M. Chen, S. Li, J. Deng, J. Li, G. Fang, F. Yang, G. Huang, *J. Med. Chem.* **2021**, *64*, 5485-5499.

[152] T. Hofbeck, U. Monkowius, H. Yersin, *J. Am. Chem. Soc.* **2015**, *137*, 399-404.

[153] A. Kobayashi, T. Hasegawa, M. Yoshida, M. Kato, *Inorg. Chem.* **2016**, *55*, 1978-1985.

[154] A. Y. Baranov, A. S. Berezin, D. G. Samsonenko, A. S. Mazur, P. M. Tolstoy, V. F. Plyusnin, I. E. Kolesnikov, A. V. Artem'ev, *Dalton Trans.* **2020**, *49*, 3155-3163.

[155] E. C. Carson, S. J. Lippard, *J. Am. Chem. Soc.* **2004**, *126*, 3412-3413.

[156] M. Kuil, P. E. Goudriaan, A. W. Kleij, D. M. Tooke, A. L. Spek, P. W. van Leeuwen, J. N. Reek, *Dalton Trans.* **2007**, 2311-2320.

[157] S. Ponsico, H. Gulyas, M. Martínez-Belmonte, E. C. Escudero-Adán, Z. Freixa, P. W. van Leeuwen, *Dalton Trans.* **2011**, *40*, 10686-10697.

[158] R. H. Laitinen, J. Soininen, P. Suomalainen, T. A. Pakkanen, M. Ahlgren, J. Pursiainen, *Acta Chem. Scand.* **1999**, *53*, 335-339.

[159] F. Y. Kwong, C. W. Lai, Y. Tian, K. S. Chan, *Tetrahedron Lett.* **2000**, *41*, 10285-10289.

[160] Y.-L. Zhao, G.-J. Wu, Y. Li, L.-X. Gao, F.-S. Han, *Chem. Eur. J.* **2012**, *18*, 9622-9627.

[161] D. M. Zink, M. Bächle, T. Baumann, M. Nieger, M. Kühn, C. Wang, W. Klopper, U. Monkowius, T. Hofbeck, H. Yersin, S. Bräse, *Inorg. Chem.* **2013**, *52*, 2292-2305.

[162] D. M. Zink, *Entwicklung neuartiger oligonuklearer Kupferkomplexe als Emittermaterialien für organische Leuchtdioden*, Logos-Verlag, **2013**.

[163] U. Monkowius, T. Hofbeck, H. Yersin, *Vol. EP2739702A1* (Ed.: Office, E. P.), CYNORA GmbH, **2013. https://patents.google.com/patent/EP2739702A1/en**.

[164] A. Gusev, E. Braga, E. Zamnius, M. Kiskin, A. Ali, G. Baryshnikov, W. Linert, *Dalton Trans.* **2023**, *52*, 14995-15008.

[165] H. Miao, P. Wang, Z. Huang, W. Zhaxi, L. Liu, W. Huang, D. Wu, *Struct. Chem.* **2023**, *34*, 2307-2314.

[166] M. Zábranský, L. Kolářová, I. Císařová, P. Štěpnička, *J. Organomet. Chem.* **2017**, *846*, 217-222.

[167] S. Dey, D. Buzsáki, C. Bruhn, Z. Kelemen, R. Pietschnig, *Dalton Trans.* **2020**, *49*, 6668-6681.

[168] H. Yersin, R. Czerwieniec, U. Monkowius, R. Ramazanov, R. Valiev, M. Z. Shafikov, W.-M. Kwok, C. Ma, *Coord. Chem. Rev.* **2023**, *478*, 214975.

[169] H. Araki, K. Tsuge, Y. Sasaki, S. Ishizaka, N. Kitamura, *Inorg. Chem.* **2007**, *46*, 10032-10034.

[170] L. Kang, J. Chen, T. Teng, X.-L. Chen, R. Yu, C.-Z. Lu, *Dalton Trans.* **2015**, *44*, 11649-11659.

[171] Q. Wang, Y.-J. Gao, T.-T. Zhang, J. Han, G. Cui, *RSC Adv.* **2019**, *9*, 20786-20795.

[172] D. Volz, M. Wallesch, S. L. Grage, J. Göttlicher, R. Steininger, D. Batchelor, T. Vitova, A. S. Ulrich, C. Heske, L. Weinhardt, T. Baumann, S. Bräse, *Inorg. Chem.* **2014**, *53*, 7837-7847.

[173] M. Wrighton, D. L. Morse, *J. Am. Chem. Soc.* **1974**, *96*, 998-1003.

[174] A. J. Lees, *Comments Inorg. Chem.* **1995**, *17*, 319-346.

[175] A. Garner, F. Wilkinson, *Chem. Phys. Lett.* **1977**, *45*, 432-435.

[176] K. F. Baranova, A. A. Titov, J. R. Shakirova, V. A. Baigildin, A. F. Smol'yakov, D. A. Valyaev, G.-H. Ning, O. A. Filippov, S. P. Tunik, E. S. Shubina, *Inorg. Chem.* **2024**, *63*, 16610-16621.

[177] A. V. Artem'ev, M. Z. Shafikov, A. Schinabeck, O. V. Antonova, A. S. Berezin, I. Y. Bagryanskaya, P. E. Plusnin, H. Yersin, *Inorg. Chem. Front.* **2019**, *6*, 3168-3176.

[178] A. V. Artem'ev, J. A. Eremina, E. V. Lider, O. V. Antonova, E. V. Vorontsova, I. Y. Bagryanskaya, *Polyhedron* **2017**, *138*, 218-224.

[179] A. Del Zotto, E. Zangrando, *Inorg. Chim. Acta* **1998**, *277*, 111-117.

[180] J. M. Busch, F. R. Rehak, V. Ferraro, M. Nieger, M. Kemell, O. Fuhr, W. Klopper, S. Bräse, *ACS Omega* **2024**, *9*, 2220-2233.

[181] B.-K. Teo, J. C. Calabrese, *Inorg. Chem.* **1976**, *15*, 2467-2474.

[182] V. Charra, P. de Frémont, P.-A. R. Breuil, H. Olivier-Bourbigou, P. Braunstein, *J. Organomet. Chem.* **2015**, *795*, 25-33.

[183] C. Janiak, *J. Chem. Soc., Dalton Trans.* **2000**, 3885-3896.

[184] J. M. Hollas, L. Goodman, *J. Chem. Phys.* **1965**, *43*, 760-761.

[185] J. Van der Waals, *Appl. Magn. Reson.* **2001**, *20*, 545-561.

[186] C. A. Zuniga, S. Barlow, S. R. Marder, *Chem. Mater.* **2011**, *23*, 658-681.

[187] M.-J. Tsai, W.-L. Huang, L.-M. Chen, G.-L. Ruan, D. Luo, Z.-L. Tseng, K.-T. Wong, *J. Mater. Chem. C* **2023**, *11*, 1056-1066.

[188] J. Wei, D. Liu, K. Sun, W. Tian, W. Jiang, Y. Sun, *Dyes and Pigments* **2020**, *182*, 108624.

[189] L. Derue, S. Olivier, D. Tondelier, T. Maindron, B. Geffroy, E. Ishow, *ACS Appl. Mater. Interfaces.* **2016**, *8*, 16207-16217.

[190] B. Ma, B. J. Kim, D. A. Poulsen, S. J. Pastine, J. M. J. Fréchet, *Adv. Funct. Mater.* **2009**, *19*, 1024-1031.

[191] Y.-Q.-Q. Yi, W. Su, *Mater. Chem. Front.* **2023**, *7*, 6130-6140.

[192] K. Sun, X. Xie, Y. Liu, W. Jiang, X. Ban, B. Huang, Y. Sun, *J. Mater. Chem. C* **2016**, *4*, 8973-8979.

[193] D. Volz, A. F. Hirschbiel, D. M. Zink, J. Friedrichs, M. Nieger, T. Baumann, S. Bräse, C. Barner-Kowollik, *J. Mater. Chem. C* **2014**, *2*, 1457-1462.

[194] Z. Ma, B. Zhao, H. Gao, Y. Gong, R. Yu, Z. a. Tan, *J. Mat. Chem. A* **2022**, *10*, 18542-18576.

[195] C. W. Tornøe, C. Christensen, M. Meldal, *J. Org. Chem.* **2002**, *67*, 3057-3064.

[196] V. V. Rostovtsev, L. G. Green, V. V. Fokin, K. B. Sharpless, *Angew. Chem.* **2002**, *114*, 2708-2711.

[197] E. Haldón, M. C. Nicasio, P. J. Pérez, *Org. Biomol. Chem.* **2015**, *13*, 9528-9550.

[198] S. Schoffelen, M. Meldal, in *Modern Alkyne Chemistry*, **2014**, pp. 113-142.

[199] A. Sradha S, Sariga, L. George, A. Varghese, *Mater. Today Chem.* **2024**, *38*, 102112.

[200] R. Castarlenas, A. Di Giuseppe, J. J. Pérez-Torrente, L. A. Oro, *Angew. Chem. Int. Ed.* **2013**, *52*, 211-222.

[201] A. B. Lowe, *Poly* **2014**, *55*, 5517-5549.

[202] H. Kuniyasu, A. Ogawa, K. Sato, I. Ryu, N. Kambe, N. Sonoda, *J. Am. Chem. Soc.* **1992**, *114*, 5902-5903.

[203] U. Ali, K. J. B. A. Karim, N. A. Buang, *Polym. Rev.* **2015**, *55*, 678-705.

[204] R. G. W. Norrish, E. F. Brookman, *Proc. R. Soc. Lond. A. Math. Phys. Sci.* **1997**, *171*, 147-171.

[205] N. Terashima, Y. Sakata, T. Meguro, T. Hosoya, S. Yoshida, *Chem. Comm.* **2020**, *56*, 14003-14006.

[206] R. Müller, T. J. Feuerstein, V. Trouillet, S. Bestgen, P. W. Roesky, C. Barner-Kowollik, *Chem. Eur. J.* **2018**, *24*, 18933-18943.

[207] Y. Inoue, T. Ishida, N. Sano, T. Yajima, H. Sogawa, F. Sanda, *Macromol.* **2022**, *55*, 5711-5722.

[208] M. Kneidinger, A. Iturmendi, C. Ulbricht, T. Truglas, H. Groiss, I. Teasdale, Y. Salinas, *Macromol. Rapid Commun.* **2019**, *40*, 1900328.

[209] S. Tasan, O. Zava, B. Bertrand, C. Bernhard, C. Goze, M. Picquet, P. Le Gendre, P. Harvey, F. Denat, A. Casini, E. Bodio, *Dalton Trans.* **2013**, *42*, 6102-6109.

[210] S. S. Gunatilleke, A. M. Barrios, *J. Inorg. Biochem.* **2008**, *102*, 555-563.

[211] B. T. Boyle, M. C. Hilton, A. McNally, *J. Am. Chem. Soc.* **2019**, *141*, 15441-15449.

[212] W.-F. Fu, X. Gan, C.-M. Che, Q.-Y. Cao, Z.-Y. Zhou, N. N.-Y. Zhu, *Chem. Eur. J.* **2004**, *10*, 2228-2236.

[213] C.-H. Lam, W. K. Tang, V. W.-W. Yam, *Inorg. Chem.* **2023**, *62*, 1942-1949.

[214] D. Volz, M. Nieger, J. Friedrichs, T. Baumann, S. Bräse, *Langmuir* **2013**, *29*, 3034-3044.

[215] J. Zheng, X. Xu, D. G. Truhlar, *Theor. Chem. Acc.* **2011**, *128*, 295-305.

[216] A. Sillen, Y. Engelborghs, *J. Photochem. Photobiol.* **1998**, *67*, 475-486.

[217] F. B. Dias, J. Santos, D. R. Graves, P. Data, R. S. Nobuyasu, M. A. Fox, A. S. Batsanov, T. Palmeira, M. N. Berberan-Santos, M. R. Bryce, A. P. Monkman, *Adv. Sci.* **2016**, *3*, 1600080.

[218] D. Kelly, L. G. Franca, K. Stavrou, A. Danos, A. P. Monkman, *J. Phys. Chem. Lett.* **2022**, *13*, 6981-6986.

[219] K. Stavrou, L. G. Franca, A. P. Monkman, *ACS Appl. Electron. Mater.* **2020**, *2*, 2868-2881.

[220] H. Tanaka, K. Shizu, H. Nakanotani, C. Adachi, *J. Phys. Chem. C* **2014**, *118*, 15985-15994.

[221] A. Shundo, Y. Okada, F. Ito, K. Tanaka, *Macromol.* **2012**, *45*, 329-335.

[222] T. Serevičius, T. Bučiūnas, J. Bucevičius, J. Dodonova, S. Tumkevičius, K. Kazlauskas, S. Juršėnas, *J. Mater. Chem. C* **2018**, *6*, 11128-11136.

[223] S. Öner, S. Kuila, K. Stavrou, A. Danos, M. A. Fox, A. P. Monkman, M. R. Bryce, *Chem. Mater.* **2024**, *36*, 7135-7150.

[224] Q. Zhang, T. Komino, S. Huang, S. Matsunami, K. Goushi, C. Adachi, *Adv. Funct. Mater.* **2012**, *22*, 2327-2336.

[225] X.-L. Chen, R. Yu, Q.-K. Zhang, L.-J. Zhou, X.-Y. Wu, Q. Zhang, C.-Z. Lu, *Chem. Mater.* **2013**, *25*, 3910-3920.

[226] F. Wei, T. Zhang, X. Liu, X. Li, N. Jiang, Z. Liu, Z. Bian, Y. Zhao, Z. Lu, C. Huang, *Org. Electron.* **2014**, *15*, 3292-3297.

[227] M. Wallesch, A. Verma, C. Fléchon, H. Flügge, D. M. Zink, S. M. Seifermann, J. M. Navarro, T. Vitova, J. Göttlicher, R. Steininger, L. Weinhardt, M. Zimmer, M. Gerhards, C. Heske, S. Bräse, T. Baumann, D. Volz, *Chem. Eur. J.* **2016**, *22*, 16400-16405.

[228] A. Mauri, P. Kiefer, P. Neidinger, T. Messer, N. M. Bojanowski, L. Yang, S. Walden, A.-N. Unterreiner, C. Barner-Kowollik, M. Wegener, W. Wenzel, M. Kozlowska, *Chem. Sci.* **2024**, *15*, 12695-12709.

[229] C. A. Spiegel, M. Hackner, V. P. Bothe, J. P. Spatz, E. Blasco, *Adv. Funct. Mater.* **2022**, *32*, 2110580.

[230] X. Pan, Z.-X. Li, G. Wang, Y. Yang, X. Xin, H. Han, J.-M. Liu, Q.-H. Jin, D. Yan, *Cryst. Growth Des.* **2021**, *21*, 6425-6436.

[231] G. Sheldrick, *Acta Crystallogr. A* **2015**, *71*, 3-8.

[232] G. M. Sheldrick, *Acta Crystallogr. C* **2015**, *71*, 3-8.

[233] A. Spek, *Acta Crystallographica Section D* **2009**, *65*, 148-155.

[234] A. Spek, *Acta Crystallogr. C* **2015**, *71*, 9-18.

[235] O. V. Dolomanov, L. J. Bourhis, R. J. Gildea, J. A. Howard, H. Puschmann, *Journal of applied crystallography* **2009**, *42*, 339-341.

[236] G. M. Sheldrick, *Acta Crystallogr. A* **2015**, *71*, 3-8.

[237] A. D. Becke, *J. Chem. Phys.* **1993**, *98*, 5648-5652.

[238] S. Grimme, S. Ehrlich, L. Goerigk, *J. Comput. Chem.* **2011**, *32*, 1456-1465.

[239] A. Schäfer, H. Horn, R. Ahlrichs, *J. Chem. Phys.* **1992**, *97*, 2571-2577.

[240] P. J. Hay, W. R. Wadt, *J. Chem. Phys.* **1985**, *82*, 270-283.

[241] W. R. Wadt, P. J. Hay, *J. Chem. Phys.* **1985**, *82*, 284-298.

[242] P. J. Hay, W. R. Wadt, *J. Chem. Phys.* **1985**, *82*, 299-310.

[243] K. Yuan, Y. Liu, Y. Zhu, G. Zuo, L. Lü, Z. Li, *Sci. Bull.* **2012**, *57*, 328-335.

[244] R. Improta, V. Barone, G. Scalmani, M. J. Frisch, *J. Chem. Phys.* **2006**, *125*.

[245] T. Yanai, D. P. Tew, N. C. Handy, *Chem. Phys. Lett.* **2004**, *393*, 51-57.

[246] T. Lu, F. Chen, *J. Comput. Chem.* **2012**, *33*, 580-592.

[247] J. W. Furness, A. D. Kaplan, J. Ning, J. P. Perdew, J. Sun, *J. Phys. Chem. Lett.* **2020**, *11*, 8208-8215.

[248] E. Caldeweyher, S. Ehlert, A. Hansen, H. Neugebauer, S. Spicher, C. Bannwarth, S. Grimme, *J. Chem. Phys.* **2019**, *150*, 154122.

[249] C. Holzer, Y. J. Franzke, *J. Chem. Phys.* **2022**, *157*.

[250] F. Weigend, R. Ahlrichs, *Phys. Chem. Chem. Phys.* **2005**, *7*, 3297-3305.

[251] Y. J. Franzke, C. Holzer, J. H. Andersen, T. Begušić, F. Bruder, S. Coriani, F. Della Sala, E. Fabiano, D. A. Fedotov, S. Fürst, S. Gillhuber, R. Grotjahn, M. Kaupp, M.

Kehry, M. Krstić, F. Mack, S. Majumdar, B. D. Nguyen, S. M. Parker, F. Pauly, A. Pausch, E. Perlt, G. S. Phun, A. Rajabi, D. Rappoport, B. Samal, T. Schrader, M. Sharma, E. Tapavicza, R. S. Treß, V. Voora, A. Wodyński, J. M. Yu, B. Zerulla, F. Furche, C. Hättig, M. Sierka, D. P. Tew, F. Weigend, *J. Chem. Theory Comput.* **2023**, *19*, 6859-6890.

[252] U. Monkowius, M. Zabel, M. Fleck, H. Yersin, *Zeitschrift für Naturforschung B* **2009**, *64*, 1513-1524.

[253] J.-L. Bredas, *Mater. Horiz.* **2014**, *1*, 17-19.

8 Appendix

8.1 List of publications

Articles published and in preparation

- **C. R. Adam**, D. Marhöfer, A. Mauri, M. Nieger, O. Fuhr, P. Weis, G. Niedner-Schatteburg, W. Wenzel, S. Bräse, Introducing TADF Copper (I) Complexes with Dual Bridging Ligands and Excitation-Dependent Emission, *Inorg. Chem.*, *submission in process.*
- **C. R. Adam**, A. Danos, K. Bareikaite, S. Roth, E. Puttock, A. Monkman, S. Bräse, Highly soluble crosslinkable TADF Copper (I) Complexes for application in solution-processed OLEDs, *in preparation.*
- **C. R. Adam**, A. Vranic, S. Roth, M. Wegener, S. Bräse.
  Crosslinkable TADF Copper (I) Complexes as photoinitiator for application in two-photon absorption 3D laser nanoprinting, *planned.*
- V. Ferraro, **C. R. Adam,** A. Vranic, S. Bräse, Recent Advances of Transition Metal Complexes for Photopolymerization and 3D Printing under Visible Light, *Adv. Funct. Mater.* **2023**, *34*, 2302157. https://doi.org/10.1002/adfm.202302157
- M. Stahlberger, O. Steinlein, **C. R. Adam**, M. Rotter, J. Hohmann, M. Nieger, B. Köberle, S. Bräse, Fluorescent annulated imidazo[4,5-*c*]isoquinolines *via* a GBB-3CR/imidoylation sequence – DNA-interactions in pUC-19 gel electrophoresis mobility shift assay, *Org. Biomol. Chem.*, **2022**, *20*, 3598-3604.
  https://doi.org/10.1039/D2OB00372D.

Conference Posters and Oral Presentations

2023

- C. Adam, A. Mauri, D. Marhöfer, W. Wenzel, G. Niedner-Schatteburg, S. Bräse, Future 3D Additive Manufacturing, the 3DMM2O Conference, Kloster Schöntal, Germany, 03/2023.
  Novel luminescent Cu(I) Complexes as TADF Emitters for OLED applications.

- C. Adam, A. Mauri, D. Marhöfer, W. Wenzel, G. Niedner-Schatteburg, S. Bräse, French, Swiss and German Conference on Photochemistry, Photophysics and Photosciences (CP2P23), Mulhouse, France, 05/2023.
  Novel luminescent Cu(I) Complexes as TADF Emitters for OLED applications.

- C. Adam, A. Mauri, D. Marhöfer, W. Wenzel, G. Niedner-Schatteburg, S. Bräse, 25th International Symposium on the Photochemistry and Photophysics of Coordination Compounds (ISPPCC), Ulm, Germany 07/2023.
  Novel luminescent Cu(I) Complexes as TADF Emitters for OLED applications.
- C. Adam, A. Mauri, D. Marhöfer, W. Wenzel, G. Niedner-Schatteburg, S. Bräse, 10/2023 Cluster Meeting, Karlsruhe, Germany.
  Novel luminescent Cu(I) Complexes as TADF Emitters for OLED applications.

2022

- C. R. Adam, S. Bräse, MRS Spring Meeting & Exhibit, 05/2022, Honolulu, Hawaii.
  Novel luminescent Cu(I) Complexes as TADF Emitters for OLED applications.
- C. R. Adam, J. M. Busch, S. Bräse, Kick-off meeting of the International Core-to-Core Project: Design, Synthesis and Application of Next-Generation Organic Semiconductors, 09/2022, London (UK).
  Novel luminescent Cu(I) Complexes $L_4Cu_2X_2$ as TADF Emitters for OLED applications.
- C. R. Adam, S. Bräse, KSOP Summer School 09/2022, Bad Herrenalb, Germany.
  Luminescent Cu(I) Complexes as TADF Emitters for OLED applications.
- C. R. Adam, S. Bräse, Winter Cluster Meeting 10/2022, Heidelberg, Germany.
  Luminescent Cu(I) Complexes as TADF Emitters for OLED applications.
- C. R. Adam, J. M. Busch, S. Bräse, 3Met Workshop, 10/2022, Heidelberg, Germany.
  Novel luminescent Cu(I) Complexes $L_4Cu_2X_2$ as TADF Emitters for OLED applications (Poster and Oral presentation)

2021

- C. R. Adam, J. M. Busch, S. Bräse, Karlsruhe Day of Optics and Photonics, KDOP 11/2021, Germany.
  Luminescent Multimetallic TADF Copper(I) Complexes bearing different NHetPhos-Units for OLED Applications. (Poster and Flash-Talk)

- C. R. Adam, J. M. Busch, S. Bräse, Young scientist retreat 3DMM2O, 11/2021, Bad Herrenalb, Germany. *Luminescent Multimetallic TADF Copper(I) Complexes bearing different NHetPhos-Units for OLED Applications.*

9 Acknowledgements

First and foremost, I would like to express my sincere gratitude to my supervisor, Prof. Dr. Stefan Bräse, for his invaluable guidance and support throughout my doctoral studies. Over the past years, I have not only gained a deeper understanding of chemistry but have also developed skills in self-organization, supervising others, and navigating professional relationships. His trust in my work and the freedom to explore my research independently provided the perfect environment for my personal and scientific growth.

Prof. Dr. Uli Lemmer is kindly acknowledged for the acceptance of the co-reference of this thesis.

I would like to extend my greatest thanks to Prof. Dr. Monkman, for the opportunity to do an international research stay in his group in Durham, UK. Thanks to the whole group for your warm welcoming, especially to the funniest girls group! I am especially grateful to Dr. Andrew Danos who made this stay possible. Thanks to, Dr. Andrew Danos and Kamile Bareikaite for your collaboration and assistance throughout my time there and your invaluable guidance during my research stay.

More thanks go to my collaborations partners. Thanks to Dr. Anna Mauri as well as Christof Holzer from KIT for conducting the calculations throughout the thesis. Furthermore, big thanks to Daniel Marhöfer (RPTU) and Dr. Donghui Chen (IFG, KIT) for measuring the photophysical data of project N°1. Thanks to the WEGENER group and especially to Aleksandra Vranic for the 3D laser nanoprinting experiments, which greatly expanded my knowledge in the last weeks and contributed to the success of my work. I would like to thank Emma Puttock, who not only opened doors for me to measure photophysical data but also patiently answered every question I had and provided invaluable support with spectroscopic insights. Another thanks goes to Prof. Colsman and Dr. Christian Sprau, for giving me the permission and instruction to use their spectroscopic devices.

I want to thank the whole IOC department, including Dr. Andreas Rapp, Dr. Norbert Foitzik, Karolin Kohnle, Angelika Mösle, Lara Hirsch, Despina Savvidou, Richard von Budberg and Christoph Götz, for the analytical service and that you keep the institute running. Moreover I want to thank PD Patrick Weis, KIT, for measuring the mass spectrometry of the first complexes where I did not know how to approach this technique. Lastly, A big thank you, to Dr. Olaf Fuhr and Dr. Martin Nieger for measuring and analyzing the single crystals.

A huge thanks to Dr. Nicole Jung and Dr. Christin Bednarek for the scientific and organizational support, and Janine Bolz, Christiane Lampert, and Sabine Ghironi for their kindness, their exceptional administrative and organizational support and the nice way of keeping the group running.

Thanks for being part of the KSOP and HEiKA graduate school of the Excellence Cluster 3DMM2O. Thanks for offering numerous opportunities that allowed me to expand my knowledge across different fields and connect with fellow scientists. I would like to especially thank them, for the opportunity to participate in the MBA Fundamentals program at the Hector School. This opened a completely new field of knowledge for me. Furthermore, I appreciate the financial support provided by the Landesgraduiertenförderung as well as the DAAD in form of an international research scholarship for my stay in England.

My deepest thanks go to Simon Osswald and Valentin Schäfer, who generously proofread nearly the entire thesis and provided strong support throughout the writing process. I would also like to thank Julian Brückel, Aleksandra Vranic, Andrew Danos, Kamile Bareikaite, Emma Puttock, Anna Mauri, and Christof Holzer for taking the time to proofread various sections of this thesis. Your insights and feedback were invaluable.

I am really grateful that I did my PhD in the Bräse group. Thanks to the whole group for the kindly atmosphere. Also, out of the lab, whether during the break or after work, I had a really good time, and new friendships have emerged in these three years. Special thanks go to Julian, with whom I shared the lab and office for three years. Thank you for listening to my problems every day and always having a good advice no matter how annoying it was for you. Our good-natured teasing made every day a little bit more fun. Thanks to Simon Osswald, for always bringing positivity and good thoughts. Thank you to all my trainees and students I was allowed to supervise and who did a really good job: Elena Foitzik, Felix Schumann, Sebastian Roth, Paul Schündler. I learned a lot while supervising you and had a great time working with you. Special thanks go to Lisa Wanner, for helping me in the last weeks of lab work.

Lastly, I want to express my gratitude to all my friends and family for their support and encouragement throughout this journey and especially during the most stressful times. A very special thank you goes to Valle. Thank you for always having an open ear and for your humor and caring nature. Thank you for putting up with my quirks and for giving me endless patience. I look forward to continuing this journey with you and sharing new adventures together, I am happy to have you by my side.